2017

Supernova Cosmology And How To Talk About It: New Approaches To Cosmological Parameter Inference With Type Ia Supernovae And An Assessment Of The Education And Public Outreach Program Of The Dark Energy Survey

Rachel Cane Wolf
University of Pennsylvania, rachelcane12@gmail.com

Supernova Cosmology And How To Talk About It: New Approaches To Cosmological Parameter Inference With Type Ia Supernovae And An Assessment Of The Education And Public Outreach Program Of The Dark Energy Survey

Abstract
The discovery of the accelerating expansion of the Universe launched a new chapter in modern cosmology. Evidence for this accelerating expansion was first observed using Type Ia supernovae, which are brilliant, standardizable explosions that can be detected at large distances and used to infer cosmological parameters. New surveys are being designed to detect thousands of Type Ia supernovae, ushering in an era where parameter inference is no longer limited by statistics, but by systematic uncertainties. One of these systematics which is not well understood is the progenitor and progenitor environment, which can be investigated by studying properties of the supernova host galaxy. In this dissertation, I use the three-year sample of photometrically-classified and spectroscopically-confirmed Type Ia supernovae from Sloan Digital Sky Survey-II Supernova Survey to explore correlations between supernova luminosity and host-galaxy mass, metallicity, and star-formation rate. Observations suggest that such correlations should be incorporated to improve the standardization of Type Ia supernova luminosities. As such, new techniques for parameter inference will need to accommodate increasingly large samples of supernovae and a variety of standardization models. In this dissertation, I also introduce the BAyesian hierarchical Modeling with BIased Simulations (BAMBIS) algorithm, a novel approach to parameter inference using Type Ia supernovae which can, in principle, include systematics such as host-galaxy correlations in a robust statistical framework.

In addition to offering new scientific research opportunities, the quest to understand the evolution of the cosmos brings excellent opportunities for astronomers to engage in science education and public outreach (EPO). I present an analysis of the Dark Energy Survey EPO program, a unique large-scale astronomy EPO initiative organized and led entirely by professional astronomers. In this analysis, I detail the development of the EPO program as well as analyze the strengths and weaknesses of a subset of specific initiatives. I also discuss scientists' reported methods of communicating science with the public.

Degree Type
Dissertation

Degree Name
Doctor of Philosophy (PhD)

Graduate Group
Physics & Astronomy

First Advisor
Masao Sako

Keywords
Cosmology, Science Education, Science Outreach, Supernovae

Subject Categories
Astrophysics and Astronomy | Science and Mathematics Education

SUPERNOVA COSMOLOGY AND HOW TO TALK ABOUT IT: NEW APPROACHES TO COSMOLOGICAL PARAMETER INFERENCE WITH TYPE IA SUPERNOVAE AND AN ASSESSMENT OF THE EDUCATION AND PUBLIC OUTREACH PROGRAM OF THE DARK ENERGY SURVEY

Rachel Cane Wolf

A DISSERTATION

in

Physics and Astronomy

Presented to the Faculties of the University of Pennsylvania

in Partial Fulfillment of the Requirements for the Degree of Doctor of Philosophy

2017

Supervisor of Dissertation	Graduate Group Chairperson
Masao Sako	Ravi Sheth
Associate Professor of Physics and Astronomy	Professor of Physics and Astronomy

Dissertation Committee:

James Aguirre, Associate Professor of Physics and Astronomy

Gary Bernstein, Professor of Physics and Astronomy

Adam Lidz, Associate Professor of Physics and Astronomy

Evelyn Thomson, Associate Professor of Physics and Astronomy

Dedication

“Research is like a giant jigsaw puzzle ... with no edge pieces." – RCW

For Mom and Dad, who have always encouraged me to reach for the stars. For your unwavering support, love, and patience I will be forever grateful.

For my sister, who has been an incredible source of laughter and comfort in times of stress and self-doubt. One of these days, I’ll learn how to properly “woosahhhh."

And for my husband, who is my everything.

Acknowledgments

I would first like to thank my advisor, Masao Sako, who has been a fantastic mentor and who has taught me so many of the skills necessary to be a professional researcher. Thank you for always having your door open and for being a constant soundboard for my ideas. I also want to thank you for supporting my engagement and leadership in science education and public outreach (EPO) and for providing me the opportunity to pursue both my scientific interests and passion for science communication.

I have been privileged to work with other early career scientists who started out as colleagues and mentors and grew to become good friends. To Chris D'Andrea, John Fischer, Ravi Gupta, Elise Jennings, Marisa March, and Jennifer Mosher, thank you for taking me under your wings and teaching me everything from computer programming tricks to astrostatistics. My experiences with you all have been invaluable and have undoubtedly made me a better scientist.

My years at Penn have been some of the greatest of my life. For that I must thank my Philly Phamily, who have made living in Philadelphia feel like home. I also want to thank Jessie Taylor, Saul Kohn, Christina Krawiec, Alyssa Barlis, Dillon Brout, and Johanna-Laina Fischer for being such wonderful officemates. Thank you for all of the instructive science discussions, for office tea parties, and for office sing-alongs and dance breaks that were such bright lights when life was so often overwhelming.

I am also indebted to my EPO colleagues. Kathy Romer and Brian Nord, thank you for being such inspiring co-coordinators and for teaching me so much about EPO and collaboration management. Jane Horwitz and Kristen Coakley Ashare, thank you for

being valuable sources of EPO knowledge and experience and for sharing your world of broader impacts with me.

Over the years, my research experience has greatly benefited from collaborative endeavors with members of the Sloan Digital Sky Survey-II Supernova Survey and the Dark Energy Survey Supernova Program. In particular, I would like to thank Richard Kessler and Dan Scolnic at the University of Chicago for their guidance and help with many key aspects of the research presented in this thesis.

Finally, I thank my committee members James Aguirre, Gary Bernstein, Adam Lidz, and Evelyn Thomson for their time, guidance, and patience.

ABSTRACT

SUPERNOVA COSMOLOGY AND HOW TO TALK ABOUT IT:
NEW APPROACHES TO COSMOLOGICAL PARAMETER INFERENCE WITH TYPE IA SUPERNOVAE AND AN ASSESSMENT OF THE EDUCATION AND PUBLIC OUTREACH PROGRAM OF THE DARK ENERGY SURVEY

Rachel Cane Wolf

Masao Sako

The discovery of the accelerating expansion of the Universe launched a new chapter in modern cosmology. Evidence for this accelerating expansion was first observed using Type Ia supernovae, which are brilliant, standardizable explosions that can be detected at large distances and used to infer cosmological parameters. New surveys are being designed to detect thousands of Type Ia supernovae, ushering in an era where parameter inference is no longer limited by statistics, but by systematic uncertainties. One of these systematics which is not well understood is the progenitor and progenitor environment, which can be investigated by studying properties of the supernova host galaxy. In this dissertation, I use the three-year sample of photometrically-classified and spectroscopically-confirmed Type Ia supernovae from Sloan Digital Sky Survey-II Supernova Survey to explore correlations between supernova luminosity and host-galaxy mass, metallicity, and star-formation rate. Observations suggest that such correlations should be incorporated to improve the standardization of Type Ia supernova luminosities. As such, new techniques for parameter inference will need to accommodate increasingly large samples of supernovae and a variety of standardization models. In this dissertation, I also introduce the BAyesian hierarchical Modeling with BIased Simulations (BAMBIS) algorithm, a novel approach to parameter inference using Type Ia supernovae which can, in principle, include systematics such as host-galaxy correlations in a robust statistical framework.

In addition to offering new scientific research opportunities, the quest to understand the evolution of the cosmos brings excellent opportunities for astronomers to engage in science education and public outreach (EPO). I present an analysis of the Dark Energy Survey EPO program, a unique large-scale astronomy EPO initiative organized and led entirely by professional astronomers. In this analysis, I detail the development of the EPO program as well as analyze the strengths and weaknesses of a subset of specific initiatives. I also discuss scientists' reported methods of communicating science with the public.

Contents

Dedication ii

Acknowledgments iii

Abstract v

List of Tables xi

List of Figures xii

1 Introduction 1
- 1.1 The Path to Modern Cosmology . . . 2
  - 1.1.1 A Cosmological Model . . . 4
  - 1.1.2 SNe Ia as Cosmological Distance Indicators . . . 6
  - 1.1.3 Evidence for Cosmic Acceleration . . . 9
- 1.2 Type Ia Supernovae . . . 9
  - 1.2.1 Progenitor Scenarios . . . 11
  - 1.2.2 SN Ia Classification . . . 13
  - 1.2.3 Light-Curve Fitting and SN Ia Standardization . . . 17
- 1.3 Supernovae in the Era of Precision Cosmology . . . 20
  - 1.3.1 The Sloan Digital Sky Survey-II Supernova Survey . . . 22
  - 1.3.2 Supernova Host-Galaxy Correlations . . . 27
  - 1.3.3 The Joint Light Curve Analysis . . . 32

2 Statistical Frameworks for Cosmological Parameter Inference using SNe Ia 37
- 2.1 Introduction . . . 38
- 2.2 Outlining the SN Ia Cosmology Problem . . . 38
- 2.3 Traditional Cosmological Parameter Estimation Methods using SNe Ia . . . 40
- 2.4 New Statistical Techniques . . . 44
  - 2.4.1 Bayesian Parameter Inference . . . 44
    - 2.4.1.1 Bayesian Hierarchical Models . . . 45
    - 2.4.1.2 Bayesian Inference with SNe Ia . . . 46

2.4.2 Approximate Bayesian Computation . . . 48
2.4.2.1 ABC Parameter Inference with SNe Ia . . . 50
2.5 Assumptions and Challenges in SN Ia Parameter Inference . . . 53

3 SDSS-II Supernova Survey: An Analysis of the Largest Sample of Type Ia Supernovae and Correlations with Host-Galaxy Spectral Properties 58
3.1 Introduction . . . 58
3.2 Observational Data . . . 60
3.2.1 Supernovae . . . 60
3.2.2 Host Galaxies . . . 61
3.3 Supernova Selection and Properties . . . 63
3.4 Host Galaxy Spectral Analysis . . . 70
3.4.1 Methods . . . 70
3.4.2 Selection Criteria . . . 74
3.5 Derived Host Galaxy Properties . . . 76
3.5.1 Metallicity . . . 78
3.5.2 Star Formation Rate . . . 79
3.5.3 Host Mass . . . 80
3.5.4 Aperture Effects . . . 80
3.6 Results . . . 85
3.6.1 Host-Galaxy Properties . . . 86
3.6.2 SN Ia Light-curve Properties . . . 90
3.6.3 HR as a Function of Host-galaxy Properties . . . 91
3.6.4 HR as a Function of Multiple Host-galaxy Properties Simultaneously . . . 99
3.7 Discussion . . . 101
3.7.1 Comparing with Previous Studies . . . 103
3.7.2 Photometric versus Spectroscopic SN Ia Subsets . . . 105
3.7.3 Star-forming and Passive Hosts in the PM Sample . . . 109
3.8 Summary and Conclusions . . . 112

4 BAMBIS: Bayesian Hierarchical Modeling with Biased Simulations For SN Ia Cosmology Including Selection Effects 115
4.1 Introduction . . . 115
4.2 Overview of Bayesian Inference and Kernel Density Estimation . . . 119
4.3 The BAMBIS Algorithm . . . 125
4.3.1 Algorithm Caveats . . . 126
4.3.1.1 Noisy Likelihoods . . . 126
4.3.1.2 Posterior Sampling . . . 129
4.3.1.3 Choice of KDE . . . 130
4.3.1.4 Model and Data Outliers . . . 131
4.4 Proof of Concept . . . 132

4.4.1 Toy Problem 1: Gaussian Linear Regression Model 132
4.4.1.1 Results 135
4.4.1.2 Conclusions 140
4.4.2 Toy Problem 2: Gaussian Linear Regression with Selection Effects 141
4.4.2.1 Results 146
4.4.2.2 Conclusions 148
4.5 SN Ia Cosmology with the SALT2 Regression Model 154
4.5.1 Sample Forward-Model Simulation and Mock Data 157
4.5.2 Results 161
4.5.3 Conclusions 164
4.6 Summary and Future Work 167

5 Engaging the Public as a Scientist-Communicator 170
5.1 Introduction 170
5.2 Astronomy: A Science to Captivate an Audience 171
5.3 Why Engage in Astronomy EPO? 172
5.4 Astronomers' Attitudes Towards Education & Public Outreach 174
5.5 Summary 176

6 Education & Public Outreach in The Dark Energy Survey 177
6.1 Introduction 177
6.2 Survey Overview, Collaboration Structure, and the Evolution of the DES EPO Program 180
6.2.1 DES Project and Science 181
6.2.2 Organization and Management 184
6.2.3 The Evolution of EPOC 187
6.2.4 DES EPO Guiding Principles 188
6.2.5 DES Social Media Strategy and User Summary 189
6.3 Programming for a Collaboration 193
6.3.1 The `darkenergysurvey.org` Website 196
6.3.1.1 Take-Home Messages 197
6.3.2 The DArchive: DES Results in a Nutshell 199
6.3.2.1 Project Organization and Implementation 199
6.3.2.2 Social Media Reach: The DArchive 202
6.3.2.3 Discussion 203
6.3.2.4 Take-Home Messages 204
6.3.3 DES Thought for the Day (DEST4TD) 205
6.3.3.1 Project Organization and Implementation 206
6.3.3.2 Social Media Reach: DEST4TD 207
6.3.3.3 Discussion 208
6.3.3.4 Take-Home Messages 210
6.3.4 DarkBites 211

6.3.4.1 Projection Organization and Implementation 212
6.3.4.2 Social Media Reach: DarkBites 213
6.3.4.3 Discussion 214
6.3.4.4 Take-Home Messages 214
6.3.5 DEScientist of the Week 215
6.3.5.1 Project Organization and Implementation 215
6.3.5.2 Social Media Reach: DEScientist of the Week 216
6.3.5.3 Discussion 216
6.3.5.4 Take-Home Messages 217
6.3.6 Multilingual EPO 218
6.3.6.1 Project Organization and Implementation 218
6.3.6.2 Discussion 219
6.3.6.3 Take-Home Messages 219
6.3.7 Image & Video Curation and Creation 219
6.3.7.1 Project Organization and Implementation 220
6.3.7.2 Discussion 221
6.3.7.3 Take-Home Messages 222
6.3.8 In-Person Outreach Activities 222
6.3.8.1 The Cosmic Kitchen 222
6.3.8.2 DES Adler After Dark 223
6.3.8.3 Discussion 226
6.4 Internal DES EPO Reporting 227
6.5 Summary and Conclusions 230

7 Conclusions **235**
7.1 Type Ia Supernova Luminosity and Host-Galaxy Correlations 235
7.2 Statistical Frameworks for SN Ia Cosmology 236
7.3 Astronomer Engagement in Education and Public Outreach 238
7.4 Scientific Acknowledgements 239

A SDSS-SNS Supplemental Data and Analysis **242**
A.1 Comparison to DR10 242
A.2 Correcting For Residual Trends with SN Color 249
A.3 PM Sample SN Ia and Host-Galaxy Data 250

B Supplemental DES Education and Public Outreach Materials and Analysis **259**
B.1 Program Logic Models 259
B.2 Internal Survey of EPO Projects 259

Bibliography **267**

List of Tables

3.1 Cumulative PM Sample Definition . . . 67
3.2 GANDALF Emission-Line Setup File . . . 75
3.3 Cumulative MZS Sample Definition . . . 78
3.4 LINMIX Linear Fit Results for HR as a Function of Derived Host-Galaxy Properties . . . 93
3.5 Comparison of Correlations Found between HR and Host-galaxy mass (M), Gas-Phase Metallicity (Z), and Specific Star Formation Rate (S) . . . 104
3.6 Fit Results for HR as a Function of Host Properties: Spec-Ia and Phot-Ia . . . 107

4.1 Standard Deviation of Gaussian Fits to KDE of $p(x)$ . . . 122
4.2 D1 Input Parameter Values . . . 134
4.3 Best fit Parameter Estimates Using D1 . . . 136
4.4 Parameter Bias Over 25 Data Realizations . . . 138
4.5 Bins and selection fractions for the example selection function . . . 143
4.6 Best Fit Parameter Estimates Using D2 . . . 148
4.7 Parameter Bias Over 25 Data Realizations . . . 150
4.8 Bins and selection fractions for example SN Ia selection function . . . 159
4.9 Parameter Values for Mock Data . . . 161
4.10 Best Fit Parameter Estimates Using D3 . . . 162

6.1 List of Online DES EPO Resources . . . 180

A.1 Properties of SNe Ia and their Host Galaxies . . . 251
A.1 Properties of SNe Ia and their Host Galaxies . . . 252
A.1 Properties of SNe Ia and their Host Galaxies . . . 253
A.1 Properties of SNe Ia and their Host Galaxies . . . 254
A.1 Properties of SNe Ia and their Host Galaxies . . . 255
A.1 Properties of SNe Ia and their Host Galaxies . . . 256
A.1 Properties of SNe Ia and their Host Galaxies . . . 257
A.1 Properties of SNe Ia and their Host Galaxies . . . 258

List of Figures

1.1 Evidence for the accelerating expansion of the Universe. Top Left: Corrected distance modulus as a function of redshift, adapted from Riess et al. (1998). Bottom Left: Effective SN Ia magnitude as a function of redshift, adapted from Perlmutter et al. (1999). As shown in both plots, data from the two experiments most closely aligned with a flat cosmology with both positive Ω_m and Ω_Λ components. Right: Ω_m-Ω_Λ contour regions from both the HZT and SCP, adapted from Perlmutter and Schmidt (2003). Constraints are presented at the 1σ, 2σ, and 3σ confidence levels; results presented here are consistent with $\Omega_{m,0} \approx 0.3$ and $\Omega_{\Lambda,0} \approx 0.7$. 10

1.2 Schematic diagram of the stellar life cycle, showing the different channels for the gravitational core-collapse and thermonuclear SNe. Image credit: SETI Institute. 15

1.3 Representative optical spectra (top) and light curves (bottom) of several SN types, reproduced from Filippenko (1997). SN Ia are unique compared to other types: their spectra exhibit no hydrogen features and their light curves have brighter maxima and fade away more gradually after peak. 16

1.4 The SN Ia "stretch-luminosity" and "color-luminosity" relations. The left panel features a plot of peak magnitude in three different filters as a function of decline rate, reproduced from Phillips (1993). The decline rate is given by $\Delta m_{15}(B)$ which signifies the decline in peak B-band magnitude in the 15 days post peak; smaller values of $\Delta m_{15}(B)$ correspond to SN Ia that fade away more slowly and are intrinsically brighter. The right panel features Hubble diagrams (μ versus redshift) for SNe Ia that have been corrected for the luminosity dispersion and extinction using light-curve stretch and color, reproduced from Riess et al. (1996). The top panel displays SNe Ia that have not been corrected; the bottom shows SNe Ia that have had this correction applied, and the corresponding reduction in Hubble diagram dispersion. 18

1.5 SNe detected since 1885. TOP: Total number of SNe detected by 1997; the two experiments which confirmed the existence of dark energy are represented in grey and yellow. BOTTOM: Total number of SNe detected by 2010, including new-large scale projects such as SDSS and SNLS. Frames adapted from `https://commons.wikimedia.org/wiki/File:Sn_discoveries.gif`. 21

1.6 Hubble diagram for subsamples of spectroscopically-confirmed (top, 457 SNe Ia) and photometrically-classified (bottom, 827 SNe Ia) SNe Ia from the full three-year SDSS-SNS, adapted from Sako et al. (2014). The large scatter for low-redshift ($z < 0.2$) objects in the photometrically-classified sample is likely due to contamination from core-collapse SNe. The black trend line is not the best fit cosmology from the sample, but a fiducial cosmology used to guide the eye. 25

1.7 Expected bias in distance modulus measurements in the SDSS-SNS, as determined from simulations, using two different sets of sample selection criteria, adapted from Sako et al. (2014). The bias using the set of stricter selection criteria (red, Selection Criteria 2) is more severe than that using Selection Criteria 1 (black). 26

1.8 HR for the full three-year set of spectroscopically-confirmed SNe Ia, adapted from Sako et al. (2014). The dashed and dot-dashed red lines represent the best fit cosmology $\pm 2\sigma$, respectively. 27

1.9 Correlation between HR and host-galaxy mass, reproduced from Kelly et al. (2010). The weighted averages in the high and low mass bins (black crosses) differ by 0.11 magnitudes (2.5σ). The upper panel features the posterior distribution of the slope obtained using MCMC sampling. . . . 28

1.10 Correlation between HR and host-galaxy mass, reproduced from Childress et al. (2013). The top panel features a linear and step fit; a non-zero slope is found with 3.4σ confidence and 0.077 magnitude difference is found between the low and high-mass bins. The bottom panel features the HR and host-mass correlation in bins, which suggest the trend is perhaps not best fit by a linear function, but by a step function with an intermediate transition region. 30

1.11 Constraints on w and Ω_m for four variations of the the SN Ia luminosity standardization relation, adapted from Campbell et al. (2016). Results shown in black are without any host-galaxy corrections. 33

1.12 Hubble diagram and corresponding Hubble residuals (top) and best fit cosmology contours (bottom), reproduced from Betoule et al. (2014). Filled gray contours represent the 68% and 95% confidence regions for the full JLA sample. Red dashed contours exclude data from the SDSS-SNS. 36

2.1 Sample BHM reproduced from March et al. (2011). Solid lines indicate probabilistic connections; dashed lines indicate deterministic connections. Parameters to be constrained are circled in red, latent variables are circled in blue, and the data are circled in green. The classic Bayesian model would not include the Σ_x hyperparameter describing the distribution of the latent x_i. 47

2.2 Sample Bayesian hierarchical networks for the SN Ia cosmology problem, reproduced from March et al. (2011, top) and Rubin et al. (2015, bottom). Solid lines indicate probabilistic connections; dashed lines indicate deterministic connections. The UNITY model builds on that of March et al. (2011) and includes the same set of cosmological and standardization parameters and hyperparameters as a subset of their larger parameter set. 49

2.3 Weyant et al. (2013) comparison of uncertainty regions in the $w - \Omega_m$ parameter space using ABC and the χ^2 method as described in Kessler et al. (2009a). 51

2.4 1σ and 2σ contour regions using the "Light-Curve" (top) and "Tripp" (bottom) metrics reproduced from Jennings et al. (2016). The yellow stars indicate the true values used in the simulated data set. Green contours represent the results using the ABC metric; purple contours represent results using traditional χ^2-minimization parameter inference. Dashed (ABC) and dot-dashed (χ^2-minimization) lines indicate the increased parameter uncertainty when including systematics. 54

3.1 Comparison of MC simulation (red histogram) and SDSS-SNS data (black points). The MC distributions are normalized to the low-z ($z < 0.25$) data. Error bars on the data points represent the square root of the number of SNe Ia in the respective bin. Distributions are displayed for the redshift (top), SALT2 color (middle) and SALT2 stretch (bottom). 66

3.2 Difference between the measured and true distance modulus (defined as $\mu_{\rm BIAS}$) from our simulations, as a function of redshift. Data points are inverse-variance weighted averages in redshift bins of width 0.025 with error bars representing the width of each bin. Each bin contains at least 500 SNe Ia. 68

3.3 Distribution of HRs calculated using the derived `SALT2mu` distance moduli. Histograms are stacked such that the Phot-Ia (blue) and Spec-Ia (green) add to the total number in a given bin. The mean of the distribution is 0.014 mag and the standard deviation is 0.228. We remove from our sample seven SNe with HRs $> 3\sigma$ from the mean (corresponding to HR < -0.668 and HR > 0.697) as it is highly unlikely that these outliers are normal SNe Ia. All outliers removed in this way are Phot-Ia. This reduces the mean and standard deviation to 0.002 and 0.187, respectively. 69

3.4 Sample GANDALF fit of the BOSS spectrum for the host of CID 13897. Wavelengths in this spectrum are given in the rest frame. Flux density is in units of 10^{-17} erg s^{-1} cm^{-2} Å^{-1}. The data are shown in black with the best fit model overplotted in red. The green dot-dashed line represents the continuum fit and the blue line shows the emission spectrum, which is obtained by subtracting the continuum model from the best fit model. Residual points between the data and the best fit spectrum are also shown in purple. Vertical dashed lines indicate the emission lines predominantly used in our analysis. The three lower panels display the specific regions that contain these lines. 72

3.5 BPT diagram for host galaxies of our SNe Ia. The galaxies displayed here have passed selection criteria through A/N cuts, as outlined in Tables 3.1 and 3.3. We have trimmed the axes to better focus on the bulk of our sample; therefore, some star-forming hosts and AGNs may not be shown. Galaxies to the right of the blue curve (Kewley 2001) are deemed AGNs (black points), while those to the left of the red curve (Kaufmann 2003b) are regarded as star-forming (green points). Those galaxies that lie between the two curves (purple points) are labeled "Composite." We continue our analysis using galaxies to the left of the blue curve, although not all will be included in the final sample for analysis. 77

3.6 Host metallicity as a function of g-band fiber fraction for hosts that satisfy BPT cuts. The dashed line at g-band fiber fraction = 0.2 represents the threshold fiber fraction above which the derived gas-phase metallicity is considered indicative of the global average (Kewley et al., 2005). Inverse-variance-weighted binned averages, of approximately equal-sized bins, are plotted in red. There is a slight (0.07 dex) decrease in metallicity with increasing fiber fraction. 82

3.7 Distribution of host gas-phase metallicities for SDSS (green) and BOSS (blue) galaxies in our MZS sample, with total number counts shown in the top panel and the corresponding cumulative distribution function in the bottom panel. To focus on the bulk of our sample, we leave out one host with $Z < 8.2$ from this figure. The vertical dashed line at 12+log(O/H) = 8.69 represents the solar metallicity value, shown for comparison. The SDSS spectra are systematically higher metallicity than the BOSS spectra due to how targets were selected for the two samples. 84

3.8 Redshift distributions of the PM and MZS samples. Histograms are stacked such that the number of Spec-Ia (green) and Phot-Ia (blue) shown in each bin add to the total number of SNe Ia in that bin. The mean and median redshifts of the PM and MZS samples are each $z = 0.24$. For both samples, the median redshift of the Spec-Ia is 0.19 and the median redshift of the Phot-Ia is 0.26. 87

3.9 Mass distributions of our PM (dashed) and MZS (solid) galaxies are displayed in the top left panel. The means of the PM and MZS mass distributions (in log(M/$M_\odot$)) are 10.5 and 10.2, respectively. The bottom left panel presents the cumulative fraction of hosts as a function of mass. The right panels show our galaxy masses as a function of redshift. 88
3.10 Left panel: metallicity distribution of galaxies in our MZS sample. The mean of the metallicity distribution is $Z = 8.84$. Right panel: sSFR distribution of galaxies in our MZS sample. The mean of the sSFR distribution is log(sSFR)$= -9.43$. The inset figures of both panels display the respective host properties as a function of redshift. Axes of the inset figures have been adjusted to focus on the metallicity and sSFR redshift dependence; as such, some data points are excluded from the plots. 89
3.11 SNe Ia color (c) and stretch (x_1) as a function of derived host properties. The left panel displays data from the PM sample; the middle and right panels show data from the MZS sample. Axes have been truncated to focus on the bulk of the data. 92
3.12 HR as a function of host-galaxy mass for the PM sample. The LINMIX linear fits to the data are shown in dashed black; red squares represent inverse-variance-weighted binned averages, with bins split at log($M/M_\odot$)$=$ 10.5. The significance of a nonzero slope is 3.6σ and the difference in HR between the high and low-mass bins is 0.048 mag. This result indicates that more massive galaxies host overluminous SNe Ia. 94
3.13 Nonparametric regression fit of HR as a function of host-galaxy mass. The best fit is presented in red with the approximate corresponding 1σ confidence interval. A span of $\alpha = 0.6$ was used for the fit. 96
3.14 HR as a function of gas-phase metallicity for the MZS sample. These points are separated at 12+log(O/H) = 8.9 to create high- and low-metallicity bins. Red squares indicate the inverse-variance-weighted average of these bins. The difference between the binned averages is 0.057 mag. The linear LINMIX fit to the data is shown in dashed-black; there is a 1.4σ significance of a nonzero slope, which suggests that more metal-rich galaxies host overluminous SNe Ia. 97
3.15 HR as a function of sSFR for the MZS sample. Points are separated at log(sSFR) = -9.4 to create high- and low-sSFR bins. Red squares indicate the inverse-variance-weighted average of these bins. The difference between the binned averages is 0.013 mag. The linear LINMIX fit to the data is shown in dashed-black; there is a 0.42σ significance of a nonzero slope. This slight correlation suggests that galaxies with lower sSFRs host overluminous SNe Ia. 98
3.16 HR as a function of metallicity and sSFR for the MZS sample in low- and high-mass bins. LINMIX linear fits to the data are shown in dashed-black. In each case, the significance of a nonzero slope is $\lesssim 0.8\sigma$. 102

3.17 HR as a function of derived host properties for the Spec and Phot SN Ia samples separately. The first row displays HR as a function of mass for the PM sample, and the lower two rows show HR as a function of derived host properties for the MZS sample. LINMIX fits to the data are shown in dashed-black. Fit results are reported in Table 3.6. 106

3.18 Contour intervals showing the 68% and 95% confidence regions of the Spec-Ia (green) and Phot-Ia (blue) LINMIX posterior distributions for the HR–mass relation. 109

3.19 HR as a function of host mass for the PM sample, separated into star-forming and passive galaxy groups. LINMIX fits to the data are shown in dashed-black. For our star-forming galaxies (left panel) we find the significance of a nonzero slope is 3.3σ. The trend with the passive galaxies (right panel) is consistent with flatness (0.09σ). 111

4.1 BHM describing the SN Ia model used for this sample implementation of BAMBIS (Section 4.5). Dashed lines represent deterministic relationships and solid lines indicate probabilistic relationships. The diagram features three distinct parameter types: parameters which will be varied in the MCMC (solid oval), fixed parameters (solid rectangle), and derived parameters (dashed oval). Blue parameters represent hyperparameters and corresponding derived parameters; green parameters represent cosmological parameters. Latent variables are enclosed by a single circle; the distributions of observed variables are enclosed by concentric circles. The variable S_i indicates whether or not a given SN Ia passes selection criteria and is included in the final observed data set. 121

4.2 KDE estimates of $p(x)$ (blue histogram) using four distinct choices of bandwidth. The bandwidth determined by Scott's Rule is ≈ 0.18. The density estimate using the narrower bandwidth is clearly too noisy (green curve), while the density estimate using too large a bandwidth (magenta curve) appears oversmoothed and does not appropriately estimate the peak of the distribution. Corresponding standard deviations of Gaussian fits to the KDEs are presented in Table 4.1. 123

4.3 Two dimensional PDF evaluated using an analytic multivariate Gaussian (left) and Gaussian KDE (right) with arbitrarily large bandwidth. Denser regions are shown in blue; regions of low density are shown in light pink. The bandwidth was selected to emphasize the effect of choosing an inappropriate kernel size; the broadening of the PDF can be seen in both the y and z dimensions. 124

4.4 Example of noisy likelihood for a sample mock data set sampling over a wide range of parameter space (Θ_a, left panel) and closer to the peak (Θ_b, right panel). The true value of the parameter used to generate the mock data is indicated by the dashed red lines. Blue dots represent an individual evaluation of the likelihood at each point in Θ_a and Θ_b; black lines connect the means at each proposed point. 128
4.5 BHM for toy example without additional measurement uncertainty or sample selection. Dashed lines indicate deterministic relationships; solid lines indicate probabilistic relationships. Model parameters are circled in green and hyperparameters are circled in blue. Latent variables are enclosed in a single circle; observed variables are enclosed in a double circle. 133
4.6 1-D marginalized distributions of observed variables w, x, y, and z for `D1`. 135
4.7 1σ and 2σ credible regions of the $\theta_{\rm ex1}$ and $\psi_{\rm ex1}$ parameter posteriors using `D1`. Yellow stars indicate the true parameter values. Priors on the parameters are listed in Table 4.3. 137
4.8 Best fit results over 25 realizations of mock data. Black points represent the 16%, 50% and 84% quantiles of the 1-D marginalized PDFs for each parameter, i.e., the connected black line represents the 1σ uncertainty region for a given 1-D marginalized PDF. Red dashed lines indicate the true value used to create the mock data sets. 139
4.9 Variance over 100 realizations of the total log likelihood as a function of simulation size at a single $\theta_{\rm ex1}$ and $\psi_{\rm ex1}$. The black star indicates the simulation size used to estimate the density for the results presented in Section 4.4.1.1. 140
4.10 True and observed w and t; note the axes have been truncated to focus on the densest region of the 2-D distribution. Black lines indicate the bin widths in the w dimension and the corresponding $t^{\rm obs}$ limit. The black lines demonstrate the sharp, step cutoffs which are difficult to estimate with a KDE. 142
4.11 1-D marginalized distributions of the true (blue) and observed (orange) variables of `D2`. The selection function used to construct the observed distribution is detailed in Table 4.5. 143
4.12 1σ and 2σ uncertainty regions for the $\theta_{\rm ex2}$ and $\psi_{\rm ex2}$ posteriors inferred using `D2`. True parameter values are indicated by yellow stars. Best fit results and priors are presented in Table 4.6. 147
4.13 Best fit results over 25 realizations of mock data including selection effects. Black points represent the 16%, 50% and 84% quantiles of the 1-D marginalized PDFs for each parameter, i.e., the connected black line represents the 1σ uncertainty region for a given 1-D marginalized PDF. Red dashed lines indicate the true value used to create the mock data sets. . . . 149

4.14 2-D marginalized densities of the 4-D $\{w,x,y,t\}$ "test data" set in bins of w_j. w_j bins are plotted in ascending order from left to right. Each pair of rows compares the discrete PDF of the "test data" (bottom) to the density estimate from the KDE evaluated at the binned "test data" points (top) in each of the five w_j bins. Dark blue indicates the densest regions, light pink indicates regions of lowest density. 152

4.15 1-D marginalized binned discrete (red) and estimated (blue) PDFs of the $50,000$ sample "test data" set in w_j bins. w_j bins are plotted in ascending order from left to right. 153

4.16 1-D marginalized distributions of the true (blue) and observed (orange) SN Ia light-curve parameters and redshifts in `D3`. The selection function used to construct the observed sample is given in Table 4.8. 160

4.17 1σ and 2σ uncertainty regions for the twelve parameters in θ and ψ_{skewnorm}. Yellow stars indicate the true values used in the simulation input. Priors and best fit results for each of the parameters are listed in Table 4.10. . . . 163

4.18 Contours of w_0 and Ω_m posteriors using five realizations of mock data. Filled contours represent 1σ and 2σ uncertainty regions; the yellow star indicates the true parameter values. Uncertainty regions inferred from `D3` are shown in purple. 164

4.19 Comparison of w_0 and Ω_m posteriors inferred with BAMBIS (blue) and a standard analytic χ^2 used in a Gaussian likelihood (green). Contours represent 1σ and 2σ uncertainty regions; posteriors have been scaled by their respective median values. 166

5.1 Number of working (blue) and free time (yellow) hours spent on average on EPO activities per week, reproduced from Dang and Russo (2015). . . 175

5.2 Percentage of research grants astronomers currently invest (blue) and suggest to allocate (yellow) into public outreach engagement, reproduced from Dang and Russo (2015). 176

6.1 Map of DES collaborating institutions. Figure credit: Judit Prat, IFAE, DES-Spain. 183

6.2 Schematic diagram illustrating various components of DES which provide inspiration for the EPO effort. Examples included here are merely a subset. 184

6.3 DES internal organization chart, including the EPOC (purple), adapted from the DES director's presentation at the Fall 2016 collaboration meeting. Solid arrows indicate a group that reports to and/or is appointed by the box to which it points. Dashed arrows indicate that the people named in that group are members of the higher-level Committee to which that box points (e.g., science working group coordinators are members of the Science Committee, and the Science Committee co-chairs are members of the Executive Committee). Dotted two-way arrows indicates a line of mutual communication. 186
6.4 Total number of DES Facebook page followers per month. The red star signifies when the EPOC assumed control of the Facebook page and began posting content regularly. 190
6.5 Percent of Facebook followers (blue), users reached (yellow), and engaged users (green) over various user ages. Information is also separated into men (left) and women (right) user groups. The 25-24 user age group is the most popular in each user group and for both men and women. While the men are roughly 75% of the total page followers ($n = 7914$), women make up nearly 40% of the total engaged users ($n \approx 500$). 192
6.6 Percent of Facebook followers (blue, $n = 7914$), users reached (yellow, $n \approx 15000$) and engaged users (green, $n \approx 500$) in the five most popular user-identified countries and languages of origin. 192
6.7 Global distribution of Facebook likes per post for DES EPO products featured on social media described in this work (DArchive – Section 6.3.2; DEST4TD – Section 6.3.3; DarkBites – Section 6.3.4; DEScientist of the Week 6.3.5) . Blue dashed and solid lines in the top panel indicate the mean and median, respectively. The bottom panel features a stacked histogram showing the number of posts per EPO product discussed in this section. 195
6.8 Screenshots of original (left) and updated (right) DES website home pages. Note that the screenshot of the new page does not capture the full screen as the template is widescreen. 198
6.9 DArchive work flow for each of the three project organization iterations. . 200
6.10 Number of people reached on Facebook by the DArchive posts each month in 2016. Points indicate an individual DArchive post or a reference to the DArchive catalog on the DES website. The mean and median number of Facebook users reached per post across all DES social media projects are shown in blue dashed and solid lines, respectively. 203
6.11 Number of Facebook users reached by DEST4TD posts in 2016. Each black point represents an individual DEST4TD post. Red points represent the average reach per month. The global mean and median number of Facebook users reached per post across our various social media projects are shown in blue dashed and solid lines, respectively. 208

6.12 Three most popular DEST4TD posts of 2016 submitted by collaboration members as determined by social media reach. Posts were submitted in January 2016 (bottom left), September 2016 (top), and December 2016 (bottom right), respectively. 209

6.13 An example DarkBite image. The associated caption: If the lifetime of the universe were compressed to a single calendar year, the entirety of human history would occur in the last 15 seconds of December 31. Image Credit: Chihway Chang, University of Chicago; Fact Credit: Daniel Nagasawa, Texas A&M University. 212

6.14 Number of people reached by DarkBites posts in 2016 on Facebook. Each black point represents an individual DarkBites post. Red points represent the average reach per month. The mean and median number of Facebook users reached per post across all the DES EPO social media projects are shown in blue dashed and solid lines, respectively. 213

6.15 Facebook reach for DEScientist of the Week posts in 2016. Black points represent an individual post; red diamonds represent the monthly average. The global mean and median number of Facebook users reached per post across our various social media projects are shown in blue dashed and solid lines, respectively. 216

6.16 EPOC coordinator A.K. Romer interacting with a young audience member during TCK, May 2015. © Erika Martin 224

6.17 Activity types for EPO projects recorded with an "In-Person" component. Note that one "In-Person" activity might include overlap between several sub-categories, e.g., one activity may include a Talk with Slides and a Demonstration. 228

A.1 Comparison of output A/N values between this work and DR10. The line $y = x$ is shown in red. The ranges in both directions have been limited to focus on the bulk of the data; 91%, 84%, 91% and 87% of the data in the Hα, Hβ, [N II], and [O III] lines are shown, respectively. For all emission lines, we find that our A/N values are systematically higher than those reported in DR10. 244

A.2 Comparison of the observed emission-line flux measurements between this work and DR10 where Hα and Hβ $A/N > 2$. All figure axes have been truncated to focus on the bulk of the data; 90%, 97%, 96%, and 95% of the data points in the Hα, Hβ, [O III], and [N II] lines are shown, respectively. The top row shows a direct comparison of line flux with the line $y = x$ shown in red. The corresponding distributions in the bottom row present the difference between the DR10 measurements and those in this work. The σ value used is the uncertainties from each work added in quadrature. 246

A.3 Comparison of extinction values used in this work (black) and in DR10 (red). While this work uses Case B recombination to calculate the extinction, DR10 relies on the GANDALF output as measured using the spectral continuum fit. 247
A.4 Comparison of KD02 gas-phase metallicities derived using emission-line fluxes from this work and DR10, where Hα and Hβ $A/N > 2$. Figure axes have been truncated to focus on the bulk of the data; 96.7% of the data points are shown here. A direct comparison of metallicity measurements is shown on the left (the line $y = x$ is plotted in red for comparison); the difference in metallicities is shown on the right. The median and standard deviation of the difference, including outliers which are not displayed, are -0.08 dex and 3.73 dex, respectively. 248
A.5 HR as a function of SALT2 color (left panel) and stretch (right panel) for the PM sample. Inverse-variance weighted average bins of width 0.025 dex and 0.5 dex, for c and x_1 respectively, are displayed in red; each bin contains at least 30 SNe Ia. 249

B.1 Logic model describing The DArchive project structure and outcomes. . . 260
B.2 Logic model describing DEST4TD project structure and outcomes. 261
B.3 Logic model describing DarkBites project structure and outcomes. 262
B.4 Logic model describing DEScientist of the Week project structure and outcomes. 263

Chapter 1

Introduction

Nearly twenty years ago, two teams of astronomers made the surprising discovery that the Universe is expanding at an accelerating rate. This ground-breaking conclusion was reached using observations of roughly 40 Type Ia supernovae (Riess et al., 1998; Perlmutter et al., 1999). The significance of this contribution was officially recognized by the global scientific community, and the analysis team leads were awarded the Nobel Prize in Physics in 2011. This discovery launched the era of modern cosmology and has led to one of the greatest unsolved problems in modern physics.

The mysterious phenomenon that drives the accelerating expansion of our Universe has been called "dark energy" - *dark* as its nature remains an enigma, and *energy* as the accelerated expansion is a behavior perhaps explained by a homogenous "vacuum energy" permeating all of space and opposing the force of gravity. Independent observations using a variety of cosmological probes have demonstrated that this dark energy constitutes roughly 70% of the mass-energy density of the Universe today.

To this day, Type Ia supernovae (SNe Ia) continue to be one of the most precise tools used to study dark energy (Howell, 2011). These standardizeable cosmological distance indicators provide an excellent means to measure the evolution of the cosmos over time. It is widely accepted that a SN Ia is the result of a thermonuclear explosion of a carbon-oxygen white dwarf in a binary system whose mass has reached the Chandresekhar limit

(Whelan and Iben, 1973; Nomoto, 1982; Iben and Tutukov, 1984; Webbink, 1984; Hillebrandt and Niemeyer, 2000). The explosion physics and the nature of the progenitor, i.e the white dwarf's companion, however, remain unknown. Our ability to more precisely standardize SN Ia may rest on furthering our understanding of these mechanics and other correlations related to the SN Ia and its environment. Measurements of dark energy will only improve if we can make the SN Ia standardization model more complete.

In this Chapter, I discuss the standard cosmological model and how SNe Ia were used in the discovery of dark energy. I also describe how SNe Ia are distinguished from other types of stellar explosions. Finally, I describe the significance of recent large-scale SNe surveys and the transition to the era of precision cosmology.

1.1 The Path to Modern Cosmology

For thousands of years, curiosity about the history and fate of our Universe, or *cosmology*, has been a key component in the evolution of science. The earliest studies of cosmology primarily focused on celestial mechanics. Ancient Greek philosophers such as Aristotle and Ptolemy sought to explain the motions of the "heavenly bodies" they observed wandering through the sky (Ptolemy and Toomer, 1984). This fascination with the cosmos only grew over time and was a major focus of the "scientific revolution" of the 16th century. Copernicus' theory of heliocentrism, Kepler's laws of planetary motion, and Galileo's critical observations of sunspots and of Jupiter's moons were just some of the remarkable contributions that emerged during the time. In the following century, Isaac Newton published his laws of motion and universal gravitation, paving the way for grander theories about the Universe at large and the era of *modern cosmology*.

The study of cosmology was transformed in the early twentieth century when Albert Einstein published his theory of General Relativity. In his work Einstein postulated, among many other things, a unified description of gravity as a property of space and time. This formalism included a *cosmological constant*, a term which would account for

the energy density of the vacuum of space. The cosmological constant was introduced to counteract the attractive force of gravity and was necessary to explain the widely accepted notion that while individual parts of the Universe, such as stars and planets, were in motion, the Universe itself was static.

One of the first astronomers to apply Einstein's theory of relativity to cosmology was Georges Lemaître. In 1927, Lemaître proposed that the Universe was not actually static, but expanding (Lemaître, 1927). Lemaître's work, however, which also included one of the first propositions of a "Big Bang," was met with much skepticism. Two years later, Edwin Hubble provided observational evidence for an expanding Universe when he plotted the velocities of galaxies as a function of their distance and found a positive linear correlation (Hubble, 1929):

$$v = H_0 d\,. \tag{1.1}$$

Here, v is the object's recessional velocity, d is its distance, and H_0 is the *Hubble constant*, often measured in $\mathrm{km\,s^{-1}\,Mpc^{-1}}$ which describes the present-day rate of expansion. Proof and acceptance of an expanding Universe was a radical departure from the status quo, transforming the way people thought about the cosmos.

Hubble's Law (Eq. 1.1) is explored, in practice, by using a more fundamental quantity proportional to an object's velocity, known as *redshift*. Redshift (z) describes how the wavelength of light from an emitted source (λ_{emit}) changes relative to the wavelength recorded by an observer (λ_{obs}). As an object recedes from an observer, the wavelength of its emitted light gets stretched and the object appears redder, thus the name red-shift. We define redshift such that

$$z \equiv \frac{\lambda_{\mathrm{obs}} - \lambda_{\mathrm{emit}}}{\lambda_{\mathrm{emit}}}\,. \tag{1.2}$$

An object's redshift can be directly obtained by measuring the absorption and emission features of its spectrum.

In contrast, an object's distance cannot be directly measured. Instead, astronomers use the light received from a distant object as a proxy for its distance. For an object with some

observed flux, F, and intrinsic luminosity, L, the *luminosity distance*, D_L, is described as

$$D_L^2 = \frac{L}{4\pi F}\,. \tag{1.3}$$

Astrophysical objects with known luminosities are referred to as *standard candles* and are incredibly useful for estimating cosmological parameters. SNe Ia fall into this category of objects and their use in cosmological analyses is detailed in Section 1.2.

Hubble's observations dramatically changed our understanding of the Universe. After making his initial observations, he concluded that the present-day expansion rate is roughly 500 $\mathrm{km\,s^{-1}\,Mpc^{-1}}$. Since then, countless experiments have sought to measure H_0 more precisely, with current estimates using different probes hovering around 70 $\mathrm{km\,s^{-1}\,Mpc^{-1}}$ (Riess et al., 2016; Grieb et al., 2017; Bonvin et al., 2017). Of course, measurements of the Hubble constant only tell us about the present expansion of the Universe. Understanding the full expansion history, which has become the crux of modern cosmology, requires analysis of the expansion rate over time, or the evolution of the more fundamental *Hubble parameter*, $H(t)$.

1.1.1 A Cosmological Model

At its core, physics (and astrophysics) relies on mathematical models to explain the phenomena of the natural world. Such is the case in cosmology, where a variety of models, each incorporating different assumptions, explain the evolution of the Universe. Many of these models make use of an arbitrary length *scale factor*, $a(t)$, where today $a(t) = 1$, and $a(t) = 0$ at the very beginning of the Universe. We can relate this scale factor to the redshift

$$1 + z = \frac{1}{a}\,, \tag{1.4}$$

and define the Hubble parameter as

$$H(t) \equiv \frac{\dot{a}}{a}\,, \tag{1.5}$$

where $\dot{a}$ signifies the change in scale factor over time.

Establishing a length scale in this way is useful for applications of Einstein's theory of general relativity, in which a *metric* describes the geometric and causal structure of spacetime. The standard metric used in cosmology, often referred to as the Friedmann-Lemaître-Robertson-Walker metric, rests on the assumptions that our Universe is homogenous and isotropic. These assumptions lead to a set of analytic equations that can be used to probe the evolution, and mass-energy density, of the Universe

$$\frac{\dot{a}^2 + kc^2}{a^2} = \frac{8\pi G\rho + \Lambda c^2}{3}, \tag{1.6}$$

and

$$\frac{\ddot{a}}{a} = -\frac{4\pi G}{3}\left(\rho + \frac{3p}{c^2}\right) + \frac{\Lambda c^2}{3}. \tag{1.7}$$

In these equations, G is Newton's constant of gravitation, Λ is the cosmological constant, c is the speed of light, k represents a constant denoting spacial curvature, ρ is the mass-energy density, and p is the pressure. Note that Einstein's cosmological constant, which was initially introduced as a term to account for the vacuum energy-density of space, remains as a crucial factor in the modern equations. Rather than being used to explain a static Universe, the cosmological constant is now used to explain the observed accelerating expansion.

As far as we are aware, there are four components that contribute to the total mass-energy of the Universe: spatial curvature, matter (majority dark matter), radiation, and dark energy. If we assume each of these entities can be described as a fluid, then we can then relate the density and pressure of each component at a particular scale factor (redshift, time) with an equation of state

$$p = w(a)\rho(a)c^2, \tag{1.8}$$

where we allow the density to evolve with scale factor and w is known as the *equation of state parameter*. In most cases, we assume w is a constant and does not evolve, i.e., $w(a) = w = w_0$. Rather than use the density directly, cosmologists prefer to use a dimensionless parameter, $\Omega = \frac{\rho}{\rho_c}$, where ρ_c is the total mass-energy density necessary for a Universe with no curvature.

Combining Eq. 1.8 with Eqs. 1.6 and 1.7 and transforming from scale factor to redshift space, we have an expression for the Hubble parameter as a function of the mass-energy densities of curvature (subscript k), matter (subscript m), radiation (subscript r), and dark energy (subscript Λ):

$$H^2(z) = H_0^2 \left(\Omega_{m,0}(1+z)^3 + \Omega_{r,0}(1+z)^4 + \Omega_{k,0}(1+z)^2 + \Omega_{\Lambda,0}(1+z)^{3(1+w_\Lambda)} \right) . \quad (1.9)$$

Observations using a variety of cosmological probes, including SNe Ia, Baryon Acoustic Oscillations (BAO), and the Cosmic Microwave Background (CMB), have been studied to estimate the components of the mass-energy density of the Universe today. The radiation component has been found to be $\Omega_{r,0} \lesssim 10^{-4}$ and evidence suggests the Universe is very close to spatially flat, i.e., $\Omega_{k,0} \approx 0$ (Komatsu et al., 2011; Planck Collaboration et al., 2016). Analyses using SNe Ia alone as well as those using combined probes find results consistent with $w_\Lambda = -1$, where w_Λ is assumed to be constant in redshift (Conley et al., 2011; Planck Collaboration et al., 2016). Currently, the most robust measurements of the mass-energy density indicate a flat Universe, comprised of 5% baryonic matter (matter that includes atoms of any sort), 27% cold dark matter, and 68% dark energy, i.e., $\Omega_{m,0} = 0.32$ and $\Omega_{\Lambda,0} = 0.68$ (Planck Collaboration et al., 2016); $\Omega_m + \Omega_\Lambda = 1$. This model is commonly referred to as a flat, Λ-Cold Dark Matter (ΛCDM) cosmology. While current observations are consistent with the ΛCDM model, w is only constrained to within 10%; therefore, there is the possibility for dark energy models with $w \neq -1$. The suite of models which allow for a varied value of w while still maintaining the current consensus of the mass-energy density are referred to as wCDM models.

1.1.2 SNe Ia as Cosmological Distance Indicators

In the context of SN Ia cosmology, what is perhaps most relevant is how the Hubble parameter relates to the luminosity distance, D_L. If we assume the Universe is spatially flat, then the luminosity distance is defined as

$$D_L = \frac{c}{H_0}(1+z) \int_0^z \frac{dz'}{H(z')} . \quad (1.10)$$

Therefore, precise measurements of the luminosity distance will yield precise estimates of the Hubble parameter and corresponding mass-energy densities.

Astronomers conventionally use *magnitude*, rather than flux, as a means of referring to the brightness of an object. This system remains as an artifact of ancient Greek astronomy, where the brightness of an object was scaled with the brightest objects having a magnitude of one and the dimmest having a magnitude of six (Ryden, 2003). In modern times, astronomers have adapted a standard, logarithmic magnitude scale, with the brightest objects having the smaller magnitudes.

The *apparent magnitude*, m, is defined as

$$m = -2.5\log(\frac{f}{f_0}), \tag{1.11}$$

where f is the observed flux of the object and f_0 is a standard reference flux, e.g., the flux of the star Vega. We also define an *absolute magnitude*, M, as a measure of the apparent magnitude the object would have were it 10 parsecs away, where

$$M = -2.5\log\left(\frac{L}{f_0 4\pi(10\text{pc})^2}\right). \tag{1.12}$$

The *distance modulus* of an object, μ, is defined as the difference between the absolute and apparent magnitude

$$\mu \equiv m - M = 5\log(D_L) - 5, \tag{1.13}$$

where D_L is measured in parsecs. In this form, μ acts a distance, but is measured in magnitudes rather than kilometers or parsecs.

This expression for the distance modulus, however, is incomplete, as the apparent magnitude m is not a direct representation of the object's flux. Photons emitted from any astrophysical object, whether observed by eye or by camera, are detected by a set of filters, either biological or instrumental, that detect light at different wavelengths. In the case of modern telescopes, filters are designed to collect light in a distinct set of passbands such that the color of an object can be obtained by comparing the amount of photons observed in each passband. Due to cosmological redshift, light from extragalactic objects will

appear redder. This shift in observed flux will depend on the transmission functions of the filters and the redshift and spectral energy distribution (SED) of the source. Furthermore, as emitted photons travel from the source they must pass through galactic dust, both from the object's own galaxy and from our Milky Way, which will make the object appear redder and dimmer. Therefore the amount of this shift in observed flux also depends on the composition of the dust through which the photons must pass.

To obtain a more accurate estimate of the object's apparent magnitude, we must correct for these two effects. Correcting for the photons in the redder passbands is known as a K-correction, and requires knowledge of or an assumption about the SED of the object of interest. The Milky Way extinction correction, referred to as A, is fairly well understood (Schlegel et al., 1998; Schlafly and Finkbeiner, 2011), but extinction from the host galaxy must be estimated and marginalized over when computing the apparent brightness. If we consider $m^{\rm obs}$ to be the apparent magnitude as measured by an observer, then the complete distance modulus is defined as

$$\mu = (m^{\rm obs} - A - K) - M = 5\log(D_L) - 5\,. \tag{1.14}$$

As described in Section 1.2, SNe Ia are in a class of astrophysical objects known as "standard candles." This means that the intrinsic luminosity, and thus absolute magnitude M, of SNe Ia are known. Using the relationship between apparent magnitude and distance modulus, and the definition of the distance modulus as a function of the Hubble parameter, we can use SNe Ia to infer cosmological parameters such as $\Omega_{m,0}$, $\Omega_{\Lambda,0}$, and w. For example, for a wCDM, cosmology, we can write the distance modulus as

$$\mu = 5\log\left(\frac{c}{H_0^2}(1+z)\int_0^z \frac{dz'}{\sqrt{\Omega_{m,0}(1+z')^3 + \Omega_{\Lambda,0}(1+z')^{3(1+w_\Lambda)}}}\right) - 5\,. \tag{1.15}$$

Rather than using the derived luminosity distance, the typical SN Ia Hubble diagram (e.g., Figures 1.6 and 1.12) features μ as a function of z. SNe Ia on the low-redshift part of the diagram help constrain the local Universe, e.g., H_0, while SNe Ia on the high-redshift part of the diagram are more useful for constraining changes in the Hubble parameter.

1.1.3 Evidence for Cosmic Acceleration

In the 1990s, two teams of astronomers set out to use SNe Ia to measure the rate of expansion of the Universe. At the time, it was believed that the Universe was matter dominated, and that the rate of expansion should be decreasing due to gravitational attraction. The goal of the members of the Supernova Cosmology Project (Perlmutter et al., 1999, SCP) and High-Z Supernova Search Team (Riess et al., 1998, HZT) was to measure the deceleration parameter q_0, where

$$q \equiv -\frac{\ddot{a}a}{\dot{a}^2}\,, \tag{1.16}$$

and $q_0 > 0$ indicates deceleration. To ensure their analyses could constrain the Hubble parameter in the local and distant Universe, both teams included SNe Ia from the nearby ($z \lesssim 0.15$) Calan/Tololo Supernova Search (Hamuy et al., 1996). Using independent, corrected (see Section 1.1.2), and standardized (see Section 1.2.3) measurements of spectroscopically-confirmed SNe Ia, both teams observed that high-redshift SNe Ia were fainter than expected and made the revolutionary conclusion that the Universe is not decelerating, but in fact accelerating in its expansion.

Figure 1.1 displays the evidence for dark energy from the SCP and HZT. The left panel of Figure 1.1 features Hubble diagrams (HZT top, SCP bottom) with SN Ia observations plotted as a function of redshift. As shown in both plots, SN Ia data from these experiments most closely aligned with a flat cosmology with positive contributions from both Ω_m and Ω_Λ, and notably $\Omega_\Lambda > 0$. The right panel presents the Ω_m-Ω_Λ contour regions at 1σ, 2σ and 3σ confidence levels. Constraints from both experiments are consistent with today's more precise measurements of $\Omega_{m,0} \approx 0.3$ and $\Omega_{\Lambda,0} \approx 0.7$.

1.2 Type Ia Supernovae

SNe Ia are critical probes of the standard cosmological model. Observations of these incredibly bright explosions ($L \sim 10^{10} L_\odot$), visible out to high redshifts, have provided evidence for the accelerating expansion of the universe (Riess et al., 1998; Perlmutter

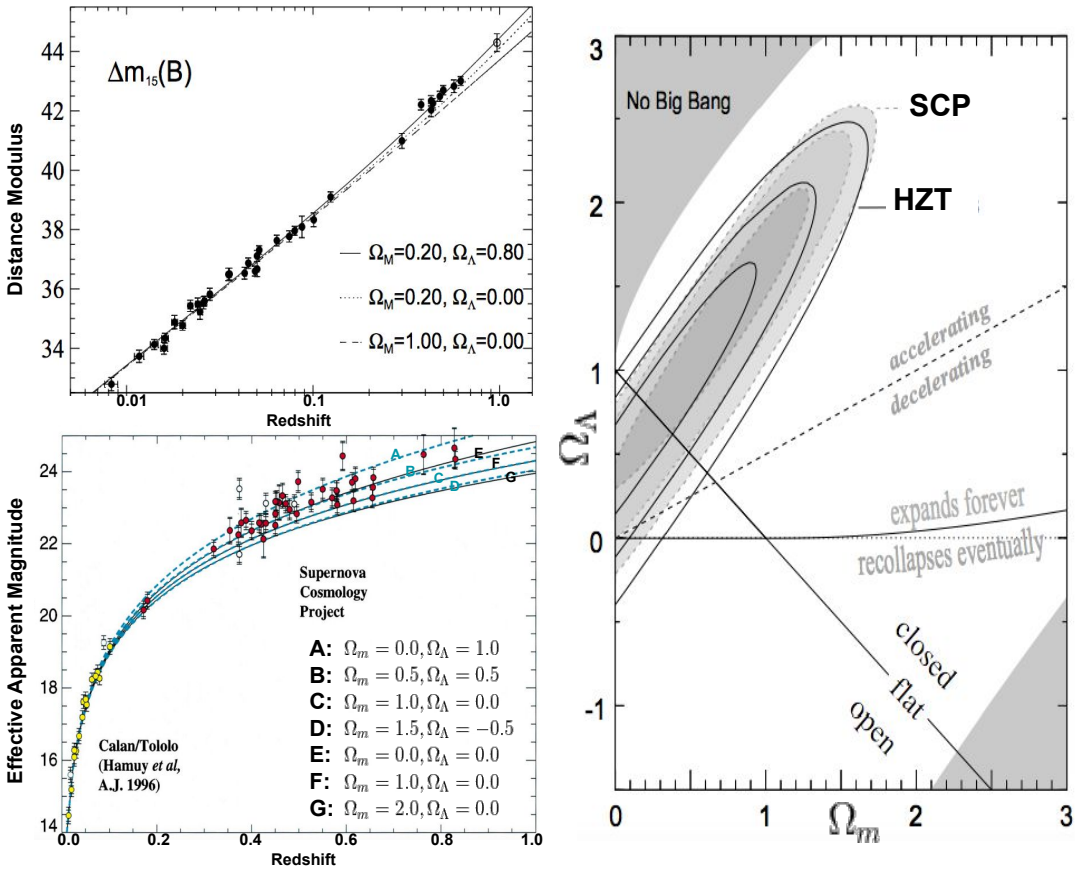

Figure 1.1: Evidence for the accelerating expansion of the Universe. Top Left: Corrected distance modulus as a function of redshift, adapted from Riess et al. (1998). Bottom Left: Effective SN Ia magnitude as a function of redshift, adapted from Perlmutter et al. (1999). As shown in both plots, data from the two experiments most closely aligned with a flat cosmology with both positive Ω_m and Ω_Λ components. Right: Ω_m-Ω_Λ contour regions from both the HZT and SCP, adapted from Perlmutter and Schmidt (2003). Constraints are presented at the 1σ, 2σ, and 3σ confidence levels; results presented here are consistent with $\Omega_{m,0} \approx 0.3$ and $\Omega_{\Lambda,0} \approx 0.7$.

et al., 1999) and the existence of dark energy. These objects are often referred to as "standardizable candles," as their intrinsic luminosity can be calibrated with light-curve width ('stretch') and optical color (Phillips, 1993; Hamuy et al., 1996; Riess et al., 1996; Tripp, 1998). After applying these corrections using light-curve fitting techniques, there remains a 1σ dispersion in peak brightness of about 0.1 magnitudes, corresponding to about five percent in luminosity distance, D_L (Conley et al., 2011; Betoule et al., 2014).

1.2.1 Progenitor Scenarios

SNe Ia are a class of stellar explosion whose physical mechanism, and thus spectra and light curves (brightness over time), are fundamentally different from other types of SNe. These other SNe, including Type II and Types Ib and Ic, are driven by the gravitational core collapse of young, massive ($M \gtrsim 8M_{\odot}$) stars (Smartt, 2009). While the progenitor of a SN Ia has yet to be observed, it is believed that SN Ia are the result of a thermonuclear explosion occurring as the mass of a carbon-oxygen white dwarf approaches the Chandresekhar limit ($M_{\mathrm{CH}} \approx 1.4M_{\odot}$) and the temperature increases enough to ignite carbon (Whelan and Iben, 1973; Nomoto, 1982; Iben and Tutukov, 1984; Webbink, 1984; Hillebrandt and Niemeyer, 2000).

While the observable features of SNe Ia provide clues about the explosion mechanism, the exact nature of the progenitor system is unknown. There are currently two leading theories describing SN Ia explosion mechanics: the single-degenerate and double-degenerate scenarios. In both cases, the white dwarf is one of two stars in a binary star system. In the single-degenerate scenario, the white dwarf's companion is a non-degenerate main sequence or red giant star. The white dwarf accretes mass from its companion via Roche lobe overflow or from stellar wind (Whelan and Iben, 1973). In the double-degenerate scenario, two white dwarfs spiral into each other and ultimately merge (Iben and Tutukov, 1984; Webbink, 1984). Recent observations suggest potential links between progenitor scenarios and sub-classes of SNe Ia, but do not constrain a definitive SN Ia progenitor channel (Maeda and Terada, 2016). Although the SN Ia progenitor has never been

directly detected, progenitor scenarios have been constrained using a variety of observational tools.

The most direct means to identify the SN Ia binary companion is to search in pre- and post-explosion images. Using archival Hubble Space Telescope (HST) and Chandra X-ray images of the location near SN 2011fe, Li et al. (2011) reject the possibility of a red giant or He main sequence ($M \gtrsim 1.0 M_{\odot}$) companion. Kelly et al. (2014) use archival Keck and HST images and post-explosion HST imaging of SN 2014J and determine observational flux constraints, which also reject a red giant companion. It has been predicted that during the explosion the companion's envelope will deposit thermal emission into the SN ejecta; this will result in excessive blue emission in the first days after explosion and is more exaggerated for a more extended companion (Marietta et al., 2000; Kasen, 2010). Such excess emission was detected in observations of SN Ia iPTF14atg and SN Ia 2015, providing evidence for the single-degenerate scenario (Cao et al., 2015; Marion et al., 2016).

SN Ia spectra, from which we can extract information about the explosion and local environment, are also useful tools for studying progenitor scenarios. There are two stages during which information about the progenitor system can be studied with spectra: explosive nucleosynthesis and radiation transport (Parrent et al., 2014). In their analysis of SN 2011fe spectra, Nugent et al. (2011) find that the early-time spectra are dominated by intermediate-mass elements and strong features from unburnt carbon and high-velocity oxygen and that the typical double ionized species features are absent. The spectra also do not exhibit features of early shock. These observations are used to constrain the luminosity of the companion star and provide support for a degenerate SN Ia companion. Spectral analysis of PTF 11kx provides evidence of the single-degenerate scenario (Dilday et al., 2012). Spectral features indicate the presence of fast-moving interior circumstellar material, velocities of absorption features that are larger than typical red giant winds, and a delay between the explosion and the emergence of Ca and H emission. These features can only be explained by a model in which the white-dwarf accretes mass through wind

from a red giant.

SN Ia explosion modeling is yet another useful tool as different explosion mechanisms should lead to differing appearances of SNe Ia. Favored models in the single-degenerate scenario include delayed detonation, failed deflagration, and double denotation (Maeda and Terada, 2016). In the double-degenerate scenario, popular explosion models include white-dwarf mergers, white-dwarf collisions, and violent mergers. Röpke et al. (2012) use observations from SN 2011fe to explore the delayed-detonation and violent merger models and find the data more closely match the white dwarf merger; yet there is not an obvious statistical preference for one model over another. A possible shortcoming of the violent merger model, however, is that it should lead to a larger diversity of light curves, spectral features, and polarization signals than currently observed (Bulla et al., 2016). While models have well-constrained the mass of the progenitor white dwarf (Maeda and Terada, 2016), no single model can best explain current SN Ia observations.

1.2.2 SN Ia Classification

The term 'super-novae' was first coined in 1934 by Baade and Zwicky to describe astrophysical objects which presented a "very curious puzzle": the "maximum brightness they emit [is] nearly as much light as the whole nebula in which they originate" (Baade and Zwicky, 1934). In the same work, Baade and Zwicky also note that this group of objects can be found, "not only in the nearer systems, but [...] all over the accessible range of nebular distances."

Today, this class of astrophysical objects is separated into two main subgroups categorically defined by their explosion mechanics. SNe Ia are believed to be the result of the thermonuclear explosion of white dwarf stars, the carbon-oxygen remnants of low-mass stars. The exact explosion mechanism remains unknown, but it is believed that the white dwarf star accretes mass from a companion and that ultimately its internal density becomes high enough to overcome electron degeneracy pressure. The increase in density reignites nuclear fusion, which spreads throughout the star. Fusion reignition sends two

shockwaves: first a wave of subsonic deflagration and then one of supersonic detonation. This process completely destroys the star and leaves behind no remnant. A typical SN Ia produces $0.4-0.9M_{\odot}$ of ^{56}Ni (Kasen and Woosley, 2007). The thermonuclear fusion of C and O in the white dwarf progenitor produces intermediate mass elements (Mg, Si, S, Ca) along with iron-peak elements (Ni, Co, Fe) (Hillebrandt and Niemeyer, 2000). The light curve is powered by the Comptonization of gamma rays produced by the radioactive decay of ^{56}Ni ($t_{\frac{1}{2}} = 6.1$ days) $\rightarrow$ ^{56}Co ($t_{\frac{1}{2}} = 77$ days) $\rightarrow$ ^{56}Fe, where $t_{\frac{1}{2}}$ indicates the half-life of decay (Colgate and McKee, 1969; Stritzinger et al., 2006).

Other SNe are believed to be the result of the gravitational core collapse of massive stars at the end of the stellar life cycle. The progenitor stars of these explosions are massive enough that the temperature and density in the core can facilitate nuclear fusion. This process begins with the fusion of hydrogen to helium and continues with heavier elements until an iron core remains. At this point, the star can no longer produce enough energy to sustain its outer layers. The end of fusion results in an imbalance between the force of gravity and electron degeneracy pressure in the core, ultimately leading to energy loss by neutrinos, photo-disintegration, and the collapse of the core to a neutron star. Observations of the remnants of this type of SN show that the explosion can leave behind a black hole or neutron star, which is likely dependent on the initial mass of the progenitor. Unlike SN Ia progenitors which have yet to be directly observed, ≈ 10 core-collapse SNe have had their progenitors identified as supergiants (Smartt, 2009). SN Types II, Ib, and Ic fall under this category of core-collapse explosions.

Figure 1.2 shows a schematic diagram of the stellar life cycle, including the distinct channels which result in core-collapse and thermonuclear SNe.

SNe Ia optical spectra and light curves are distinct from other types of SNe (Filippenko, 1997). SN Ia spectra are devoid of hydrogen and have strong Si II lines at peak brightness. SN Ib and SN Ic spectra also lack hydrogen; SN Ib feature helium and Si II at peak brightness, while SN Ic spectra do not have helium or silicon features. SN II are defined by the presence of hydrogen in their spectra. Generally, the shape of SN Ia

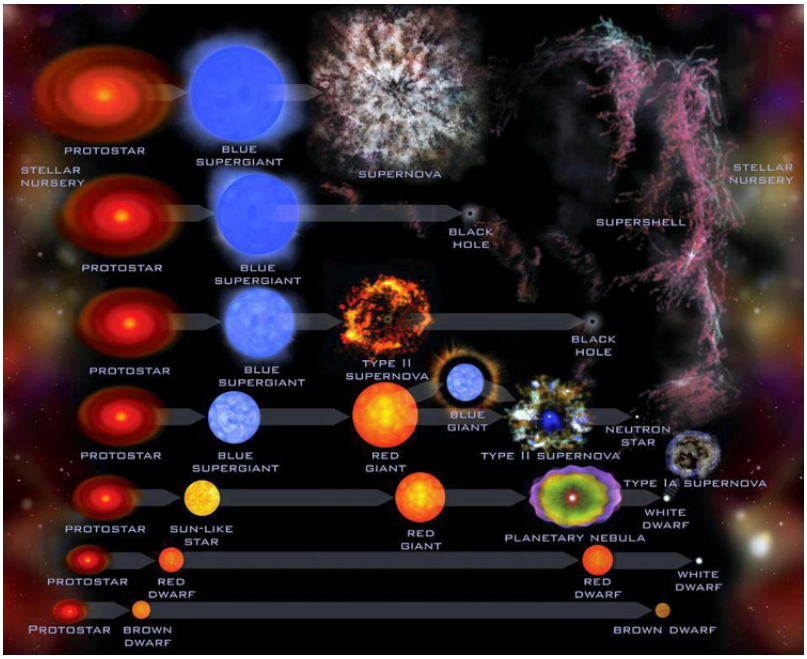

Figure 1.2: Schematic diagram of the stellar life cycle, showing the different channels for the gravitational core-collapse and thermonuclear SNe. Image credit: SETI Institute.

light curves are roughly similar from event to event, while there is much dispersion in the shapes of SN II light curves. SN Ia light curves exhibit narrow maxima and fade away gradually, while SN II light curves tend to have broader peaks and fade away more sharply. Figure 1.3 presents a comparison of representative optical spectra and light curves for the different SN types.

SNe Ia can be classified by either their spectra or light curves. *Spectroscopic confirmation* is the surest way to identify a SN Ia, but spectroscopic classification of an entire SN sample may be difficult due to limited resources. *Photometric classification*, on the other hand, is a means of identifying SN Ia using observed photometry and assigning a type probability to an individual SN light curve. Photometrically-classified SN Ia samples, however, are more likely to contain contaminants from other SN types. Pure and efficient photometric classification is essential as SN surveys grow in size and scope.

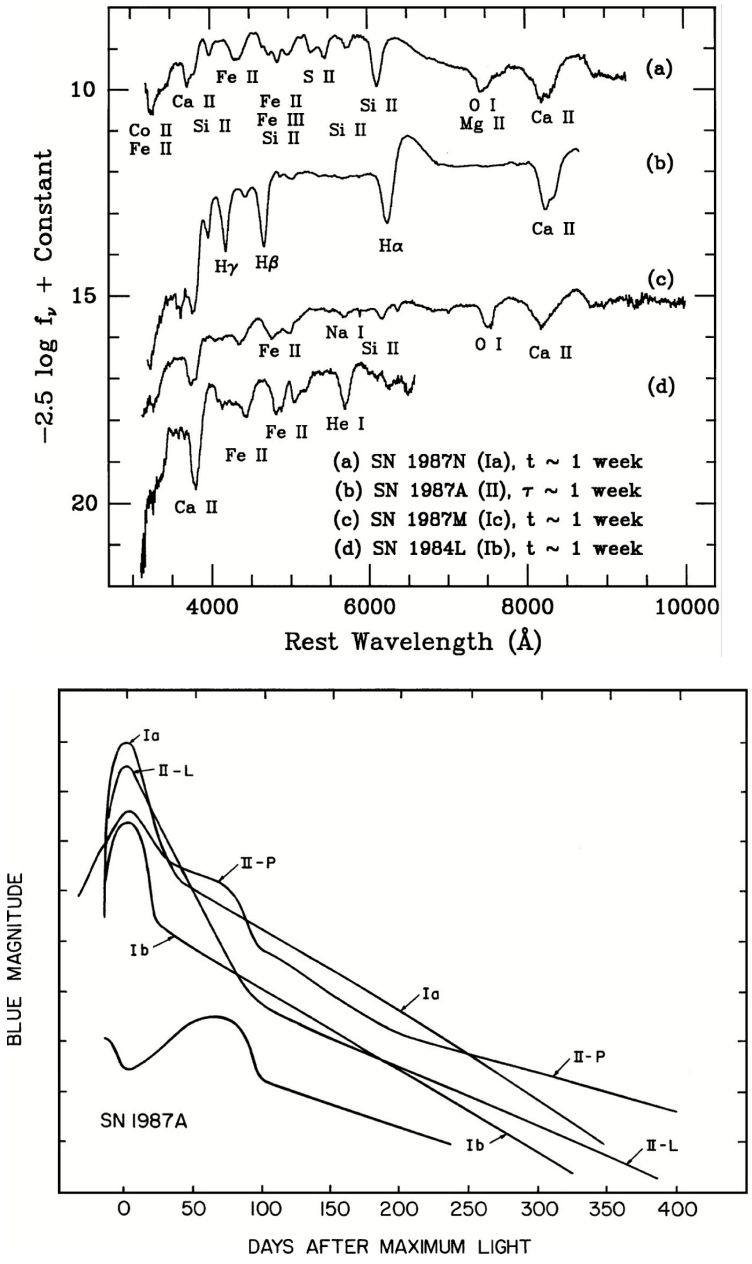

Figure 1.3: Representative optical spectra (top) and light curves (bottom) of several SN types, reproduced from Filippenko (1997). SN Ia are unique compared to other types: their spectra exhibit no hydrogen features and their light curves have brighter maxima and fade away more gradually after peak.

1.2.3 Light-Curve Fitting and SN Ia Standardization

The introduction of charge-coupled device (CCD) technology to modern astronomy revolutionized SN Ia research, as it dramatically increased the number of observed events and significantly improved photometry and light curve sampling (Phillips, 1993). With this advance in data quality came the opportunity to explore, in greater detail, the intrinsic dispersion of SN Ia peak absolute magnitudes. In his work, Phillips (1993) discovered a strong correlation between SN Ia peak brightness and decline rates; he observed that SN Ia with brighter peak magnitudes tend to fade away more slowly. SN Ia with longer decline times have wider light curves, and so this became known as the "width-luminosity" or "stretch-luminosity" relation. Riess et al. (1996) and Tripp (1998) also observed a correlation between SN Ia luminosity and observed color, which has come to be known as the 'color-luminosity' relation; brighter SN Ia tend to be bluer, while redder SN Ia tend to be dimmer. Although the cause for these relationships is not well-understood, correcting SN Ia luminosity using correlations with light-curve properties has been shown to reduce the scatter in magnitude. Figure 1.4 presents examples of SN Ia luminosity corrections using these correlations. The left panel features a plot of peak magnitude in three different filters as a function of decline rate (Phillips, 1993). The decline rate is given by $\Delta m_{15}(B)$ which signifies the decline in peak B-band magnitude in the 15 days post peak; smaller values of $\Delta m_{15}(B)$ correspond to SN Ia that fade away more slowly and are intrinsically brighter. The right panel features Hubble diagrams (μ versus redshift) for SNe Ia that have been corrected for the luminosity dispersion and extinction using light-curve stretch and color (Riess et al., 1996). The top panel displays SNe Ia that have not been corrected; the bottom shows SNe Ia that have had this correction applied, and the corresponding reduction in Hubble diagram dispersion.

To make use of these standardizing relations, SN Ia light curves must be measured with proper temporal cadence to estimate the decline rate (stretch), and in multiple filters to estimate the color. Obtaining these light curve parameters requires fitting observational data to a set of models. Currently, there are two popular frameworks for light-curve mod-

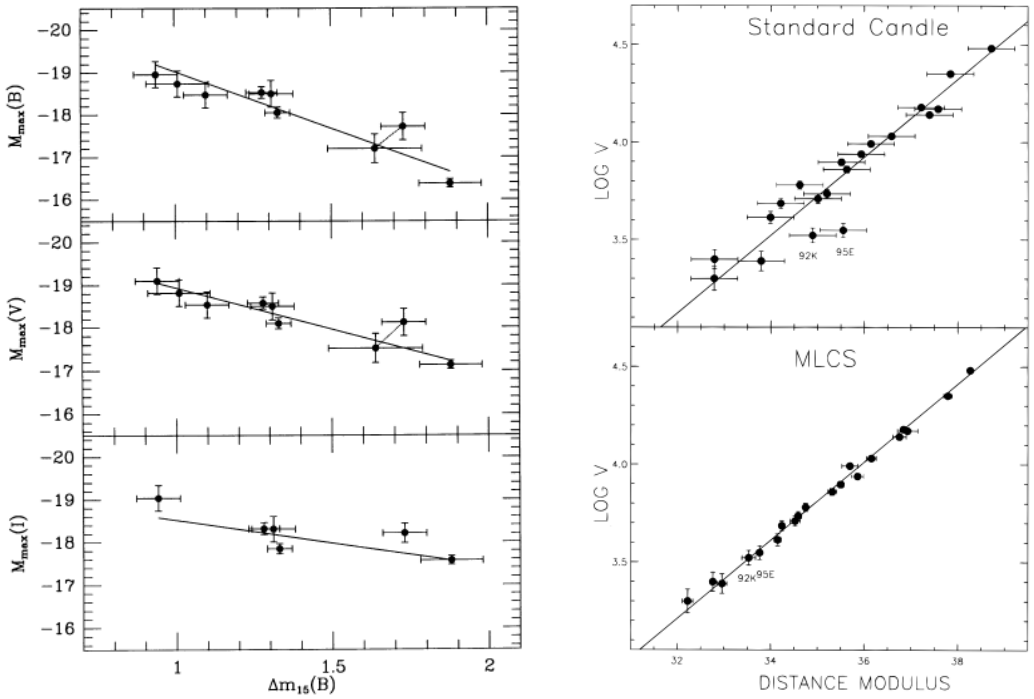

Figure 1.4: The SN Ia "stretch-luminosity" and "color-luminosity" relations. The left panel features a plot of peak magnitude in three different filters as a function of decline rate, reproduced from Phillips (1993). The decline rate is given by $\Delta m_{15}(B)$ which signifies the decline in peak B-band magnitude in the 15 days post peak; smaller values of $\Delta m_{15}(B)$ correspond to SN Ia that fade away more slowly and are intrinsically brighter. The right panel features Hubble diagrams (μ versus redshift) for SNe Ia that have been corrected for the luminosity dispersion and extinction using light-curve stretch and color, reproduced from Riess et al. (1996). The top panel displays SNe Ia that have not been corrected; the bottom shows SNe Ia that have had this correction applied, and the corresponding reduction in Hubble diagram dispersion.

eling: the Multicolor Light Curve Shape (MLCS2k2; Jha et al., 2007) and the Spectral Adaptive Lightcurve Template (SALT2; Guy et al., 2007).

MLCS2k2 uses model photometry in the $UBVRI$ bands to fit the light-curve data. Variation in the observed light curves is parameterized by a single parameter, Δ, called the "luminosity correction." The model trains on low-redshift events where the distances are known, and so outputs a value of the distance modulus when fitting. Before fitting the data, observations passed to MLCS2k2 must be K-corrected. One primary advantage to MLCS2k2 is that it claims to separate variations in SN color into contributions from dust and from intrinsic differences in SN color. Each SN that is fit by the model has an output μ, Δ, V-band extinction (A_V), and a date of maximum light.

SALT2 is a fundamentally different approach that uses template SEDs to fit observed fluxes; this means K-corrections are relatively straightforward. The SALT2 algorithm uses model SN Ia SEDs that evolve with time to find the expected rest-frame flux in a given passband. Unlike MLCS2k2, SALT2 does not make any assumptions about the source of color variations or variations in the SN light curve. In fact, one of a few select scatter models can be incorporated. For example, the "coherent" scatter model assumes that the SN Ia dispersion is coherent at all times and wavelengths, i.e., constant scatter $\sigma_{\rm COH} \approx 0.1$. The "G10" model assumes 70% of the scatter comes from coherent variation and 30% from variation in SN Ia color (Guy et al., 2010). In the "C11" model, 75% of the SN Ia dispersion comes from variation in color, while 25% comes from coherent variation (Chotard et al., 2011). The latter two models are based on observation and were converted into spectral variation models in Kessler et al. (2013).

The SALT2 model assumes that a SN Ia light curve can be parameterized by an epoch of maximum light in the B-band (t_0), stretch (x_1), color (c), and the overall normalization, or amplitude, of the SED (x_0). These model parameters are output upon fitting light-curve observations using the SALT2 algorithm. The peak B-band magnitude is defined as the transformation of x_0 into magnitude space, i.e., $m_B = -2.5\log(x_0)$. Using this

parameterization, the distance modulus is defined as

$$\mu = m_B - M + \alpha \times x_1 - \beta \times c\,, \tag{1.17}$$

where M is the SN absolute magnitude, and α and β are global regression parameters. The difference between the standardized, observed distance modulus and the theoretical, or best fit, distance modulus (Eq. 1.15) is quantified as the Hubble Residual (HR).

This representation of the distance modulus using the light-curve color, stretch, and peak B-band magnitude has become one of the most popular SN Ia standardization models. Attempts to improve and expand upon this model have been a substantial focus of SN Ia cosmology in the last ten years. For further detail on extensions to and parameter inference using this standardization model, see Chapter 2.

1.3 Supernovae in the Era of Precision Cosmology

In the last fifty years, there has been a dramatic shift in the structure of astronomy surveys; projects have evolved from those with a few co-located astronomers to large international collaborations creating new world-class instruments (National Research Council, 2010b). Together, these surveys have detected thousands of new supernovae, of all types, in the redshift range $0 < z < 1.5$. In the last decade alone, projects such as the Sloan Digital Sky Survey-II Supernova Survey (Frieman et al., 2008, SDSS-SNS), the Equation of State Supernovae: Trace Cosmic Expansion survey (Miknaitis et al., 2007, ESSENCE), the Supernova Legacy Survey (Guy et al., 2010, SNLS), the Panoramic Survey Telescope & Rapid Response System (Kaiser et al., 2002, Pan-STARRS), and The Dark Energy Survey (Bernstein et al., 2012; Kessler et al., 2015, DES) have detected hundreds of SNe Ia to use for cosmology analyses and to improve photometric classification software. Figure 1.5 shows the dramtatic increase in the number of detected SNe since the discovery of dark energy. By combining SNe Ia detected by these different surveys (e.g., Figure 1.12), we can more completely fill in the SN Ia Hubble diagram and thus better constrain cosmological parameter estimates.

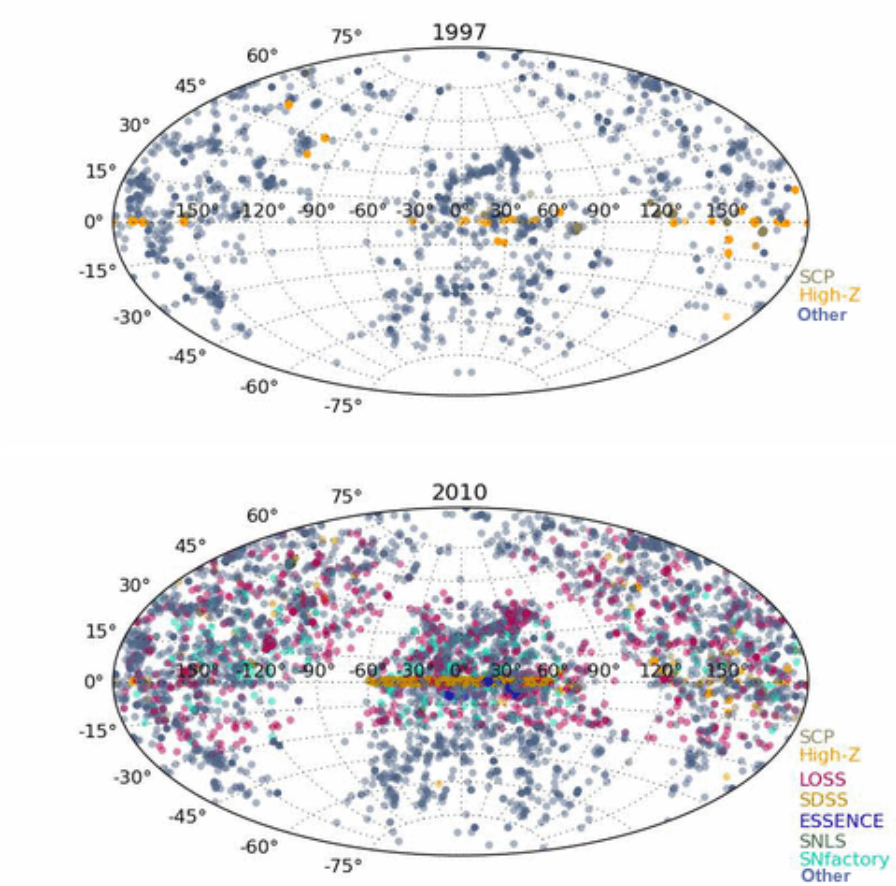

Figure 1.5: SNe detected since 1885. TOP: Total number of SNe detected by 1997; the two experiments which confirmed the existence of dark energy are represented in grey and yellow. BOTTOM: Total number of SNe detected by 2010, including new-large scale projects such as SDSS and SNLS. Frames adapted from `https://commons.wikimedia.org/wiki/File:Sn_discoveries.gif`.

The detection of thousands of new SN Ia candidates means that SN cosmology analyses will no longer be limited by statistics. Uncertainties will instead be dominated by systematic errors which affect many measurements simultaneously and with some type of correlation (Howell, 2011). Such systematics include: calibration, selection effects, SN Ia evolution with redshift, host-galaxy correlations, and contamination from other SN types. This transition from statistics-dominated to systematics-dominated analyses signifies a new "era of precision cosmology."

1.3.1 The Sloan Digital Sky Survey-II Supernova Survey

The SDSS[1] is an international collaboration of hundreds of scientists at dozens of institutions worldwide. For more than fifteen years, SDSS scientists have been working to create the largest map of the large-scale structure of the Universe. The SDSS began taking data in 2000, and recently published its thirteenth data release (SDSS Collaboration et al., 2016). The SDSS camera is mounted on the $2.5m$ telescope at the Apache Point Observatory in New Mexico (Gunn et al., 1998, 2006) and the imaging array uses five optical filters, *ugriz*, that span from 3000-11,000 Å (Fukugita et al., 1996).

In 2005, the SDSS began its second phase of operations, which included the SDSS-SNS. Data were collected over a three month observing season (September - November) in 2005, 2006, and 2007. The survey observed Stripe 82, a 300 deg^2 equatorial region of the Southern sky located approximately between 20 and 4 hours of right ascension ($20^h \lesssim \alpha \lesssim 4^h$) and between -1.25 and $+1.25$ degrees in declination ($-1.25^\circ \lesssim \delta \lesssim +1.25^\circ$), in drift-scan mode obtaining nearly simultaneous 55 second exposures in each of the *ugriz* SDSS filters. The average cadence of the survey, including losses due to weather and sky brightness, was roughly four days. Point sources were observed with 50% detected completeness at $r = 22.6$ on average, where the typical peak magnitude for a SN Ia at $z = 0.2$ is $r \approx 20.8$ (Frieman et al., 2008).

SDSS images were processed in the SDSS pipeline (Stoughton et al., 2002). Astro-

[1] `www.sdss.org`

physical objects were identified via a difference imaging pipeline where template images were subtracted from search images with potential transients. Light curves were constructed using the technique known as "scene modeling photometry" (Holtzman et al., 2008) and fluxes were calibrated to the standard star catalog to obtain photometry accurate to roughly 1% Ivezić et al. (2007). Objects detected in two or more filters after frame subtraction were then visually scanned and marked as transients if they were not obvious artifacts. Spectroscopic measurements were made for likely SN candidates when resources were available. The candidate selection and filtering algorithms, as well as the spectroscopic identification, are described in Sako et al. (2008). After three observing seasons, the SDSS-SNS discovered 10,258 new transient objects and spectroscopically identified 500 SNe Ia and 81 core-collapse SNe (Sako et al., 2014).

In addition to spectroscopically confirming 500 SNe Ia, the SDSS-SNS also photometrically classified 907 SNe Ia. Light-curves of these likely SNe Ia were analyzed using the Photometric SN IDentification software (PSNID; Sako et al., 2011). PSNID uses the observed photometry of the SNe to first compute a Bayesian probability associated with each of the assumed three SN types (SN Ia, SN Ibc, and SN II), as well as parameters and errors assuming a SN Ia model, using Markov Chain Monte Carlo (MCMC). The same procedures are then performed on a large simulated mixture of SN Ia and core-collapse SNe. For each SN candidate in the sample, the measured SN Ia parameters (extinction, light-curve stretch, and redshift) are compared with those of the simulated set to calculate Cartesian distances to the SN's neighbors which are used then to determine a nearest-neighbor probability. The combination of the χ^2-fit, Bayesian, and nearest-neighbor probabilities are used for the final classification.

Figure 1.6 displays the Hubble diagrams for subsets of spectroscopically-confirmed and photometrically-classified SNe Ia from the SDSS-SNS which meet additional light-curve quality and redshift uncertainty cuts (Sako et al., 2014). As shown in Figure 1.6, the Hubble diagram of the photometrically-classified sample is more scattered than that of the spectroscopically-confirmed sample. This is particularly noticeable in the low-redshift

range ($z < 0.2$), where the photometrically-classified sample is likely contaminated by core-collapse SNe. Note that the black best fit line does not correspond with the best fit cosmology from the sample, but is a fiducial cosmology used to guide the eye.

The Hubble diagrams shown in Figure 1.6 have not been corrected for *selection bias*. In a magnitude limited survey, only the brighter objects are observed at large distances, resulting in selection biases. The severity of this selection bias will depend on the completeness of the survey as well as any additional selection cuts imposed on the SNe Ia to create a final sample for analysis. Expected selection bias can be quantified, often as a function of redshift, using rigorous simulations of a SN survey and comparing the expected to the observed distance moduli. Figure 1.7 presents the expected selection bias ($\mu_{\rm fit} - \mu_{\rm sim}$) for the SDSS-SNS sample for two distinct sets of selection criteria. As shown in Figure 1.7, the degree of the bias depends on the selection criteria imposed. Not accounting for this bias will yield higher-than-expected values of Ω_m. Treatment of this bias remains a complex problem in SN Ia cosmology and is further discussed in Chapters 2 and 4. Assuming a flat, ΛCDM model, the best fit cosmology using the spectroscopically-confirmed sample after correcting for selection bias is $\Omega_m = 0.315 \pm 0.093$.

As described in Section 1.2.3, one of the goals of modern SN Ia cosmology experiments is to reduce the scatter in the Hubble diagram. HR as a function of redshift for the spectroscopically-confirmed sample from the SDSS-SNS is presented in Figure 1.8.

The wealth of data available from the SDSS-SNS has led to several analyses with the goal of better understanding, and reducing, this HR scatter. Several works have explored correlations between HR and properties of the SN Ia environment. Correlations between HR and host-galaxy mass, metallicity, and star formation rate have been observed (Lampeitl et al., 2010; Gupta et al., 2011; D'Andrea et al., 2011; Hayden et al., 2013; Wolf et al., 2016; Campbell et al., 2016). The relationships between SN Ia properties, including light-curve color and stretch and spectral features, have also been investigated (Nordin et al., 2011). While a strong correlation between HR and host-galaxy mass ($> 3\sigma$) is observed using the SDSS-SNS, there is no physical reason why mass should cause this effect

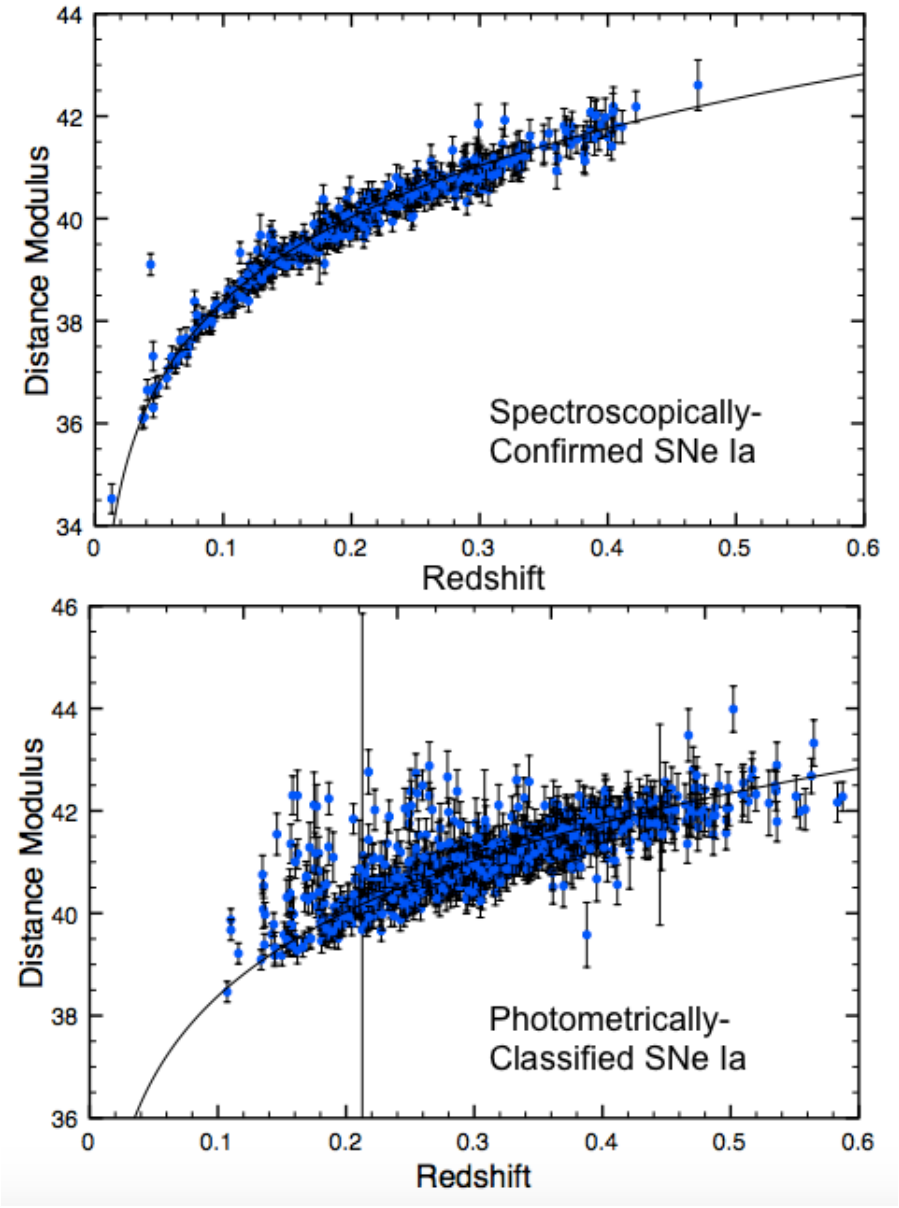

Figure 1.6: Hubble diagram for subsamples of spectroscopically-confirmed (top, 457 SNe Ia) and photometrically-classified (bottom, 827 SNe Ia) SNe Ia from the full three-year SDSS-SNS, adapted from Sako et al. (2014). The large scatter for low-redshift ($z < 0.2$) objects in the photometrically-classified sample is likely due to contamination from core-collapse SNe. The black trend line is not the best fit cosmology from the sample, but a fiducial cosmology used to guide the eye.

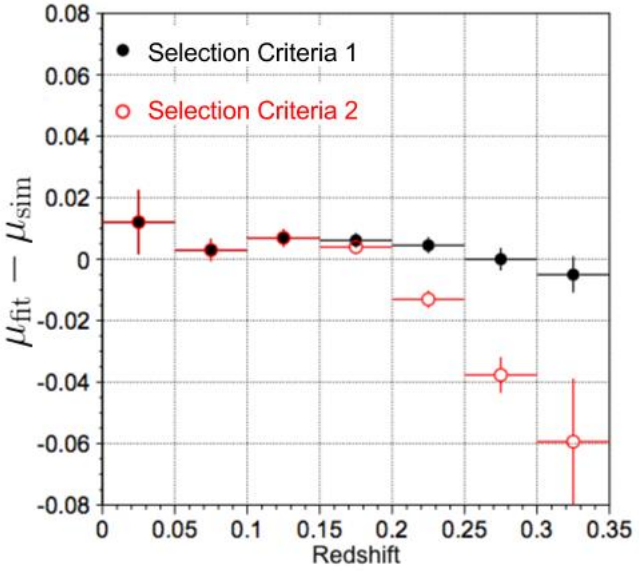

Figure 1.7: Expected bias in distance modulus measurements in the SDSS-SNS, as determined from simulations, using two different sets of sample selection criteria, adapted from Sako et al. (2014). The bias using the set of stricter selection criteria (red, Selection Criteria 2) is more severe than that using Selection Criteria 1 (black).

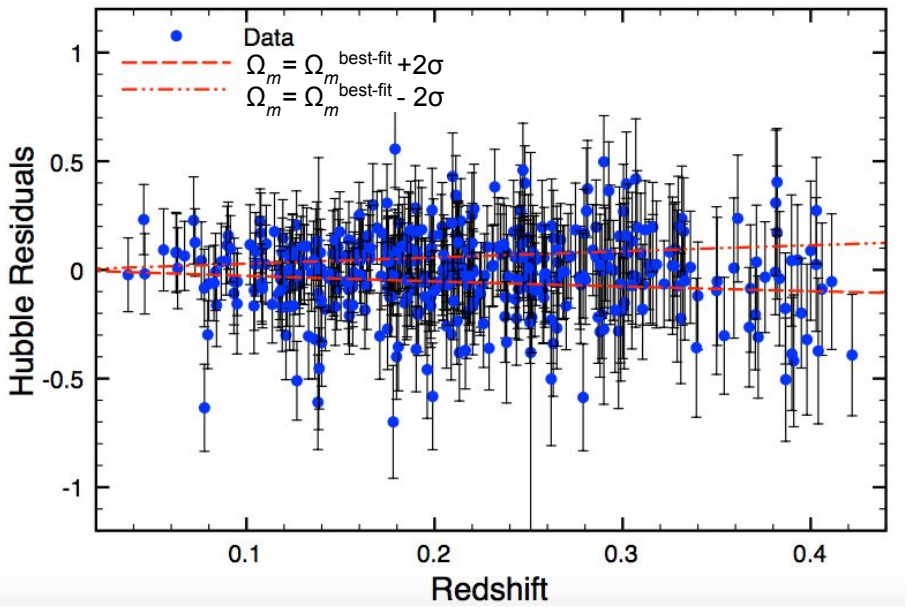

Figure 1.8: HR for the full three-year set of spectroscopically-confirmed SNe Ia, adapted from Sako et al. (2014). The dashed and dot-dashed red lines represent the best fit cosmology $\pm 2\sigma$, respectively.

and the exact driver of the HR scatter remains unknown.

1.3.2 Supernova Host-Galaxy Correlations

It is widely believed that standardization of SNe Ia luminosity can be improved by including correlations between host-galaxy properties and HR. One of the first explorations of this correlation is presented in Gallagher et al. (2005), who studied the host-galaxy properties of nearby SNe Ia and found a tenuous correlation between the HR and host-galaxy gas-phase metallicity. More recently, Kelly et al. (2010), Sullivan et al. (2010), and Lampeitl et al. (2010), using independent data sets, demonstrated that SNe Ia in more massive hosts are about $\sim$0.1 magnitudes brighter (after light-curve corrections) than those in lower mass hosts. Figure 1.9 features the observed correlation between HR and host-galaxy mass presented in Kelly et al. (2010). In their analysis, Kelly et al. (2010) used $\sim$60 nearby SNe Ia $(0.015 < z < 0.08)$ with host stellar masses computed from photom-

etry from the Sloan Digital Sky Survey. After analyzing their data with both MLCS and SALT2, they concluded that SNe Ia in massive hosts are 10% brighter than those in low mass hosts. Linear regression analysis of the SN Ia and host-mass data yielded a non-zero slope with $\sim 3\sigma$ significance.

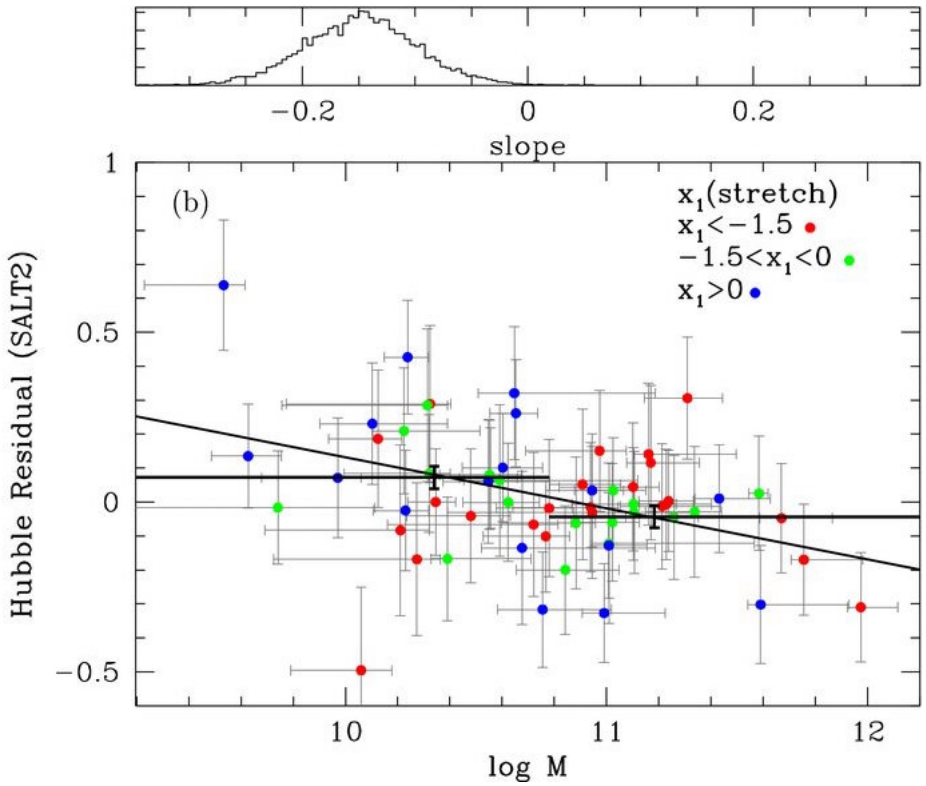

Figure 1.9: Correlation between HR and host-galaxy mass, reproduced from Kelly et al. (2010). The weighted averages in the high and low mass bins (black crosses) differ by 0.11 magnitudes (2.5σ). The upper panel features the posterior distribution of the slope obtained using MCMC sampling.

In the recent literature, there have been several studies indicating that rather than a continuous linear slope, the HR trend with host stellar mass behaves more like a "step" function, which has a transition region connecting the two levels (Childress et al., 2013; Johansson et al., 2013; Rigault et al., 2013). This trend has become known as the "mass step." In their analysis, Childress et al. (2013) combine their sample of SNe Ia from the

Nearby Supernova Factory with SNe Ia from the literature (namely Kelly et al. 2010, Sullivan et al. 2010, and Gupta et al. 2011) to create a sample of 601 SNe Ia spanning low and high redshift. Figure 1.10 presents HR and host-galaxy mass data from the combined Childress et al. (2013) SNe Ia sample. The top figure shows data from the individual SNe Ia and the best fit linear and step function trends. When performing a linear fit, they find a non-zero linear slope with $\sim 3.4\sigma$ confidence. If instead the data are separated into low and high-mass bins, the bin difference is found to be 0.077 magnitudes with 5.6σ confidence. Binned values in HR and host mass are presented in the bottom figure, and suggest the trend is not linear, but in fact consistent with a plateau at low and high mass separated by a transition region from $\log(M/M_{\odot}) = 9.8$ to $\log(M/M_{\odot}) = 10.4$. Several physical models for this behavior were expounded and compared to the data, and the authors concluded that the cause of the trend may be due to a combination of the shape of the galaxy mass-metallicity relation, the evolution of SN Ia progenitor age along the galaxy mass sequence, and the uncertain effects of SN color and host galaxy dust.

Johansson et al. (2013) analyzed a sample of 247 SDSS SNe Ia using only SDSS host-galaxy photometry. They find that, as in Childress et al. (2013), the HR-mass relation behaves as a sloped step function, with essentially zero slope at the high- and low-mass ends and a non-zero slope in the region $9.5 < \log(M/M_{\odot}) < 10.2$. They report that the step in the HR-mass plane is close to the evolutionary transition mass of low-redshift galaxies first described by Kauffmann et al. (2003b). This transition mass occurs at $\log(M/M_{\odot}) \sim 10.5$ and signifies a change in galaxy morphology and stellar populations. Johansson et al. (2013) concluded that differences between SN Ia progenitors in these populations could imply the existence of two samples of SNe Ia with high and low HR.

Following on the work of Childress et al. (2013), Rigault et al. (2013) use integral field spectroscopy for a sample of 89 SNe Ia from the Nearby Supernova Factory to measure Hα emission within a 1 kpc radius around each SN. This Hα surface brightness was used to define SN environments as either "locally star-forming" or "locally passive" and

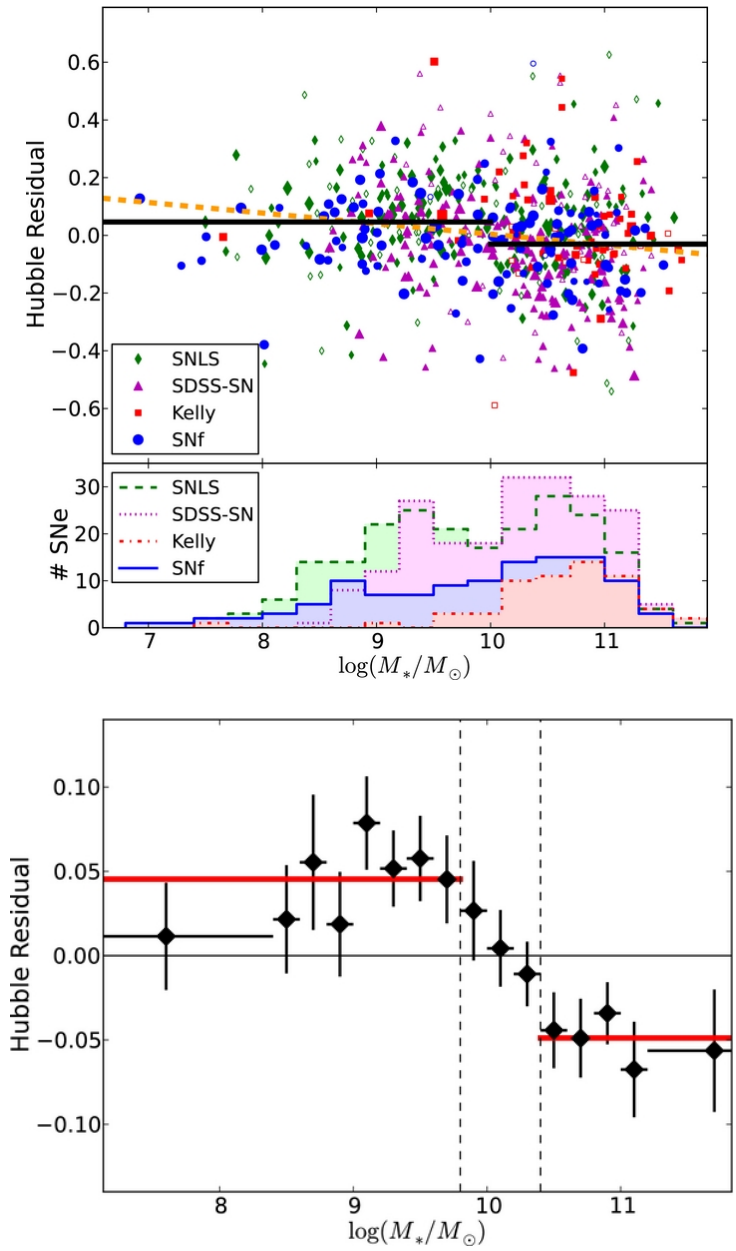

Figure 1.10: Correlation between HR and host-galaxy mass, reproduced from Childress et al. (2013). The top panel features a linear and step fit; a non-zero slope is found with 3.4σ confidence and 0.077 magnitude difference is found between the low and high-mass bins. The bottom panel features the HR and host-mass correlation in bins, which suggest the trend is perhaps not best fit by a linear function, but by a step function with an intermediate transition region.

Rigault et al. (2013) found that the mean standardized brightness for SNe Ia with local Hα emission is on average 0.09 magnitudes fainter than for those without. They find a bimodal structure in HR, and claim that the intrinsically brighter mode, exclusive to locally passive environments, is responsible for the mass step. They argue that HRs are highly dependent on local environment, with local Hα emission being more fundamental than global host properties.

There is no known mechanism by which the mass of the host galaxy can directly influence the explosion of a single white dwarf; therefore, other host properties that are correlated with galaxy mass must be invoked to explain the underlying physical mechanism of this relation. For example, host galaxy gas-phase metallicity is widely assumed to be a proxy for progenitor metallicity, and there are models suggesting that SN Ia luminosities depend on the stellar metallicity of the progenitor (Timmes et al., 2003; Kasen et al., 2009). Therefore, correlations between host metallicity and SN properties have been of recent interest as well. D'Andrea et al. (2011) use a complete sample of all 34 SNe Ia with $z < 0.15$ detected by the SDSS-SNS and corresponding host-galaxy spectra and found significant correlations between gas-phase metallicity and specific star formation rate with HR. Similar trends were observed by Childress et al. (2013) and Pan et al. (2014) using data from the SuperNova Factory and Palomar Transient Factory, respectively. Konishi et al. (2011) also analyzed host spectra of SDSS SNe and concluded that SNe Ia in metal-rich galaxies are 0.13 magnitudes brighter after correcting for light-curve width and color. Given that broadband photometry of galaxies is more readily available than galaxy spectra, several studies have estimated host galaxy physical properties from photometry. Gupta et al. (2011) used 206 SNe Ia from the SDSS-SNS and host-galaxy multi-wavelength photometry and found that while the relation of HR with host stellar mass was highly significant, the relation with mass-weighted age of the host was not. Building on this work, Hayden et al. (2013) calibrated the fundamental metallicity relation (FMR) of Mannucci et al. (2010) to better estimate host metallicity from photometry, and found that using the FMR improves HR correlation beyond the stellar mass alone.

More recently, using empirical models of galaxy star formation histories and theoretical SN delay time distribution models, Childress et al. (2014) have argued that the mean ages of SNe Ia progenitors are responsible for driving the HR correlation with host mass.

Many recent studies utilize host-galaxy spectroscopy to study these relations (D'Andrea et al., 2011; Childress et al., 2013; Pan et al., 2014). Using spectroscopy rather than photometry provides direct access to the galaxy SED and a better estimate of dust extinction. It also allows for derivations of the gas-phase metallicity and star-formation rates via narrow emission lines. Campbell et al. (2016) use a set of 581 photometrically-classified and spectroscopically-confirmed SNe Ia from the SDSS-SNS to explore correlations with spectroscopic host-galaxy properties, using published spectroscopy from the SDSS DR10 catalog (Ahn et al., 2014) and focusing on the impact on cosmological parameter constraints. In their analysis, Campbell et al. (2016) explored changes in parameter constraints when including correlations with host-galaxy mass, metallicity, and star-formation rate. Figure 1.11 presents the change in 1σ and 2σ constraints on w and Ω_m using only SNe Ia for four different variations of the SN Ia luminosity standardization including host-galaxy mass; results using the standard relation are shown in black. As shown in Figure 1.11, the choice of host-galaxy correction model can significantly change the position of the 1σ credible region.

Clearly, correlations between SN Ia luminosity and host-galaxy properties are an important systematic that has implications for cosmological parameter inference. Understanding these correlations is an active area of study, as the community believes it will lead to more precise, unbiased cosmological estimates and illuminate the nature of the SN Ia progenitor.

1.3.3 The Joint Light Curve Analysis

Observations of spectroscopically-confirmed SNe Ia from the SDSS-SNS, together with SNe Ia from the SNLS and several low-redshift samples, were used in a joint light curve analysis which obtained one of the most precise cosmological parameter estimates using

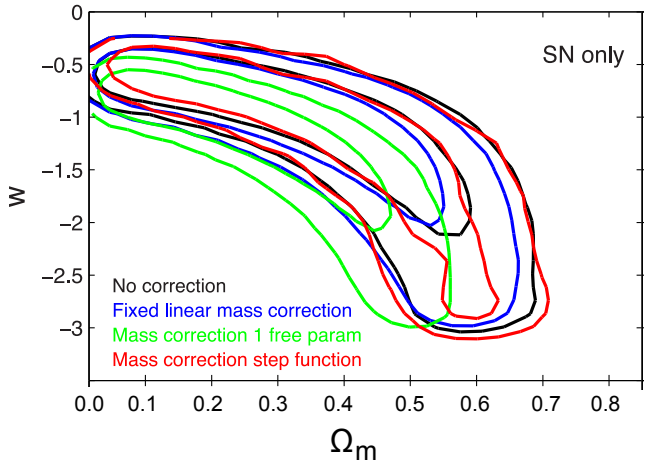

Figure 1.11: Constraints on w and Ω_m for four variations of the the SN Ia luminosity standardization relation, adapted from Campbell et al. (2016). Results shown in black are without any host-galaxy corrections.

SNe Ia to date (Betoule et al., 2014, hereafter JLA). The complete JLA sample consists of 740 spectroscopically confirmed SNe Ia with redshifts out to $z \sim 1$. SNe Ia in the intermediate redshift range $(0.05 < z < 0.4)$ were drawn from the SDSS-SNS (Sako et al., 2014). The high- and low-redshift sample was taken from Conley et al. (2011). High-redshift SNe Ia were culled from the first three years of SNLS (Guy et al., 2010; Conley et al., 2011). The remaining low-redshift SNe Ia were drawn from a compilation of low-redshift surveys, most with photometric observations from the Harvard-Smithsonian Center for Astrophysics (CfA3).

The main goal of the JLA analysis was to provide stronger cosmological parameter constraints using a sample spanning a large redshift range and with reductions in systematic uncertainties. The effort was primarily focused on 1) improving photometric calibration, 2) more rigorously determining uncertainties in light curve models, and 3) including the SDSS-SNS sample in the light-curve training and cosmological analysis (Betoule et al., 2014).

The similarity in design and implementation of the SDSS-SNS and SNLS surveys,

as well as their complementarity in redshift, motivated the effort for joint photometric calibration. Photometric measurements for the SDSS-SNS and SNLS were made independently but using similar methods, and relied on relative calibration to HST solar analog stars and Landolt standards, respectively. After including corrections for the survey transmission functions, analysis of the cross-calibration sample showed that the photometry of the two instruments was uniform at the 3 mmag level (Betoule et al., 2014). Remaining calibration uncertainties, including uncertainties of the flux standards, the low-redshift sample, and the HST SNe Ia, were combined with this photometric calibration uncertainty to compute the total contribution necessary for accurate parameter estimation.

Rather than utilize a more conventional SN Ia distance estimator (Eq. 1.17), the JLA analysis incorporated host-galaxy mass as a standardizing parameter in their SALT2 model. They define the standardized distance modulus as

$$\mu = m_B - (M_B - \alpha \times x_1 + \beta \times c)\,, \tag{1.18}$$

where m_B, x_1 and c are the light curve peak B-band magnitude, stretch, and color, and M_B is the absolute SN Ia magnitude. Unlike the standard relation, however, the JLA analysis assumes the absolute magnitude is a function of host-galaxy stellar mass (M_{stellar}), where

$$M_B = \begin{cases} M_B^1 & \text{if } M_{\text{stellar}} < 10^{50} M_\odot \\ M_B^1 + \Delta_M & \text{otherwise} \end{cases}, \tag{1.19}$$

and M_B^1 and Δ_M are additional fit parameters in the model. This particular model form was based on that of Conley et al. (2011), which aimed to correct for effects due to the observed correlations between host-galaxy properties and M_B and β (Sullivan et al., 2011; Johansson et al., 2013). Observed distance moduli were computed using Eq 1.18 and used to compute the best fit ΛCDM cosmology. Details for this fitting procedure are described in Chapter 2.

The Hubble diagram of the combined JLA sample and corresponding best fit cosmology contours are presented in Figure 1.12. The distance modulus-redshift relation of the best fit ΛCDM cosmology for a fixed $H_0 = 70$ km s^{-1} Mpc^{-1} is featured in black.

Weighted averages of the residuals in bins of width $\Delta z/z \sim 0.24$ are shown in black dots. The filled gray contours represent the 68% and 95% confidence regions using the full JLA SNe Ia sample; red dashed contours represent fit results excluding the SDSS-SNS sample.

The best fit value of the matter-energy density using the full JLA sample was $\Omega_m = 0.295 \pm 0.034$ and the correlation between Ω_m and any of the nuisance parameters (α, β, Δ_M) was less than 10%. They find that the SDSS-SNS sample exacts as an alternative anchor for the SNLS+low-redshift sample and that including these intermediate range SNe Ia reduces the total uncertainty in Ω_m by 25%.

Since the initial discovery of dark energy, constraints on Ω_m using SNe Ia have improved by nearly 70% (Perlmutter et al., 1999; Riess et al., 1998; Conley et al., 2011; Betoule et al., 2014). This is largely attributed to increases in statistical power, as well as better understanding of systematic uncertainties such as those from photometric calibration and the SN Ia spectral evolution model (Kessler et al., 2013; Mosher et al., 2014). Despite improvements in calibration, the accuracy of photometric calibration remains the dominant limiting systematic uncertainty in SN Ia cosmology. However, improvements in the accuracy of spectrophotometric standards or in the production of laboratory-made calibration sources should make approaching the systematic limit of $\sim$1 mmag possible, particularly with CCD-based photometric measurements (Astier et al., 2013). Large-scale surveys such as DES and LSST will be equipped to ease the calibration problem, however these surveys will still have to contend with issues of photometric classification and correlations between SN Ia luminosity and host-galaxy properties in order to achieve even more precise cosmology estimates.

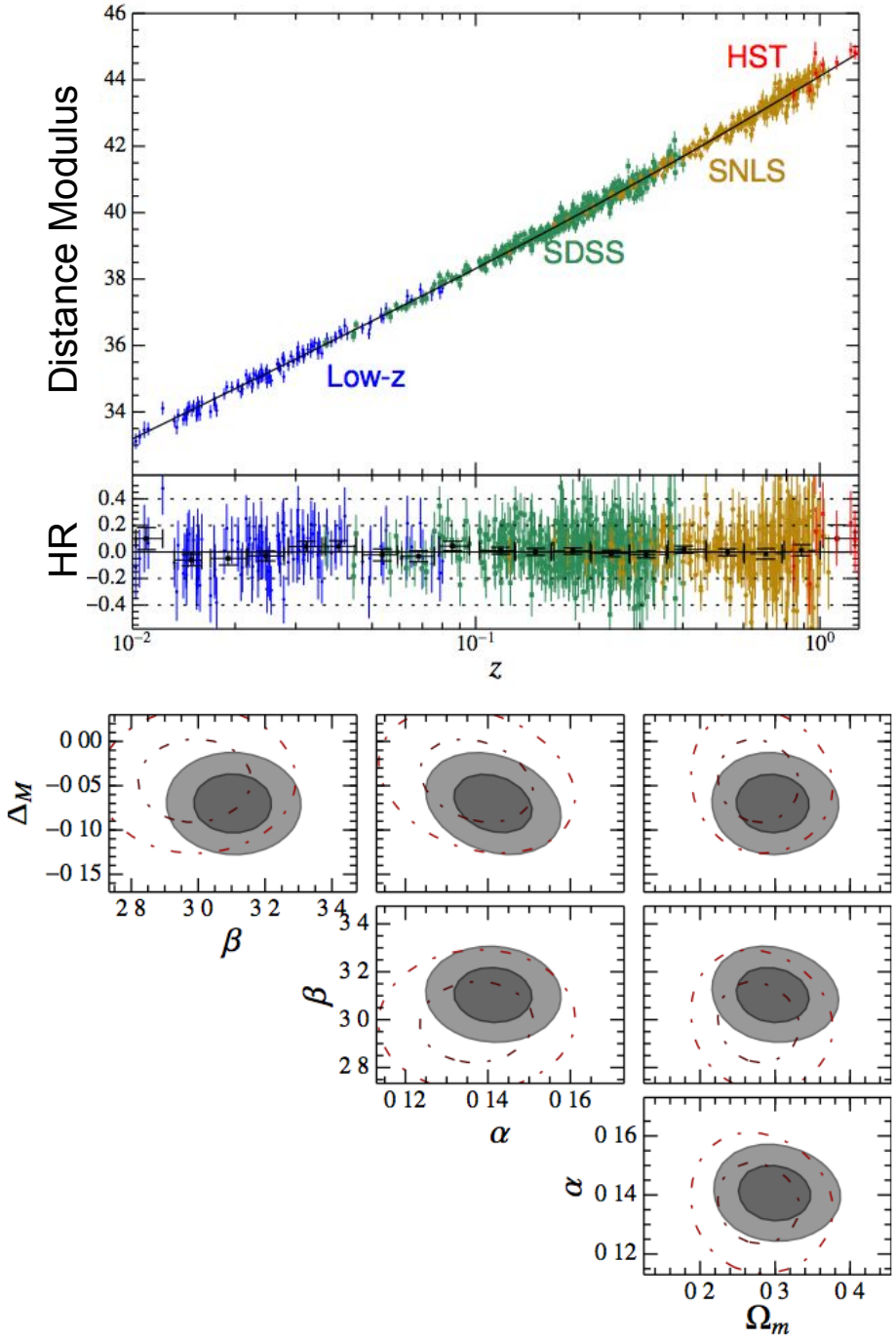

Figure 1.12: Hubble diagram and corresponding Hubble residuals (top) and best fit cosmology contours (bottom), reproduced from Betoule et al. (2014). Filled gray contours represent the 68% and 95% confidence regions for the full JLA sample. Red dashed contours exclude data from the SDSS-SNS.

Chapter 2

Statistical Frameworks for Cosmological Parameter Inference using SNe Ia

SNe Ia are powerful tools for cosmological parameter inference. By comparing SNe Ia observations to theory, we can constrain parameters such as Ω_m and w_0 (see Chapter 1). Conventionally this comparison is made via a two-stage process, given a particular SN Ia model. First, SN Ia fluxes are fit to obtain light-curve properties, e.g., color, stretch, and $\Delta m_{15}(B)$. How these summary statistics are then used depends on the choice of SN Ia model and light-curve fitter. For example, the μ values output by MLCS2k2 can be used to fit the SN Ia Hubble diagram. In the case of the SALT2 model, the light-curve fit parameters are used to simultaneously constrain cosmological parameters and the SN Ia luminosity correction coefficients (e.g., α and β).

A variety of statistical frameworks exist to obtain estimates of cosmological parameters from SNe Ia light-curve data. This includes traditional χ^2-minimization, Bayesian inference, and Approximate Bayesian Computation. While some of these frameworks have the functionality to compare cosmological models and provide a relative measure of model "goodness," this will not be discussed in this thesis. For a review of model selec-

tion, see e.g., Trotta (2008); Gelman et al. (2014). In this Chapter, I review commonly-used techniques for cosmological parameter inference using spectroscopically-confirmed SNe Ia and discuss several remaining systematic challenges. Throughout this dissertation, I will discuss cosmological parameter inference in the context of the SALT2 SN Ia model, unless otherwise specified.

2.1 Introduction

A common problem in statistical inference is how to estimate *parameters* (e.g., Ω_m) of a theoretical *model* using empirical *observations*. Statistical approaches to this problem have been divided into two primary schools of thought: frequentist and Bayesian. In the frequentist approach, a model parameter is believed to have a single true value; in the Bayesian approach, a parameter is believed to be fixed, but drawn from some probability distribution. Fundamentally, the difference between frequentist and Bayesian methods lies in the interpretation of probability. In the frequentist perspective, probability is considered to be a relative frequency; in contrast, Bayesian probability is considered to be a degree of belief (D'Agostini, 1995).

These differences inspire an important distinction between the frequentist and Bayesian approaches to parameter estimation. Frequentists seek to explore the data *likelihood*, the probability of the data given some model. Bayesians, on the other hand, are interested in the *posterior probability*, or the probability of the model given the data. These two interpretations and the ways in which they are evaluated, are related, yet fundamentally distinct.

2.2 Outlining the SN Ia Cosmology Problem

We consider SN Ia light curves (observed flux over time) as the most fundamental observations of a SN survey. However, rather than use light-curve fluxes directly, we frequently

use light-curve fit parameters as data for cosmological parameter inference. For the purpose of this discussion we consider the *data* ($\mathcal{D}$, elements of which are noted with the superscript "obs") to be the set of measured SALT2 light-curve fit parameters and their associated errors:

$$\mathcal{D}_i = \{z_i^{\rm obs}, m_{Bi}^{\rm obs}, x_{1i}^{\rm obs}, c_i^{\rm obs}, \mathcal{C}_i^{\rm obs}\}\,, \tag{2.1}$$

where $z_i^{\rm obs}$ is the redshift of the ith SN Ia in the dataset, and $m_{Bi}^{\rm obs}$,$x_{1i}^{\rm obs}$, and $c_i^{\rm obs}$ are the light-curve fit parameters. $\mathcal{C}_i^{\rm obs}$ is the covariance matrix of measurement uncertainties defined by the experiment:

$$\mathcal{C}_i^{\rm obs} = \begin{pmatrix} \sigma_{m_{Bi}}{}^2 & \sigma_{m_{Bi},x_{1i}} & \sigma_{m_{Bi},c_i} \\ \sigma_{m_{Bi},x_{1i}} & \sigma_{x_{1i}}{}^2 & \sigma_{x_{1i},c_i} \\ \sigma_{m_{Bi},c_i} & \sigma_{x_{1i},c_i} & \sigma_{c_i}{}^2 \end{pmatrix}. \tag{2.2}$$

We define the set of light-curve fit parameters only as d_i

$$d_i = \{m_{Bi}^{\rm obs}, x_{1i}^{\rm obs}, c_i^{\rm obs}\}\,, \tag{2.3}$$

as it will be useful for discussion later in this chapter.

Of interest are the set of cosmological model parameters and the global SN Ia standardization parameters that minimize the scatter about the SN Ia Hubble diagram. For reference, the SALT2 SN Ia *model* of the distance modulus (μ) is given by

$$\mu_i = m_{Bi} - M_0 + \alpha \times x_{1i} + \beta \times c_i\,, \tag{2.4}$$

where M_0 is the reference SN Ia absolute magnitude and α and β are the global standardization (regression) parameters. The intrinsic scatter in SN Ia magnitude, often referred to as $\sigma_{\rm int}$, is also included as an unknown parameter in the model. This represents the currently unexplained remaining scatter about the SN Ia Hubble diagram after correcting for correlations between SN Ia luminosity and light-curve properties (Section 1.2.3). The exact form of this intrinsic scatter, e.g., as a global parameter added to the SN Ia magnitude, depends on the model under investigation. In many cases, this is treated a single coherent scatter in SN Ia magnitude, i.e.,

$$m_{Bi}^{\rm scat} \sim N(m_{Bi}, \sigma_{\rm int}^2)\,. \tag{2.5}$$

Other models incorporate scatter in both magnitude and SN Ia color (Guy et al., 2010; Chotard et al., 2011; Kessler et al., 2013). In the `SALT2mu` parameter estimation algorithm (Marriner et al., 2011), the intrinsic scatter is treated as function of the model parameters and observed light-curve fit property covariances

$$\sigma^2_{\text{int}_\text{i}} = C^{\text{obs}}_{i00} + \alpha^2 C^{\text{obs}}_{i11} + \beta^2 C^{\text{obs}}_{i22} + 2\alpha C^{\text{obs}}_{i01} - 2\beta C^{\text{obs}}_{i02} - 2\alpha\beta C^{\text{obs}}_{i12} \,. \tag{2.6}$$

We define θ_c as the set of cosmological parameters and θ_s as the set of SN Ia standardization parameters. θ is defined as the complete set of these parameters, e.g., for a flat ΛCDM cosmological model and the standardization model of Eq. 2.4:

$$\theta \equiv [\theta_c, \theta_s] = [\Omega_m, M_0, H_0, \alpha, \beta, \sigma_{\text{int}}] \,. \tag{2.7}$$

As M_0 is completely degenerate with H_0, most analyses fix H_0 to the current best estimate of the Hubble constant.

2.3 Traditional Cosmological Parameter Estimation Methods using SNe Ia

The χ^2-minimization technique has traditionally been used for estimating cosmological parameters and SN Ia standardization parameters from SN Ia light-curve fit data (Riess et al., 1998; Perlmutter et al., 1999; Kessler et al., 2009a; Marriner et al., 2011; Conley et al., 2011; Betoule et al., 2014). χ^2-minimization relies on constructing an optimal statistic which compares observations to theory, and using that statistic to evaluate the likelihood of the data given a proposed model. In the conventional framework, the best-fit model will be that which minimizes the value of the statistic and maximizes the value of the likelihood. However, this is not necessarily the case in the SN Ia cosmology problem, which requires a complex statistic to fully capture survey systematics.

The χ^2 statistic is frequently used in regression analyses to measure how well a data set matches a theoretical model. For a set of N observed events $x = \{x_i^{\text{obs}} ... x_N^{\text{obs}}\}$, the

random variable χ^2 is defined as

$$\chi^2 \equiv \sum_{i=1}^{N} \frac{(x_i^{\rm obs} - x_i^{\rm mod})^2}{\sigma_i^2}\,, \tag{2.8}$$

where $x_i^{\rm mod}$ is a function of the model parameters and σ_i^2 is the uncertainty of the data. If the data $x_i^{\rm obs}$ are independent with Gaussian errors, then χ^2 follows a chi-squared distribution χ^2_ν with mean ν, where ν indicates the number of degrees of freedom. When the data are a good fit to the model, we expect $\chi^2/\nu \approx 1$. $\chi^2/\nu >> 1$ or $\chi^2/\nu << 1$ indicate the model is not a good fit to the data and should be rejected.

The likelihood, $\mathcal{L}$, is defined in terms of this χ^2, i.e.,

$$\mathcal{L} \equiv p(\mathcal{D}|\theta) \tag{2.9}$$

$$\mathcal{L} = (2\pi\sigma^2)^{-N/2}\exp\left(-\chi^2/2\right)\,. \tag{2.10}$$

In this description of the likelihood, the parameter set θ which minimizes χ^2 also maximizes the likelihood. The particular $\theta_{\rm max}$ which satisfies this condition is known as a *maximum likelihood estimator*. Values of $\theta_{\rm max}$ obtained using a χ^2-minimization (maximum-likelihood) technique are single-valued and are assumed to have Gaussian uncertainties.

In practice, the likelihood is evaluated by sampling $p(\mathcal{D}|\theta)$ over the model parameter space. In simple cases, this can be done by evaluating the likelihood across a grid of points in parameter space. However, as the dimensionality of the problem increases and/or the likelihood function becomes more complex, more sophisticated sampling mechanisms are required. It becomes more efficient to explore regions of parameter space near the peak of the likelihood distribution, rather than sampling across every possible point in θ.

One technique commonly used to explore the parameter space is Markov Chain Monte Carlo (MCMC). MCMC algorithms construct a "chain" of points in parameter space, where the position of each element in the chain is only informed by the position of its predecessor. For example, in the subclass of "random walk" MCMC algorithms, the chain "moves" by drawing new steps from a proposal distribution and comparing the likelihood of the new step to that of the previous step. Features of the proposal distribution can be

altered to adjust parameters such as the step size. A crucial property of an MCMC chain is that it ultimately evolves to a stationary or "target state" distribution independent of the starting point. If the chain has converged properly, this "target state" distribution is proportional to the probability distribution of interest. Several MCMC algorithms exist, with a variety of proposal distributions and other tunable parameters. Popular MCMC algorithms include the Metropolis-Hastings (Metropolis et al., 1953), Gibbs sampling, and ensemble sampling (Goodman and Weare, 2010).

In the context of SN Ia cosmology, the χ^2 statistic takes the form

$$\chi^2 = (\mu^{\rm obs} - \mu^{\rm mod})^T \mathcal{C}^{-1} (\mu^{\rm obs} - \mu^{\rm mod}), \tag{2.11}$$

where $\mu^{\rm mod}$ is the vector of theoretical distance moduli evaluated using the set of cosmological model parameters (Eq. 1.15). $\mu^{\rm obs}$ is the set of observed distance moduli computed for each SN Ia using the observed light curve and subsequent light-curve fit parameters (e.g., using Eq. 2.4). $\mathcal{C}_\mu$ is the total covariance matrix which is often a linear combination of measurement uncertainties ($\mathcal{C}^{\rm obs}$), the intrinsic Hubble diagram dispersion, redshift uncertainties, and other systematics. For example, the full covariance matrix used in the Betoule et al. (2014) analysis is given by

$$\mathcal{C} = C_\eta + {\rm diag}\left(\frac{5\sigma_z}{z\log 10}\right)^2 + {\rm diag}(\sigma^2_{\rm lens}) + {\rm diag}(\sigma^2_{\rm coh}). \tag{2.12}$$

In this formalism, $\mathcal{C}_\eta$ includes contributions from systematics: uncertainties stemming from the error propagation of light-curve fitting, i.e., $\mathcal{C}^{\rm obs}$; light-curve model uncertainties (which will depend on the regression cofficients α and β) and selection bias uncertainties estimated from rigorous simulations of the SN Ia sample; uncertainties of the SN Ia host-galaxy masses; corrections for Milky Way extinction; peculiar velocities; and sample contamination from core-collapse SNe. The other terms account for uncertainties in cosmological redshift, the variation in SN Ia magnitudes due to gravitational lensing, and any remaining intrinsic scatter not captured by other terms, respectively. Clearly, computing the full covariance matrix is nontrivial. Furthermore, this technique assumes that contributions to the covariance matrix are fixed across all of parameter space. While this

is a justified assumption for global systematics including Milky Way extinction and core-collapse contamination, it is possible that uncertainties related to selection effects vary across parameter space.

Although χ^2-minimization has been widely adopted and tested by the SN Ia community, a few significant issues remain:

1. Unlike Eq 2.8, the SN Ia χ^2 includes parameters in θ, namely α and β, in the uncertainty ($\mathcal{C}$); i.e., the contribution to $\mathcal{C}$ from light-curve fitting is dependent on α and β. From Eqs. 2.11, it is apparent that certain values of (α, β) may maximize the covariance, and thus minimize the χ^2, but also maximize the difference between $\mu^{\rm mod}$ and $\mu^{\rm obs}$. Because α and β act as both range and location parameters, their errors are not necessarily Gaussian. This means that $\chi^2/\nu \approx 1$ is no longer a satisfactory measure of goodness-of-fit. Furthermore, the value which minimizes the χ^2 may no longer maximize the likelihood.

2. Although the intrinsic dispersion is treated as a model parameter, there is much variety in the way in which it is estimated. In many cases, the χ^2 is first minimized and $\sigma_{\rm int}$ is adjusted until $\chi^2/\nu \approx 1$. This is precisely what is done in Conley et al. (2011), where a single $\sigma^2_{\rm int}$ is determined for each of the SN survey samples. Betoule et al. (2014) add additional degrees of freedom to their χ^2 by splitting the SN Ia sample into redshift bins and calculating a minimized χ^2 per bin. They then use these minimized χ^2 values to iteratively determine the intrinsic scatter. Fitting for the intrinsic dispersion in this way means that only a single number can be estimated without any uncertainty.

3. Many of the χ^2-minimization analyses involve a combination of parameter inference techniques. A single analysis may include χ^2-minimization, iterative updates, and marginalization to infer best-estimates of the parameters of interest. Therefore, it is difficult to compare uncertainties from these analyses to those that use more standard sampling techniques.

2.4 New Statistical Techniques

2.4.1 Bayesian Parameter Inference

In contrast to χ^2-minimization techniques, Bayesian analyses aim to construct the posterior probability of the model parameters given the data, or $p(\theta|\mathcal{D})$. To do this, we make use of Bayes' theorem, which relates the posterior probability to the likelihood

$$p(\theta|\mathcal{D}) = p(\mathcal{D}|\theta)\frac{p(\theta)}{p(\mathcal{D})} = \mathcal{L}\frac{p(\theta)}{p(\mathcal{D})}. \tag{2.13}$$

It is often more useful to rewrite Bayes' theorem in the context of a particular model $\mathcal{M}$ which is a function of the parameter set θ. In this case, Eq. 2.13 becomes

$$p(\theta|\mathcal{D}) = \mathcal{L}\frac{p(\theta|\mathcal{M})}{\int \mathcal{L}(\mathcal{D}|\mathcal{M}(\theta))p(\theta)d\theta}. \tag{2.14}$$

The probability $p(\theta|\mathcal{M})$ in Eq. 2.14 is known as the *prior*. The prior describes where we believe the true value of the parameters lie and is generally informed by the data and current or past experiments. While the inclusion of a prior is controversial to many frequentists, well-motivated priors, e.g., a physical prior requiring galaxy mass to be positive, ensure that we are using prior information to the best of our ability before gathering and analyzing the data. While there exists a wide range of prior functions, there are a few which are common in the SN Ia literature: uniform, Gaussian, and Jeffreys. A uniform (flat) prior indicates that all points in parameter space are equally probable, but explicitly prohibits points in parameter space outside the prior range. The shape of Gaussian priors can be easily manipulated, and their long tails do not definitively exclude specific parts of parameter space. A Jeffreys prior goes as $1/\theta$, is uniform in log space, and is often used for inference of scale parameters. The choice of priors primarily depends on how much information is available. Broader priors should be used in cases with little information; narrow priors, e.g., from a well-tested theory, are useful in cases with poor data. Ultimately, the choice of prior should not dominate the likelihood. Analyses where the prior is the dominant driver of the posterior indicate that the data cannot constrain the parameters of interest or that the prior was inappropriately chosen.

The denominator of Eq 2.14 is the product of the likelihood and prior integrated over all points in parameter space. This quantity is often referred to as the *model evidence* and is used to determine the "best" model in a set of competing models.

Just as the likelihood is sampled in the χ^2-minimization technique, the joint posterior probability, $p(\theta|\mathcal{D})$, is sampled in Bayesian inference. Rather than sample the full joint posterior, however, we often sample the product of the likelihood and the prior as this is proportional to the posterior and does not require the integration over the full range of parameter space. Therefore, a likelihood is also essential for this method of parameter inference.

2.4.1.1 Bayesian Hierarchical Models

Linear regression with uncertainties in both the independent and dependent variables, as is the case with the SN Ia cosmology problem, is nontrivial in the classical Bayes formalism. The Bayesian Hierarchical Model (BHM) framework was introduced in Gull (1989) to address this issue. Gull proposes a two-part solution:

1. Hidden variables, which represent the latent or "true" values of measured quantities are introduced. These are treated as nuisance variables and ultimately marginalized over.

2. Informative priors are imposed on the *hyperparameters*, parameters describing the latent variables. These priors are particularly important for hyperparameters representing the locations of the latent variables, e.g., the mean of a distribution.

Gull (1989) asserts that this hierarchical or "sub-model" structure recovers unbiased estimates of the parameters, particularly of the slope parameters, as long as informative priors are included. Here, bias in an estimated parameter refers to a systematic deviation from the true value of the parameter, i.e.,

$$\text{bias} \equiv \left\langle \theta^{\text{best fit}} - \theta^{\text{true}} \right\rangle , \tag{2.15}$$

and can only be estimated over multiple realizations of the data.

Figure 2.1 displays a sample BHM for a simple toy regression problem with errors in the independent (x_i) and dependent (y_i) variables (March et al., 2011). In Figure 2.1, solid lines indicate probabilistic connections and dashed lines indicate deterministic connections. Parameters to be constrained are circled in red, latent variables are circled in blue, and data are circled in green. As shown in Figure 2.1, there are two types of parameters to be constrained: the conventional set of model parameters (θ) and the hyperparameter describing the width of the latent x distribution (Σ_x). To achieve unbiased estimates of θ, informative priors must be imposed on the hyperparameters. The classic Bayesian approach would not include the hyperparameter Σ_x which describes the distribution of the latent x_i.

2.4.1.2 Bayesian Inference with SNe Ia

Recently, Bayesian inference has become a more popular technique in SN Ia cosmology analyses due to its flexibility and computational efficiency. The BHM framework easily incorporates a variety of SN Ia standardization models and can be used to explore model nuances and build sophisticated model networks.

Figure 2.2 features two example hierarchical frameworks designed for cosmological parameter inference using SNe Ia. The top panel of Figure 2.2 displays the BHM network presented in March et al. (2011), the first application of BHM to the SN Ia cosmology problem. The bottom panel features a more recent and complex BHM presented in Rubin et al. (2015). In both networks shown in Figure 2.2, dashed lines indicate deterministic relations and solid lines indicate probabilistic relations. Both models include cosmological parameters and the SALT2 SN Ia standardization coefficients α and β. They also include hyperparameters describing the position and scale of the latent light-curve color and stretch distributions. The Rubin et al. (2015) model builds on that of March et al. (2011) by including other parameters such as host-galaxy standardization coefficients and parameters describing systematic uncertainties and sample limiting magnitudes. For fur-

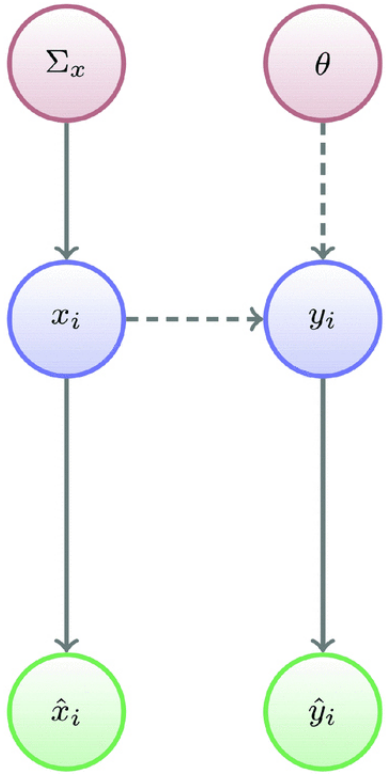

Figure 2.1: Sample BHM reproduced from March et al. (2011). Solid lines indicate probabilistic connections; dashed lines indicate deterministic connections. Parameters to be constrained are circled in red, latent variables are circled in blue, and the data are circled in green. The classic Bayesian model would not include the Σ_x hyperparameter describing the distribution of the latent x_i.

ther examples of the diversity of BHM models applied to SN Ia data, see Mandel et al. (2009), Shariff et al. (2016), and Mandel et al. (2016).

In many SN Ia BHM analyses, deriving the analytic form of the likelihood involves change of variables, marginalization over latent variables and nuisance parameters, assumptions about variable covariances, etc. This leads to analytic prescriptions of the likelihood that are rather complex and may be incomplete. For example, after marginalizing over latent variables, nuisance parameters, and SN Ia redshift uncertainties, the March et al. (2011) likelihood is expressed by

$$p(d|\theta) = \int d\log R_c d\log R_x |2\pi\Sigma_C|^{-1/2} |2\pi\Sigma_P|^{-1/2} |2\pi\Sigma_0|^{-1/2} |2\pi K|^{1/2} \times \exp\left[-\frac{1}{2}\left(X_0^T \Sigma_C^{-1} X_0 - \Delta^T \Sigma_A^{-1} \Delta - k_0^T K^{-1} k_0 + b_m^T \Sigma_0^{-1} b_m\right)\right]. \tag{2.16}$$

Definitions of the parameters used in the likelihood are described in Appendix C of March et al. (2011). We do not define them here as we include the likelihood merely as an illustrative example of SN Ia BHM likelihood complexity.

Rubin et al. (2015) employ several variations of their BHM for cosmological parameter inference, using the Union2.1 compilation of 580 SNe Ia assembled by the Supernova Cosmology Project (Suzuki et al., 2012). When comparing their BHM posteriors to the corresponding best-fit results obtained using the traditional χ^2-minimization approach and the same SN Ia standardization model, they find their 1-D marginalized posteriors give roughly the same 1σ uncertainty region for Ω_m.

2.4.2 Approximate Bayesian Computation

Approximate Bayesian Computation (ABC) offers a "likelihood free" means of sampling from the posterior distribution when the likelihood is intractable. This idea of an alternative means of parameter inference was first introduced in Rubin (1984) and the algorithm and official name of ABC was established in Beaumont et al. (2008).

The goal of the ABC algorithm is to simulate samples directly from the posterior distribution $\mathrm{p}(\theta|\mathcal{D})$ without assuming a particular form for the likelihood. At each proposed

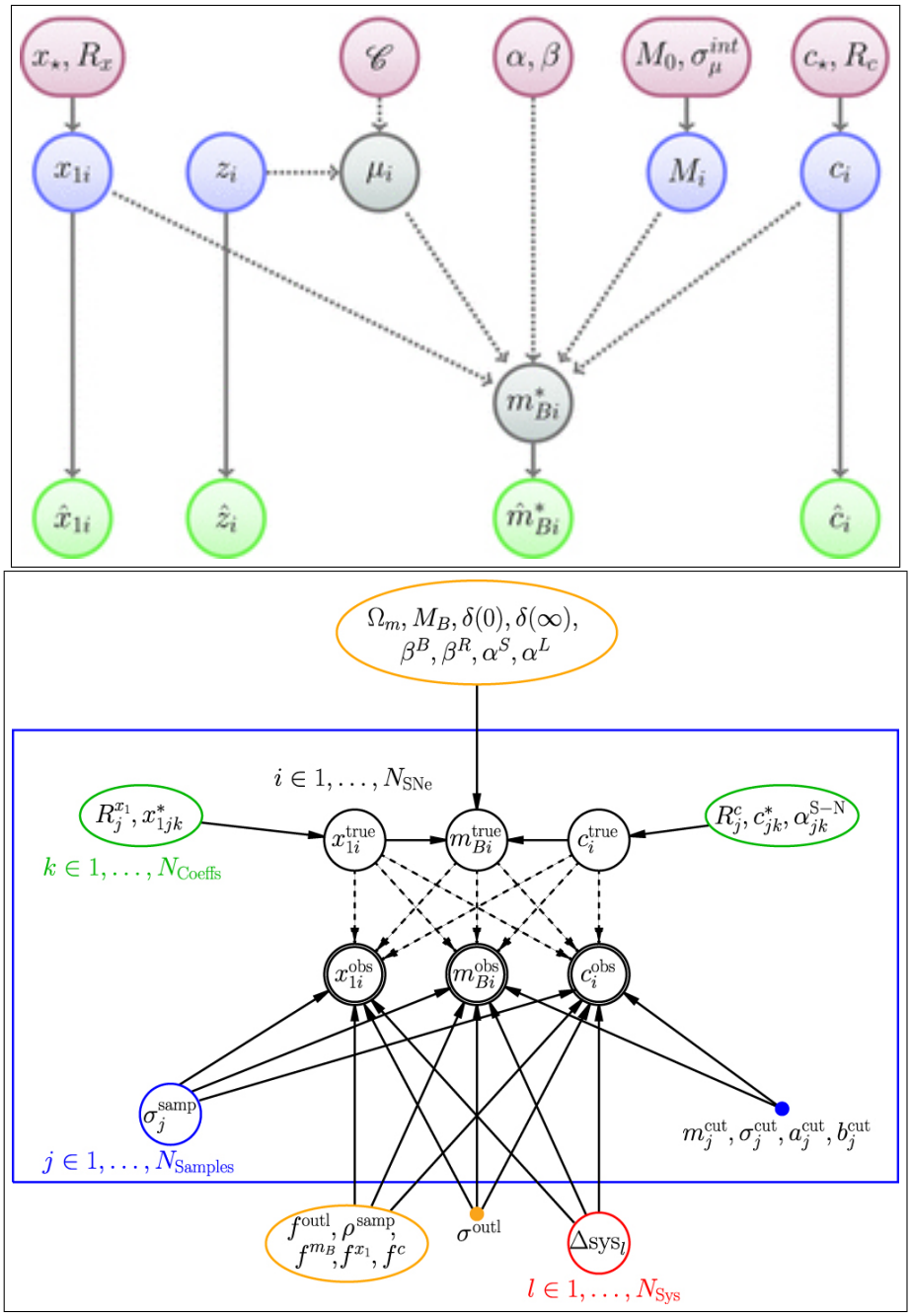

Figure 2.2: Sample Bayesian hierarchical networks for the SN Ia cosmology problem, reproduced from March et al. (2011, top) and Rubin et al. (2015, bottom). Solid lines indicate probabilistic connections; dashed lines indicate deterministic connections. The UNITY model builds on that of March et al. (2011) and includes the same set of cosmological and standardization parameters and hyperparameters as a subset of their larger parameter set.

point in parameter space θ^*, a simulation of the data is drawn, i.e., $\mathcal{D}^* \sim f(\mathcal{D}|\theta^*)$. Sampling the posterior by forward-modeling the data allows for the inclusion of complicated systematics and other survey-specific effects that are not trivial to include in standard χ^2-minimization or other likelihood-based techniques (e.g., BHM). The simulated data set is then compared to the data by way of a metric ρ. Simulations which are "close" to the data are accepted, while others are rejected. The criterion for acceptance is determined by a tolerance threshold ε, which is initially large, but decreased at each step as the simulated distribution converges on the true distribution. Proposed parameters θ^* are accepted if

$$\rho(\mathcal{D}^* - \mathcal{D}) < \varepsilon\,. \tag{2.17}$$

This form of "rejection sampling" is the most common implementation of the ABC algorithm. The process of adapting the threshold to ensure reasonable acceptance rates and proper convergence is known as Sequential Monte Carlo (SMC). SMC will produce samples from $p(\theta|\rho(\mathcal{D}^* - \mathcal{D}) < \varepsilon)$ which will approximate the posterior if ε is small.

Cases of higher dimensional data may reduce the acceptance rate and efficiency of the ABC algorithm. In some instances, it may be simpler to use a lower dimensional *summary statistic* of the data, e.g., a sample mean or variance. Summary statistics used in this way should be *sufficient statistics*, where information contained in the data is also contained in the summary statistic. Using these sufficient statistics ensures that we have not reduced our ability to constrain the parameters of interest.

2.4.2.1 ABC Parameter Inference with SNe Ia

The development of sophisticated supernova light-curve simulation software, such as the SuperNova ANAlysis package (`SNANA`; Kessler et al., 2009b) offer an excellent opportunity for ABC SN Ia cosmology analyses. Such analyses have only recently been explored in works such as Weyant et al. (2013) and Jennings et al. (2016).

Weyant et al. (2013) use the `SNANA` suite to simulate SNe Ia from the SDSS-SNS (Section 1.3.1) and apply their algorithm to data used in the SDSS-SNS first year cosmology analysis (Kessler et al., 2009a). They choose to fit the simulated light curves with

MLCS2k2 (Section 1.2.3) and use the difference between the observed distance modulus and simulated distance modulus as their metric. To evaluate their metric, they smooth the distance moduli as a function of redshift using nonparametric linear regression (`loess`; Cleveland et al., 1992) and take the difference between the theoretical and observed values at the observed redshifts. They define ρ as the median absolute difference between the smoothed curves.

Figure 2.3 compares the uncertainty regions in the inference of w_0 and Ω_m using the Weyant et al. (2013) ABC framework and the χ^2-minimization analysis described in Kessler et al. (2009a). As demonstrated in the Figure, the ABC inference recovers a roughly equivalent uncertainty region as the χ^2-minimization treatment even when incorporating a complex forward-model simulation of the data.

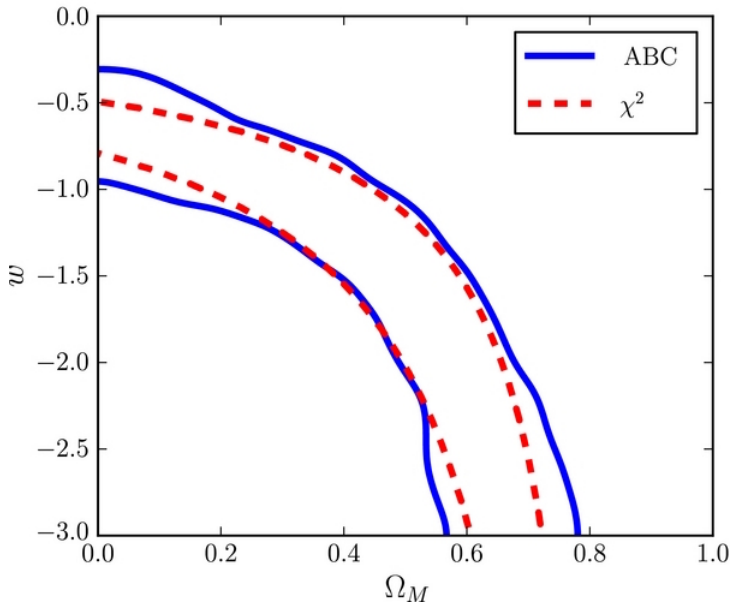

Figure 2.3: Weyant et al. (2013) comparison of uncertainty regions in the $w - \Omega_m$ parameter space using ABC and the χ^2 method as described in Kessler et al. (2009a).

Jennings et al. (2016) proposes alternative ABC metrics using light-curve flux measurements and the SALT2 light-curve fit parameters (Section 1.2.3) using a set of `SNANA`-simulated SNe Ia light curves from the Dark Energy Survey Supernova Program (Kessler

et al., 2015). Their analysis includes parameter inference with two distinct metrics and with and without including systematic uncertainties as parameters in the model. In the "Tripp Metric," the difference between the observed and theoretical distance moduli is computed for the sets of simulated and observed SNe

$$\Delta_{\rm data} = \frac{1}{N_{\rm data}} \sum_{i}^{N_{\rm data}} \frac{[\mu(z_i^{\rm data}, \theta^*) - (m_{b,i}^{\rm data} + \alpha^* x_{1,i}^{\rm data} - \beta^* c_i^{\rm data} - M_0 - \delta M_0^*)]^2}{\sigma_{m_{b,i}}^2 + (\alpha^* \sigma_{x_{1,i}})^2 + (\beta^* \sigma_{c_i})^2 + \sigma_{\rm int}^2}$$

$$\Delta_{\rm sim} = \frac{1}{N_{\rm sim}} \sum_{j}^{N_{\rm sim}} \frac{[\mu(z_j^{\rm sim}, \theta^*) - (m_{b,j}^{\rm sim} + \alpha^* x_{1,j}^{\rm sim} - \beta^* c_j^{\rm sim} - M_0 - \delta M_0^*)]^2}{\sigma_{m_{b,j}}^2 + (\alpha^* \sigma_{x_{1,j}})^2 + (\beta^* \sigma_{c_j})^2 + \sigma_{\rm int}^2},$$

and the metric is defined as the difference between the two offsets:

$$\rho_{\rm Tripp} = |\Delta_{\rm data} - \Delta_{\rm sim}|. \tag{2.18}$$

Rather than use the light-curve fit parameters, the "Light-Curve" metric uses the light-curve fluxes directly and compares the differences in observed fluxes in the *griz* bands for the simulated and observed SNe Ia. This is done by comparing the difference in fluxes to a "reference difference" distribution that accounts for sampling variance in a fixed cosmology. The metric is defined as

$$\rho_{\rm LC} = \sum_{j=0}^{N_{\rm bins}} \chi_j^2, \qquad \text{where} \tag{2.19}$$

$$\chi_j^2 \equiv \frac{(\mathcal{O}_{c_T \tilde{c},j} - \mathcal{E}_{cc,j})^2}{\mathcal{E}_{cc,j}}, \tag{2.20}$$

$\mathcal{O}_{c_T \tilde{c}}$ is the observed distribution of flux differences, and $\mathcal{E}_{cc}$ is the expected distribution of flux differences.

Figure 2.4 presents example 1σ and 2σ contour regions using the "Light-Curve" (top) and "Tripp" (bottom) metrics. Dashed lines in both plots indicate the posterior distributions when systematic uncertainties are included as parameters in the model and the yellow star indicates the true values of the parameters used to generate the simulated data set.

As Figure 2.4 shows, both ABC metrics successfully recover the input value in the 1σ uncertainty region. The 1σ posterior is narrower using the "Tripp" metric than when using the "Light-Curve" metric, yet including systematics tightens the uncertainty region using the "Light-Curve" metric. The bottom figure also includes results using traditional χ^2-minimization parameter inference with MCMC (purple contours). The ABC algorithm recovers similar 1σ and 2σ uncertainty regions to those inferred with χ^2-minimization while including more complicated survey-specific effects such as weather conditions and spectroscopic selection efficiency.

2.5 Assumptions and Challenges in SN Ia Parameter Inference

Each of the methods described in Sections 2.3 and 2.4 has its own advantages and disadvantages. For example, likelihood-based frameworks are often computationally more efficient than ABC; likelihood evaluation and sampling typically requires much less computing time than the forward-model simulations and SMC necessary for ABC parameter inference. On the other hand, ABC methods which rely on simulations of the data can more robustly account for survey-specific effects which are difficult to describe analytically. When performing cosmological parameter inference, it is critical that one is aware of the different ways in which these methods deal with several key assumptions and challenges:

1. *Analytic Likelihood Assumptions*

   In the standard likelihood-based technique, the likelihood $p(\mathcal{D}|\theta)$ is often assumed to be a Gaussian, multivariate Gaussian, or product of Gaussian distributions (March et al., 2011; Betoule et al., 2014; Rubin et al., 2015; Shariff et al., 2016). This implies that each data point is normally distributed about the model value with the variance (covariance) as indicated by the likelihood. While this treatment has become convention, there is no reason to assume that all SNe Ia data follow this pre-

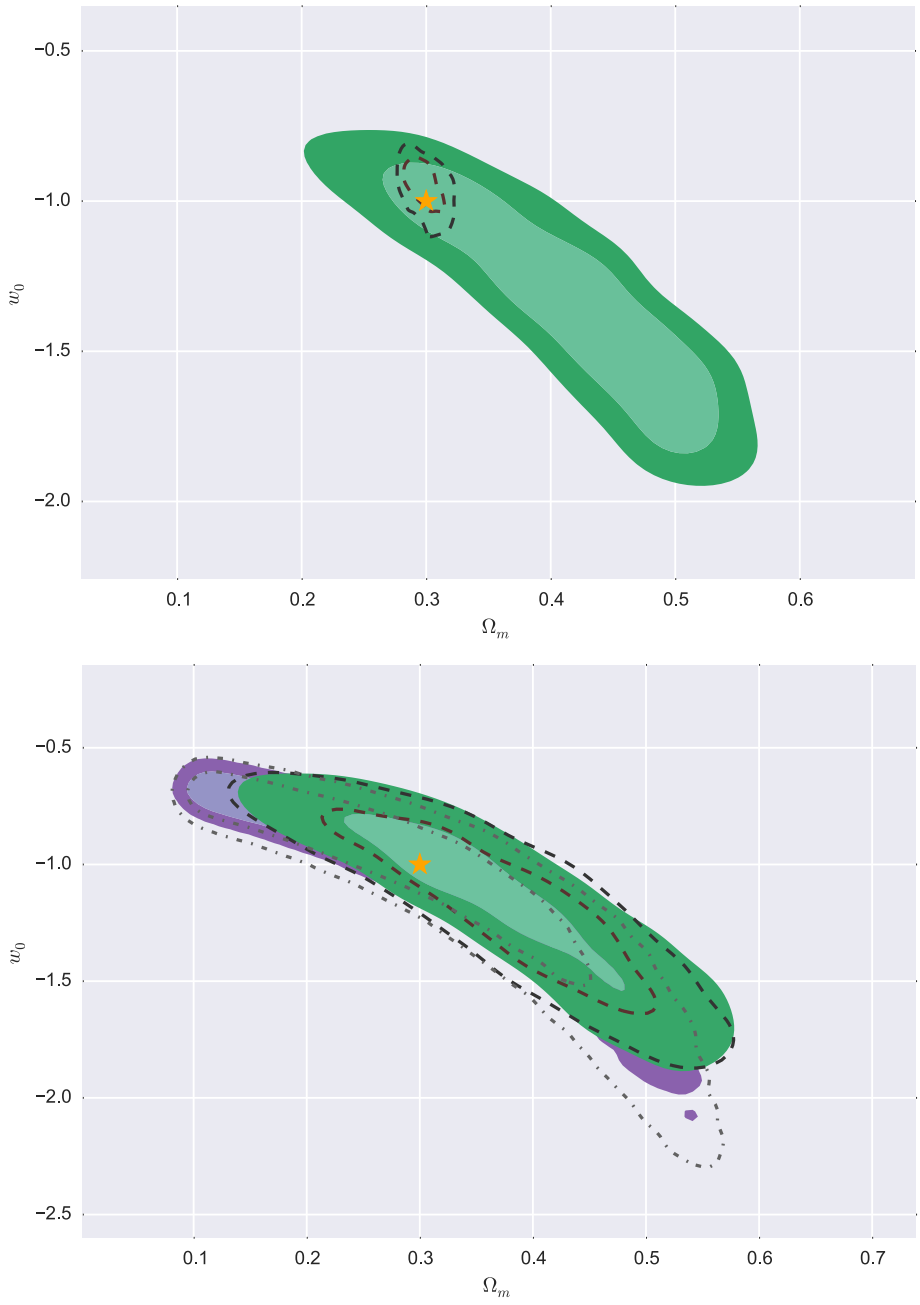

Figure 2.4: 1σ and 2σ contour regions using the "Light-Curve" (top) and "Tripp" (bottom) metrics reproduced from Jennings et al. (2016). The yellow stars indicate the true values used in the simulated data set. Green contours represent the results using the ABC metric; purple contours represent results using traditional χ^2-minimization parameter inference. Dashed (ABC) and dot-dashed (χ^2-minimization) lines indicate the increased parameter uncertainty when including systematics.

scription. ABC methods avert this assumption by avoiding the use of the likelihood entirely.

2. *Analytic Model Assumptions*

   Conventional likelihood-based techniques also require an analytic description of the model, e.g., in the SN Ia case, we utilize a regression equation to parameterize $\mu_i^{\rm mod}$. However, including parameters to account for more realistic effects, such as selection bias, is nontrivial and may result in a model parameterization that is incomplete or incorrect. ABC methods do not rely on such a model prescription, but must instead design an effective metric by which to compare the observations to simulated data. Developing such a metric is also nontrivial and choice of metric can significantly effect the resulting posterior distributions of interest (Jennings et al., 2016).

3. *Systematic Uncertainties*

   Properly including systematics is essential, particularly in the era of precision cosmology (Section 1.3). In likelihood-based techniques, it has become standard practice to incorporate systematic effects into the covariance matrix used in the likelihood (Kessler et al., 2009a; Conley et al., 2011; Betoule et al., 2014). However, accounting for modeling and instrumental systematics, as well as correlations between parameters of interest is not straightforward (Morrison and Schneider, 2013; Betoule et al., 2014). Estimating some systematic effects, such as those from light-curve fitting, requires rigorous simulations; if these estimates are drawn from too few a number of simulations, or if the simulations are drawn from a fixed cosmology, then the estimated covariance may be insufficient. Therefore methods which rely on a fixed derived covariance matrix must be used with caution, as uncertainties in the covariance propagate to uncertainties in the inferred cosmological parameters (Dodelson and Schneider, 2013). Frameworks which rely on forward-model simulations of the data, such as ABC, avoid many of these issues as the effect of

various systematics are reevaluated at each proposed point in parameter space.

4. *Selection Bias*

   Perhaps one of the most significant remaining challenges in SN Ia cosmology is how to appropriately treat selection bias. This is particularly important in a magnitude-limited survey where only the brightest objects are detected at high redshifts.

   As discussed in Section 1.3.1, this selection bias can be quantified using survey-specific simulations:

$$\mu_{\mathrm{bias}\,i} \equiv \mu_{\mathrm{fit}\,i} - \mu_{\mathrm{sim}\,i}\,, \tag{2.21}$$

   where $\mu_{\mathrm{fit}\,i}$ is the distance modulus derived from the best fit cosmology and $\mu_{\mathrm{sim}\,i}$ is the simulated observed distance modulus. This bias is typically quantified in bins of redshift (i.e., $\mu_{\mathrm{bias}\,i'} =< \mu_{\mathrm{bias}\,i} >$; $z_{i'} < z_i \leq z_{i'+1}$) and derived from simulations at a fixed cosmology, but has been shown to yield more accurate inference when also binned as a function of light-curve parameters (Scolnic and Kessler, 2016). Several analyses have included this estimation of the bias when using an incomplete sample of SNe Ia for cosmological parameter inference. In this case, the observed distance moduli are "corrected" for selection bias by adding an additional bias factor to the observed distance moduli or peak B-band magnitude, i.e., $\mu_i^{\mathrm{obs}} \rightarrow \mu_i^{\mathrm{obs}} + \mu_{\mathrm{bias}\,i'}$ (Kessler et al., 2009a; Conley et al., 2011; Campbell et al., 2013; Betoule et al., 2014; Shariff et al., 2016). While this solution results in unbiased cosmological parameter estimates, there is no statistical justification for accounting for this global effect on an individual SN Ia basis.

   Another proposed solution is to parameterize the selection as part of the SN Ia standardization model. To this effect, Rubin et al. (2015) include sample limiting magnitudes as fit parameters in their model. This approach also yields unbiased estimates in the cosmological parameters, but is entirely dependent on the analytic model description.

Methods which incorporate forward-model simulations of the data and accurately simulate survey-specific selection effects can account for selection bias in a robust, statistical framework. A particular advantage of this treatment is that rather than include a correction derived from a fixed cosmology, the simulation can explore the difference in selection effects at all proposed points in parameter space.

5. *Data and Parameter Covariance*

   In addition to properly accounting for systematic uncertainties, methods of cosmological parameter inference must also be able to accommodate covariances between the data points and/or the model parameters. This becomes increasingly difficult when selection effects must also be included in the framework, i.e., it is unclear how imposing a magnitude cut on a SN Ia sample affects covariance between $m_{Bi}^{\rm obs}$ and $c_i^{\rm obs}$. This can be addressed in an analytic model by making assumptions about parameter covariance or by using forward-model simulations to explore these covariances at different proposed points in parameter space.

As we move forward in the era of precision cosmology, developing statistical frameworks which can accommodate photometrically-classified samples will be essential. While promising methods have been introduced (e.g., Kunz et al., 2013; Hlozek et al., 2012; Kessler and Scolnic, 2017), new frameworks will have to addresses not only the issues described here, but others such as type contamination and host-galaxy misidentification.

Chapter 3

SDSS-II Supernova Survey: An Analysis of the Largest Sample of Type Ia Supernovae and Correlations with Host-Galaxy Spectral Properties

3.1 Introduction

Type Ia supernovae (SNe Ia) are crucial observational probes for investigating the history of our expanding universe. The origin of these phenomena remains a mystery, although there is evidence for two distinct SN Ia progenitor systems (the so-called single-degenerate and double-degenerate scenarios) that result in a thermonuclear explosion occurring as the mass of a carbon-oxygen white dwarf approaches the Chandresekhar limit (Whelan and Iben, 1973; Nomoto, 1982; Iben and Tutukov, 1984; Webbink, 1984; Hillebrandt and Niemeyer, 2000). Observations of these incredibly bright explosions, visible

This chapter has modified for this thesis from the published Wolf et al. (2016).

out to high redshifts, have provided evidence for the accelerating expansion of the universe (Riess et al., 1998; Perlmutter et al., 1999) and are used to measure cosmological parameters with increasing precison (Astier et al., 2006; Kessler et al., 2009a; Conley et al., 2011; Betoule et al., 2014; Scolnic et al., 2014a). Their efficacy as "standard candles," however, relies on the ability to calibrate intrinsic luminosity with SN light-curve width ("stretch") and optical color (Phillips, 1993; Hamuy et al., 1996; Riess et al., 1996; Tripp, 1998). After applying these corrections using light-curve fitting techniques, there remains a 1σ dispersion in peak brightness of about 0.1 mag, corresponding to about 5% in distance (Conley et al., 2011; Betoule et al., 2014). The origin of this scatter remains unknown, yet it is postulated that both the progenitor and its environment play a role (Gallagher et al., 2005, 2008; Neill et al., 2009; Howell et al., 2009; Kelly et al., 2010).

In this chapter, we study the relationship between SN Ia Hubble residuals (HRs) and properties of their host galaxies, including mass, metallicity, and star-formation rate, using SN Ia data and host-galaxy photometry from the full three-year Sloan Digital Sky Survey-II Supernova Survey (Sako et al., 2014, SDSS-SNS; hereafter S14) and a combination of host-galaxy spectra from an ancillary program of the SDSS-III Baryon Oscillation Spectroscopic Survey (Dawson et al., 2013; Olmstead et al., 2014, hereafter BOSS) and from the SDSS I/II spectroscopic survey (Strauss et al., 2002; Abazajian et al., 2009). In comparison to recent literature, this is the largest single-survey sample of spectroscopically-confirmed or photometrically-classified SN Ia light curves and host-galaxy spectroscopic data. As newer, larger surveys, such as the Dark Energy Survey (Bernstein et al., 2012), Pan-STARRS (Kaiser et al., 2002), and LSST (LSST Science Collaboration et al., 2009) will also heavily rely on photometrically-classifed samples of SNe Ia, the biases and selection effects discussed in this analysis will be critical for future host-galaxy studies.

We adopt the best fit flat, ΛCDM cosmology for SNe Ia alone as determined by Betoule et al. (2014, hereafter B14), a joint analysis of 740 spectroscopically-confirmed SNe Ia from a compilation of surveys of low-, intermediate-, and high-redshift ranges

($\Omega_m = 0.295$). Since the value of the Hubble constant is degenerate with the absolute magnitude of SNe Ia, we adopt $H_0 = 70$ km s^{-1} Mpc^{-1}. We use this cosmology to compute HR, defined as HR $\equiv \mu_{\rm SN} - \mu_z$, where $\mu_{\rm SN}$ is the distance modulus estimated from fitting SN Ia light curves and μ_z is the distance modulus computed using the redshift and the assumed cosmology. The HR quantifies whether our SNe Ia are overluminous (negative HR) or underluminous (positive HR) after light-curve correction.

The general structure of this analysis is as follows: in Section 3.2 we describe our SN and galaxy data. Section 3.3 highlights light-curve quality requirements for the SNe Ia sample and describes the treatment of effects such as Malmquist bias. Section 3.4 details our methods for extracting galaxy spectroscopy and the selection cuts we impose on the host-galaxy sample. Section 3.5 outlines how we derive host-galaxy properties from emission-line fluxes. The sample selection requirements discussed in Sections 3.3, 3.4, and 3.5 ultimately yield two final samples for analysis, which contain 345 and 144 SNe Ia, respectively. In Section 3.6 we present our findings, and we discuss our results in Section 3.7.

3.2 Observational Data

Observations from the SDSS-SNS were used for our SN Ia sample, and a combination of spectra from SDSS and BOSS was utilized for host-galaxy spectroscopy. Spectra of host galaxies are important not only for securing redshifts of their SNe but also as probes of the physical properties of galaxies themselves. As summarized in Chapter 1, these properties can influence the SN Ia progenitor and the subsequent explosion. We describe how we obtain our SN and host galaxy data in Sections 3.2.1 and 3.2.2, respectively.

3.2.1 Supernovae

All SNe in this work were discovered and observed by the SDSS-SNS (see Chapter 1). A full description of data acquisition and reduction from the SDSS-SNS can be found in

the final Data Release paper (S14). Over its three-year run, the SDSS-SNS discovered 10,258 new variable objects in the redshift range $0.01 < z < 0.55$. Of these, 499 were spectroscopicallyclassified as SNe Ia ("Spec-Ia"). In S14, these SNe Ia are typed "SNIa."

Analyses that use spectroscopically identified samples of SNe Ia (e.g., Kessler et al., 2009a; Betoule et al., 2014) are highly pure, as they contain, to high confidence, only SNe Ia. However, such samples, as in the case of the SDSS-SNS, can be biased, as the likelihood of an SN Ia being spectroscopically classified is a function of many factors: its location within the host galaxy, its relative brightness compared to the surface brightness of the host galaxy, and its color (but not the intrinsic brightness; see Figure 10 of S14). Additionally, the expense of spectroscopy is a limiting factor in rolling SN surveys such as the SDSS-SNS: resources are typically unavailable (or observing conditions disadvantageous) for a complete spectroscopic program. For these reasons, we also use in this chapter SDSS-SNS transients that have been *photometrically-classified*, using the host-galaxy spectroscopic redshift as a prior, as SNe Ia ("Phot-Ia"). In S14, these SNe Ia are typed "zSNIa." We describe the classification and data-quality cuts applied to this catalog of transients in Section 3.3.

3.2.2 Host Galaxies

Our primary source of SN host-galaxy spectroscopy is the BOSS survey of SDSS-III (Eisenstein et al., 2011). BOSS, which ran from 2008 to 2014, was designed to measure the scale of baryon acoustic oscillations (BAOs) by observing 1.5 million galaxies to redshift $z < 0.7$ and 150,000 quasars at redshifts $2.15 < z < 3.5$ over an area of $10,000$ deg^2. To accommodate this survey, the original SDSS spectrograph was rebuilt with smaller fibers ($2''$ diameter, allowing a larger number of targets per pointing), more sensitive detectors in both the blue and red channels, and a wider wavelength range ($361 - 1014$ nm). These improvements allowed the survey to reach higher galaxy redshifts and observe about one magnitude deeper than SDSS. A detailed description of the BOSS spectrograph (as the upgraded instrument is now known) can be found in Smee et al. (2013).

Approximately 5% of the BOSS fibers were allocated to ancillary science programs, one of which was the systematic targeting of host galaxies of SN candidates from the SDSS-SNS. Targets for this program were prioritized based on the probability of the observed transient being a Type Ia or core-collapse (CC) SN using the photometric–classification software PSNID (see Section 1.3.1), as well as on the *r*-band fiber magnitude of the host galaxy ($r_{\rm fiber} < 21.25$). A total of 3761 of the 4777 requested targets were observed, with non-observations primarily due to the finite availability of fibers and clashes with higher priority targets. The SDSS-SNS target selection for this ancillary program is detailed in Olmstead et al. (2014) and Campbell et al. (2013).

We use in this analysis the host-galaxy matching done in S14. Here each detected transient is matched to the SDSS Data Release 8 (Aihara et al., 2011) catalog using an algorithm that identifies the "nearest" galaxy in a parameter space that accounts for the apparent size and surface brightness profile of each galaxy within a $30''$ radius of the transient coordinates. It is estimated that this method is able to match host galaxies with 97% accuracy (S14).

The host-galaxy matching that defined the target selection for BOSS spectroscopy was performed years prior to the development of the algorithm used in S14. Therefore, it would not be unexpected if some fraction of the BOSS targets do not correspond to the currently identified host galaxy, resulting in an incorrect assumed redshift for some SNe. We find that the existing redshifts (either from the SN spectrum or from a non-BOSS host spectrum) of three SNe Ia disagree with those of their respective BOSS targets. For each of these cases, the BOSS spectrum is of a galaxy that is offset from the currently identified host by more than $8''$, indicating that the BOSS target is not the correct host. To avoid possible ambiguity, we remove these three SNe from our sample. For further discussion of BOSS targeting and host-galaxy mismatches see S14.

As all of Stripe 82 lies within the area observed by the SDSS-I/II spectroscopic survey, many of our transients have pre-existing host spectra. The BOSS ancillary program targeted the location of the SN within the galaxy where spectroscopy of the host galaxy

already exists in the SDSS database. This work derives global spectroscopic properties of the host galaxies and thus preferentially uses SDSS spectra where they exist, as these spectra typically have higher signal-to-noise ratio (S/N) than BOSS spectra due to their larger fiber width ($3''$ diameter) and being centered on the host galaxy.

We will return to this point briefly in Section 3.5, where we discuss the breakdown of spectra passing various cuts for data quality.

3.3 Supernova Selection and Properties

We select our sample of photometrically classified SNe Ia using the Photometric SN IDentification (PSNID) software (Sako et al., 2011) described in S14. In this work we use only those classifications from S14 where the host-galaxy redshift is included as a prior on the light-curve fit, which is important for precise placement of SNe Ia on the Hubble diagram. We impose the PSNID selection criteria outlined in Section 4 of S14: the PSNID fit probability is ≥ 0.01 for the SN Ia model; the Bayesian probability of being an SN Ia is ≥ 0.9; and the nearest-neighbor probability of being an SN Ia is greater than that of being a CC SN. We place an additional requirement on light-curve sampling, requiring the candidate to have at least one detection at $-5 \leq T_{\rm rest} \leq +5$ days and one at $+5 < T_{\rm rest} \leq +15$ days, where $T_{\rm rest}$ is the rest-frame time such that $T_{\rm rest} = 0$ corresponds to peak brightness in rest-frame B band. Imposing these criteria yields a sample of 824 photometrically-classified SNe Ia with a purity and efficiency of $\sim$96% (determined from simulations; for more complete definitions of sample purity and efficiency see S14).

The photometrically classified SNe selected by the above requirements, combined with the 499 Spec-Ia, define a maximally large sample of SNe Ia in SDSS-SNS. As we are interested in host-galaxy correlations with the derived distance modulus to these SNe, we apply additional cuts to create a sample that can produce reliable distance estimates. We fit these light curves using the implementation of SALT2 (Guy et al., 2010) in the SuperNova ANAlysis package (`SNANA`; Kessler et al., 2009b), keeping only SNe Ia that

meet the following criteria:

1. At least one detection before peak brightness ($T_{\rm rest} < 0$).
2. At least one measurement with $T_{\rm rest} > +10$ days.
3. At least five detections between $-15 < T_{\rm rest} < +60$ days.
4. At least three filter-epoch detections with $S/N > 5$.
5. The measured color (c) and stretch (x_1) are within the elliptical cut outlined in Campbell et al. (2013, Figure 6).
6. $P_{\rm FIT} > 0.01$, where $P_{\rm FIT}$ is the SALT2 light-curve fit probability based on the χ^2.

Distance moduli are then estimated using the code `SALT2mu` (Marriner et al., 2011), also a part of the `SNANA` suite. In the SALT2 model, the distance modulus is given by

$$\mu_{\rm SN} = m_B - M_0 + \alpha x_1 - \beta c, \tag{3.1}$$

where m_B (peak apparent B-band magnitude), x_1, and c are fit for each individual SN and M_0 (absolute magnitude), α, and β are global parameters of the SN sample. `SALT2mu` computes α and β (cosmology-independent corrections for the light-curve stretch and color) from a given SN Ia sample, allowing us to determine $\mu_{\rm SN}$ for each SN in the sample.

This computation of the distance modulus, however, has not been corrected for selection effects (i.e. Malmquist Bias). The well-known Malmquist bias stipulates that for a magnitude limited survey, a given SN Ia may appear brighter due to random statistical fluctuations. These fluctuations can be seen to a greater distance and thus a larger portion will be detected in a magnitude-limited sample. To determine the correction for this effect, as well as other corrections stemming from SALT2 fitting (e.g., poor fits to low *S/N* data), we run SDSS-like simulations (with approximately 10 times the data statistics) and compare the expected ($\mu_{\rm TRUE}$) and observed ($\mu_{\rm FIT}$) distance moduli. Realistic light curves are simulated using the `SNANA` code, where the MC is used to make detailed comparisons

with the data using different models of intrinsic SN Ia brightness variations (Kessler et al., 2013). The simulations assume the best fit flat ΛCDM cosmology of B14 ($\Omega_{\rm m} = 0.295$) and SN Ia are generated using the SALT2 model (Guy et al., 2010). As in Kessler et al. (2013), we simulate asymmetric Gaussian distributions for our input color and stretch. The following parameters best match our data: $\bar{c} = -0.09$, $\sigma_{+,c} = 0.13$, $\sigma_{-,c} = 0.02$, $\bar{x_1} = 0.5$, $\sigma_{+,x_1} = 0.5$, and $\sigma_{-,x_1} = 1.5$. Comparisons between the data and simulations are presented in Figure 3.1.

The average difference in distance modulus as a function of redshift, which we define as $\mu_{\rm BIAS}$, is presented in Figure 3.2. In the lower-redshift range ($z \lesssim 0.3$) the bias is very small; however, as the redshift exceeds $z = 0.3$, the offset noticeably grows with redshift. In the higher redshift regime, the magnitude of the bias approaches that of our host-galaxy effects; therefore, correcting for this bias may potentially misconstrue any observed host-galaxy correlations. To ensure that our sample is not contaminated by this bias, we choose to limit the redshift of our SNe Ia to $z < 0.3$. If we recompute the bias for this lower redshift sample only, we find $-0.006 < \mu_{\rm BIAS} < 0.008$ and conclude that this effect is negligible and does not require additional corrections.

As presented in Table 3.1, 473 SNe Ia meet the light-curve sampling, c and x_1, $P_{\rm FIT}$, and redshift requirements.

The elliptical cut in the c–x_1 plane removes much of the contamination from CC SNe in the photometric sample. We apply this cut on light-curve fit parameters to both the Phot-Ia and Spec-Ia samples, as we wish to maintain homogeneity across our combined sample and as these light-curve fit parameters are used to estimate the SN distance moduli. Given our data, we find best fit values of $\alpha = 0.14 \pm 0.012$ and $\beta = 3.11 \pm 0.140$. In order to obtain $\chi^2_{\rm red} \approx 1$, an intrinsic scatter of 0.167 mag must be added when performing the fit. HRs for our SNe are then calculated from $\mu_{\rm SN}$ and μ_z computed with the assumed B14 cosmology. However, we note that we do not incorporate this intrinsic scatter into the uncertainty on the distance moduli μ_{SN} used in this analysis. Rather, we independently fit for the intrinsic scatter when analyzing correlations between HR and

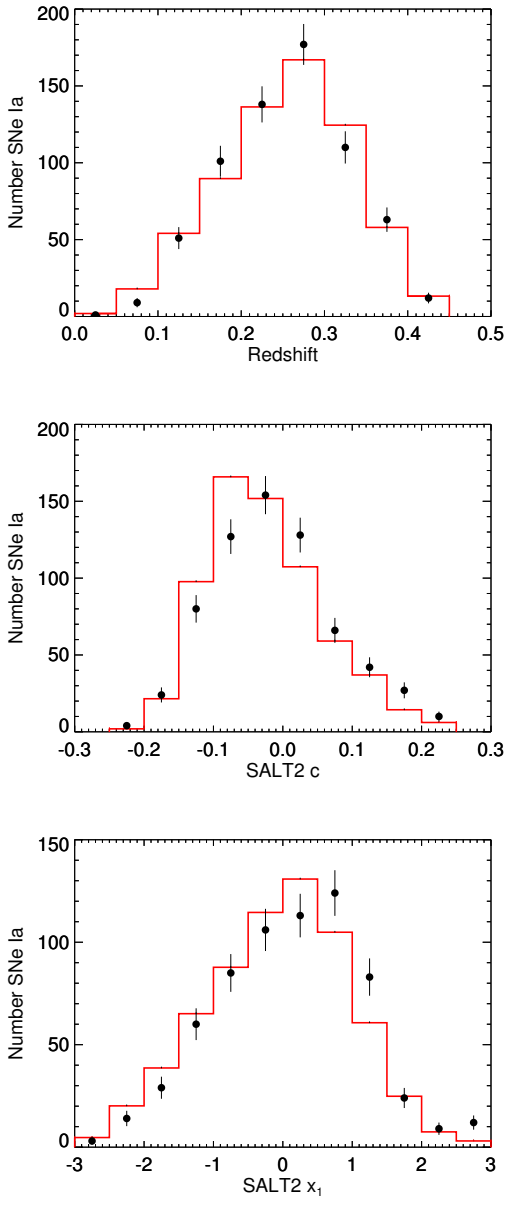

Figure 3.1: Comparison of MC simulation (red histogram) and SDSS-SNS data (black points). The MC distributions are normalized to the low-z ($z < 0.25$) data. Error bars on the data points represent the square root of the number of SNe Ia in the respective bin. Distributions are displayed for the redshift (top), SALT2 color (middle) and SALT2 stretch (bottom).

Table 3.1. Cumulative PM Sample Definition

Selection Requirements	Removed SNe Ia	Total	Phot-Ia	Spec-Ia
Total SDSS-SNS Transients	–	10,258	–	–
S14 SNe Ia[a]	8935	1323	824	499
Nonpeculiar SNe Ia	8	1315	824	491
Light-curve sampling	534	770	434	336
Elliptical c, x_1 cuts	67	703	382	321
$P_{\rm FIT} > 0.01$	41	662	361	301
$z < 0.3$	189	473	215	258
HR outlier rejection	7	466	208	258
Host spectrum identified	116	350	177	173
Host, SN redshift agreement	3	347	176	171
Well-defined host mass	2	345	176	169

[a]This removes transients, such as CC SNe, that were not identified as SNe Ia in Sako et al. (2014).

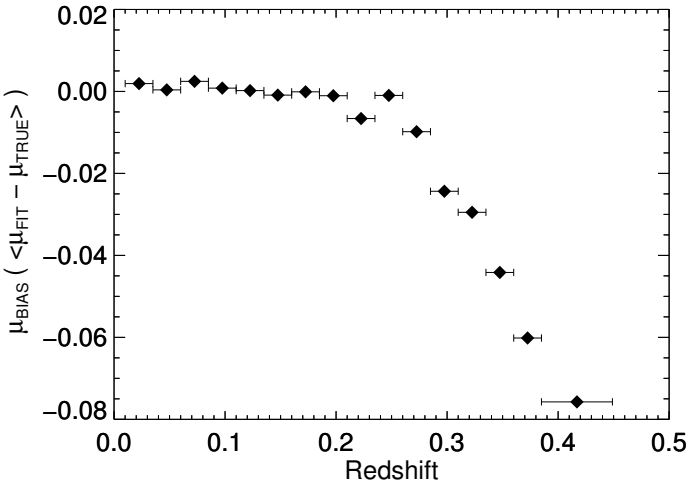

Figure 3.2: Difference between the measured and true distance modulus (defined as $\mu_{\rm BIAS}$) from our simulations, as a function of redshift. Data points are inverse-variance weighted averages in redshift bins of width 0.025 with error bars representing the width of each bin. Each bin contains at least 500 SNe Ia.

host-galaxy properties. This is further explained in Section 3.6.

When examining the HR for our data, we notice a strong correlation between HR and c, particularly for $c < 0$; we do not observe such a correlation between HR and x_1. Both trends are also apparent in our simulations and this trend with c has been seen previously in SN surveys at both low and high redshift (Sullivan et al., 2011; Ganeshalingam et al., 2013). We elect not to correct for this effect in our analysis as this is not done in previous works and we wish to compare our results in the most consistent manner possible. A discussion of HR-c corrections and the effect on our results can be found in Appendix A.

Figure 3.3 displays the distribution of HRs of those SNe Ia passing our selection requirements. The mean of the distribution is 0.014 mag and the standard deviation is 0.228. We remove from our sample seven SNe with HRs $> 3\sigma$ from the mean (corresponding to HR < -0.668 and HR > 0.697) as it is highly unlikely that these are normal SNe Ia. All SNe removed in this way are Phot-Ia; this outlier rejection method does not affect the number of spectroscopically-confirmed SNe Ia in our sample. After removing

these outliers, the mean and standard deviation of the HR distribution reduce to 0.002 and 0.187, respectively. Imposing this requirement leaves 208 Phot-Ia and 258 Spec-Ia in our sample. As a check, we have examined the Hubble diagram of this sample and found that imposing these criteria removes the majority of potential contaminants and shows no noticeable redshift-dependent pollution. Overall, this Hubble diagram is much cleaner than what is presented in Sako et al. (2014), due to the fact that we impose stricter S/N requirements and temporal coverage of our SN Ia light curves.

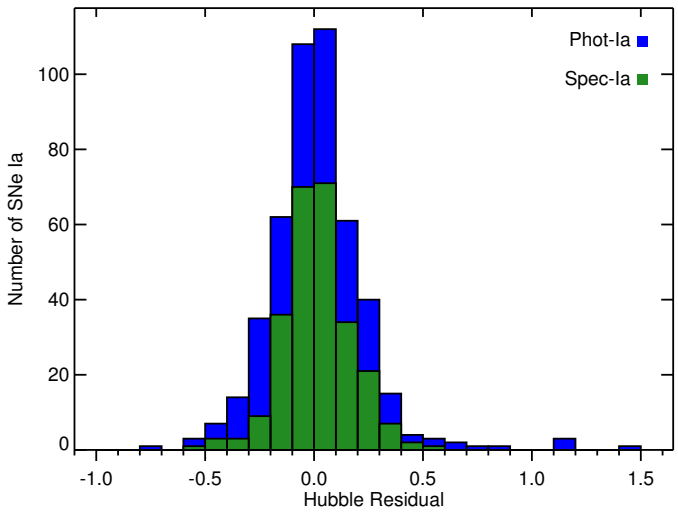

Figure 3.3: Distribution of HRs calculated using the derived `SALT2mu` distance moduli. Histograms are stacked such that the Phot-Ia (blue) and Spec-Ia (green) add to the total number in a given bin. The mean of the distribution is 0.014 mag and the standard deviation is 0.228. We remove from our sample seven SNe with HRs $> 3\sigma$ from the mean (corresponding to HR < -0.668 and HR > 0.697) as it is highly unlikely that these outliers are normal SNe Ia. All outliers removed in this way are Phot-Ia. This reduces the mean and standard deviation to 0.002 and 0.187, respectively.

Finally, we require that the SNe Ia have an observed host-galaxy spectrum and photometrically derived host-galaxy mass with well-defined uncertainties (as described in Section 3.5.3). The requirement that each host has a BOSS or SDSS spectrum is necessary to ensure that we are correctly matching the SN Ia with its host. This requirement removes

both Phot-Ia and Spec-Ia with host spectra followed up by programs other than BOSS or SDSS, as well as hostless Spec-Ia. Although each host in our sample has an observed spectrum, we do not use spectral absorption features to obtain host masses (discussed in Section 3.4.1) and instead rely on photometric mass measurements.

We remove those SNe Ia that do not meet these criteria and are left with a sample of 345, which we define as the PM (Photometric Mass) sample. These cuts, in addition to all those previously described in this section, are outlined in Table 3.1. The PM sample is one of two samples of SNe Ia we analyze in Section 3.6; further spectroscopic requirements imposed to cull the second sample are detailed in Section 3.4.2

3.4 Host Galaxy Spectral Analysis

We describe here our analysis of BOSS and SDSS-I/II spectra of the host galaxies of SNe Ia from the SDSS-SNS. Section 3.4.1 outlines the procedure used to measure fluxes, equivalent widths, and amplitude-to-noise ratio (the ratio of the peak flux of the emission line to the continuum; hereafter A/N) from the spectra, which we optimize and use instead of existing catalog data. Section 3.4.2 details the requirements, both physical (e.g., active galactic nucleus [AGN] contamination) and observational (e.g., S/N), we impose on the spectra to be included in our subsequent analysis of host-galaxy emission-line properties.

3.4.1 Methods

Emission-line properties of galaxy spectra obtained as part of the BOSS and SDSS-I/II programs are calculated using Version 1.8 (v1.8) of the code `GANDALF` (Gas AND Absorption Line Fitter; Sarzi et al., 2006). `GANDALF` simultaneously fits for the stellar population and the emission-line spectrum, which prevents the presence of absorption lines from biasing the measurement of ionized gas emission. `GANDALF` uses pPXF (penalized Pixel-Fitting; Cappellari and Emsellem, 2004) to measure the stellar kinematics of the galaxy while masking the emission-line regions. The code then fits the gas kinematics (velocity

and velocity dispersion) and measures emission-line fluxes for a user-determined set of (Gaussian) emission lines. The effects of dust in the observed galaxy are corrected for by simultaneously fitting for extinction under the assumption of a Calzetti (2001) reddening law. A sample GANDALF spectral fit is shown in Figure 3.4.

Our work with GANDALF closely follows that of Thomas et al. (2013, hereafter T13), which details the method used for measuring emission-line properties in SDSS DR9 (Ahn et al., 2012). As in T13, our galaxy templates are simple stellar population (SSP) models from Maraston and Strömbäck (2011, hereafter M11). The particular set of models we use is built on the MILES stellar library, which is extended into the UV based on a theoretical library (necessary to constrain the blue end of our observed spectra). Our template library is derived using a Salpeter initial mass function (IMF) (Salpeter, 1955), as an extended UV library for M11 is not available with Chabrier (Chabrier, 2003) or Kroupa (Kroupa, 2001) IMFs. We resample the M11 galaxy templates to have a wavelength-independent resolution of $R = 2000$. This is an approximation to the true instrumental resolutions of both SDSS I/II and BOSS, which are wavelength dependent. Before conducting our analysis, we convert the observed spectra from the SDSS-standard vacuum wavelengths into air wavelengths. We additionally assume only a single metallicity (solar) and a subset of 19 of the 47 available galaxy ages in the model. These choices are motivated by the fact that the primary goal is to remove the continuum; small variations in the underlying spectrum only matter to the extent that they affect the emission-line measurements. It also results in a significant reduction in computation time. We ran GANDALF on a subset of our spectra using both the full and reduced sets of temporal templates and found that our results were in no way affected by this choice.

We have made a few changes from the analysis of T13 that are optimized to our data set. The most significant of these is how we tie spectral lines in the fitting procedure, fixing the velocity and width of the Balmer and forbidden lines to values derived for Hα and [N II], respectively. T13 does not adopt this procedure as Hα and [N II] are redshifted beyond the BOSS wavelength range at $z > 0.45$, and their goal is a homogeneous deriva-

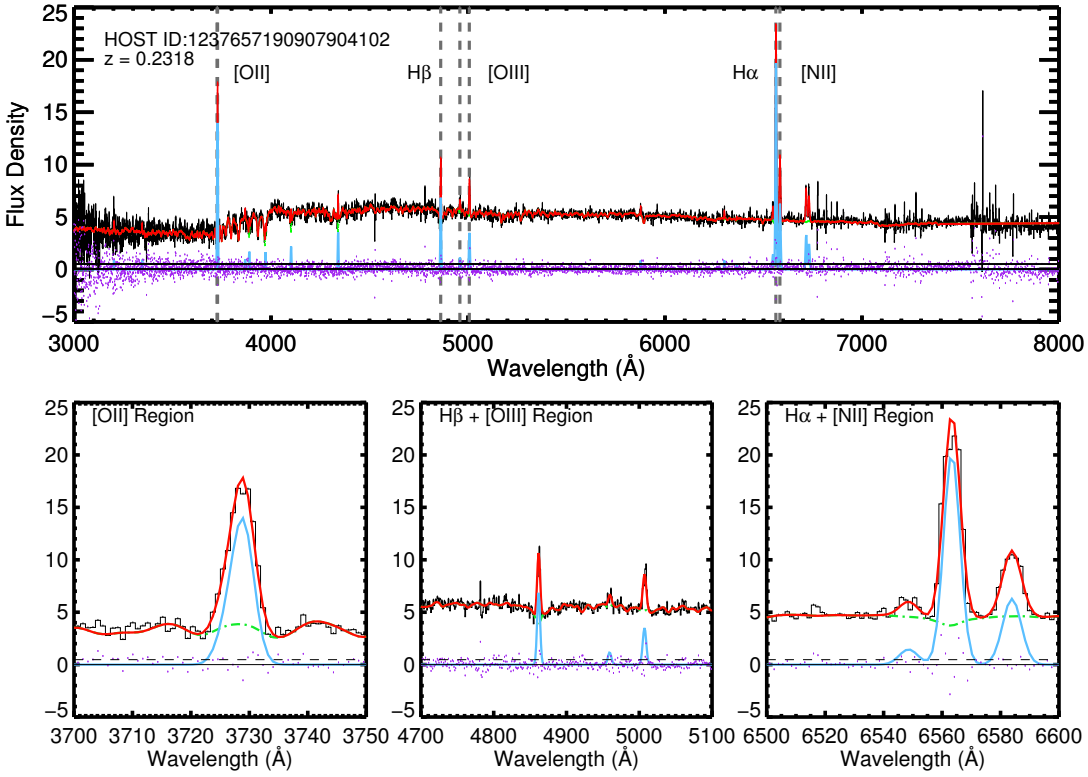

Figure 3.4: Sample GANDALF fit of the BOSS spectrum for the host of CID 13897. Wavelengths in this spectrum are given in the rest frame. Flux density is in units of 10^{-17} erg s^{-1} cm^{-2} Å^{-1}. The data are shown in black with the best fit model overplotted in red. The green dot-dashed line represents the continuum fit and the blue line shows the emission spectrum, which is obtained by subtracting the continuum model from the best fit model. Residual points between the data and the best fit spectrum are also shown in purple. Vertical dashed lines indicate the emission lines predominantly used in our analysis. The three lower panels display the specific regions that contain these lines.

tion of emission-line fluxes across the entire BOSS sample. Thus, they allow the velocity, width, and amplitude of each emission line to be fit freely. However, all of the SNe Ia included in this analysis are below this redshift. Therefore, we explicitly restrict our analysis to galaxies where we observe Hα and [N II] and take advantage of the constraining power added by tying the line velocities and widths together.

Unlike in T13, we first correct the observed spectra for the effects of dust absorption in the Milky Way before running GANDALF. We use the extinction values from Schlegel et al. (1998) and assume the Cardelli et al. (1989, CCM) extinction law (with $R_V = 3.1$). In addition, we use Case B recombination (Osterbrock, 1989), which assumes a ratio of intrinsic Hα to Hβ flux (the "Balmer decrement") of 2.86, to correct for host-galaxy extinction, while T13 utilizes the extinction output by GANDALF, derived from a fit to the underlying galaxy continuum. We find that in three cases, the observed Hβ flux output by GANDALF is so large ($> 10^{-13}$ erg s^{-1} cm^{-2} Å^{-1}) that the computed extinction value is unphysical. These large Hβ flux values are also unphysical, and so we remove these spectra from our sample.

The emission-line file used in our GANDALF fits is given in Table 3.2. This file allows the user to specify how to tie spectral lines together or fit them freely, and whether certain lines should be masked in the fit. We note as an example that, unlike T13, we mask the Na I absorption feature when fitting the continuum. For more details on how to create a user-specific emission-line file, see Sarzi et al. (2006).

We also make some adjustments to the GANDALF code. We have modified GANDALF to return flux uncertainties for lines where the velocity and width of the species are tied to those of a stronger line. GANDALF v1.8 treats the uncertainty of the velocity and line width in these cases as zero and thus computes no uncertainty. We treat the uncertainties of the fitted parameters for these weaker lines in the same way as those to which they are tied. In addition, GANDALF v1.8 incorrectly measures the EW of spectral lines; the flux density of the continuum needs to be scaled up by a factor of $(1+z)$. We include this correction, which is also discussed in T13, in our analysis. Finally, we note that the stellar kinematics

from pPXF are derived over the region $4000-6500$ Å in the rest frame of the galaxy. This is the same band as in T13, although it is incorrectly stated in that work. Comparisons between our GANDALF results and those in the SDSS DR10, which include modifications on the published SDSS DR9 results as stipulated in T13, are presented in Appendix A.

Recent analyses of SN Ia host-galaxy spectra by Johansson et al. (2013, hereafter J13) and Pan et al. (2014, hereafter P14) used GANDALF to extract absorption spectra, as well as emission lines. Absorption spectra can be used to estimate galaxy age and stellar metallicity but require that the spectra be of sufficient S/N to measure absorption-line indices. J13 used host-galaxy spectra from SDSS-II ($z \lesssim 0.2$) while P14 obtained most of their host spectra from Gemini observations ($z < 0.09$). The redshift limit for these samples is much lower than for our sample presented here (and in the case of P14, the host observations were taken using telescopes with larger apertures), and thus their host spectra are higher S/N. Like J13, we make use of SDSS-II spectra; however, the majority of our spectra are from BOSS and are generally lower S/N (see discussion in Section 3.5.4). Therefore, for this work we analyze only emission-line spectra and do not attempt to extract properties from absorption spectra. As noted in T13, one could attempt to do so by stacking spectra to increase the S/N, but we leave this exercise for future study.

3.4.2 Selection Criteria

Here we describe the requirements placed on our host-galaxy spectroscopy, which allow us to take the emission-line fluxes, measured as described in the previous section, and derive reliable host-galaxy properties in Section 3.5.

To ensure accurate spectral line fits and emission-line fluxes, T13 requires $A/N > 2$ for the Hα, Hβ, [O III], and [N II] lines. However, we have many cases where these four emission lines are detected and yet not all their $A/N > 2$. Requiring $A/N > 2$ for only the Hα and Hβ lines removes the bulk of our low S/N spectra, as well as the majority of our passive-galaxy sample, without sacrificing the large sample size. Therefore, we impose this A/N criterion on the Balmer lines only.

Table 3.2. GANDALF Emission-Line Setup File

Line Index	Line Name	Rest Wavelength (r A)	Action[1]	L-kind[2]	A_i[3]	V_g/i[4]	sig_g/i[5]	Fit-Kind[6]
0	He II	3203.15	m	l	1.000	0	10	f
1	[Ne V]	3345.81	m	l	1.000	0	10	f
2	[Ne V]	3425.81	m	l	1.000	0	10	f
3	[O II]	3726.03	m	l	1.000	0	10	t25
4	[O II]	3728.73	m	l	1.000	0	10	t25
5	[Ne III]	3868.69	m	l	1.000	0	10	f
6	[Ne III]	3967.40	m	l	1.000	0	10	f
7	H5	3889.05	m	l	1.000	0	10	f
8	Hε	3970.07	m	l	1.000	0	10	f
9	Hδ	4101.73	m	l	1.000	0	10	t24
10	Hγ	4340.46	m	l	1.000	0	10	t24
11	[O III]	4363.15	m	l	1.000	0	10	f
12	He II	4685.74	m	l	1.000	0	10	f
13	[Ar IV]	4711.30	m	l	1.000	0	10	f
14	[Ar IV]	4740.10	m	l	1.000	0	10	f
15	Hβ	4861.32	m	l	1.000	0	10	t24
16	[O III]	4958.83	m	l	1.000	0	10	t25
17	[O III]	5006.77	m	l	1.000	0	10	t25
18	[N I]	5197.90	m	l	1.000	0	10	f
19	[N I]	5200.39	m	l	1.000	0	10	f
20	He I	5875.60	m	l	1.000	0	10	f
21	[O I]	6300.20	m	l	1.000	0	10	f
22	[O I]	6363.67	m	l	1.000	0	10	f
23	[N II]	6547.96	m	l	1.000	0	10	t25
24	Hα	6562.80	m	l	1.000	0	10	f
25	[N II]	6583.34	m	l	1.000	0	10	f
26	[S II]	6716.31	m	l	1.000	0	10	t25
27	[S II]	6730.68	m	l	1.000	0	10	t25
90	sky	5577.00	m	l	1.000	0	10	f
91	sky	6300.00	m	l	1.000	0	10	f
92	sky	6363.00	m	l	1.000	0	10	f
100	Na I	5890.00	m	l	-1.000	0	10	t101
101	Na I	5896.00	m	l	-1.000	0	10	f

[1]The "action" sets whether each of the listed lines should be fit (f), ignored (i), or whether the surrounding spectral region should be masked (m). As GANDALF runs, the "action" is changed by the code; e.g., if the "action" is set to "m," the line will be masked when fitting for the continuum, then changed to "f" when fitting for the emission lines. The subsequent fields in the setup file are only used when the "action" is set to "f."

[2]The line-kind "l-kind" allows GANDALF to identify whether or not a line should be treated as belonging to a doublet or multiplet. All lines can be treated individually (l) or can be tied to the strongest element of their multiplet (dXX), where XX is the line index. If a line is identified as part of a doublet or multiplet, its amplitude is fixed to that of the strongest element via A_i.

[3]Used to set the relative emission (A_i > 0) or absorption (A_i < 0) strength of lines in a multiplet. If a line is to be treated individually, A_i is set to unity.

[4]Initial estimate for line velocity, km s^{-1}.

[5]Initial estimate for line velocity dispersion, km s^{-1}.

[6]Indicates if the position and width of the line are found freely (f) or tied (tXX) to another line, where XX is the line index.

We then use BPT diagnostics (Baldwin et al., 1981) to separate the star-forming galaxies from those dominated by AGNs. This classification requires an analysis of the optical diagnostic plane spanning log([O III]/Hβ) versus log([N II]/Hα). We first utilize the hyperbolic division of the plane in Kewley et al. (2001) and then adopt the stricter division presented in Kauffmann et al. (2003a) to select star-forming galaxies more carefully. Hosts for which Kewley et al. (2001) and Kauffmann et al. (2003a) disagree are deemed "Composite," as in Brinchmann et al. (2004). It is crucial to separate the AGN-dominated spectra as their emission lines are produced by different physical processes and thus will produce inaccurate metallicity estimates. The BPT diagram for our sample after imposing A/N cuts is presented in Figure 3.5.

In Table 3.3 we list the cuts applied in this section which reduce the PM sample, given in Table 3.1, to a sample of 144 SN Ia host galaxies for which we produce (see Section 3.5) reliable measurements of mass (M), metallicity (Z), and specific star-formation rate (S); we refer to this as the MZS sample. The A/N cut is the most significant, reducing our sample by $\approx 50\%$, demonstrating the difficulty in measuring emission-line properties from low S/N data. We note that the final cut in Table 3.3 (not described in this section) is a requirement on the fraction of galaxy light obtained within the BOSS/SDSS fiber. This is necessary to ensure the properties derived from our spectra are *global* host-galaxy properties. As this cut is not based on the spectroscopy itself, but rather on host-galaxy photometry, it is detailed in Section 3.5.4.

3.5 Derived Host Galaxy Properties

In this section we describe the methods used to derive the host-galaxy properties, both spectroscopic and photometric, used in this analysis. Sections 3.5.1 and 3.5.2 detail the processes for computing, respectively, gas-phase metallicities and star-formation rates (SFRs) from the measurements obtained in Section 3.4. In Section 3.5.3 we describe the source for our host-galaxy masses. We discuss fiber aperture effects—what biases may

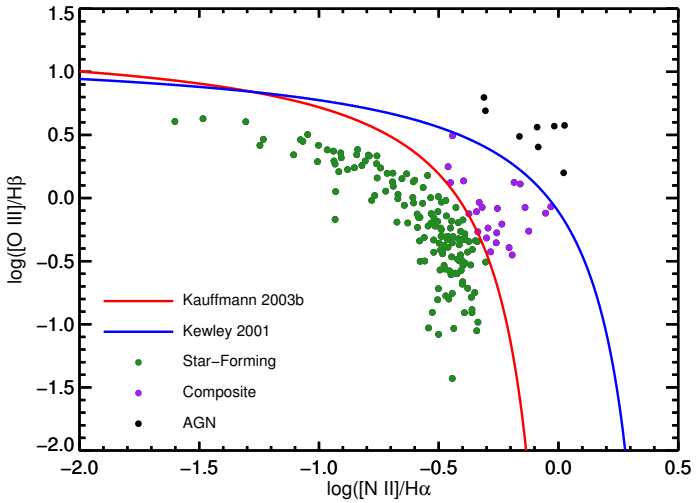

Figure 3.5: BPT diagram for host galaxies of our SNe Ia. The galaxies displayed here have passed selection criteria through A/N cuts, as outlined in Tables 3.1 and 3.3. We have trimmed the axes to better focus on the bulk of our sample; therefore, some star-forming hosts and AGNs may not be shown. Galaxies to the right of the blue curve (Kewley 2001) are deemed AGNs (black points), while those to the left of the red curve (Kaufmann 2003b) are regarded as star-forming (green points). Those galaxies that lie between the two curves (purple points) are labeled "Composite." We continue our analysis using galaxies to the left of the blue curve, although not all will be included in the final sample for analysis.

Table 3.3. Cumulative MZS Sample Definition

Selection Requirements	Removed SNe Ia	Total	Phot-Ia	Spec-Ia
PM Sample	–	345	176	169
[a] Observed Hβ flux $< 10^4$	3	342	176	166
Hα and Hβ $A/N > 2$	149	184	88	96
Star-forming or "Composite" host	9	175	80	95
$0.2 \leq g$-band fiber fraction < 1	31	144	78	66

[a]Flux density in units of 10^{-17} erg s^{-1} cm^{-2} Å^{-1}

be present, how we correct for them, and their impact on sample selection—in Section 3.5.4.

3.5.1 Metallicity

There are several methods for estimating gas-phase metallicity ($Z \equiv \log(\mathrm{O/H}) + 12$) from emission-line fluxes. Although the metallicities from each method do not have the same absolute values, relative values tend to remain consistent (i.e., a galaxy with low metallicity in one method will have low metallicity in another). Kewley and Ellison (2008, hereafter KE08) summarize these techniques and derive conversions from one metallicity calibration into another. In this analysis we adopt the calibration of Kewley and Dopita (2002, hereafter KD02), as recommended by (and updated in) KE08.

The KD02 algorithm is split into upper (high Z) and lower (low Z) branches based on the ratio of the [N II] and [O II] line fluxes obtained from the galaxy spectrum ([O II] $=$ [O II λ3727] + [O II λ3729]; [N II] $=$ [N II λ6584]). For galaxies with log([N II]/[O II]) > -1.2, the metallicity is found via the real roots of the polynomial

$$\begin{aligned} \log([\mathrm{N\ II}]/[\mathrm{O\ II}]) =& 1106.8660 - 532.15451Z + 96.373260Z^2 \\ & - 7.8106123Z^3 + 0.2392847Z^4 . \end{aligned} \tag{3.2}$$

The systematic accuracy of this method on the high-Z branch, as stated in KE08, is $\sim$0.1 dex.

For galaxies with log([N II]/[O II]) < -1.2, the KD02 method derives metallicities using an average of two distinct R_{23} calibrations (for a more complete discussion of R_{23} see KE08) with a systematic uncertainty of $\sim$0.15 dex. The first method utilizes the iterative procedure of Kobulnicky and Kewley (2004, hereafter KK04) in the lower R_{23} branch, while the second (McGaugh, 1991) is based on the photoionization code `CLOUDY` (Ferland et al., 1998) with associated analytic solutions from Kobulnicky et al. (1999). We require that a solution is found using both techniques to determine an accurate metallicity.

3.5.2 Star Formation Rate

The Hα line flux is used to determine the SFR of our host galaxies, as it traces luminosity from young ($\sim 10^6$ yrs), massive (M $> 10 M_\odot$) stars (Kennicutt, 1998). It also allows for a direct coupling of nebular emission to instantaneous SFR, independent of any previous star formation history. As outlined in Kennicutt (1998), the SFR for a galaxy with a Salpeter IMF can be found by

$$\text{SFR}\ (M_\odot\ \text{yr}^{-1}) = 7.9 \times 10^{-42} L(\text{H}\alpha)\ (\text{erg s}^{-1}), \tag{3.3}$$

where the Hα luminosity is determined using the line flux and the assumed B14 cosmology. Brinchmann et al. (2004) have shown that the conversion factor between $L(\text{H}\alpha)$ and SFR is dependent on the mass and metallicity of the galaxy. To account for this variation, as in D'Andrea et al. (2011, hereafter D11), we assume a systematic uncertainty in log(SFR) of 0.2.

We note that we correct our SFR values for aperture effects (see Section 3.5.4). In addition, we compute the specific star-formation rate (sSFR) by dividing the SFR by the photometrically derived galaxy stellar mass, which is described in the following subsection.

To test the validity of our methods, we compare our metallicity and sSFR measure-

ments to those reported in D11, as they also extract emission-line fluxes from BOSS and SDSS host-galaxy spectra and also compute metallicity using the KD02 algorithm. We find that for the 39 hosts that overlap in the two samples, we recover the gas-phase metallicity and SFR measurements reported in D11. The distribution of the difference between our measurements and those of D11 shows no bias and has an approximately Gaussian distribution; 95% of the sample agrees to within 2σ.

3.5.3 Host Mass

Stellar masses for our host galaxies are taken from S14 and were computed using the method of Gupta et al. (2011). This method employs model SEDs generated on a fixed grid using the Flexible Stellar Population Synthesis code (FSPS; Conroy et al., 2009; Conroy and Gunn, 2010). Synthetic photometry computed from these model SEDs in the SDSS *ugriz* bands was compared to SDSS photometry of our host galaxies[2] while fixing the redshift to the spectroscopic value. For more details on the FSPS model parameters used and on the exact method of estimating stellar mass, see Gupta et al. (2011). Systematic uncertainties in stellar mass estimates for normal galaxies are generally < 0.2 dex (Conroy, 2013). At best it is 0.1 dex (25%), and so we incorporate this 0.1 dex into our systematic uncertainty.

3.5.4 Aperture Effects

As we are deriving some galaxy properties from fixed-aperture spectra, we require a parameter that indicates the degree to which each spectrum is representative of a global average. To do this we compute in *ugriz* for each spectrum the ratio of flux observed within the fiber (the fiberMag) to the total flux of the target galaxy based on a profile fit (the modelMag). The fiber and model magnitudes are taken from the SDSS Catalog Archive Server. We refer to the derived ratio in each band as the fiber fraction. Because

[2]Obtained from the DR8 Catalog Archive Server (CAS) at `http://skyservice.pha.jhu.edu/casjobs/`

our sample consists of spectra from both $2''$ and $3''$ diameter fibers, we compute fiber fractions for both cases.

Based on the *g*-band fiber fraction, we remove the star-forming and "Composite" spectra whose properties are not indicative of the global average of the target galaxy. First, we find that some hosts have a *g*-band fiber fraction greater than 1. Although objects are deblended before the modelMag is computed, this is not the case for the fiberMag; thus, we obtain fiber fractions > 1. After visual inspection of these cases, we conclude that these hosts have bright, nearby neighbors that contribute to the observed fiber magnitude. Since these spectra include contamination from a galaxy other than the target, the derived properties cannot be assumed to be representative of the SN Ia host. Second, all hosts with a *g*-band fiber fraction < 0.2 are removed from our sample. At these low fiber fractions too little of the galaxy is being measured to compute a global, rather than core, metallicity (Kewley et al., 2005). These two aperture cuts, as mentioned in Section 3.4.2, finalize our MZS sample at 144 galaxies (Table 3.3).

Figure 3.6 shows the derived host gas-phase metallicities as a function of *g*-band fiber fraction, with the dashed line indicating the lower-limit for inclusion in the MZS sample. We compute inverse-variance-weighted averages over three bins of *g*-band fiber fraction (such that the bins are approximately equally sized) and find little correlation between *g*-band fiber fraction and gas-phase metallicity. This indicates that our use of different physical scales does not have a significant effect on our metallicity, and thus we make no aperture-based corrections.

We also use the *u*-band fiber fraction to adjust our estimate of the SFR based on the measured Hα line flux (Gilbank et al., 2010). Because our emission-line flux measurements are affected by the fixed aperture size, the Hα flux we measure is not a global representation of the entire galaxy. Therefore, to obtain a more reasonable estimate of the total SFR for the host, the Hα flux measurement is corrected by dividing by the *u*-band fiber fraction as in Gilbank et al. (2010, Appendix A).

Another important aperture effect to consider is that our analysis uses both SDSS and

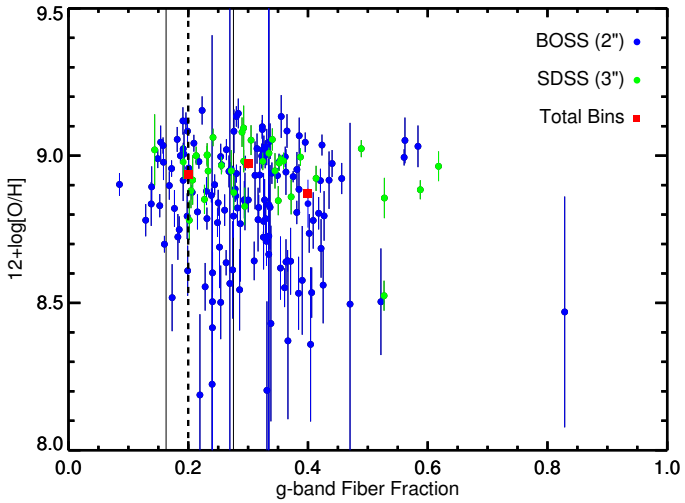

Figure 3.6: Host metallicity as a function of *g*-band fiber fraction for hosts that satisfy BPT cuts. The dashed line at *g*-band fiber fraction = 0.2 represents the threshold fiber fraction above which the derived gas-phase metallicity is considered indicative of the global average (Kewley et al., 2005). Inverse-variance-weighted binned averages, of approximately equal-sized bins, are plotted in red. There is a slight (0.07 dex) decrease in metallicity with increasing fiber fraction.

BOSS spectra, with $3''$ and $2''$ fiber diameters, respectively. For 19 of our SNe Ia, the hosts were targeted by both SDSS and BOSS; we use spectra from these observations to compare the derived metallicities. We find the difference between the metallicity measurements to be within 0.1 dex (equivalent to systematic uncertainties) for 83% of hosts, approximately Gaussian, and centered at zero. This indicates that our sample suffers no metallicity bias due to aperture effects.

The majority of the host-galaxy spectra we use were obtained from BOSS rather than from SDSS-I/II. Priority for BOSS targets was given to galaxies with a $3''$ r-band fiber magnitude < 21.25, though some galaxies fainter than this limit were observed (Olmstead et al., 2014). By contrast, SDSS-I/II spectra were obtained from the SDSS Legacy Survey and other targeted surveys within SDSS, many of which had much brighter limiting magnitudes. As a result, the SDSS spectra tend to have higher S/N and their corresponding galaxies are at lower redshift. In addition, since they are the brightest galaxies at a given redshift, they are generally more massive and more metal-rich. This effect is displayed in Figure 3.7. The BOSS spectra peak at slightly lower metallicity compared to the SDSS spectra while also extending much farther into the low-metallicity regime. The median metallicity for the BOSS spectra is $Z = 8.85$, while the median metallicity for the SDSS spectra is $Z = 8.97$. It is important to remember that this offset is an effect of target selection, not a bias due to the fiber aperture size, as we have demonstrated from hosts present in both spectroscopic samples.

Where spectra exist for both BOSS and SDSS galaxies, we choose to use the SDSS spectrum for our analyses in Section 3.6. In addition to being higher-S/N spectra on average, all SDSS spectra targeted the core of the galaxy, while some spectra from the BOSS ancillary program targeted the location of the SN itself (Olmstead et al., 2014). In all cases where only BOSS spectra exist for a galaxy, the fiber was centered on the galaxy core. Together with the cuts in this section and examination of potential sources for aperture bias, this selection creates a consistent, high-quality set of data for our analyses.

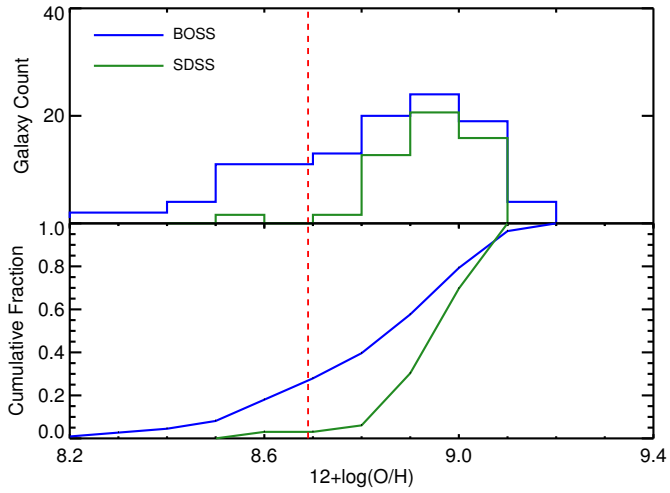

Figure 3.7: Distribution of host gas-phase metallicities for SDSS (green) and BOSS (blue) galaxies in our MZS sample, with total number counts shown in the top panel and the corresponding cumulative distribution function in the bottom panel. To focus on the bulk of our sample, we leave out one host with $Z < 8.2$ from this figure. The vertical dashed line at 12+log(O/H) = 8.69 represents the solar metallicity value, shown for comparison. The SDSS spectra are systematically higher metallicity than the BOSS spectra due to how targets were selected for the two samples.

3.6 Results

In Table A.1, we present our derived SN Ia and host-galaxy properties for all data used in this analysis. All 345 of these SNe Ia have passed SN light-curve quality cuts, have an identified host-galaxy spectrum, and have a photometrically derived host mass (the PM sample; Table 3.1). For a subset of 144 of these SNe Ia, the MZS sample, we have spectroscopically measured global host-galaxy metallicities and SFRs. Table 3.3 summarizes the requirements placed on this sample.

The derived host-property uncertainties quoted in Table A.1 do not include any systematic uncertainties previously discussed (0.1, 0.2, and 0.1 dex for metallicity, SFR, and stellar mass, respectively). Similarly, error bars in subsequent plots (e.g., Figures 3.11 and 3.12) reflect only statistical uncertainties for clarity. However, when fitting for linear trends, systematic uncertainties are added in quadrature to the quoted statistical uncertainties. As S14 reports asymmetric mass uncertainties, we choose the larger value as the single, conservative estimate.

In the following analysis, we discuss our derived host properties and SN Ia properties, as well as explore correlations between them. We use the IDL LINMIX routine, which employs the linear regression model presented in Kelly (2007), to assess the strength of observed correlations:

$$\hat{y} = m\hat{x} + b + \varepsilon\,. \tag{3.4}$$

Here m is the fit slope, b is the fit intercept, and ε is the scatter about the best fit regression line. As described in Kelly (2007), we assume that ε is drawn from a normal distribution with mean zero and variance σ^2. Throughout this work we report the intrinsic dispersion (σ) and its uncertainty, computed by taking the square root of the posterior distribution of the best fit variance. We define the significance of a nonzero slope as m/σ_m, where m is the best fit slope and σ_m is the error on the slope. LINMIX allows for uncertainties in the dependent and independent variables (assuming Gaussianity) and employs a Bayesian approach using Markov Chain Monte Carlo (MCMC). Posterior distributions

for at least 10,000 iterations of the MCMC are used to determine the regression coefficients and their errors. For completeness, we report the median and standard deviation of the posterior distributions of the best fit slope, intercept, and dispersion in our results tables. This method of linear fitting was chosen over other linear regression techniques (such as least-squares) as we find that the LINMIX fits provide more realistic estimates for our fit parameter errors.

We also use the Spearman rank correlation coefficient and corresponding significance test to study the relationship between SN Ia and host-galaxy properties. This is a non-parametric measure of statistical dependence that requires that the relationship between the two variables of interest is monotonic, but not necessarily linear. The value of the coefficient, ρ, ranges from -1 to $+1$ with $|\rho| = 1$ indicating a perfectly monotone relation. The null hypothesis for this test states that there is no correlation between the dependent and independent variable; the associated p-value describes the chance that random sampling of the data would have generated the observed correlation. While this technique provides important insight into our SN Ia–host-galaxy correlations, we must be cautious as it does not account for large differences in the measurement errors of different data points when computing the correlation coefficient.

A general outline is as follows: Section 3.6.1 describes our derived host-galaxy properties. Section 3.6.2 discusses the stretch and color of our SNe Ia and correlations between these parameters and host-galaxy properties. Section 3.6.3 examines the individual relations between HR and host-galaxy mass, gas-phase metallicity, and sSFR, separately. In Section 3.6.4 we explore the interplay between these host properties and how they affect trends with HR when fit simultaneously.

3.6.1 Host-Galaxy Properties

The redshift distributions of the PM and MZS hosts are shown in Figure 3.8. The mean and median redshifts for both the PM and MZS samples is $z = 0.24$, and the shapes of the redshift distributions are consistent. The median redshifts of the Spec-Ia and Phot-Ia in

subsamples are 0.19 and 0.26, respectively, in both the PM and MZS. We thus conclude that the requirements we impose on our host-galaxy spectroscopic data when creating the MZS sample does not result in any redshift bias relative to the PM sample.

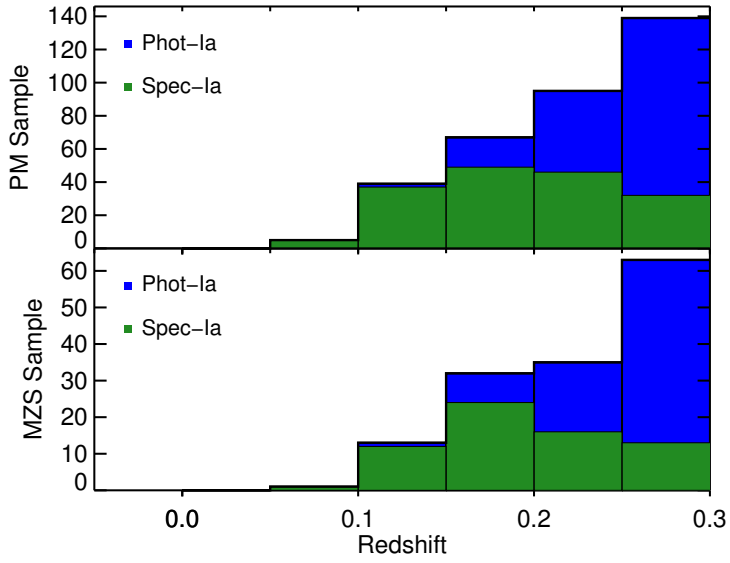

Figure 3.8: Redshift distributions of the PM and MZS samples. Histograms are stacked such that the number of Spec-Ia (green) and Phot-Ia (blue) shown in each bin add to the total number of SNe Ia in that bin. The mean and median redshifts of the PM and MZS samples are each $z = 0.24$. For both samples, the median redshift of the Spec-Ia is 0.19 and the median redshift of the Phot-Ia is 0.26.

We present in Figure 3.9 the host-galaxy stellar mass distribution for both our PM and MZS samples, both as a whole and as a function of redshift. While the MZS host-galaxy sample only contains star-forming galaxies through the requirement of measurable emission lines, the PM sample consists of both star-forming and elliptical galaxies. The inclusion of elliptical galaxies, which have a higher mass on average, results in the PM sample spanning a slightly larger range in masses with a higher mean mass ($\log(M/M_{\odot}) = 10.5$) than the MZS sample ($\log(M/M_{\odot}) = 10.2$). We also see in the right panels of Figure 3.9 that there is no noticeable trend of host mass with redshift for our sample over this redshift

range, indicating that our sample has no strong differential bias with redshift.

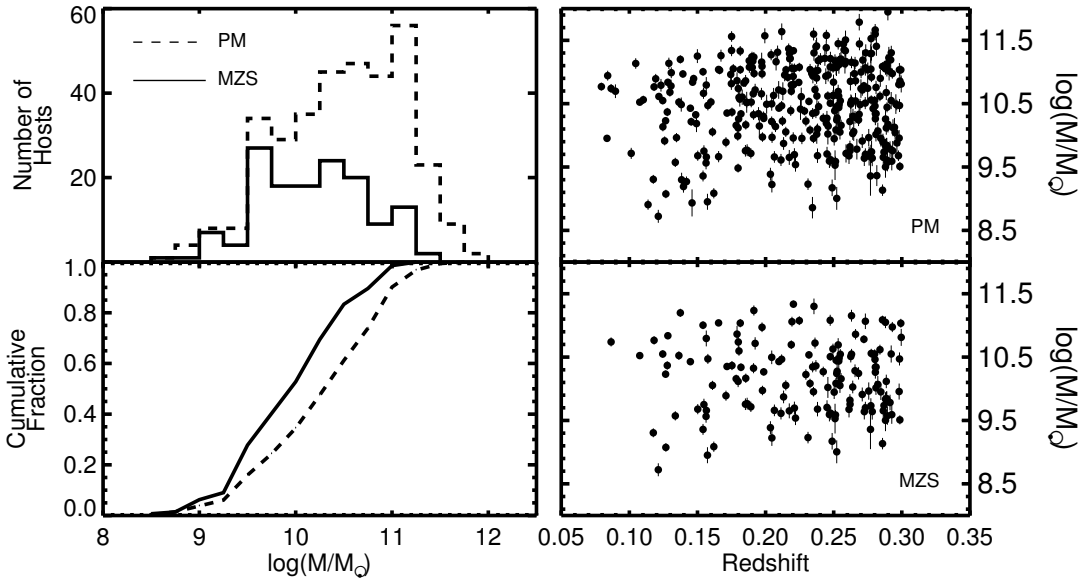

Figure 3.9: Mass distributions of our PM (dashed) and MZS (solid) galaxies are displayed in the top left panel. The means of the PM and MZS mass distributions (in log(M/$M_\odot$)) are 10.5 and 10.2, respectively. The bottom left panel presents the cumulative fraction of hosts as a function of mass. The right panels show our galaxy masses as a function of redshift.

In Figure 3.10 we show the distributions of metallicity and sSFRs from our MZS sample. The mean gas-phase metallicity for our sample is $Z = 8.84$, and the mean sSFR is log(sSFR)$= -9.43$. While the sSFR distribution is roughly Gaussian, the metallicity distribution is negatively skewed, although there are few galaxies with subsolar metallicities even in the long low-metallicity tail. As shown in the inset panels in Figure 3.10, we see no evolution of metallicity or sSFR with redshift.

As we use different IMFs, methods, selection criteria, and calibration techniques, we cannot directly compare our results to previous studies. However, we can qualitatively assess how our host-property distributions compare to those of other surveys. The peak host-galaxy mass in the PM sample is consistent with that in the PTF (P14), SNFactory

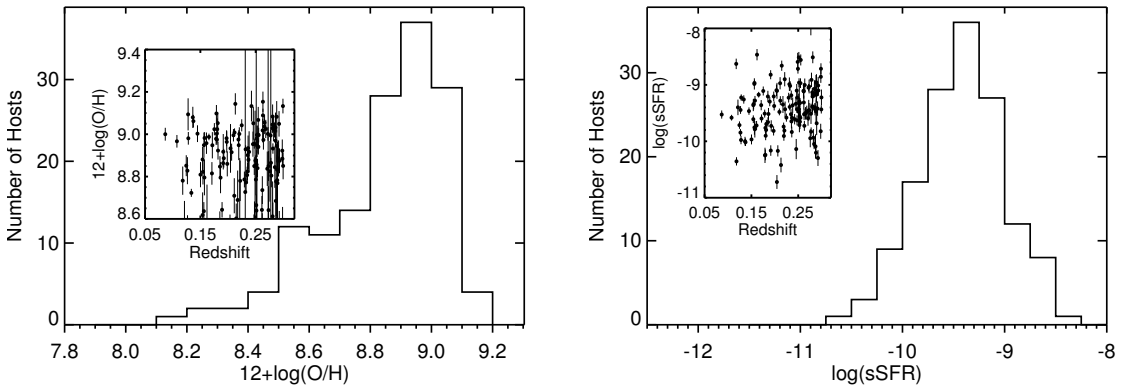

Figure 3.10: Left panel: metallicity distribution of galaxies in our MZS sample. The mean of the metallicity distribution is $Z = 8.84$. Right panel: sSFR distribution of galaxies in our MZS sample. The mean of the sSFR distribution is log(sSFR)$= -9.43$. The inset figures of both panels display the respective host properties as a function of redshift. Axes of the inset figures have been adjusted to focus on the metallicity and sSFR redshift dependence; as such, some data points are excluded from the plots.

(Childress et al., 2013, hereafter C13), SNLS (Sullivan et al., 2010), and Pan-STARRS1 (Scolnic et al., 2014a, hereafter PS1).

We notice that our host-galaxy mass distribution contains relatively fewer galaxies with $\log(M/M_{\odot}) \lesssim 9.0$. We attribute this primarily to the BOSS targeting criteria and the use of the SDSS DR8 catalog for host identification. Given that our Phot-Ia sample depends on redshifts from BOSS, which only targeted hosts brighter than a certain magnitude, we expect this sample to be biased against SNe in low-luminosity (low-mass) hosts. We also lose low-mass hosts due to the *r*-band magnitude limit of 22.2 for SDSS DR8, which is the catalog used to select host galaxies in S14.[3] In addition, our choice of mass-fitting technique may also contribute to the dearth of low-mass hosts. We use FSPS masses in this work, which are shown in Figure 23 of S14 to be ≈ 0.3 dex higher than the

[3]Though a deep co-added image catalog exists for SDSS Stripe 82 (Annis et al., 2014), these images contain SN light for SNe occurring in 2005. Ideally, SN surveys in the future should create custom co-added images excluding images with SNe and use these for host identification and host-galaxy studies.

masses derived from ZPEG (a code commonly used by other works). Therefore, we note that our reduced host-mass range may affect our derived trends with HR (Section 3.6.3).

In the MZS sample, the derived metallicities of P14 for PTF host galaxies are biased substantially lower than our metallicities, but as the typical offset between the calibration used by us and in that work is $0.2-0.3$ dex, the range of measured values is consistent. C13 uses a calibration that typically returns a wider range of metallicities, and this is seen in their results compared to this work. However, although C13 also finds the peak of their distribution at 12+log(O/H)$\approx$ 9.0, they have a greater fraction of their host-galaxies at subsolar than can be explained through calibration techniques alone. In addition, we find that the sSFR distribution of the MZS sample also exhibits a lack of low-sSFR hosts when compared to other studies. One reason for this difference is that some studies (Sullivan et al., 2010; Childress et al., 2013) with hosts with lower SFRs rely on host photometry, rather than spectroscopy, to obtain SFR measurements and are thus not limited by spectral quality requirements.

The differences in these property distributions likely stem from our spectral quality requirements. We impose a cut on the A/N of the Hα and Hβ lines to ensure good spectral quality, but by doing so reject those spectra with lower emission-line flux measurements. If we remove this A/N criterion, an additional 41 hosts would be included in the MZS sample. Of these 41, 26.8% have subsolar metallicity. Additionally, we find that 58.5% of the 41 additional hosts have low sSFR ($\log(\text{sSFR}) < -10$). Adding these hosts into our sample would not significantly impact the fraction of low-metallicity hosts, but would raise the fraction of low-sSFR hosts from 9.7% to 20.5%. However, we believe that the quality of these spectra is not sufficient to produce reliable host-property estimates, and so we do not include these in our sample.

3.6.2 SN Ia Light-curve Properties

SN Ia light-curve parameters such as color (c) and stretch (x_1)—the essential calibration tools for using SNe Ia as distance indicators—have long been known to correlate with

host environment (Hamuy et al., 1996; Gallagher et al., 2005). Figure 3.11 shows the SN Ia stretch and color as a function of our derived host-galaxy properties. We observe the correlations seen by Howell et al. (2009) and Sullivan et al. (2010): more massive galaxies host fainter, redder SNe Ia. We also find that SNe Ia with higher c occur in galaxies with lower sSFRs. Since the SN Ia color parameter contains information not just on the intrinsic color of the SN but also effects of host-galaxy dust extinction, it is expected that both massive galaxies and those with low specific star formation should host redder SNe Ia. It is interesting to note that we find that low-metallicity galaxies tend to host only blue SNe Ia, to an extent not seen in low-mass or high-sSFR galaxies (properties that are correlated with low metallicity). This metallicity–color relation is consistent with what is found in C13 and P14.

To quantify the strengths of these correlations, we perform a Spearman rank test on each combination of SN Ia and host property displayed in Figure 3.11. In each of the six cases, the correlation coefficient is nonzero; however, only the SN Ia stretch–host mass correlation exhibits enough evidence to reject the null hypothesis ($\rho = -0.308$, $p = 5.305 \times 10^{-9}$).

3.6.3 HR as a Function of Host-galaxy Properties

We now examine whether the stretch- and color-corrected luminosities of SNe Ia (and thus HRs) show correlations with properties of their host galaxies. Linear fits to the data using the LINMIX routine are shown on the figures included in this section, and the corresponding results are reported in Table 3.4. Spearman rank correlation statistics for each linear fit are also presented in Table 3.4. We note that the posterior distributions of the model parameters of these fits are roughly Gaussian. To determine the model parameters of these fits, we choose the point estimator to be the median of the posterior distribution, limiting the effects of outliers in the distribution. Errors on the fit parameters are obtained using the standard deviation of the respective posterior distribution. Host-galaxy properties are also split to create low- and high- mass (metallicity, sSFR) bins which are then

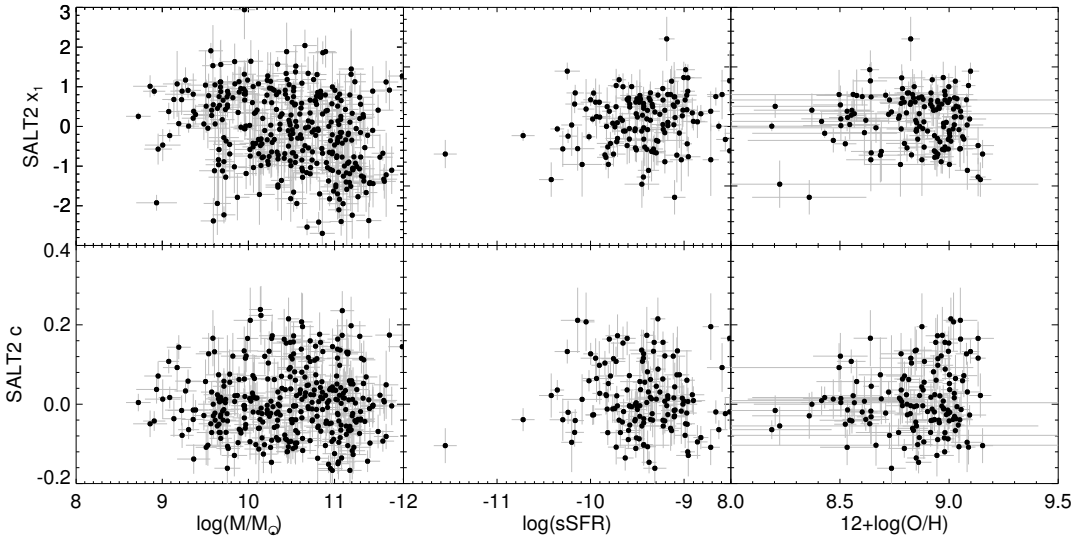

Figure 3.11: SNe Ia color (c) and stretch (x_1) as a function of derived host properties. The left panel displays data from the PM sample; the middle and right panels show data from the MZS sample. Axes have been truncated to focus on the bulk of the data.

used to compute the difference between the HR in these bins ("HR step"). The split point of each property is chosen to be the median of its respective distribution, thus creating two bins of equal number. We define the "HR step" as the difference between the high- and low-binned inverse-variance-weighted averages. When computing the significance of the step (the mean and uncertainties on the mean), we fit for the unknown intrinsic scatter that ensures $\chi^2/\mathrm{dof} \approx 1$ after the step is removed. These bins are also included in relevant figures in this section. We note that when we refer to the over- or under-luminosity of SNe Ia in this section, this refers to the luminosity after light-curve corrections have been applied.

Figure 3.12 shows HR as a function of mass for the PM sample. Using LINMIX, a nonzero slope of the linear fit is detected at 3.6σ. We also take the difference between the inverse-variance weighted averages of the high- and low-mass bins and measure the "HR step" to be -0.048 ± 0.019 mag. A similar trend is present in the MZS sample; the best fit slope and the HR step are both shown to be consistent within 1σ that of the

Table 3.4. LINMIX Linear Fit Results for HR as a Function of Derived Host-Galaxy Properties

Host Property	Sample	N[a]	Split[b] Value	HR Step [mag]	Slope	Intercept	σ [mag]	Sig[c]	ρ	p-value
Mass	PM	345	10.5	0.048 ± 0.019	-0.055 ± 0.015	0.570 ± 0.160	0.121 ± 0.009	3.62σ	-0.1708	0.0015
Mass	MZS	144	10.2	0.082 ± 0.030	-0.071 ± 0.029	0.728 ± 0.293	0.136 ± 0.014	2.46σ	-0.2094	0.0118
12+log(O/H)	MZS	144	8.9	0.057 ± 0.031	-0.579 ± 0.409	5.162 ± 3.641	0.125 ± 0.021	1.42σ	-0.1811	0.0299
sSFR	MZS	144	-9.4	0.013 ± 0.031	0.019 ± 0.046	0.190 ± 0.437	0.140 ± 0.014	0.42σ	0.0965	0.2500

[a]Sample size.

[b]Value used to create high- and low-mass (metallicity, sSFR) bins of equal number. The median of the respective host-property distribution.

[c]Significance of a nonzero slope.

full PM sample. Our results show that more massive galaxies host overluminous SNe Ia, supporting previous findings (Lampeitl et al., 2010; Sullivan et al., 2010; Gupta et al., 2011; Childress et al., 2013; Betoule et al., 2014).

The results of the Spearman rank correlation test for both the PM and MZS samples further support the significance of the HR–mass relation. In both cases, we find $\rho \approx -0.2$, which indicates that more massive galaxies host overluminous SN Ia. For both samples, there is a less than 2% chance that this correlation is due to chance, and thus we again conclude that this correlation is significant.

Several recent studies suggest that HR as a function of host-galaxy mass resembles a smoothly-varying step function rather than a line. To explore this idea of a "mass step," we fit an empirical continuous step function to our data in the PM sample. We choose a function of the form

$$\mathrm{HR} = A\left(\frac{2}{1+e^{-B(x-C)}} - 1\right), \tag{3.5}$$

where the parameter A controls the amplitude, B controls the steepness of the step, and C indicates the step position. The independent variable, x, is the host mass, $\log(M/M_{\odot})$. We use the IDL routine MPFITFUN (Markwardt, 2009) to perform a least-squares fit, using input parameters motivated by results in previous works, and find that the resulting best fit to the data is highly sensitive to the choice of input parameters. We also compute the best fit to inverse-variance-weighted average bins of varying bin width and minimum

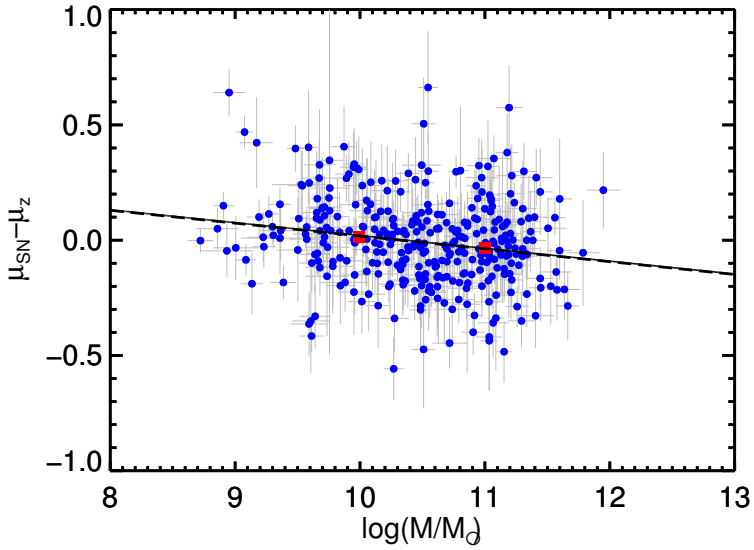

Figure 3.12: HR as a function of host-galaxy mass for the PM sample. The LINMIX linear fits to the data are shown in dashed black; red squares represent inverse-variance-weighted binned averages, with bins split at $\log(M/M_{\odot})= 10.5$. The significance of a nonzero slope is 3.6σ and the difference in HR between the high and low-mass bins is 0.048 mag. This result indicates that more massive galaxies host overluminous SNe Ia.

number of SNe Ia per bin and find that choice of bin width and number of SNe Ia per bin significantly affects the best fit results.

Therefore, we choose to explore the shape of the HR–mass relation using nonparametric regression. We employ the `loess` routine in the R statistical software package, which is based on the `cloess` regression detailed in Cleveland et al. (1992). This method of locally weighted smoothing combines linear regression in a k-nearest-neighbor-based model and relies on a user-input bandwidth, also known as the span (α), to determine the proportion of the data to be used in each local regression (i.e., a fit at some point x is computed using its neighbors, and contributions from neighboring points are weighted based on their distance from x). While this method cannot produce an empirical model, it does illustrate the general shape of the data.

The results of the `loess` regression are presented in Figure 3.13, with the HR axis truncated to better focus on the fit. The best fit to the data is shown in red with an approximate corresponding 1σ confidence interval. This method of local regression is sensitive to edge effects but has no consequence on the resulting best fit for the bulk of the data. Therefore, the behavior of the best fit at the low- and high-mass extremes must be interpreted with caution. After testing multiple spans, we determine a span that responds best to fluctuations in the data of $\alpha = 0.6$.

As shown in Figure 3.13, there appears to be a relatively smooth transition region in the HR–mass relation between $10.0 \lesssim \log(M/M_{\odot}) \lesssim 10.4$. However, because of the sensitivity of the fit at the edges, the shape of the "step regions" is not well represented. In addition, the computation of the best fit did not include measurement error, which may affect the observed behavior. The shape of the HR–mass relation is similar to the behavior reported in C13 and J13; the slope of the transition region in J13, C13, and this work is roughly -0.2. We note that our results should be correlated with what is presented in J13 and C13 as their analyses utilize a subset of the SDSS SNe Ia. Despite the shortcomings of our chosen fitting technique, the nonparametric fit is an interesting interpretation of the HR–mass relation, and a more rigorous treatment should be considered for future studies.

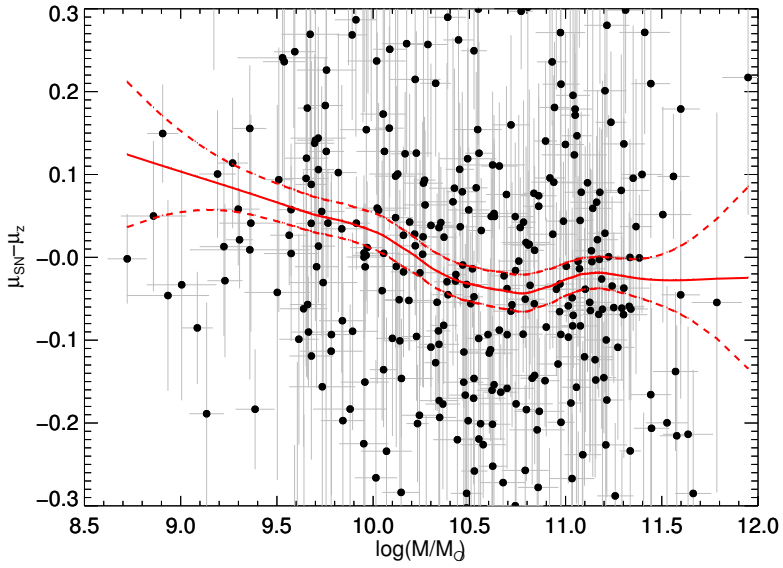

Figure 3.13: Nonparametric regression fit of HR as a function of host-galaxy mass. The best fit is presented in red with the approximate corresponding 1σ confidence interval. A span of $\alpha = 0.6$ was used for the fit.

We next examine the correlation between HR and host-galaxy gas-phase metallicity; the results are shown in Figure 3.14. The best-fit linear relation has a negative slope with 1.4σ significance, suggesting that more metal-rich galaxies host more overluminous SNe Ia. Examining the difference between our low- and high-metallicity bins reveals an "HR step" of 0.057 magnitudes with 1.86σ significance. When analyzing this relation using the Spearman coefficient, we find a statistically significant correlation ($\rho = -0.1811$, $p = 0.0299$) between HR and gas-phase metallicity. Although the LINMIX results do not recover a significant correlation, the other statistical analysis tools indicate that there is a significant difference between the low- and high-metallicity populations. This suggests that the behavior of HR–metallicity relation may not be adequately represented by the LINMIX linear fit.

Finally, we investigate HR as a function of sSFR. These results are shown Figure 3.15. The significance of this trend deviating from a nonzero slope as determined by LINMIX,

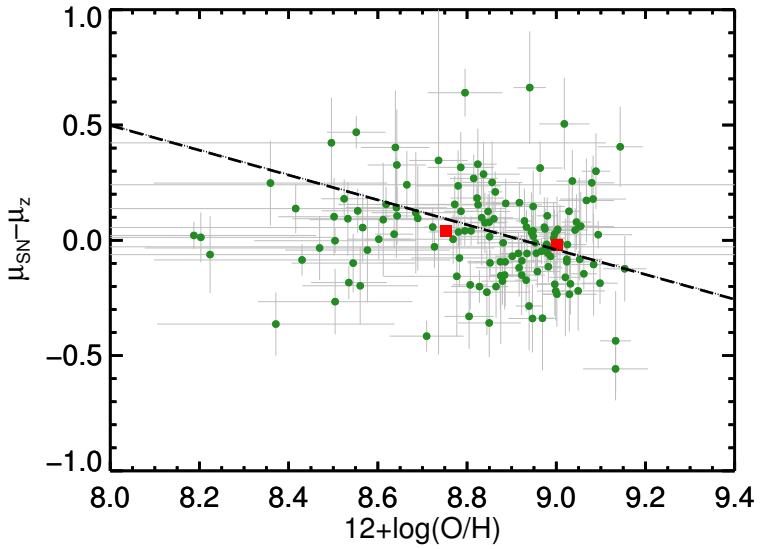

Figure 3.14: HR as a function of gas-phase metallicity for the MZS sample. These points are separated at 12+log(O/H) = 8.9 to create high- and low-metallicity bins. Red squares indicate the inverse-variance-weighted average of these bins. The difference between the binned averages is 0.057 mag. The linear LINMIX fit to the data is shown in dashed-black; there is a 1.4σ significance of a nonzero slope, which suggests that more metal-rich galaxies host overluminous SNe Ia.

however, is only 0.42σ. In addition, the difference between the average HR in the high- and low-sSFR bins is 0.013 mag with 0.42σ significance. The trend seen here is the weakest correlation observed between HR and host-galaxy properties. The results of the Spearman correlation test ($\rho = 0.0965$, $p = 0.25$) suggest that we do not have enough evidence to reject our null hypothesis; the HR–sSFR trend resembles a random sampling of uncorrelated variables.

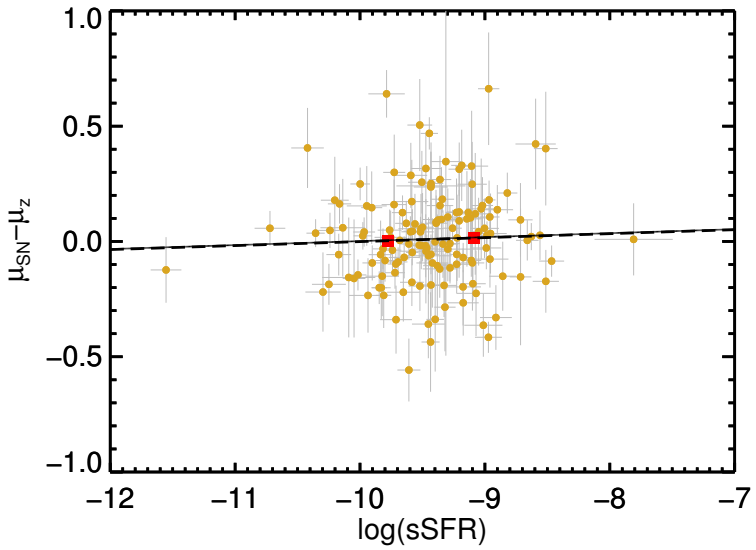

Figure 3.15: HR as a function of sSFR for the MZS sample. Points are separated at log(sSFR) = -9.4 to create high- and low-sSFR bins. Red squares indicate the inverse-variance-weighted average of these bins. The difference between the binned averages is 0.013 mag. The linear LINMIX fit to the data is shown in dashed-black; there is a 0.42σ significance of a nonzero slope. This slight correlation suggests that galaxies with lower sSFRs host overluminous SNe Ia.

As discussed in Section 3.6.1, our cut on the Hα and Hβ A/N, which is imposed to ensure spectral quality, removes 41 hosts from the MZS sample. If we add these hosts back into the MZS sample and recompute the slope of the HR-sSFR relation we find a slope of 0.021 ± 0.02, which is within 0.1σ of the slope observed using the MZS sample.

A Spearman rank test on this new sample also shows little evidence of an HR–sSFR correlation ($\rho = 0.1337$, $p = 0.0695$). This indicates that the A/N requirement and the lack of very low sSFR hosts do not have a strong effect on our trend of HR with host sSFR.

3.6.4 HR as a Function of Multiple Host-galaxy Properties Simultaneously

Our wealth of data allows an investigation of HR not only as a function of an individual host-galaxy property but also as a function of several host properties simultaneously. We perform linear fits of HR using combinations of two, and a combination of all three, derived host-galaxy parameters. For these linear fits, we include the relation with SFR as a opposed to sSFR as the sSFR and mass uncertainties are correlated. We then examine the HR–metallicity and HR–sSFR relation in several mass bins and also after correcting for the HR–mass relation. Since mass appears to have the most dominant effect on HR, removing this dependence could provide important insight into the degeneracy of our host-galaxy properties.

We first use the LINMIX package for multiple linear regression to determine the best fit relation between HR and multiple host-galaxy parameters. When using all three host properties, this function takes the form:

$$\mathrm{HR} = a \times \log(M/M_{\odot}) + b \times (12 + \log(\mathrm{O/H})) + c \times \log(\mathrm{SFR}) + d + \sigma^2\,, \tag{3.6}$$

where the coefficients a, b, c, d, and σ^2 are the parameters to be fit. These same coefficients are fit using combinations of two host properties, i.e.,

$$\mathrm{HR} = a \times \log(M/M_{\odot}) + b \times (12 + \log(\mathrm{O/H})) + d + \sigma^2 \tag{3.7}$$

$$\mathrm{HR} = a \times \log(M/M_{\odot}) + c \times \log(\mathrm{SFR}) + d + \sigma^2 \tag{3.8}$$

$$\mathrm{HR} = b \times (12 + \log(\mathrm{O/H})) + c \times \log(\mathrm{SFR}) + d + \sigma^2\,. \tag{3.9}$$

We assume that the errors on the host-parameters are uncorrelated.

When fitting for Equation 3.6, repeated trials (i.e., running LINMIX multiple times) do not yield the same fit results. For each fit parameter, results between trials are consistent within 1σ but can have dramatically different values (e.g., $a = -0.374 \pm 31.68$ compared to $a = 0.53 \pm 2.67$). We perform 20 trials of the same linear fit and find a substantial variance between fit-parameter outputs for each trial and strong skewness in the fit-parameter distributions. Although repeated fit-parameter outputs are not identical, the results of each fit are consistent with no significant correlation between HR and all host-galaxy properties.

In addition, we perform 20 trials of each of the fits using two host-galaxy properties (Equations 3.7-3.9). Fit-parameter distributions with similar variance and skewness are observed using Equations 3.7 and 3.9; these fits are also consistent with no correlation. The output fit parameters using host-galaxy mass and SFR are nearly identical between the different trials, and the mass component is significant at $\approx 1\sigma$, again suggesting that the fit is consistent with no correlation.

We find that the large errors on our model parameters are due, in part, to an inappropriate choice of interval estimator. Upon further analysis, we find that many of the LINMIX model parameter posterior distributions are highly non-Gaussian with strong skewness and high kurtosis. While we continue to use the median of the distribution as our point estimator, we recompute a new interval estimator rather than use the standard deviation; we find the interval, about the median, that contains approximately 68% of the distribution. We take the average of the lower and upper bounds and use this as the uncertainty. Using this method, we obtain more reasonable errors on our fit parameters (i.e., $a = -0.374 \pm 31.68$ becomes $a = -0.374 \pm 2.67$). However, utilizing this new estimator does not generally affect the significances of correlations observed between HR and multiple host-galaxy properties simultaneously.

We also study the dependence of HR on metallicity, as well as on sSFR, while imposing different criteria on host mass to try to control for the apparently dominant effect

of mass. First, we remove the HR–mass dependence by adding the measured PM sample "HR step" of 0.049 mag to the HR of our higher-mass ($\log(M/M_{\odot}) \geq 10.2$) MZS hosts. We then re-fit HR as a function of metallicity and also HR as a function of sSFR (this time including measurement errors again). In both cases, the direction of the best fit slope is the same as that fit with the entire MZS sample. However, the significance of nonzero slopes in both cases is $< 1\sigma$. We next investigate HR as a function of metallicity and sSFR in mass bins. Our first separation is into low and high-mass bins, split at $\log(M/M_{\odot}) = 10.2$, shown in Figure 3.16. In each case, the significance of a nonzero slope for the best fit to the data is $\lesssim 0.8\sigma$, which is consistent with flatness.

Unfortunately, each of these tests is consistent with no correlation between HR and multiple host-galaxy properties. This is perhaps largely due to the variation in measurement errors between the properties, i.e., photometric stellar masses are much easier to estimate and have smaller uncertainties than spectroscopically derived properties such as metallicity and SFR. We recommend that future surveys interested in studying these correlations obtain high-S/N host-galaxy spectra for as many SN Ia host galaxies. We also recommend further investigation of how to incorporate correlations, both physical and in measurement uncertainty, between various host-galaxy properties in future studies of this type. Hopefully, combining the results of these efforts will provide a better understanding of the physical mechanism driving these observed trends.

3.7 Discussion

In this section, we compare our linear fit results of HR as a function of host-galaxy properties to those reported in previous studies. We also separate the PM and MZS samples into Spec-Ia and Phot-Ia subsets to assess the effect of including a sample of photometrically-classified SNe Ia on studies of HR and host properties. Finally, we discuss the differences between the star-forming and passive galaxies in our PM sample.

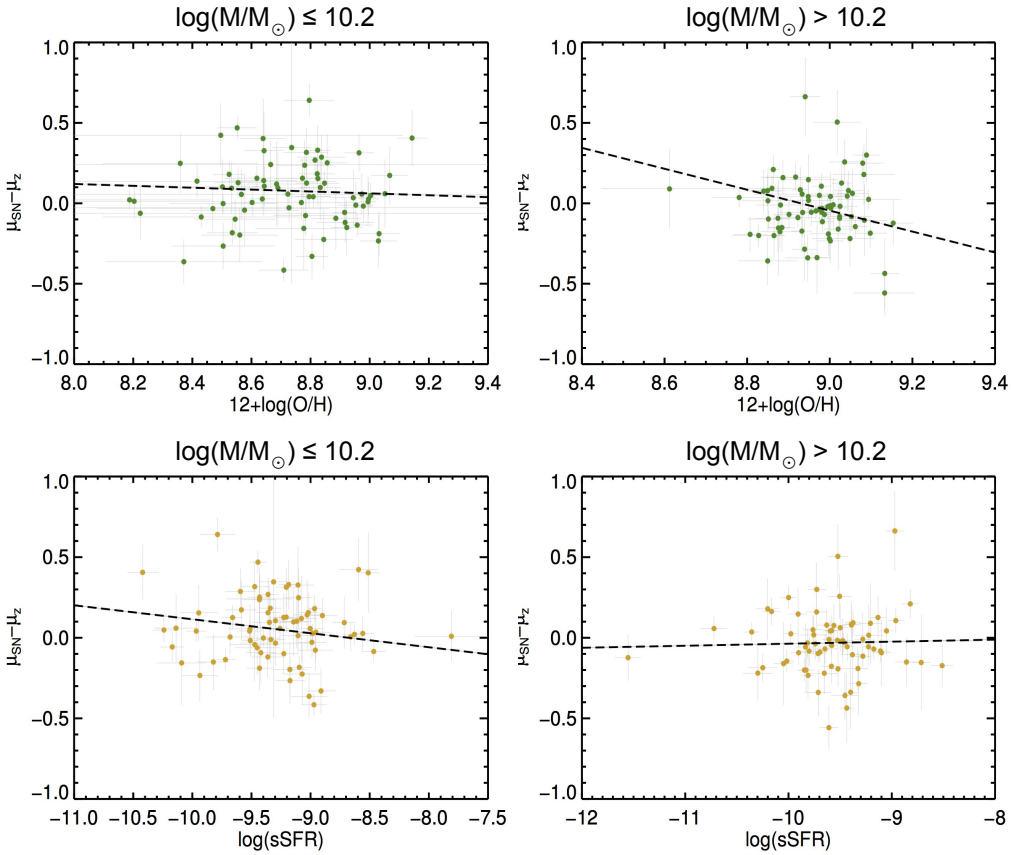

Figure 3.16: HR as a function of metallicity and sSFR for the MZS sample in low- and high-mass bins. LINMIX linear fits to the data are shown in dashed-black. In each case, the significance of a nonzero slope is $\lesssim 0.8\sigma$.

3.7.1 Comparing with Previous Studies

We compare the correlations observed in this work between HR and host-galaxy properties with those reported in previous studies and present a sample of HR–host-galaxy correlations as well as fit significances as they are reported in the literature. In some cases, a linear best fit to the data was not provided, and thus we provide the significance of the binned-average HR step. Because of differences in metallicity calibrations and IMFs used for host-mass calculations, we encourage the reader to use caution when comparing linear fit results from all previous works directly. However, we can consider the strengths and significances of the linear correlations between HR and host-galaxy properties to get a qualitative sense of how these studies compare. We present this summary in Table 3.5 and note that the list of works included only represents a subset of the literature.

As seen in Table 3.5, the results of this study confirm much of what is established in the literature. In five studies using a sample of more than 100 SNe Ia, a significant linear correlation ($\gtrsim 3\sigma$) was found suggesting that more massive galaxies host overluminous SNe Ia; it is possible that the three studies that did not detect such a correlation did not have large enough samples to detect as strong of an effect. Although the HR step with host-galaxy mass observed for the PM sample in this work is smaller than what is reported in several other studies, it is consistent at $\lesssim 1.7\sigma$. The trend observed between HR and host-galaxy gas-phase metallicity and sSFR is also consistent with existing results, particularly that the HR–sSFR correlation is the weakest observed.

When comparing to D11, it is important to clarify that they computed two estimates of sSFR: "$\mathrm{sSFR_{spec}}$" (using host-galaxy masses determined from the spectroscopic fit to the galaxy continuum) and "$\mathrm{sSFR_{phot}}$" (using masses derived from host-galaxy photometry). In their study, they find a $> 3\sigma$ correlation between HR and $\mathrm{sSFR_{spec}}$. Unfortunately, we are unable to compute spectroscopic masses (and thus $\mathrm{sSFR_{spec}}$) in our current emission-line analysis and suggest this for future study. However, D11 find that the correlation between HR and $\mathrm{sSFR_{phot}}$ is only significant at the 1.2σ level.[4] Given that the method

[4] As expounded in D11, the difference between $\mathrm{sSFR_{spec}}$ and $\mathrm{sSFR_{phot}}$ (and thus their trends with HR)

Table 3.5. Comparison of Correlations Found between HR and Host-galaxy mass (M), Gas-Phase Metallicity (Z), and Specific Star Formation Rate (S)

Work	SN Survey	Host Property	Sample Size	HR Step (mag)	Slope [a] (mag/dex)	Slope[b] Significance (σ)
This work (PM)	SDSS-SNS	M	345	0.048 ± 0.019	-0.055 ± 0.015	3.6σ (L)
This work (MZS)	SDSS-SNS	M	144	0.082 ± 0.030	-0.071 ± 0.029	2.5σ (L)
Sullivan '10	SNLS	M	195	0.080 ± 0.020	-0.042 ± 0.013	3.3σ (L)
Lampeitl '10	SDSS ($z \leq 0.21$)	M	162	0.100 ± 0.025	-0.072 ± 0.018	4.9σ (L)
Gupta '11	SDSS	M	206	0.096 ± 0.028	-0.057 ± 0.019	3σ (L)
Kelly '10	CfA3	M	62	0.094 ± 0.045	-0.150 ± 0.060	2σ (L)[c]
C13	SNf	M	115	0.085 ± 0.028	-0.043 ± 0.014	3.1σ (L)
P14	PTF	M	50	0.085 ± 0.047	-0.041 ± 0.030	1.4σ (L)
Scolnic '14	Pan-Starrs1	M	112	0.040 ± 0.032	–	1.25σ (B)
This work (MZS)	SDSS-SNS	Z	144	0.057 ± 0.031	-0.579 ± 0.409	1.4σ (L)
Konishi '11	SDSS	Z	72	0.130 ± 0.060	–	1.8σ (B)
D11	SDSS ($z \leq 0.15$)	Z	34	0.091 ± 0.021	–	1.3σ (L)[d,e]
C13	SNf	Z	69	0.103 ± 0.036	-0.106 ± 0.043	2.5σ (L)
P14	PTF	Z	36	0.115 ± 0.046	-0.358 ± 0.176	2σ (L)
This work (MZS)	SDSS-SNS	S	144	0.013 ± 0.031	0.019 ± 0.046	0.4σ (L)
P14	PTF	S	48	0.070 ± 0.041	-0.019 ± 0.077	0.25σ (L)
D11	SDSS ($z \leq 0.15$)	S[c]	34	–	–	1.2σ (L)[d]

[a]Slopes presented use the sign convention where Hubble residuals are defined as $\mathrm{HR} = \mu_{\mathrm{SN}} - \mu_z$. This switches the sign of the values reported in Sullivan et al. (2010) and Lampeitl et al. (2010).

[b]We have included significances for linear fits (L) and differences in high- and low-mass (metallicity, sSFR) bins (B) (for those paper that do not provide linear fit results).

[c]Result quoted is from using SALT2.

[d]$\mathrm{sSFR}_{\mathrm{phot}}$ (see D'Andrea et al., 2011).

[e]The uncertainty quoted on the HR Step is as reported and does not include intrinsic scatter.

we use to compute sSFR in this work is analogous to D11's $\mathrm{sSFR}_{\mathrm{phot}}$, it is not unexpected that we see a significance of similar strength.

3.7.2 Photometric versus Spectroscopic SN Ia Subsets

Here we consider the Phot-Ia and Spec-Ia subsets of the PM and MZS samples separately and recompute correlations between HR and host-galaxy properties. Figure 3.17 displays the linear fits for the separate datasets, and the fit results are presented in Table 3.6. Generally, in each study of HR as a function of host property using just the Spec-Ia, the significance of a nonzero slope is $\lesssim 2\sigma$. The significance of a nonzero correlation between HR and host-galaxy mass using the Phot-Ia is 3.9σ, while the significance of the relation using only the Spec-Ia is 1.5σ. When using the Phot-Ia MZS subsample, the significances of a nonzero HR-metallicity correlation and nonzero HR–sSFR correlation are 1.6σ and 1.1σ, respectively. As evident in Figure 3.17, the correlation between HR and metallicity for the Phot-Ia may be best fit by a nonlinear function. We find that in all cases of HR as a function of host property, the linear fits obtained for the Spec-Ia are in the same direction as those for the Phot-Ia. The slopes of the linear fits for the Phot-Ia and Spec-Ia subsamples, for the HR–metallicity and HR–sSFR relations, are consistent within 1.3σ. The slopes of the fits of the HR–mass relation between the Phot-Ia and Spec-Ia samples are consistent at 2.3σ; however, both are consistent with the slope recovered using the full PM sample within 1.5σ.

might be due to corrections for aperture effects which are applied to $\mathrm{sSFR}_{\mathrm{phot}}$ but not to $\mathrm{sSFR}_{\mathrm{spec}}$. See Section 4.2 of D11 for more details.

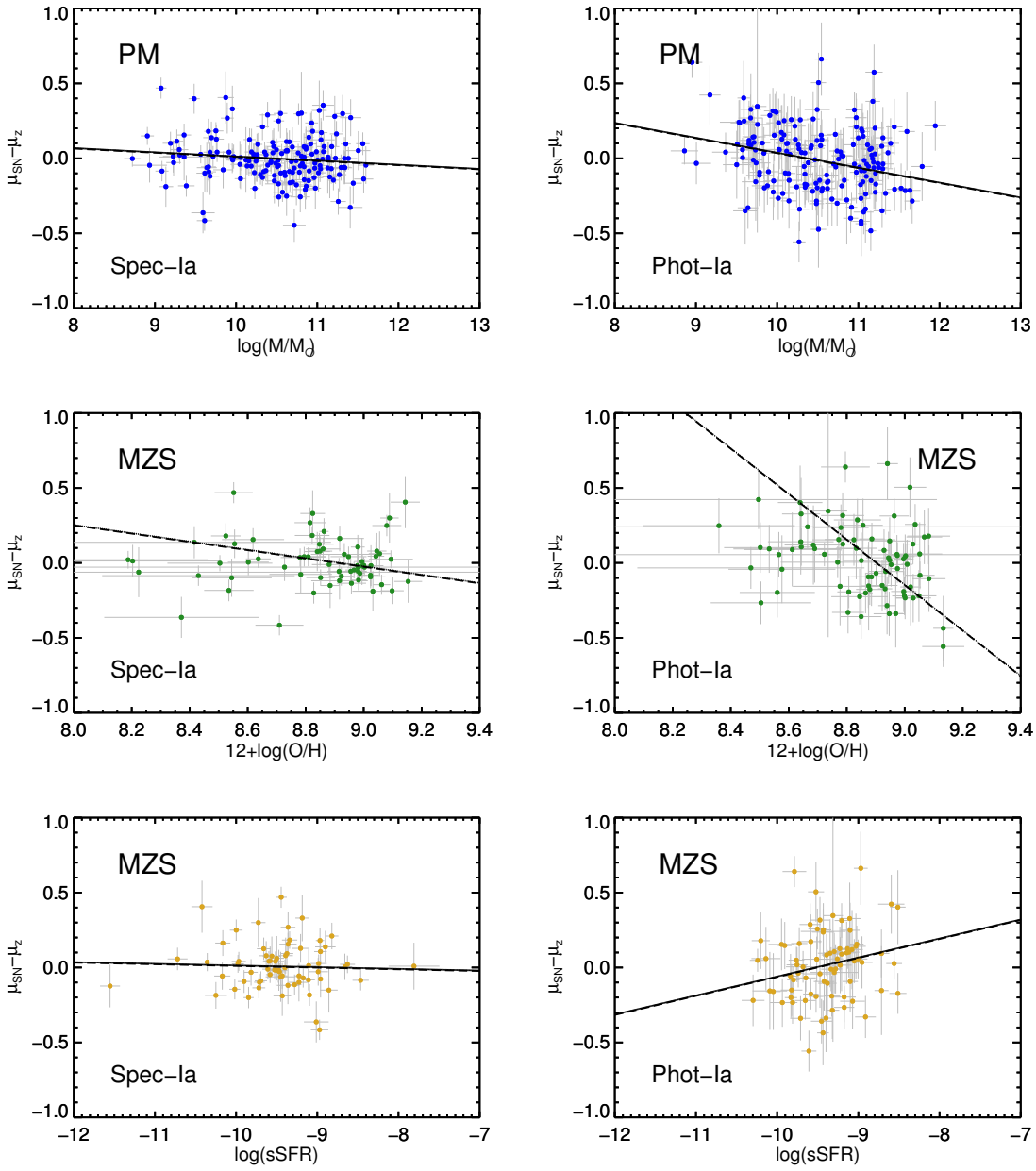

Figure 3.17: HR as a function of derived host properties for the Spec and Phot SN Ia samples separately. The first row displays HR as a function of mass for the PM sample, and the lower two rows show HR as a function of derived host properties for the MZS sample. LINMIX fits to the data are shown in dashed-black. Fit results are reported in Table 3.6.

Table 3.6. Fit Results for HR as a Function of Host Properties: Spec-Ia and Phot-Ia

Host Property	Sample	SN Type[a]	N[b]	Slope	Intercept	σ [mag]	Sig[c]	ρ	p-value
Mass	PM	S	169	-0.028 ± 0.018	0.287 ± 0.188	0.113 ± 0.010	1.54σ	-0.0718	0.3538
Mass	PM	P	176	-0.101 ± 0.026	1.042 ± 0.270	0.137 ± 0.017	3.87σ	-0.2496	0.0008
12+log(O/H)	MZS	S	66	-0.277 ± 0.250	2.464 ± 2.240	0.119 ± 0.019	1.11σ	-0.0718	0.5668
12+log(O/H)	MZS	P	78	-1.518 ± 0.960	13.512 ± 8.640	0.133 ± 0.043	1.58σ	-0.2797	0.0132
sSFR	MZS	S	66	-0.011 ± 0.046	-0.102 ± 0.440	0.126 ± 0.017	0.24σ	-0.0130	0.9177
sSFR	MZS	P	78	0.127 ± 0.120	1.204 ± 1.140	0.170 ± 0.026	1.06σ	0.1845	0.1058

[a]Indicates Spec-Ia (S) or Phot-Ia (P).

[b]Number of SNe Ia in the sample.

[c]Significance of a nonzero linear slope.

The weaker HR–mass correlation in the Spec-Ia sample is a bit unexpected, especially when comparing to previous analyses using SDSS SNe Ia. In particular, we would expect a similar significance to that reported in Gupta et al. (2011), which uses a comparably-sized sample of spectroscopically-confirmed SNe Ia, also from the SDSS-SNS. However, we note that while many of the SNe Ia used in this analysis overlap with those in the Gupta et al. (2011) sample, there are several key differences in our sample construction, namel,: sample redshift cuts, SN Ia light-curve quality criteria, requirements on host-galaxy spectroscopy, and host-galaxy photometry used to compute stellar masses. We find that only 94 SNe Ia overlap between the Gupta et al. (2011) sample and our PM sample. A comparison of the median of the best fit LINMIX posterior slopes of each overlapping sample yields an agreement of 0.08σ, indicating that sample construction, rather than methodology, plays a large role in the differing results between the two works.

Initially, we believed that the magnitude limit of the host spectroscopic follow-up may have biased our Spec-Ia host sample against low-mass hosts. To test this, we create a sample of SN Ia hosts using all criteria in Table 3.1, *without imposing any requirements on the host spectra*, and compare this mass distribution to that of the Spec-Ia hosts. Using the two-sided Kolmogorov–Smirnov test, we find no significant difference between the Spec-Ia host-mass distribution and that of this new sample, even when only considering the low-mass hosts. This indicates that our spectral quality requirement does not change our results.

The disagreement between the Spec-Ia and Phot-Ia results when fitting for HR as a function of mass is also surprising, particularly if the Spec-Ia and Phot-Ia samples are indeed drawn from a homogenous sample of SNe Ia. To further explore the results, we plot the 68% and 95% confidence intervals of the slope and intercept LINMIX posterior distributions for both samples. As shown in Figure 3.18, the two samples show poor agreement. We also see that the Phot-Ia slope is definitively negative and that both the slope and intercept distributions are wider than those of the Spec-Ia.

While the differences we observe between the Spec-Ia and Phot-Ia samples could be

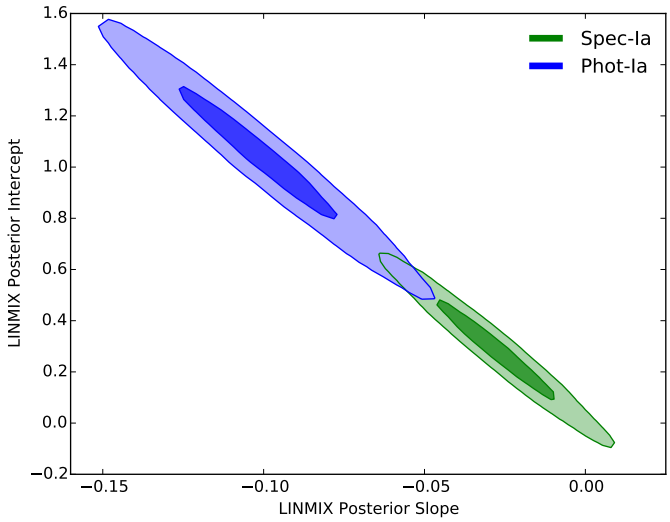

Figure 3.18: Contour intervals showing the 68% and 95% confidence regions of the Spec-Ia (green) and Phot-Ia (blue) LINMIX posterior distributions for the HR–mass relation.

attributed to random statistical fluctuations, the contour plots strongly allude to a more fundamental discrepancy between the Phot-Ia and Spec-Ia subsamples. Issues with photometric typing, for example, may seriously affect the homogeneity of the two datasets, thus limiting the ability to perform comparable analyses with each independently. While probing the differences between the Spec-Ia and Phot-Ia subsamples is beyond the scope of this work, we encourage future studies to explore this problem further.

3.7.3 Star-forming and Passive Hosts in the PM Sample

Although we require the host-galaxies in the MZS sample to have active star formation (as indicated by strong Hα emission), we do not require this of the PM hosts. Therefore, the PM sample is comprised of both actively star-forming and passive galaxies. Motivated by the fact that SN properties and rates are correlated with the amount of star formation in their hosts (e.g., Hamuy et al., 2000; Sullivan et al., 2006), we study correlations between HR and mass separately for star-forming and passive hosts using the

FSPS photometric measurements of SFR reported in S14 and the suggested division at $\log(\mathrm{sSFR_{FSPS}}) = -12$. We require a "star-forming" galaxy to have $\log(\mathrm{sSFR_{FSPS}}) > -12$ and a "passive" galaxy to have $\log(\mathrm{sSFR_{FSPS}}) \leq -12$. While this separation may not be absolute, it provides a reasonable estimate of star formation activity, yielding 259 star-forming hosts and 86 passive hosts. We fit for linear trends of HR with host mass for these two groups separately; results are shown in Figure 3.19. In star-forming galaxies, there is a 3.3σ significance of a nonzero slope; however, in passive galaxies, the significance of a nonzero slope is only 0.09σ. This may be due, in part, to the fact that we lose the low-mass end of the mass distribution for the passive hosts, which significantly reduces the mass range for this subsample. The inverse-variance-weighted average HR of the star-forming and passive samples is calculated, including the best fit intrinsic scatter, and we find that SNe Ia in the passive galaxies are 0.041 mag more luminous, with a confidence of 1.87σ, than those in star-forming galaxies after light-curve correction. This trend is consistent to 1.3σ with Lampeitl et al. (2010) who also used SDSS SNe and reported a $\simeq 0.1$ mag difference between star-forming and passive hosts at the $2-3\sigma$ level. [5]

In the recent study by Childress et al. (2014), they predict that SNe Ia in star-forming hosts are a more uniform sample than those in passive hosts due to the homogeneity of young progenitors. We expect that this uniformity would be apparent in the distribution of HRs in the sense that the HR distribution in the star-forming sample would exhibit less scatter than that of the passive sample. A comparison of the HR distributions for the two samples reveals no statistical difference in their medians or standard deviations. However, further analysis with a larger sample of low-mass host galaxies is necessary to make a definitive statement about the findings of Childress et al. (2014).

[5] We note that readers should approach the comparison to the Lampeitl et al. (2010) results cautiously, as the sample construction (96 overlapping SNe Ia) and calculation of HRs differs significantly between the two works.

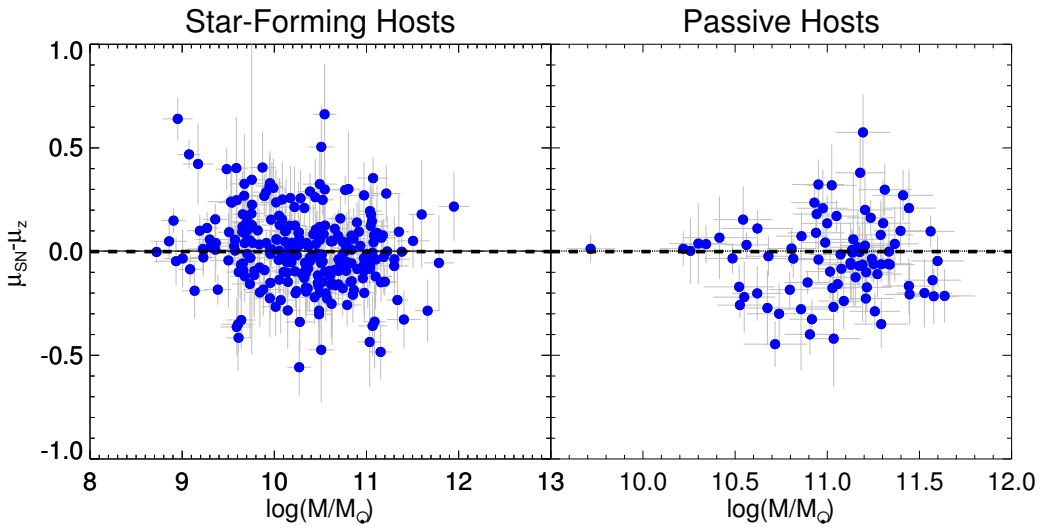

Figure 3.19: HR as a function of host mass for the PM sample, separated into star-forming and passive galaxy groups. LINMIX fits to the data are shown in dashed-black. For our star-forming galaxies (left panel) we find the significance of a nonzero slope is 3.3σ. The trend with the passive galaxies (right panel) is consistent with flatness (0.09σ).

3.8 Summary and Conclusions

In this chapter we have examined the relationship between SN Ia HRs and derived host-galaxy properties for subsamples of SNe Ia from the SDSS-SNS. Host-galaxy masses are determined using SDSS photometry as described in S14, and gas-phase metallicity and SFRs are derived using host-galaxy spectroscopy as detailed in Section 3.5. We utilize one sample of 345 SNe Ia with well-constrained host mass measurements (PM sample) and a subset of 144 SNe Ia that also have metallicity and SFR measurements from host spectra (MZS sample). The PM sample is the largest single-survey set of SNe Ia and host-galaxy spectroscopic data used in a study of this type.

To determine the relation between HR and host-galaxy properties, we perform linear fits with the LINMIX IDL routine and quote the significances of nonzero correlations. Using the PM sample, we observe with a significance of 3.6σ that more massive galaxies tend to host overluminous SNe Ia after light-curve corrections, confirming what is previously reported in the literature. This is one of the most significant detections of this effect, second only to Lampeitl et al. (2010), who also use SDSS SNe Ia. We find less significant correlations between HR and metallicity (1.4σ) and HR and sSFR (0.4σ), in agreement with the results presented in previous works. We also utilize the Spearman rank test as a nonparametric measure of the correlations between HR and host-galaxy properties; we find strong evidence for a nonzero correlation ($p < 0.03$) for the HR–mass and HR–metallicity relations. The result of the HR-metallicity hypothesis test somewhat contradicts the LINMIX fit results, as it suggests that there is evidence for a monotonic relation between HR and host-galaxy metallicity. This indicates that perhaps the HR–metallicity correlation is nonlinear and should be further explored using other fitting techniques.

Our large sample size also allows us to study correlations between HR and host-galaxy properties using multiple host-galaxy parameters simultaneously. We use the multiple linear regression LINMIX package to fit for HR as a function of linear combinations of host mass, metallicity, and SFR. When using a combination of all three host parameters, no statistically significant correlation is recovered. Similarly, no significant correlation is

recovered when fitting for HR as a function of mass and metallicity and of metallicity and SFR. We also split our sample into two mass bins and study HR as function of metallicity and sSFR in each bin. We find that in these mass bins, the linear trends of HR–metallicity and HR–sSFR are consistent with zero slope to within 1σ. With each multiparameter test, we find that the HR correlation is consistent with flatness. Unless we are able to measure other host-galaxy properties as accurately as mass and appropriately account for the physical correlations between these host properties, then determining the true nature of this correlation will remain challenging.

To study the effects of including photometrically-classified SNe Ia in our analysis, we divide the MZS and PM samples into spectroscopically-confirmed (Spec-Ia) and photometrically-classified (Phot-Ia) SNe. We recompute our linear fits of HR with host-galaxy mass (metallicity, sSFR) in these subsamples; in all cases, for a respective host-galaxy property, linear fits from both subsets are in the same direction and slopes are consistent $< 2.5\sigma$. Using the Phot-Ia alone generally produces a fit with greater significance than that found when using the Spec-Ia alone. The fits obtained from the Spec and Phot-Ia samples are also consistent with the larger PM and MZS samples as a whole. However, we also find that the results obtained using the Spec-Ia and Phot-Ia, particularly when comparing the HR–mass relation, could point to a striking difference between the two sets of SNe Ia. If we cannot assume that the PM sample is a homogeneous set of SNe Ia, or we cannot trust the purity of the photometric sample, this raises serious concerns about the usefulness of large-area surveys like DES and LSST that will observe thousands of photometrically-classified SNe Ia. As photometric typing is improved, we are confident that these Phot-Ia will be critical tools in HR–host-property studies.

Throughout this analysis we determine, in several variations, correlations between HR and host-galaxy properties. Yet we remain unsure about the physical mechanisms driving these relationships. If progenitor age is truly responsible for the host bias, as proposed by Childress et al. (2014), and if host-galaxy stellar age traces the progenitor age (which is likely true for star-forming galaxies), then a large sample of high-S/N host-

galaxy spectra of a size comparable to the sample in this work would be helpful in further probing these correlations. Obtaining such a large number of high-quality spectra will be difficult, but good S/N of the continuum is necessary to measure absorption lines and therefore infer stellar population age as was done by Johansson et al. (2013). In this work, requiring that each host galaxy has a spectrum from SDSS or BOSS greatly reduced the size of our sample. While the number of SNe Ia being discovered continues to rapidly increase, the number of host galaxies targeted for spectroscopic follow-up lags behind. We strongly advocate that current and future SN surveys strive for completeness of host-galaxy spectral follow-up so that further analyses of host-galaxy correlations will benefit from the increased statistics and suffer minimal bias. We are hopeful that future work using larger, higher-quality datasets will contribute valuable insight into the nature of SN–host correlations and the complex combination of intrinsic and environmental features that affect SNe Ia.

Chapter 4

BAMBIS: Bayesian Hierarchical Modeling with Biased Simulations For SN Ia Cosmology Including Selection Effects

4.1 Introduction

Type Ia supernovae (SNe Ia) are excellent probes for measuring the properties of dark energy and the accelerating expansion of the universe (Riess et al., 1998; Perlmutter et al., 1999). Using these objects for cosmological parameter inference has enabled precise estimates of the current dark matter density, Ω_m, and the dark energy equation of state parameter, w (Betoule et al., 2014). The uncertainties of SNe Ia cosmology have, however, become dominated by systematic errors, and this limitation is driving the strategy for new, large-scale SN programs. Surveys such as The Dark Energy Survey Supernova Program (Bernstein et al., 2012, DES-SN) and the Large Synoptic Survey Telescope (LSST Science Collaboration et al., 2009, LSST) will detect thousands of SNe Ia and new analysis tools will need to be developed to use these large samples most effectively.

In this chapter we introduce the framework for a novel Bayesian hierarchical model (BHM) algorithm for cosmological parameter inference using SNe Ia. The BAyesian hierarchical Modeling with BIased Simulations (BAMBIS) algorithm adds two new key features to the available suite of SN Ia cosmology tools. First, BAMBIS uses forward modeling of the data at every proposed point in parameter space, allowing for treatment of any selection effects or other observational systematics that can be properly simulated, regardless of whether they can robustly be accounted for in analytic likelihoods. This includes effects such as weather variations or down-selection due to limited follow-up resources. Second, BAMBIS then estimates each model's probability distribution function (PDF) in the observational space using Kernel Density Estimation (KDE) of the simulated data; this provides a non-parametric estimate of the PDF that does not require analytically tractable likelihoods.

The use of SNe Ia as cosmological probes rests on the ability to standardize their peak luminosities (magnitudes m), which are derived from observed light-curve fluxes. Typically, this standardization uses a model that relates SN Ia luminosity to light-curve fit parameters. One common model is the "Tripp" regression relation which relates SALT2 (Guy et al., 2010) light-curve fit color c and width x_1 ("stretch") to SN Ia peak B-band luminosity (Phillips, 1993; Tripp, 1998). In this case, the light curve data are thus compressed into $\{m_{Bi}, c_i, x_{1i}\}$ for events i at redshifts z_i. To obtain estimates of cosmological parameters (such as Ω_m), traditional analyses maximized the likelihood of these data varying the cosmological parameters and the SN Ia luminosity regression coefficients α and β of x_1 and c, respectively. Several recent analyses have moved beyond this technique to conduct Bayesian parameter inference in a hierarchical (layered) model, which vary not only the conventional model parameters, but also the "hyperparameters" describing the intrinsic population distributions of SN redshift, color, stretch, or host mass.

In a conventional Bayesian analysis, posterior distributions of parameters of interest are obtained by comparing a set of observed data to an analytic model. These posterior distributions are often sampled using Markov Chain Monte Carlo (MCMC) techniques,

which construct a sequence of points in parameter space, known as a "chain." Various techniques are distinguished by nuances in the model, forms of the likelihood PDF, or differences in sampling algorithms. Rubin et al. (2015), for example, develop a sophisticated model and likelihood that account for correlations between SN Ia luminosity and host-galaxy mass, and allow for evolution of SN Ia color and stretch with redshift. Shariff et al. (2016) incorporate similar correlation and evolution parameters into their model and use Partially Collapsed Gibbs Sampling (PCG) and Ancillarity-Sufficiency Interweaving Strategy (ASIS) to improve the convergence of their MCMC chains. Mandel et al. (2016) improve upon the standard color-correction model by accounting for host-galaxy dust and intrinsic SN Ia scatter separately.

BHM approaches also vary in their treatment of observational biases; some simply assume the data set is complete, while others incorporate selection effects as parameters of the model. In a magnitude-limited survey, only the more luminous objects are observed at large distances; this effect is known as Malmquist bias. This selection biases the observed SN Ia sample to be bluer and brighter than the intrinsic population and must be accounted for to obtain unbiased cosmological parameter estimates. To address this point, Rubin et al. (2015) included sample limiting magnitudes (i.e., a parameter describing the maximum magnitude observed in a given survey) as analytic parameters of their model and were able to recover Ω_m and w_0 without bias, but recovered biased values of the regression coefficients. Shariff et al. (2016) add distance corrections, determined using simulations presented in Betoule et al. (2014), to SN Ia magnitudes obtained from the Joint Light Curve Analysis (Betoule et al., 2014) and find w_0 to be 1.6σ larger and Ω_m to be 2.8σ larger than previously reported.

Such approaches are informative but remain limited in some respects, e.g., by approximating a complex selection process with a simplified parametric form, or by making ad hoc "corrections" to the measurements. Often these corrections are derived for a single choice of cosmology and/or population parameters, whereas in reality the selection or other biases may vary across the model space. Furthermore, the model is assumed to

have a fixed uncertainty, and hyperparameters – that may be of interest in SN Ia population studies – are marginalized over and not reported.

A promising alternative to conventional MCMC techniques for cases with intractable likelihood functions is Approximate Bayesian Computation (ABC), which offers a "likelihood-free" approach to parameter estimation. In contrast to typical MCMC analyses, the ABC method (Beaumont et al., 2008) relies on forward-modeling the data at every point in parameter space, and compares data to simulation via a distance metric with a specified tolerance level. This tolerance level evolves with each iteration, and decreases as the forward-model simulation converges on the data distribution. Jennings et al. (2016) present SUPERABC as an application of ABC to SN Ia cosmology. While these methods can include selection effects and systematics in a more robust way than conventional BHM frameworks, the ABC metric is often difficult to construct, and chain convergence can be less efficient than likelihood-based techniques.

The BAMBIS approach to parameter estimation allows us to address several limitations of current SN Ia cosmological parameter estimation by combining non-parametric likelihood evaluation with full forward-modeling of the data. While the method as outlined here only applies to spectroscopically-confirmed SNe Ia, its features allow for a natural extension to a photometrically classified sample.

Before demonstrating BAMBIS on a set of simulated SN Ia light-curve parameters (Section 4.5), we illustrate fundamental components of the algorithm using two toy-model examples. In the first example (Section 4.4.1), we model a hierarchical regression problem, similar to that of SN Ia standardization, but without any additional complications such as selection effects or measurement uncertainty. In the second problem (Section 4.4.2), we include a complex selection function as part of the model.

In the examples presented in this chapter, we do not include systematic uncertainties, e.g., light-curve fitting error, in the models under investigation. Including such systematics is straightforward in the BAMBIS algorithm, as long as they can be accurately modeled by the simulator. In traditional likelihood-based approaches, including systematics

in the analytic likelihood can be nontrivial and serve as a potential source of systematic parameter bias. For example, the covariance matrix must account for measurement uncertainty if the model used in the likelihood does not include random noise. As BAMBIS does not use analytic likelihoods and would, in practice, estimate the likelihood using a noisy model at each proposed point in parameter space, we do not expect systematic uncertainties to impose any additional parameter bias. Rather, we expect parameter bias may stem from the algorithm itself, e.g., from the non-parametric estimation of the likelihood. Therefore, we explore parameter bias *without* including systematics as this will more clearly illuminate effects incurred from the algorithm.

4.2 Overview of Bayesian Inference and Kernel Density Estimation

In the Bayesian framework, one of the primary goals is to estimate the posterior probability distribution, $p(\Theta|\mathcal{D})$, of the parameters Θ of a model $\mathcal{M}$, given some data $\mathcal{D}$. Using Bayes' theorem, the posterior can be written as

$$p(\Theta|\mathcal{D}) = \frac{\mathcal{L}(\mathcal{D}|\mathcal{M}(\Theta))\pi(\Theta)}{\int \mathcal{L}(\mathcal{D}|\mathcal{M}(\Theta))\pi(\Theta)d\Theta}, \tag{4.1}$$

or more commonly

$$p(\Theta|\mathcal{D}) \propto \mathcal{L}(\mathcal{D}|\mathcal{M}(\Theta))\pi(\Theta), \tag{4.2}$$

where $\mathcal{L}(\mathcal{D}|\mathcal{M}(\Theta))$ is the likelihood, or the probability of the data given a particular set of model parameters, $\pi(\Theta)$ contains prior information about the data, e.g., a physical prior can be imposed on a mass variable to restrict the parameter space to positive values, and the denominator of Eq. 4.1 is the product of the likelihood and prior integrated over all points in parameter space.

In the SN Ia analysis, the likelihood, $\mathcal{L}$, can be written in hierarchical (multi-level) form, i.e., Figure 4.1. Atop the hierarchy are some hyperparameters, which are parameters governing the distribution of some other stochastic parameters in Θ. For example, if $\pi(\Theta)$

is drawn from a normal distribution with mean m and variance s^2 (i.e., $\pi(\Theta) \sim \mathcal{N}(m, s^2)$), then m and s could be treated as hyperparameters of the model. In the SN Ia case, many of the parameters thus generated are unobserved or "latent" (such as the intrinsic, noiseless characteristics of individual SNe). Bayesian hierarchical modeling allows for simultaneous inference of these latent variables with the hyperparameters of interest.

In practice, one generates MCMC samples from the posterior distribution by evaluating the likelihood of the data given different values in the model parameter space. In many cases, the likelihood can be parameterized as a multivariate Gaussian distribution, where the mean is dictated by the choice of physical model and the covariance is measured or estimated either analytically or numerically. However, direct evaluation of the likelihood may require unreliable assumptions about the analytic form of the likelihood PDF (e.g., about the mean and covariance of a Gaussian, or the Gaussian assumption itself). In the case of SN Ia cosmology, the processes of detecting transient events, measuring their light curves, fitting these to parametric functions, and obtaining redshift information are complex and impossible to describe exactly as analytic functions of the underlying SN Ia event characteristics, especially regarding the selection criteria that are implicit or explicit to this process. The standard approach cannot be used without forcing an analytic approximation onto the likelihood of the data.

What can be done instead, however, is to simulate these processes and generate samples of $\mathcal{D}$ that are drawn from the likelihood. In the SN Ia application, the data are points in the 4-dimensional space spanned by three light-curve fit parameters and the redshift for each selected SN Ia event. We can then apply density estimators to the simulated set of SNe Ia to assign a likelihood $\mathcal{L}$ to each SN Ia in the observed $\mathcal{D}$.

A kernel density estimator (KDE) smooths the discrete simulated distribution with a kernel of a chosen size (bandwidth). This effectively assigns each real event a likelihood by measuring the distances to neighboring events in the simulated data for each model being tested. The quality of the estimated PDF is largely dependent on choice of bandwidth. If the chosen bandwidth is too small, then the resulting PDF is noisy or "un-

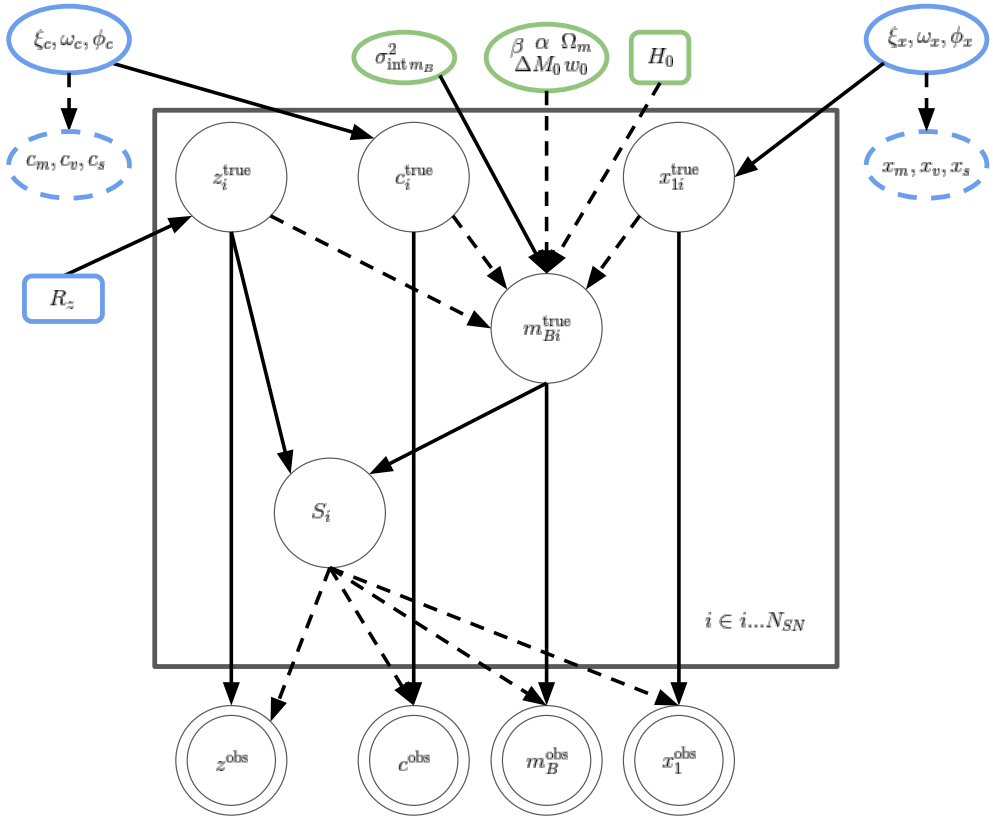

Figure 4.1: BHM describing the SN Ia model used for this sample implementation of BAMBIS (Section 4.5). Dashed lines represent deterministic relationships and solid lines indicate probabilistic relationships. The diagram features three distinct parameter types: parameters which will be varied in the MCMC (solid oval), fixed parameters (solid rectangle), and derived parameters (dashed oval). Blue parameters represent hyperparameters and corresponding derived parameters; green parameters represent cosmological parameters. Latent variables are enclosed by a single circle; the distributions of observed variables are enclosed by concentric circles. The variable S_i indicates whether or not a given SN Ia passes selection criteria and is included in the final observed data set.

Table 4.1. Standard Deviation of Gaussian Fits to KDE of $p(x)$

Bandwidth	σ_x
0.02	3.066
0.18 (Scott's Rule)	3.116
1.0	4.235

dersmoothed;" if the bandwidth is too large, then the resulting PDF is likely insensitive to irregular features or "oversmoothed." Common rules of thumb exist to help inform bandwidth selection including Gaussian approximation and Scott's rule (Sturges, 1926; Scott, 2015).

In Figure 4.2, we present a simple example of estimates of a Gaussian PDF (blue histogram) using SciPy's `gaussian_kde` with four distinct choices of bandwidth. For this realization of $5,000$ samples of the random variable $x \sim \mathcal{N}(0,3)$, the optimal bandwidth using Scott's Rule is ≈ 0.18. As shown in Figure 4.2, the density estimate using the narrower choice of bandwidth (green curve) is noisy, while the estimate using the larger bandwidth (magenta curve) is oversmoothed and does not capture the peak of the PDF well.

To further explore the estimated densities, we fit a Gaussian distribution to each and compare the mean and standard deviation to that of x. For the realization of $5,000$ samples, $\sigma_x = 3.049$. The standard deviations of the KDE Gaussian fits are summarized in Table 4.1. In all cases, the KDE generates an estimated PDF that is broader than the true distribution. The broadening of the distribution decreases as the number of samples used to construct the KDE increases; however, this is inevitable when constructing a density estimate with a finite sample.

The effects of kernel size and resulting PDF smoothing increases with dimensionality. We illustrate this effect in Figure 4.3 where we present the two-dimensional density for

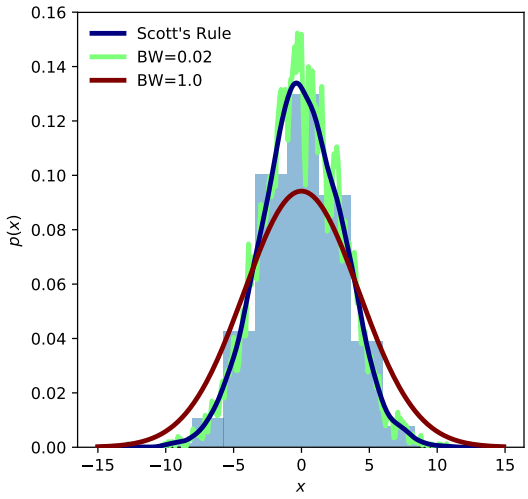

Figure 4.2: KDE estimates of $p(x)$ (blue histogram) using four distinct choices of bandwidth. The bandwidth determined by Scott's Rule is ≈ 0.18. The density estimate using the narrower bandwidth is clearly too noisy (green curve), while the density estimate using too large a bandwidth (magenta curve) appears oversmoothed and does not appropriately estimate the peak of the distribution. Corresponding standard deviations of Gaussian fits to the KDEs are presented in Table 4.1.

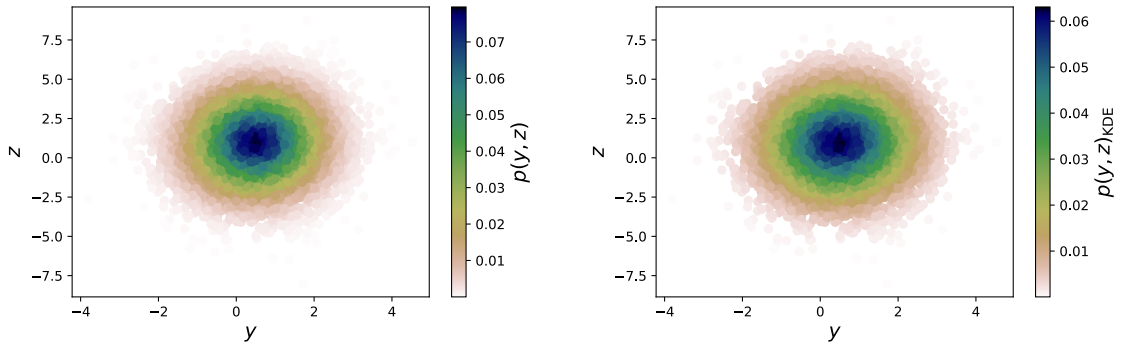

Figure 4.3: Two dimensional PDF evaluated using an analytic multivariate Gaussian (left) and Gaussian KDE (right) with arbitrarily large bandwidth. Denser regions are shown in blue; regions of low density are shown in light pink. The bandwidth was selected to emphasize the effect of choosing an inappropriate kernel size; the broadening of the PDF can be seen in both the y and z dimensions.

correlated Gaussian variables y and z,

$$\begin{pmatrix} y \\ z \end{pmatrix} \sim \mathcal{N}\left(\begin{pmatrix} 0.5 \\ 1.0 \end{pmatrix}, \begin{pmatrix} 1 & 0.25^2 \\ 0.25^2 & 4 \end{pmatrix}\right) \tag{4.3}$$

evaluated using an analytic multivariate Gaussian (left) and the Gaussian KDE (right). The bandwidth selected in this example was chosen to be arbitrarily large to emphasize the effect of choosing an inappropriate bandwidth. As shown in Figure 4.3, the estimated PDF is broader in both the y and z dimensions. This is particularly evident near the peak of the distribution.

As Figures 4.2 and 4.3 show, we must keep in mind that KDE estimators are invariably biased in the sense of being broader than the true distribution as a result of the convolution of the sample by the kernel function. We will remain alert to the possibility of this bias propagating into biased parameter inferences.

4.3 The BAMBIS Algorithm

BAMBIS uses MCMC sampling of the model parameters, but differs from previous algorithms in that the likelihood $\mathcal{L}(\mathcal{D}|\Theta)$ is determined via density estimation from a Monte Carlo simulation of events generated for each sampled model. In this section we detail the BAMBIS algorithm and describe particular features which should be carefully considered upon implementation.

The BAMBIS algorithm for a generic set of model and hyperparameters, Θ, using a generic data set of d dimensions (corresponding to the number of observed variables per data point), $\mathcal{D}_d$, proceeds as follows:

Step 1: A point in parameter space, Θ_p, is proposed by the MCMC sampler.

Step 2: Simulated data are drawn using Θ_p, which provide a sampling of the distribution of points in the data space produced by the model.

Step 3: A KDE is used to estimate the non-parametric, d-dimensional PDF of the model from the simulated sample.

Step 4: The likelihood of the data given the model is estimated by evaluating the KDE PDF at each data point in $\mathcal{D}_d$.

Step 5: The MCMC algorithm accepts or rejects the point Θ_p based on this likelihood.

The details of the MC simulation procedure required for Step 2 depend on the parameter set Θ and choice of forward-model simulation package. We note that the BAMBIS algorithm is designed to be independent of simulation package choice. Any simulation package may be introduced, as long as it can effectively simulate 1) the astrophysical processes that generate the real data, and 2) the measurement processes that are applied to the real observations, including features such as selection effects and survey systematics.

The resulting simulated data are used in the likelihood as a non-analytic estimate of the model. The size of the simulated data set should be large enough to ensure proper

sampling of the d-dimensional PDF. This "synthetic likelihood" technique is an effective means of evaluating the likelihood using summary statistics when the model and/or likelihood is intractable (Wood, 2010). For more details on Bayesian synthetic likelihoods, see Price et al. (2017).

These MC simulations also allow us to incorporate complex selection effects in a robust statistical framework. In traditional cosmological analyses, a bias correction - on individual SN Ia magnitude, color, etc, as determined by simulations - is added to the data to account for biases stemming from selection effects (Betoule et al., 2014; Shariff et al., 2016). Such bias corrections are often computed as a function of redshift, e.g., by simulating the observation of a population of events (see e.g., Scolnic and Kessler, 2016; Betoule et al., 2014). But in fact, these biases can depend on many model parameters including w_0, α, and β, and thus it becomes inaccurate to apply a fixed set of corrections to the data while exploring the model posterior. In BAMBIS, we do not create an ad hoc model for selection. Rather, we apply to the simulation the same selection process experienced by the data. The use of MC simulations in this way also allows us to properly treat other effects, such as measurement errors that vary from event to event, or systematic errors in the measurement tools, which are not straightforward to include in an analytic likelihood.

We note that BAMBIS is written in the open-source Python programming language. Any simulation packages, KDE routines, or sampling algorithms also written in Python are straightforward to incorporate; other programs not written in Python can be included via a Python wrapper.

4.3.1 Algorithm Caveats

4.3.1.1 Noisy Likelihoods

One of the more challenging aspects of the approach is the impact of including a stochastic model on the sampling of parameter space. In conventional likelihood-based techniques,

the value of the model at a given point in parameter space is fixed. This allows for trivial comparison of the likelihood at two points in parameter space, which is the crux of sampling methods such as Metropolis Hastings MCMC. For example, in the Metropolis Hastings (MH) algorithm, the acceptance probability (a_p) which dictates whether a proposal from point Θ_1 to point Θ_2 is accepted is governed by

$$a_p = \min\left[1, \frac{\mathcal{L}(\Theta_2)q(\Theta_1|\Theta_2)}{\mathcal{L}(\Theta_1)q(\Theta_2|\Theta_1)}\right], \tag{4.4}$$

where q is some proposal density and $a_p = 1$ indicates the point is a more likely match to the data and should therefore be accepted. In typical cases, we assume the process exhibits detailed balance – the probability of transitioning from Θ_1 to Θ_2 is equivalent to transitioning from Θ_2 to Θ_1.

In the BAMBIS algorithm, estimating the model using MC simulations means that the model, and thus, the likelihood, will vary over multiple evaluations of the likelihood at the same point in parameter space. Therefore, such a comparison of $\mathcal{L}(\Theta_1)$ and $\mathcal{L}(\Theta_2)$ is not immediately straightforward. While we expect the noisy likelihood to retain the approximate shape of the desired posterior, variations in the likelihood may be particularly worrisome near the peak of the distribution. Figure 4.4 presents an example of these likelihood variations for a mock data set sampling over a wide range of parameter space (Θ_a, left panel) and closer to the peak (Θ_b, right panel). As shown in the left panel of Figure 4.4, the general shape of the posterior peaks at the true value (dashed red line), despite the noise in the individual evaluations of the likelihood (blue points). While this maximum is still discernible when we explore closer to the peak (right panel), the fluctuations in the likelihood at a particular Θ_b indicate that the maximum likelihood value may not necessarily correspond to the peak of the posterior. This also means that the likelihood at a proposed Θ_p, perhaps far from the peak of the posterior, may fluctuate to be higher than the likelihood at the peak, causing the proposal to be accepted when it should in fact be rejected.

The "exact approximate" psuedo-marginal MCMC approach was proposed as a solution to the problem of MCMC sampling using model estimation from MC simulations

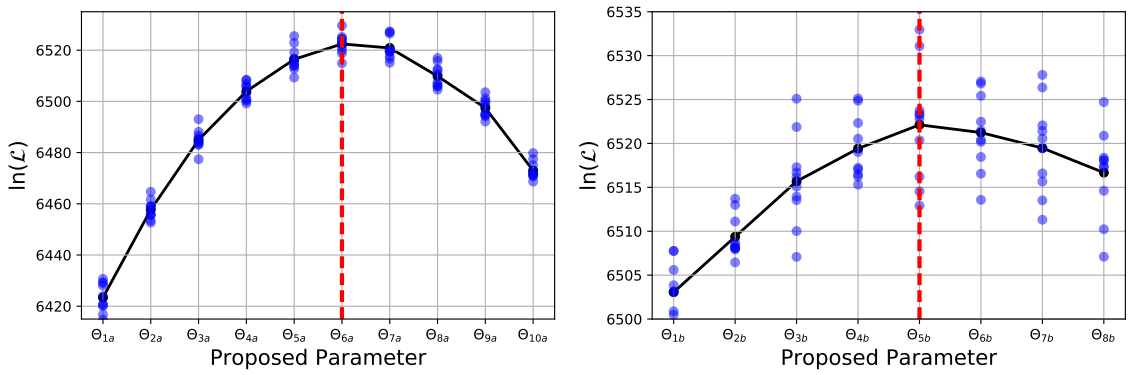

Figure 4.4: Example of noisy likelihood for a sample mock data set sampling over a wide range of parameter space (Θ_a, left panel) and closer to the peak (Θ_b, right panel). The true value of the parameter used to generate the mock data is indicated by the dashed red lines. Blue dots represent an individual evaluation of the likelihood at each point in Θ_a and Θ_b; black lines connect the means at each proposed point.

(Beaumont, 2003; Andrieu and Roberts, 2009). In this approach, the acceptance probability is a function of an *estimate* of the likelihood, rather than the exact $\mathcal{L}$, which is precisely the problem at hand. In this case,

$$a_p = \min\left[1, \frac{p(\hat{\Theta}_2)q(\Theta_1|\Theta_2)}{p(\hat{\Theta}_1)q(\Theta_2|\Theta_1)}\right], \tag{4.5}$$

where $p(\hat{\Theta}_2)$ and $p(\hat{\Theta}_1)$ are noisy estimates of the likelihood. It can be shown that using these noisy estimates in the MCMC sampling will still generate an exact sampling of the posterior.

Consider the noise in the likelihood to be the random variable $W_p = p(\hat{\Theta}_p)/\mathcal{L}(\Theta_p)$ where W_p is drawn from the joint distribution of Θ_p and a random variable w_p introduced for the purpose of illustration, i.e., $W_p \sim \mathcal{L}_p(w_p|\Theta_p)$. If we treat the proposal density as not only an update of Θ, but as an update of w, then the proposal draws (Θ_2, w_2) from the density

$$(\Theta_2, w_2) \sim w_2 q(\Theta_2|\Theta_1)p(w_2|\Theta_2), \tag{4.6}$$

and we therefore have the approximate acceptance probability

$$a_p = \min\left[1, \frac{w_2\mathcal{L}(\Theta_2)p(w_2|\Theta_2)q(\Theta_1|\Theta_2)p(w_1|\Theta_1)}{w_1\mathcal{L}(\Theta_1)p(w_1|\Theta_1)q(\Theta_2|\Theta_1)p(w_2|\Theta_2)}\right]. \tag{4.7}$$

Further inspection of Eq. 4.7 reveals that the target density of interest is proportional to

$$w_p\mathcal{L}(\Theta_p)p(w_p|\Theta_p), \tag{4.8}$$

which is equivalent to $\mathcal{L}(\Theta_p)$, the target density of interest, after marginalizing over all w_p. Note that this analysis relies on two important assumptions: 1) that the estimator $p(\hat{\Theta}_p)$ is unbiased, and 2) that we must keep and re-use the noisy $p(\hat{\Theta}_p)$ when we compute the acceptance ratio for the subsequent proposals.[6] If these conditions are satisfied, then we expect standard MCMC algorithms to reach the target density, but that convergence may take longer than the classical problem (Beaumont, 2003).

4.3.1.2 Posterior Sampling

There exists a wide variety of sampling algorithms, each with its own set of tunable parameters and designed to be optimized to a particular problem. When using BAMBIS, it is essential to use a sampler that can accommodate the stochastic nature of the model and likelihood.

We elect to explore the parameter space using the affine-invariant ensemble sampler `emcee` (Foreman-Mackey et al., 2013). `emcee` makes use of the "stretch move" algorithm which updates the position of a point, or walker, in an ensemble based on the positions of the walkers in the complementary ensemble (Goodman and Weare, 2010). To update the position of a walker at position X_1, a walker X_2 is drawn randomly from the positions of the remaining walkers and a new position is proposed

$$X_1 \to Y = X_2 + Z[X_1 - X_2], \tag{4.9}$$

[6] `https://darrenjw.wordpress.com/2010/09/20/the-pseudo-marginal-approach-to-exact-approximate-mcmc-algorithms/`

where Z is a random variable drawn from a distribution $g(Z = z)$. This distribution is a function of an adjustable scale parameter a

$$g(z) \propto \begin{cases} \frac{1}{\sqrt{z}} & \text{if } z \in \left[\frac{1}{a}, a\right] \\ 0 & \text{otherwise} \end{cases}, \tag{4.10}$$

with the corresponding acceptance probability,

$$a_p = \min\left[1, Z^{N-1}\frac{p(Y)}{p(X_1)}\right], \tag{4.11}$$

where N is the dimension of the parameter space.

Algorithm performance and chain convergence are measured by the acceptance fraction (f_a) and autocorrelation time (τ), which is a direct measure of the number of evaluations of the posterior required to produce independent samples of the target density. When using `emcee`, we evaluate f_a and τ periodically as the chain converges. It is recommended to run the chain for $\approx 10-20\tau$ to achieve convergence. We expect that as the chain moves, the acceptance fraction may be lower than typically recommended ($f_a \sim 20-40\%$). This is due to the fact that walkers may get "stuck" at randomly large values of the log likelihood and it may take several proposals to move to a new point in parameter space. If sampling performance becomes an issue, Foreman-Mackey et al. (2013) suggest adjusting the scale factor a or increasing the number of walkers. We discuss any necessary deviations from the default sampler settings in each presented BAMBIS sample implementation.

4.3.1.3 Choice of KDE

To minimize the artificial broadening of the PDF of the observed variables, we want to select an interpolation kernel that smooths over the maximal number of samples for a given kernel volume.

We produce a "matched elliptical Gaussian kernel density estimator" (MEGKDE) via the following algorithm:

1. Determine the covariance matrix of the training sample $\{\mathbf{X}_i\}$ as $\Sigma = \left\langle (\mathbf{X} - \langle \mathbf{X} \rangle)(\mathbf{X} - \langle \mathbf{X} \rangle)^T \right\rangle$.

2. Perform the Cholesky decomposition $\Sigma^{-1} = L^T L$ for a lower-triangular matrix L, and transform the training samples to $\mathbf{Y}_i = L(\mathbf{X}_i - \langle \mathbf{X} \rangle)$. The variable $\mathbf{Y}$ has identity covariance matrix.

3. Choose a size σ for a spherical KDE kernel in the $\mathbf{Y}$ space. The rule $\sigma = N_s^{-1/(q+4)}$, where N_s is the number of samples and $q = 4$ is the dimensionality of the data, is shown by Silverman (1986) to minimize interpolation error for nearly-Gaussian distributions.

4. Define the density at a target point $\mathbf{X}_0$ as

$$\rho(\mathbf{X}_0) = \frac{\det \mathrm{L}}{(2\pi\sigma^2)^{q/2}} \sum_{i=1}^{N_s} e^{-|L(\mathbf{X}_0 - \langle \mathbf{X} \rangle) - \mathbf{Y}_i|^2 / 2\sigma^2}, \tag{4.12}$$

   where the exponent now contains the Euclidean distances between samples and the target point in the $\mathbf{Y}$ space. The routine can be accelerated by using a *kD* tree to rapidly isolate the sample points that are close enough to $\mathbf{Y}_0$ to contribute significantly to the sum.

4.3.1.4 Model and Data Outliers

Another important issue to consider is the size of the simulation used to estimate the density. There is a correlation between the variance of the likelihood at a given point in parameter space and the size of the simulation used to estimate the model. This effect will depend on the dimensionality of the problem and is explored in Section 4.4.1.

A final issue to consider is how to handle outlier points. There could be a Θ_p from which a simulation is drawn where $p(\mathcal{D}_i|\Theta_p) = 0$. In this case, we set a "floor" on the PDF to ensure that all data points are used in the evaluation of the likelihood. We choose a value such that the model will be penalized, but not completely rejected, as this should

not be the primary reason for the point rejection. After extensive testing, we find that setting $p(\mathcal{D}_i|\theta_p) = 0.95$ in these cases is a sufficient floor.

4.4 Proof of Concept

While the physical process by which nature generates SN Ia light curves is unknown, a model of this process can be incorporated into a simulator and used to simulate realistic SN Ia fluxes. Tools for parameter inference such as BAMBIS will only be successful if there exists at least one set of parameters for which the simulation accurately reflects the natural process. Before demonstrating the BAMBIS algorithm on SN Ia simulations, we present two simpler examples, which we can use as proof of concept. We choose to simulate a four dimensional hierarchical regression model, as a similar model is frequently used in the SN Ia cosmology problem.

4.4.1 Toy Problem 1: Gaussian Linear Regression Model

In this example, we assume the observed data set $\mathcal{D}$ consists of N observed variables: w, x, y, and t. We draw these variables using the following hierarchical model:

$$w_i^{\text{true}} \sim N\left(\bar{w}, \sigma_w^2\right) \tag{4.13}$$

$$x_i^{\text{true}} \sim N\left(\bar{x}, \sigma_x^2,\right) \tag{4.14}$$

$$y_i^{\text{true}} \sim N\left(\bar{y}, \sigma_y^2,\right) \tag{4.15}$$

$$t_i^{\text{true}} \sim N\left(\alpha \times w_i + \beta \times x_i + \gamma \times y_i + \delta, \sigma_{\text{int}}^2\right). \tag{4.16}$$

This essentially mimics the SALT2 SN Ia regression model (Eq. 2.4), where t is analogous to the SN Ia distance modulus or peak B-band magnitude. In this first example, we do not include additional measurement uncertainty nor apply any selection. Therefore each "true" variable is also observed (denoted by the superscript "obs"), i.e., $w_i^{\text{obs}} = w_i^{\text{true}}$,

$x_i^{\text{obs}} = x_i^{\text{true}}$, $y_i^{\text{obs}} = y_i^{\text{true}}$, $t_i^{\text{obs}} = t_i^{\text{true}}$. We define the set of hyperparameters describing the latent distributions as

$$\psi_{\text{ex1}} \equiv [\bar{w}, \sigma_w, \bar{x}, \sigma_x, \bar{y}, \sigma_y], \tag{4.17}$$

and the set of model parameters as

$$\theta_{\text{ex1}} \equiv [\alpha, \beta, \gamma, \delta, \sigma^{\text{int}}]. \tag{4.18}$$

The complete hierarchical model for this example is presented in Figure 4.5.

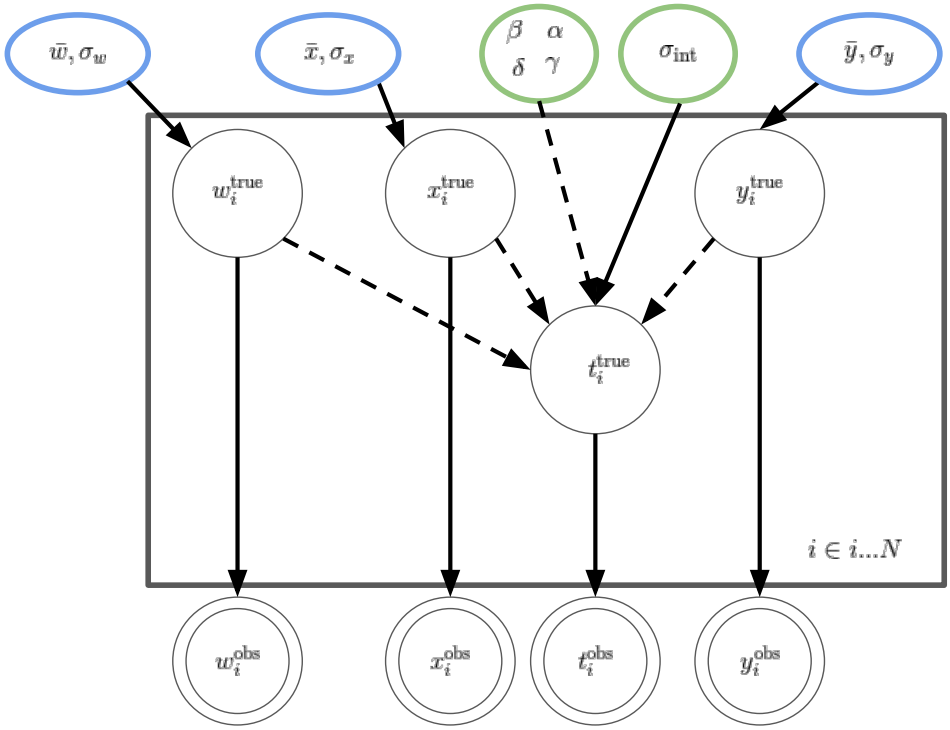

Figure 4.5: BHM for toy example without additional measurement uncertainty or sample selection. Dashed lines indicate deterministic relationships; solid lines indicate probabilistic relationships. Model parameters are circled in green and hyperparameters are circled in blue. Latent variables are enclosed in a single circle; observed variables are enclosed in a double circle.

For the purpose of demonstration, we draw a mock data set of 700 observations using this toy model and denote this data set as `D1`. We elect to draw a sample of 700 obser-

Table 4.2. D1 Input Parameter Values

Parameter	Input Value
$\bar{w}$	0.5
σ_w	1.0
$\bar{x}$	0.0
σ_x	0.1
$\bar{y}$	0.5
σ_y	2.0
α	0.15
β	3.0
γ	0.2
δ	0.0
$\sigma_{\rm int}$	0.15

vations as this is roughly the expected size of the three-year spectroscopically-classified SN Ia sample of the DES-SN (see Section 4.5). The input values used to draw D1 are presented in Table 4.2. Values listed in Table 4.2 were chosen arbitrarily as this first test is only used to validate the BAMBIS algorithm. 1-D marginalized distributions of the observed variables in D1 are shown in Figure 4.6.

We define the posterior probability for each data point in the 4-D data space as $p(\theta_{\rm ex1}, \psi_{\rm ex1}|w_i^{\rm obs}, x_i^{\rm obs}, y_i^{\rm obs}, z_i^{\rm obs})$. Using Bayes' theorem, we relate this to the product of the likelihood $\mathcal{L}$ and prior $\Pi(\theta_{\rm ex1}, \psi_{\rm ex1})$

$$p(\theta_{\rm ex1}, \psi_{\rm ex1}|w_i^{\rm obs}, x_i^{\rm obs}, y_i^{\rm obs}, z_i^{\rm obs}) \propto \mathcal{L}_i \times \Pi(\theta_{\rm ex1}, \psi_{\rm ex1}), \tag{4.19}$$

where $\mathcal{L}_i$ is given by

$$\begin{aligned}\mathcal{L}_i &= p(w_i^{\rm obs}, x_i^{\rm obs}, y_i^{\rm obs}, z_i^{\rm obs}|\theta_{\rm ex1}, \psi_{\rm ex1}) \\ &= p(w_i^{\rm obs}, x_i^{\rm obs}, y_i^{\rm obs}, z_i^{\rm obs}|w_i^{\rm true}, x_i^{\rm true}, y_i^{\rm true}, z_i^{\rm true}) \times p(w_i^{\rm true}, x_i^{\rm true}, y_i^{\rm true}, z_i^{\rm true}|\theta_{\rm ex1}, \psi_{\rm ex1}).\end{aligned} \tag{4.20}$$

We assume each observation is independent and therefore define the likelihood for the

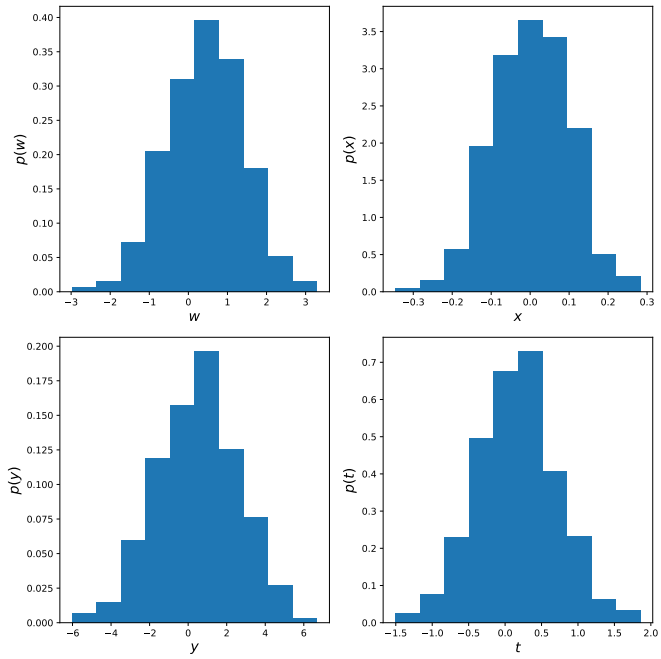

Figure 4.6: 1-D marginalized distributions of observed variables w, x, y, and z for `D1`.

full data sample as the product of the likelihoods of the individual observations, i.e.,

$$\mathcal{L}_{\rm ex1} = \prod_i \mathcal{L}_i \,. \tag{4.21}$$

4.4.1.1 Results

To test the BAMBIS algorithm, we use `D1` to infer $\theta_{\rm ex1}$ and $\psi_{\rm ex1}$. At each proposed point in parameter space, we draw a simulation from θ_p and ψ_p using the same model which generated `D1`. When quoting results, we report the best fit value of each parameter as the median of its 1-D marginalized PDF. As we do not assume our posterior distributions are Gaussian, errors are quoted at the corresponding 16% and 84% quantile levels; we refer to these uncertainties as σ_- and σ_+, respectively. As with any MCMC analysis, the contours of the prior are noisy due to finite sampling.

In this first example, the forward-simulation, density estimate, and likelihood evaluation take $\approx$ 1s at each proposed point in parameter space. We run `emcee` using 100 walkers, over four compute cores, for $\approx$ 24 hours. Our chains converge after $\approx 150,000$

Table 4.3. Best fit Parameter Estimates Using D1

Parameter	Prior*	Input Value	Best fit	σ_-	σ_+
$\bar{w}$	Flat	0.5	0.507	0.043	0.046
σ_w	$\mathcal{U}(0,2.0)$	1.0	0.989	0.026	0.028
$\bar{x}$	Flat	0.0	0.004	0.005	0.003
σ_x	$\mathcal{U}(0,0.5)$	0.1	0.098	0.002	0.003
$\bar{y}$	Flat	0.5	0.49	0.073	0.067
σ_y	$\mathcal{U}(0,4.0)$	2	2.009	0.056	0.041
α	Flat	0.15	0.152	0.006	0.006
β	Flat	3	3.027	0.062	0.051
γ	Flat	0.2	0.2	0.003	0.003
δ	Flat	0.0	0.002	0.006	0.008
$\sigma_{\rm int}$	$\mathcal{U}(0,0.3)$	0.15	0.149	0.004	0.004

*A "Flat" prior indicates an unbounded uniform prior.

total samples (including burn-in) have been drawn. We use $\approx 20,000$ samples from the converged chain to estimate median and uncertainties of the 1-D marginalized posterior distributions. We used the default settings for the `emcee` algorithm. The average acceptance fraction over all the walkers was 12% and τ ranged from $40-80$ for the eleven parameters.

Figure 4.7 displays the posterior distributions of $\theta_{\rm ex1}$ and $\psi_{\rm ex1}$ inferred using D1; priors and best fit results are presented in Table 4.3. As shown in Figure 4.7, BAMBIS successfully recovers all input parameters within the 1σ uncertainty region. The 1-D marginalized posterior distributions are each roughly Gaussian.

To explore potential bias in the BAMBIS algorithm, we run BAMBIS on 24 additional sets of mock data realized using the same model and parameter values listed in Table 4.2. Each mock data set contains 700 observed data points. The 1σ uncertainty regions for each of the data realizations is shown in Figure 4.8. For each data realization, the connected points represent the 16%, 50%, and 84% quantiles of the given 1-D marginalized

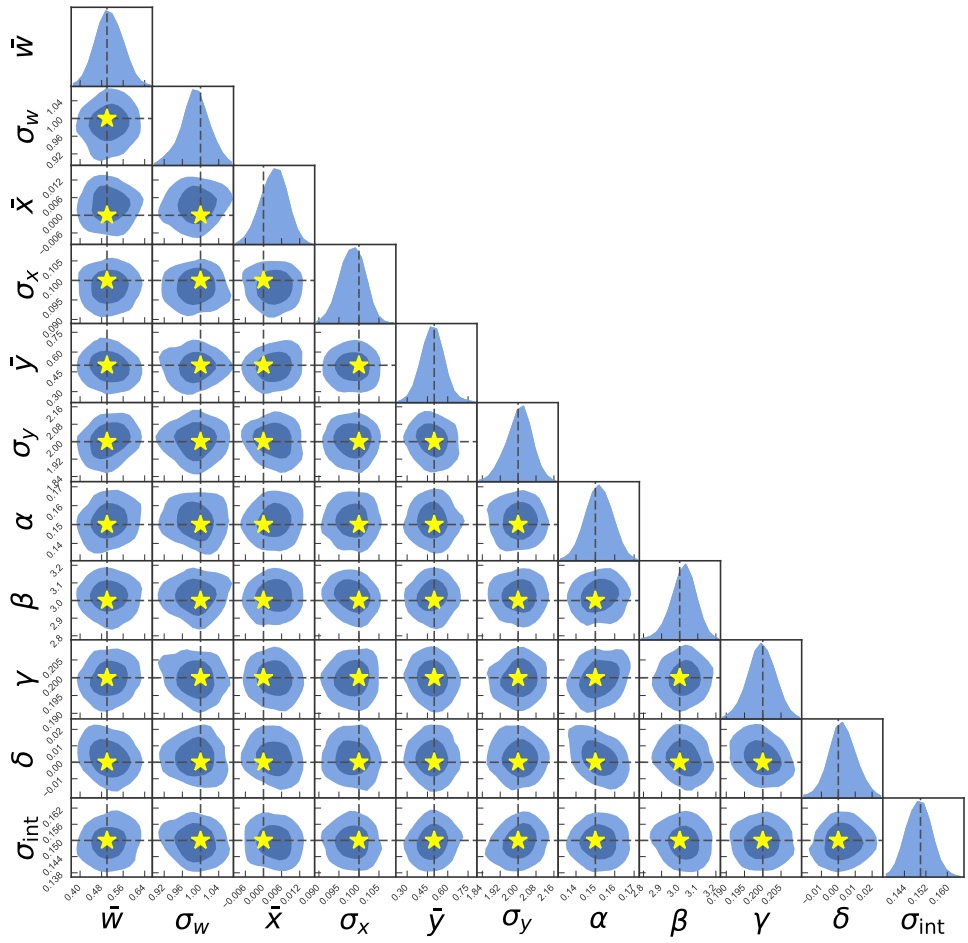

Figure 4.7: 1σ and 2σ credible regions of the θ_{ex1} and ψ_{ex1} parameter posteriors using `D1`. Yellow stars indicate the true parameter values. Priors on the parameters are listed in Table 4.3.

Table 4.4. Parameter Bias Over 25 Data Realizations

Parameter	True Value	Mean † Bias (b)	$\sigma_{\rm avg}$ *	Fractional Bias ($\lvert b/\sigma_{\rm avg}\rvert$)
$\bar{w}$	0.5	0.002	0.039	0.051
σ_w	1.0	−0.011	0.026	0.423
$\bar{x}$	0.0	0.0	0.004	0.0
σ_x	0.1	−0.001	0.003	0.333
$\bar{y}$	0.5	−0.016	0.075	0.213
σ_y	2	−0.012	0.054	0.222
α	0.15	−0.0	0.006	0.0
β	3	−0.004	0.056	0.071
γ	0.2	−0.0	0.003	0.0
δ	0.0	−0.0	0.007	0.0
$\sigma_{\rm int}$	0.15	−0.001	0.004	0.25

†Bias for an individual data realization is defined as the difference between the median of the 1-D marginalized PDF and the true parameter value, i.e., $b_{\bar{w}} = \bar{w}^{\rm bestfit} - \bar{w}^{\rm true}$.

*We define $\sigma_{\rm avg}$ as the average of $\frac{\sigma_+ + \sigma_-}{2}$ over the 20 data realizations.

posteriors. The true values used to generate the mock data (Table 4.2) are designated by dashed red lines. We quantify the bias for a given parameter as the difference between the true value and the median of the 1-D marginalized PDF, i.e., $b_{\bar{w}} = \bar{w}^{\rm bestfit} - \bar{w}^{\rm true}$. In Table 4.4, we present the mean bias, average error, and fractional bias over the 25 data realizations. The data realizations suggest that the best fit values of each of our 11 parameters are biased by < 0.43 times the 1σ uncertainty of the mock data.

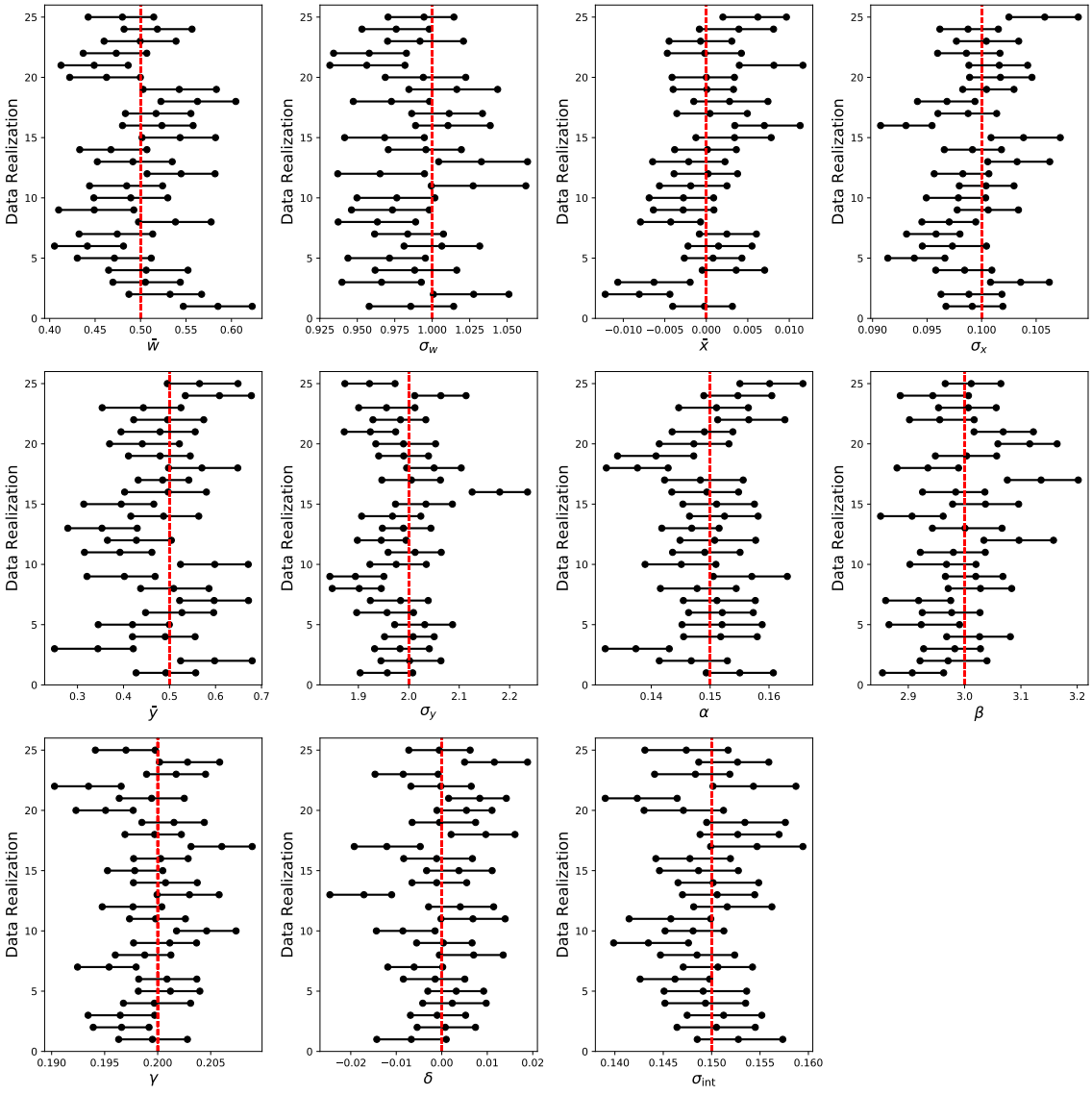

Figure 4.8: Best fit results over 25 realizations of mock data. Black points represent the 16%, 50% and 84% quantiles of the 1-D marginalized PDFs for each parameter, i.e., the connected black line represents the 1σ uncertainty region for a given 1-D marginalized PDF. Red dashed lines indicate the true value used to create the mock data sets.

4.4.1.2 Conclusions

In this first example, we have validated the BAMBIS algorithm for a simple toy regression problem. Using a mock data set of 700 observed data points, we recover 11 model and hyperparameters within their respective 1σ uncertainty regions. The 1-D marginalized posteriors of the model parameters and hyperparameters are roughly Gaussian and well constrained despite the use of wide, uniform priors. Over 25 realizations of the data, we recover the parameters within < 0.43 times their 1σ uncertainties. These results validate the basic premise of the BAMBIS algorithm for this simple toy example.

In the results presented here, we simulated 100,000 samples of the observed data at each proposed point in parameter space. This number was chosen to be arbitrarily large such that variance in the total log likelihood would be reduced. To explore the effect of simulation size on the log likelihood variance, we evaluated the log likelihood at the same θ_{ex1} and ψ_{ex1} 100 times using the same data set and for six different choices of simulation size. In Figure 4.9 we show the variance of these evaluations as a function of the simulation size; the sample size used in this example is indicated by a black star.

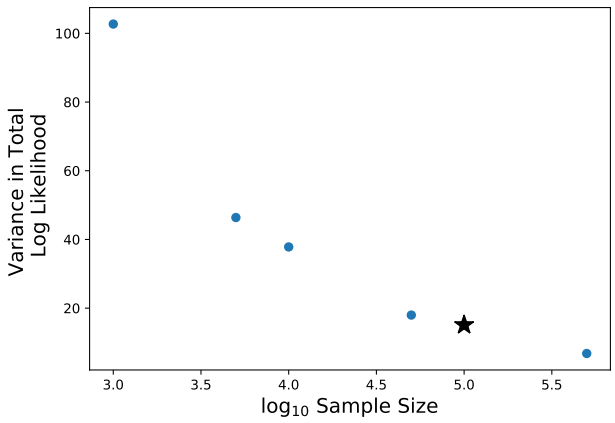

Figure 4.9: Variance over 100 realizations of the total log likelihood as a function of simulation size at a single θ_{ex1} and ψ_{ex1}. The black star indicates the simulation size used to estimate the density for the results presented in Section 4.4.1.1.

As Figure 4.9 indicates, the variance of the log likelihood is strongly dependent on the simulated sample size. However, we note that despite a variance of $\sigma^2 \approx 20$ in log-likelihood space, we are still able to constrain the parameters of interest.

4.4.2 Toy Problem 2: Gaussian Linear Regression with Selection Effects

One of the most significant remaining challenges of SN Ia cosmology is the treatment of selection bias. By forward modeling the data at every proposed point in parameter space, we can include selection effects in a statistically robust framework without making concessions for analytic approximations.

In this section, we expand the model presented in Section 4.4.1 to include a selection function which censors data based on observational limits of the dependent variable, t. This is analogous to a realistic magnitude-limited SN Ia survey in which the only the brightest objects are detected and submitted for spectroscopic follow-up. We implement selection via the following:

Step 1: Draw w^{true}, x^{true}, y^{true} and t^{true} from the model described in Section 4.4.1 and using the input parameters listed in Table 4.2.

Step 2: Divide w^{true} into J bins, each denoted as w_j. Define the total number of samples in each bin as N_j.

Step 3: In each w_j, select the M_j smallest values of t^{true}; M_j is defined by a survey-specific *selection fraction*, f_j, such that $M_j = N_j f_j$.

A sample comparison of the true t and observed t after selection in w_j bins is shown in Figure 4.10.

Although we typically do not know the total number of true samples, by using a simulation at each point in parameter space we can keep track of the total number of

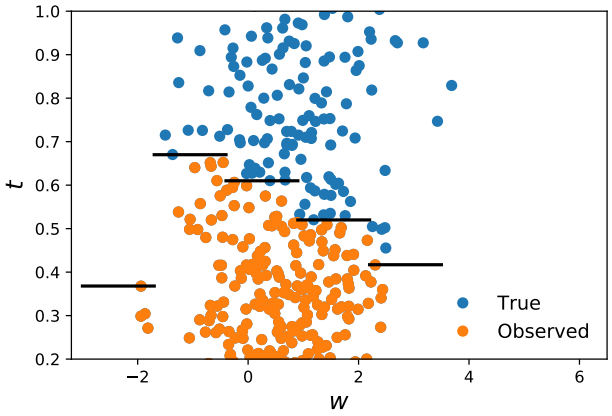

Figure 4.10: True and observed w and t; note the axes have been truncated to focus on the densest region of the 2-D distribution. Black lines indicate the bin widths in the w dimension and the corresponding t^{obs} limit. The black lines demonstrate the sharp, step cutoffs which are difficult to estimate with a KDE.

simulated objects and the number which pass the selection criterion. In this example, we elect to use an arbitrary selection function detailed in Table 4.5.

We draw a true mock data set of 700 objects using the model described in Section 4.4.1 with parameters listed in Table 4.2. After selection, 539 observed data points remain; we denote this set of mock data as `D2`. True and observed distributions of the variables in `D2` are presented in Figure 4.11. As shown in Figure 4.11, the selection function results in the dramatic truncation of t^{true}.

This sharp truncation is also evident in each of the w_j bins. Figure 4.10 shows the true and observed w and t, where f_j of the smallest t^{true} values are selected in each w_j bin. Black lines indicate the width of the w_j bin and the corresponding t^{obs} limit. These steep step cutoffs are difficult for a KDE to reproduce accurately. Therefore, in the case where we apply selection, we estimate the density in each w_j bin separately as it allows us to build the KDE on a smoother detection of objects.

As we are no longer using a complete set of observations, we must modify the likelihood (Eq. 4.20) to account for the objects which are not included in the final observed

Table 4.5. Bins and selection fractions for the example selection function

Lower Bin Value	f_j
$w^{\text{true}} = -3.0$	1.0
$w^{\text{true}} = -1.7$	0.9
$w^{\text{true}} = -0.4$	0.8
$w^{\text{true}} = 0.9$	0.7
$w^{\text{true}} = 2.2$	0.6

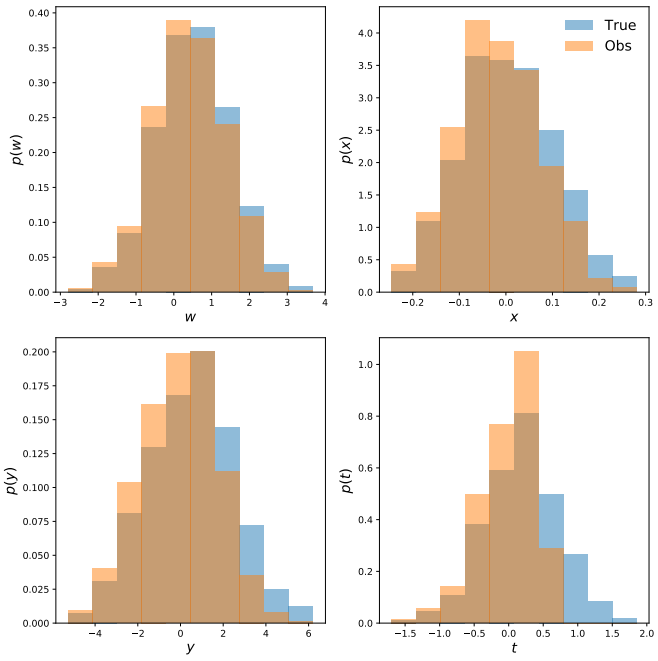

Figure 4.11: 1-D marginalized distributions of the true (blue) and observed (orange) variables of D2. The selection function used to construct the observed distribution is detailed in Table 4.5.

data set. The model described here is akin to a two-stage SN Ia survey with a complex selection process. The first stage is the "detection," where the data vector $\mathbf{X} \equiv \{w^{\text{true}}, x^{\text{true}}, y^{\text{true}}, t^{\text{true}}\}$ is assigned. We assume that the simulator can yield a density $n(\mathbf{X}) = \bar{N} p_d(\mathbf{X})$ of events that will pass all "detection" criteria. We normalize $\int d\mathbf{X}\, p_d(\mathbf{X}) = 1$ so that $\bar{N}$ is the expectation of the sample size, and scales with the overall w^{true} distribution in the w_j bin under consideration.

The second stage of the survey is "selection," where we posit as a test case that there were only M slots available for observing, and that these were allocated to the M most negative events in a given w_j bin. More generally we imagine some selection function $s(\mathbf{X})$ and that the detailed analysis is restricted to events with $s_i = s(\mathbf{X}_i) \leq s_0$, where s_0 is the Mth-smallest s_i. After selection, the detailed information of the remaining $N - M$ un-selected events is lost; we only retain knowledge of how many were discarded in this way. Our data vector is hence $D \equiv (\{\mathbf{X}_i\}, N)$, the union of the M selected data points and the total number of detected objects. This kind of data-dependent selection process is common in real-life experiments but often difficult to incorporate into a chi-squared-minimization analysis. In BAMBIS, we assign a probability $p_s(D|M, \bar{N}, p_d)$: the probability of obtaining the selected data given the predetermined selection count M and the simulation-derived model of the occurrence rate of the data. We assume that the data are independent events, so that the detected events are Poisson-distributed. With N as the total number of objects detected in the data, we can write

$$p_s(D|M, \bar{N}, p_d) = p(\{\mathbf{X}_i\}|s_0, M, p_d) \times p(s_0|N, M, p_d) \times p(N|\bar{N}). \tag{4.22}$$

The last term is the standard Poisson probability. The middle term is the probability of the selection cutoff landing between s_0 and $s_0 + \delta s$. This is better understood by introducing the cumulative distribution function

$$f(s_0) = \int_{s(\mathbf{X}) < s_0} d\mathbf{X}\, p_d(\mathbf{X}) \tag{4.23}$$

By definition, f is uniformly distributed between 0 and 1 for the detected objects. The condition $p(s_0)$ is met if a) one of the N data points has $s_0 < s_j < s_0 + \delta s$, *and* b) $M - 1$

of the remaining $N-1$ points have $s_i < s_0$. Defining $f_0 = f(s_0)$, we therefore can use the binomial distribution B to express

$$\begin{aligned} p(s_0|N,M,p_d) &= N \left.\frac{df}{ds}\right|_{s_0} B(M-1,N-1,f_0) \\ &= \frac{N!}{(M-1)!(N-M)!} f_0^{M-1}(1-f_0)^{N-M} \left.\frac{df}{ds}\right|_{s_0} . \end{aligned} \tag{4.24}$$

The first term is the probability for the distribution of $M-1$ independent values of $\mathbf{X}$ given that all are in the selection region, plus one point somewhere in $s_0 < s_j < s_0 + \delta s$. Combining these probabilities, and marginalizing over $\bar{N}$ with a Jeffreys prior $\propto 1/\bar{N}$, yields

$$\begin{aligned} p_s(D|M,p_d) = \int \frac{d\bar{N}}{\bar{N}} p_s(D|M,\bar{N},p_d) &= \frac{N!}{(M-1)!(N-M)!} f_0^{M-1}(1-f_0)^{N-M} \prod_{i=1}^{M} p_d(\mathbf{X}_i) \\ &= MB(M,N,f_0) \prod_{i=1}^{M} p_d(\mathbf{X}_i)/f_0 \,. \end{aligned} \tag{4.25}$$

The marginalization over the total w^{true} rate ($\bar{N}$) yields a simpler form, with one term giving the probability of the selection cutoff occurring at the s_0 of the data, and the second half describing the distribution of the M selected events in the observed data space. Our selection process is posited to have different thresholds in each of a series of w_j bins; we apply Eq. 4.25 to each w_j bin separately. This means that we are implicitly marginalizing over a distinct w^{true} rate, analogous to a distinct SN rate, in each w_j bin, and hence it would be redundant to include any parameters describing the w^{true} rate explicitly in our MCMC (we do of course need to choose a "truth" distribution when creating the mock data vector).

In this case including selection, the total likelihood over all w_j bins can be written as

$$\mathcal{L} = \prod_{j=1}^{J} M_j B(M_j,N_j,f_{0j}) \prod_{i=1}^{M_j} p_d(\mathbf{X}_{ij})/f_{0j} \,, \tag{4.26}$$

where J is the total number of bins and each of the j bins are assumed to be independent. We define the parameters of interest which will be varied in the MCMC as

$$\psi_{\text{ex2}} \equiv [\bar{x}, \sigma_x, \bar{y}, \sigma_y] \,, \tag{4.27}$$

and

$$\theta_{\rm ex2} \equiv [\alpha, \beta, \gamma, \delta, \sigma^{\rm int}]\,. \tag{4.28}$$

Note that unlike $\psi_{\rm ex1}$, $\psi_{\rm ex2}$ does not include the hyperparameters describing the latent w distribution.

4.4.2.1 Results

When including a selection function in the simulation, we find that additional measures must be taken to ensure proper and efficient MCMC sampling. First, by evaluating the KDE in bins of the larger simulation sample, we must be careful that a simulation drawn from a particular θ_p and ψ_p will generate enough samples in each of the bins. For example, there may be a θ_p and ψ_p which, for a particular bin, generates too few or no samples. To address this issue, we require that a proposed model generate at least $1,000$ samples in each bin; if this criterion is not met, then we reject the model entirely. Second, we find that when including selection, the default `emecee` scale factor $a = 2$ is too large to ensuring proper chain mixing near the peak of the posterior; we therefore change the scale factor to $a = 1.2$. By doing so, we find that it is more difficult for a walker to move away from regions of low log likelihood. This is particularly troublesome if the walker starts in a low-likelihood region as it tends to get "stuck." To address this issue, we require that the log likelihood values of the initial walker positions do not correspond to a model that would be rejected outright by the algorithm.

As in Section 4.4.1, we simulate 100,000 samples at every point proposed by the sampler. We use 100 walkers, spread over 10 compute cores, and run BAMBIS for 10 hours. We find that $\approx 150 - 200,000$ samples are required for convergence (including burn in) and the final acceptance fraction is $\approx 15\%$. Marginalized posteriors for $\theta_{\rm ex2}$ and $\psi_{\rm ex2}$ using `D2` are shown in Figure 4.12 and best fit results are presented in Table 4.6.

We recover roughly Gaussian posteriors for each of nine parameters in $\theta_{\rm ex2}$ and $\psi_{\rm ex2}$. Each of the true parameters is recovered within the 1σ uncertainty region except for $\sigma_{\rm int}$, which we recover just outside the 1σ uncertainty region. We find the uncertainties on the

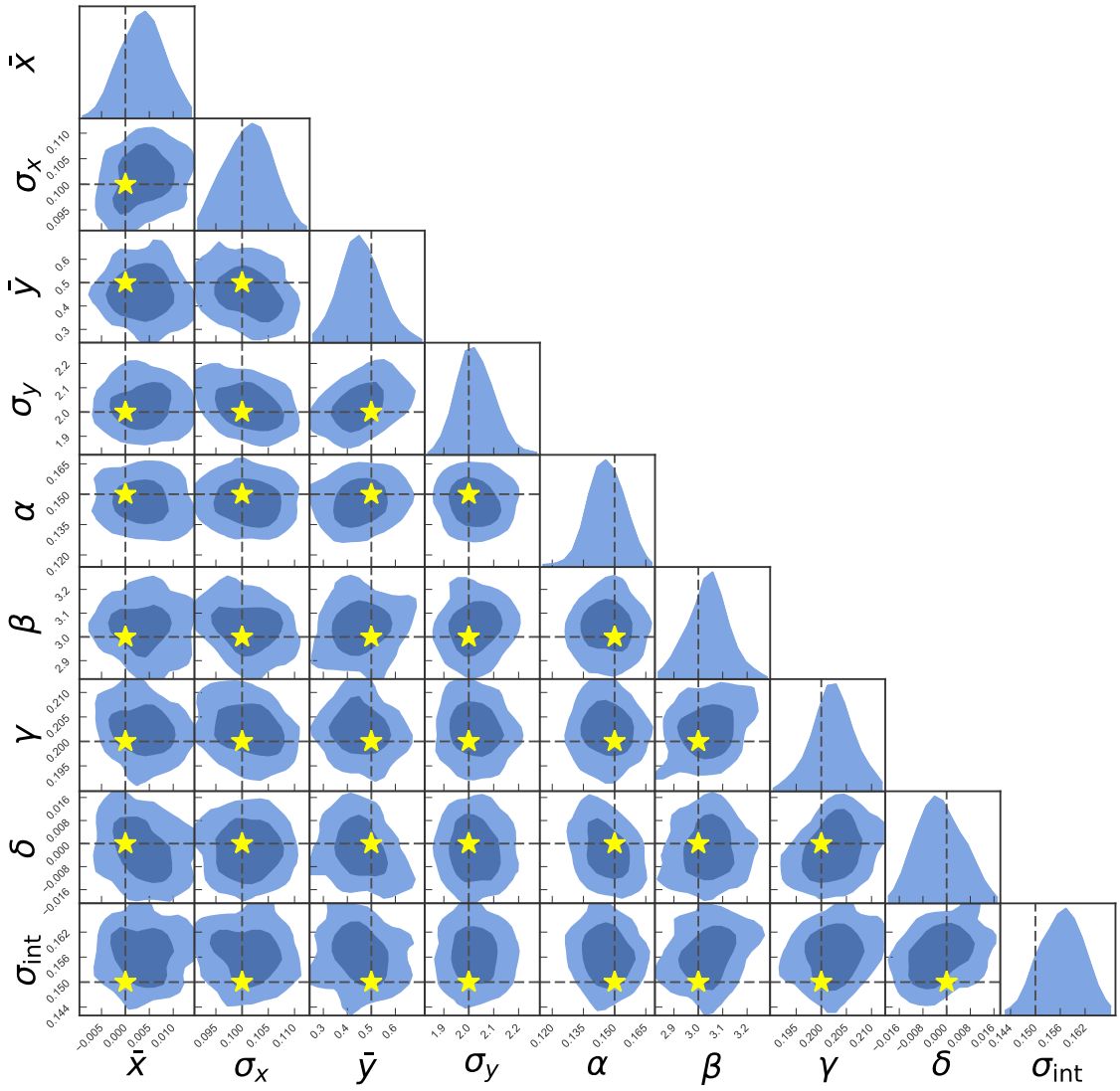

Figure 4.12: 1σ and 2σ uncertainty regions for the θ_{ex2} and ψ_{ex2} posteriors inferred using `D2`. True parameter values are indicated by yellow stars. Best fit results and priors are presented in Table 4.6.

Table 4.6. Best Fit Parameter Estimates Using D2

Parameter	Prior*	Input Value	Best Fit	σ_-	σ_+
$\bar{x}$	Flat	0.0	0.004	0.005	0.004
σ_x	$\mathcal{U}(0,0.5)$	0.1	0.101	0.005	0.004
$\bar{y}$	Flat	0.5	0.452	0.071	0.087
σ_y	$\mathcal{U}(0,4.0)$	2	2.02	0.055	0.074
α	Flat	0.15	0.146	0.007	0.008
β	Flat	3	3.044	0.087	0.069
γ	Flat	0.2	0.202	0.003	0.004
δ	Flat	0.0	-0.003	0.007	0.009
σ_{int}	$\mathcal{U}(0,0.3)$	0.15	0.157	0.006	0.004

*A "Flat" prior indicates an unbounded uniform prior.

model and hyperparameters are roughly the same as the average uncertainties reported in Table 4.4, despite our including a complex selection function in the forward-model simulation and likelihood evaluation.

As in Section 4.4.1.1, we explore potential algorithm bias by performing parameter inference using 25 realizations of mock data. Bias results are illustrated in Figure 4.13 and presented in Table 4.7. Although six of the nine parameters are biased < 0.3 times their respective 1σ uncertainties, we observe a systematic bias in σ_y (0.5σ), σ_x (1σ) and σ_{int} (0.8σ). In particular, we note that σ_x and σ_{int} are both biased to be systematically larger than the input value.

4.4.2.2 Conclusions

Using D2, we have demonstrated that when selection effects are included in the model, BAMBIS can successfully recover eight of the nine model and hyperparameters within their respective 1σ uncertainty regions. However, over 25 realizations of mock data, we find bias in the recovery of σ_y (0.5σ), σ_x (1σ), and σ_{int} (0.8σ). We suspect that this is

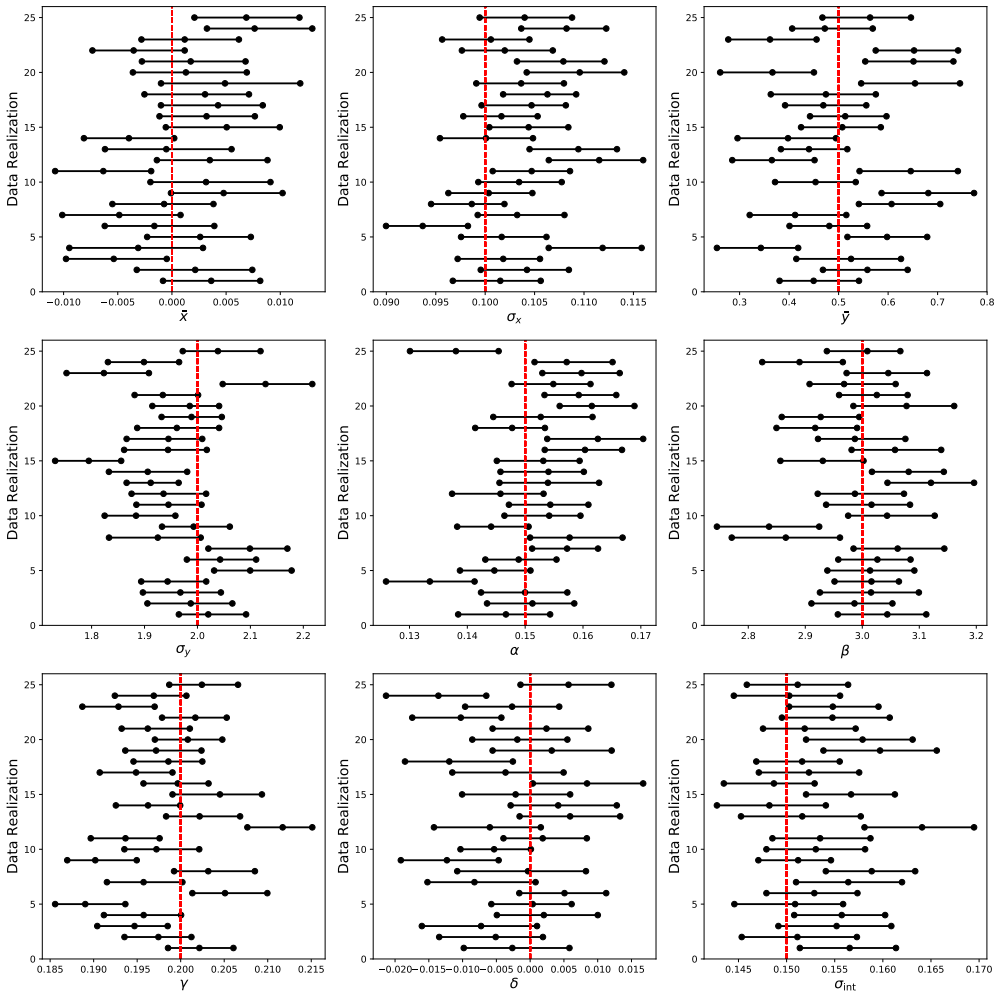

Figure 4.13: Best fit results over 25 realizations of mock data including selection effects. Black points represent the 16%, 50% and 84% quantiles of the 1-D marginalized PDFs for each parameter, i.e., the connected black line represents the 1σ uncertainty region for a given 1-D marginalized PDF. Red dashed lines indicate the true value used to create the mock data sets.

Table 4.7. Parameter Bias Over 25 Data Realizations

Parameter	True Value	Mean † Bias (b)	$\sigma_{\rm avg}$ *	Fractional Bias ($\lvert b/\sigma_{\rm avg}\rvert$)
$\bar{x}$	0.0	0.001	0.005	0.2
σ_x	0.1	0.004	0.004	1.0
$\bar{y}$	0.5	0.006	0.088	0.068
σ_y	2	−0.036	0.069	0.522
α	0.15	0.002	0.007	0.286
β	3	−0.002	0.074	0.027
γ	0.2	−0.002	0.004	0.5
δ	0.0	−0.002	0.007	0.286
$\sigma_{\rm int}$	0.15	0.004	0.005	0.8

†Bias for an individual data realization is defined as the difference between the median of the 1-D marginalized PDF and the true parameter value, i.e., $b_{\bar{x}} = \bar{x}^{\rm bestfit} - \bar{x}^{\rm true}$.

*We define $\sigma_{\rm avg}$ as the average of $\frac{\sigma_+ + \sigma_-}{2}$ over the 25 data realizations.

related to density estimation in each of the w_j bins.

To explore potential biases from the KDE, we compare the difference between the discrete PDF of the 4-D simulated data and the PDF constructed using the KDE. We first draw a simulation of $100,000$ samples from $\theta_{\rm ex2}^{\rm true}$ and $\psi_{\rm ex2}^{\rm true}$ and estimate the 4-D density in each of the w_j bins. We then draw a set of $50,000$ samples of "test data," also drawn from $\theta_{\rm ex2}^{\rm true}$ and $\psi_{\rm ex2}^{\rm true}$ and *without applying selection*. Figure 4.14 shows the 2-D marginalized densities in each of the w_j bins obtained from the discrete binning of the "test data" and evaluating the KDE estimate at each of the "test data" bin points. We note that no selection or PDF floor (Section 4.3.1) has been applied here; this is purely a comparison of the binned densities.

In each of the 2-D marginalized plots, we see that the estimated PDF is broader at the peak than the discrete PDF constructed by binning the "test data." We also observe that the estimated PDFs are steeper than their discrete counterparts. The estimated PDFs (top rows) appear slightly more rounded than their discrete counterparts (bottom rows), likely due to the KDE smoothing. These estimated PDFs are also more broadly peaked than the discrete distributions. We note the starkest difference between the edge bins on both extremes of the distribution; however, we expect these differences are not the primary source of bias as the bulk of the likelihood is evaluated using points in the middle three bins.

As another means of comparing the estimated and discrete densities, we plot the binned, 1-D marginalized PDFs of the $50,000$ sample "test data" set in Figure 4.15.[7] These 1-D distributions provide further confirmation of the observations made from Figure 4.14. In each of the w_j bins, the $w^{\rm true}$ distribution is markedly non-Gaussian. In the three central bins, the estimated PDFs have broader and shorter peaks than the discrete PDFs.

At this time, we are unable to make a definitive statement about the source of the parameter bias and cannot predict how the bias will materialize for each parameter in the

[7] Note that these densities are plotted with different bin sizes than those used in Figure 4.14.

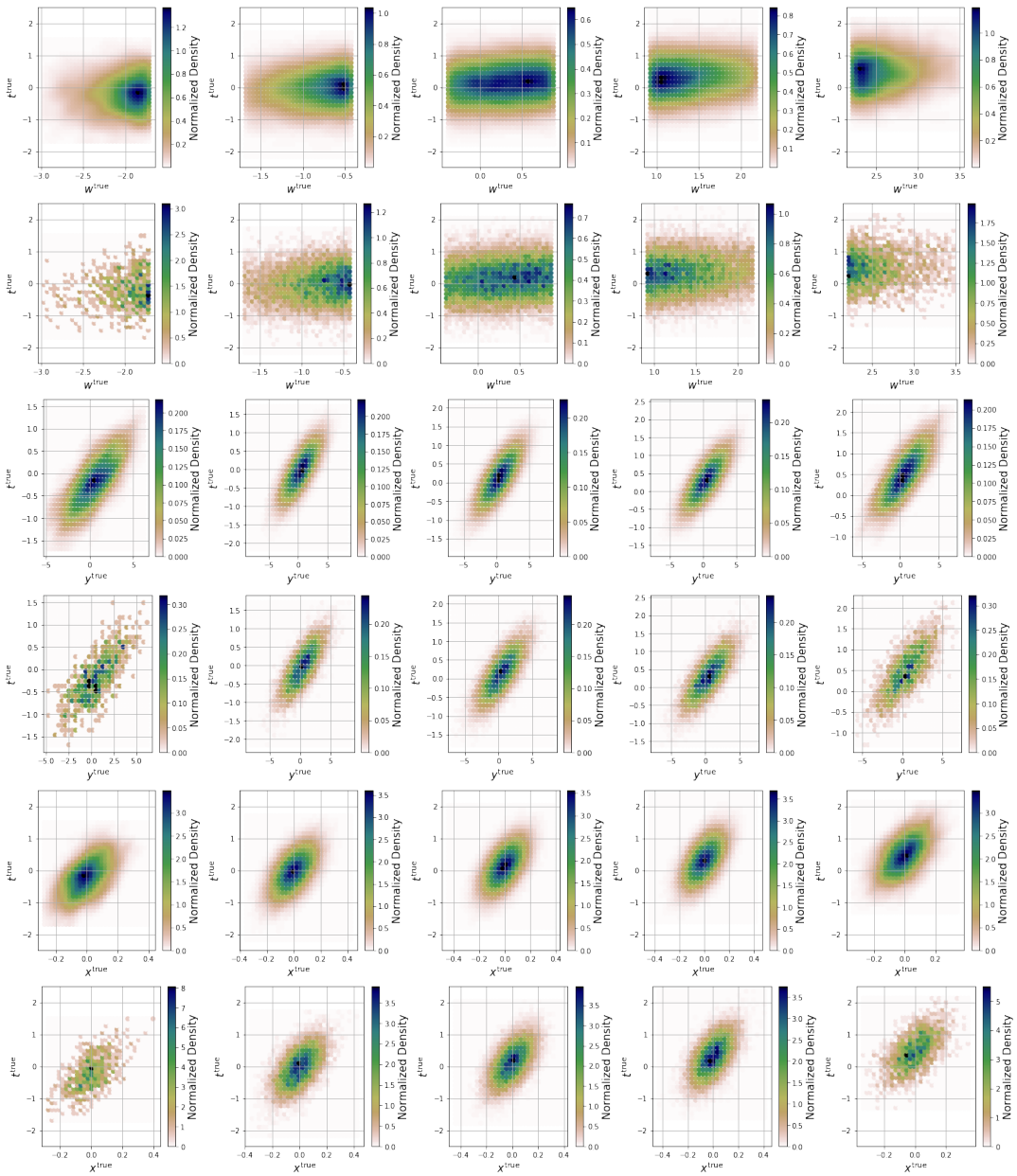

Figure 4.14: 2-D marginalized densities of the 4-D $\{w,x,y,t\}$ "test data" set in bins of w_j. w_j bins are plotted in ascending order from left to right. Each pair of rows compares the discrete PDF of the "test data" (bottom) to the density estimate from the KDE evaluated at the binned "test data" points (top) in each of the five w_j bins. Dark blue indicates the densest regions, light pink indicates regions of lowest density.

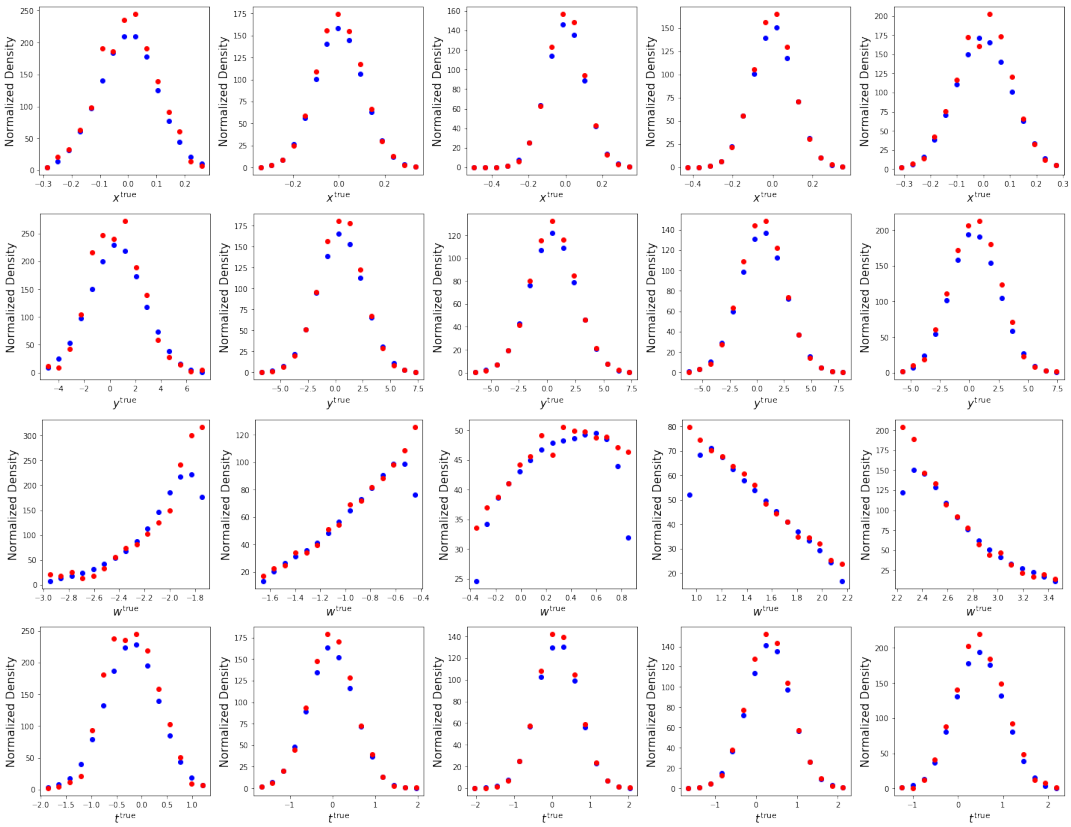

Figure 4.15: 1-D marginalized binned discrete (red) and estimated (blue) PDFs of the $50,000$ sample "test data" set in w_j bins. w_j bins are plotted in ascending order from left to right.

model. We remind the reader that PDFs presented in Figures 4.14 and 4.15 were constructed *without applying selection*. Therefore, we do not believe that including selection effects is causing the parameter bias. In fact, preliminary tests in which θ_{ex2} and ψ_{ex2} were inferred without applying selection (i.e., $f_j = 1, \forall j$), but by evaluating the likelihood in w_j bins, also produced parameter biases. We leave further exploration of these effects to future work.

4.5 SN Ia Cosmology with the SALT2 Regression Model

Here we apply BAMBIS to the specific problem of cosmological parameter estimation using SNe Ia. In the previous two sections, we demonstrated the capabilities of the BAMBIS algorithm using Gaussian linear regression models. When including selection in the model, we observe systematic parameter biases in the latent width hyperparameters. The source of this bias will be further explored in future work, and thus this section is included as an illustration of how a complex cosmological model may be integrated into the BAMBIS framework.

We present a simplified regression model, based on that of SALT2, and include selection effects in a manner which is similar to that presented in Section 4.4.2. Other systematics such as measurement uncertainty are not included in this demonstration, but are discussed in Section 4.6.

For the purpose of demonstration, we assume our data set is derived from a sample of spectroscopically-confirmed SNe Ia; we assume that in this survey, the supernova light-curve fluxes are being fit to the SALT2 model with these parameters: scaled light-curve amplitude (m_B^{obs}), stretch (x_1^{obs}), and color ($c^{\text{obs}} \simeq B - V$ at the epoch of peak brightness).

We use a BHM to describe the probabilistic relationships between these observed variables and the corresponding "true" variables. In our BHM, x_1^{true}, c^{true} and z^{true} are drawn from distributions determined by a set of hyperparameters, ψ. These variables, along with the set of model parameters, θ, are used to standardize each i SN Ia brightness

via the Tripp regression relation (Tripp, 1998; Phillips, 1993):

$$m_{Bi}^{\text{true}} = M + \Delta M_0 + \mu(z_i^{\text{true}}, \Omega_m, w, H_0) + \alpha \times x_{1i}^{\text{true}} + \beta \times c_i^{\text{true}} . \tag{4.29}$$

In this model, M is the rest-frame SN Ia absolute magnitude and m_{Bi}^{true} is the peak B-band magnitude scaled from the light-curve amplitude. The calculated distance modulus, μ, is a function of H_0, Ω_m, w, and each SN Ia redshift, z_i^{true}. ΔM_0 is a correction factor to the rest-frame SN Ia magnitude and α and β are global standardization parameters, where typically $\alpha < 0$ and $\beta > 0$. In this demonstration, we assume a flat wCDM cosmology model where the dark energy equation of state parameter, w, is constant in time, i.e., $w = w_0$. We hold $M = -19.36$ and $H_0 = 70$ km s^{-1} Mpc^{-1} fixed, as its value is fully degenerate with ΔM_0.

In addition to the cosmological parameters described in Eq. 4.29, our model contains a parameter giving an intrinsic Gaussian variance $\sigma^2_{\text{int}\,m_B}$ of the apparent magnitude at fixed (z_i, x_i, c_i). We include $\sigma^2_{\text{int}\,m_B}$ in the parameter set θ. As we are simulating a spectroscopically-confirmed sample, we assume no uncertainty on the SN Ia redshift (i.e., $z_i^{\text{obs}} = z_i^{\text{true}}$).

We define the full set of model parameters as

$$\theta \equiv [\Delta M_0, \alpha, \beta, \sigma^2_{\text{int}\,m_B}, \Omega_m, w_0] . \tag{4.30}$$

The set of hyperparameters, ψ, includes the SN Ia rate (R_z) and the parameters describing the distributions of x_1^{true} and c^{true}. The particular form of R_z used in this analysis is further detailed in Section 4.5.1. In this model, we assume x_1^{true} and c^{true} are drawn from skew normal distributions, each parameterized by variables location (ξ), scale (ω), and shape (ϕ):

$$p(x) = \frac{1}{\omega\pi} e^{-\frac{(x-\xi)^2}{2\omega^2}} \int_{-\infty}^{\phi\left(\frac{x-\xi}{\omega}\right)} e^{-\frac{t^2}{2}} dt , \tag{4.31}$$

where $\phi = 0$ corresponds to a Gaussian distribution. This is motivated by recent SN Ia population studies which suggest the light-curve parameter distributions, particularly the light-curve color, are best described by asymmetric Gaussian or skew normal distributions (Scolnic and Kessler, 2016; Kessler et al., 2013).

The mean, variance, and skewness of the skew normal distribution (subscripts m, v and s, respectively) are derived from the variables ξ, ω and ϕ, e.g., for the color distribution

$$c_m = \xi_c + \omega_c \delta_c \sqrt{\frac{2}{\pi}}, \tag{4.32}$$

$$c_v = \omega_c^2 \left(1 - \frac{2\delta_c^2}{\pi}\right), \tag{4.33}$$

$$c_s = \frac{4-\pi}{2} \frac{(\delta_c \sqrt{2/\pi})^3}{(1-2\delta_c^2/\pi)^{\frac{3}{2}}}, \tag{4.34}$$

where $\delta_c = \frac{\phi_c}{\sqrt{1+\phi_c^2}}$ and the subscript c indicates the parameters describing the color distribution. Corresponding parameterizations exist for the stretch distribution.

We define the set of hyperparameters defining the skew normal color and stretch distributions as

$$\psi_{\text{skewnorm}} \equiv [\xi_x, \omega_x, \phi_x, \xi_c, \omega_c, \phi_c], \tag{4.35}$$

the corresponding set of derived parameters as

$$\Psi_{\text{skewnorm}} \equiv [x_m, x_v, x_s, c_m, c_v, c_s], \tag{4.36}$$

and the full set of hyperparameters as

$$\psi \equiv [R_z, \psi_{\text{skewnorm}}]. \tag{4.37}$$

Figure 4.1 presents a graphical representation of this SN Ia model. Note that in addition to θ, ψ, and the random variables of interest, Figure 4.1 includes a variable S_i. This variable indicates whether or not a given SN Ia passes the survey selection criteria and is included in the final data set. As shown in the diagram, we assume this selection function depends on the redshift and apparent magnitude of the SNe Ia. Details of the selection function are described in Section 4.5.1.

The sample SN Ia cosmology BHM implemented here (Figure 4.1), while generating realistic light-curve fit parameter distributions, is not any more complex or sophisticated than existing analyses. In fact, unlike in Rubin et al. (2015) or Shariff et al. (2016), we

do not include any correlations with SN Ia host mass or allow for evolution of light-curve parameters with redshift. Nor do we separate the SN Ia color from host dust as in Mandel et al. (2016). Our model was chosen for demonstration purposes only and as a means to validate the method. Incorporating these model components is straightforward, and will be explored in future work. In this implementation, however, we do include SN Ia rate as a parameter in the model, which is ultimately marginalized over.

We define the posterior distribution describing the probability of the model parameters given the data for each i SN Ia as $p(\theta, \psi, \Psi | m_{Bi}^{\rm obs}, x_{1i}^{\rm obs}, c_i^{\rm obs}, z_i^{\rm obs})$; the corresponding likelihood is given by $p(m_{Bi}^{\rm obs}, x_{1i}^{\rm obs}, c_i^{\rm obs}, z_i^{\rm obs} | \theta, \psi, \Psi)$. As we are incorporating a two-stage selection process, we use the likelihood described in Eq. 4.26 and apply it to the specific SN Ia problem. In this case, we evaluate the likelihood in bins of $z^{\rm obs}$; therefore, we can fix the SN Ia rate as it is implicitly marginalized over in each redshift bin.

4.5.1 Sample Forward-Model Simulation and Mock Data

Our simulation bypasses the generation and analysis of light-curve data by directly generating simulated observations of the $\{m_B, z, x_1, c\}$ values assigned to each SN Ia. We assume a survey consisting of the union of two samples: a highly complete low-redshift sample (`S1`: $z^{\rm true} \leq 0.1$), and a high-redshift sample (`S2`: $0.05 \lesssim z^{\rm true} \lesssim 1.2$) modeled after the DES-SN.

Color and stretch distribution shapes, and the selection function for SNe Ia from `S1` and `S2`, are loosely based on 5,000 SNe Ia simulated in the conditions of the first DES-SN observing season, generated by the SuperNova ANAlysis package (`SNANA`; Kessler et al., 2009b) and its implementation of SALT2. Details of the DES-SN can be found in Kessler et al. (2015) and a description of the Dark Energy Camera (DECam) can be found in Flaugher et al. (2015). The DES-SN observes ten 3 deg^2 fields (eight "shallow" and two "deep"), roughly once per week, in the *griz* filters. The "shallow" fields are observed to an average depth of 23.5, while the "deep" fields are observed out to an average depth of 24.5 in each of the *griz* bands (Kessler et al., 2015).

In what follows we detail the procedure for simulating the observed redshift, color, stretch, and peak B-band magnitude distributions from θ and ψ. Most of the procedure is identical for `S1` and `S2` and performed for both populations. We assume the sizes of `S1` and `S2` are fixed such that `S1` is 10% the size of `S2`, i.e., the total number of SNe Ia in the population is 1.1 times the number of SNe Ia in `S2`. Variables drawn from the respective populations are denoted with the subscripts $S1$ and $S2$.

Step 1: Draw the redshift distribution.

`S1`: Draw $z_{S1}^{\text{true}} \sim \mathcal{U}(0, 0.1)$.

`S2`: Draw z_{S2}^{true} from

$$R_z = \frac{dN}{dz} = \begin{cases} 2.65 \times 10^{-5}(1+z)^{\gamma}, 0.05 \leq z \leq 1.0 \\ 7.35 \times 10^{-5}, z > 1.0 \end{cases}, \tag{4.38}$$

where the rate is given in units of SNe $\text{Mpc}^{-3}\text{h}_{70}^{3}\text{yr}^{-1}$. Here γ is a parameter typically between 1 and 3.[8]

Step 2: Draw x_1^{true} and c^{true} from Eqs. 4.31 - 4.34 using ψ.

Step 3: Draw m_B^{true} such that

$$m_{Bi}^{true} \sim \mathcal{N}(M + \Delta M_0 + \mu(z_i^{\text{true}}, \Omega_m, w_0, H_0) + \alpha \times x_{1i}^{\text{true}} + \beta \times c_i^{\text{true}}, \sigma^2_{\text{int}\, m_B}) \tag{4.39}$$

Step 4: Apply selection criteria to determine which SNe Ia will remain in the observed sample.

`S1`: We assume all of the low-redshift SNe Ia $(z \leq 0.1)$ pass selection cuts and so we do not apply any additional selection.

`S2`: A model for selection that mimics the assignment of scarce spectroscopic followup time is applied. As in Section 4.4.2, we assume the f_j brightest objects are selected in each redshift bin. The selection function utilized for this example is described in Table 4.8.

[8] The exact form of this rate was chosen via private communication with R. Kessler, but is roughly based on the SN Ia rate published in Perrett et al. (2012).

Table 4.8. Bins and selection fractions
for example SN Ia selection function

Lower Bin Value	f_j
$z^{\rm true} = 0.0$	1.0
$z^{\rm true} = 0.1$	0.95
$z^{\rm true} = 0.3$	0.9
$z^{\rm true} = 0.5$	0.8
$z^{\rm true} = 0.6$	0.7
$z^{\rm true} = 0.7$	0.6
$z^{\rm true} = 0.8$	0.3

Step 5: Compile the remaining observed variables that pass selection cuts, $m_B^{\rm obs}$, $x_1^{\rm obs}$, $c^{\rm obs}$, and $z^{\rm obs}$, from both `S1` and `S2` for a full-forward model of the data.

Following this procedure, we generate a mock data set of 667 spectroscopically-confirmed SNe Ia using the parameter values listed in Table 4.9, and denote this as `D3`. To generate a mock data set of this size, we draw an initial high-redshift population of 1,200 SNe Ia and a low-redshift population of 120 SNe Ia; roughly 50% of the population remain in the observed sample after selection. We remind the reader that our mock data set is derived using the same model used in the simulations for the purpose of method validation. We also note that we keep track of how many SNe Ia are simulated and how many are selected so we can evaluate the binomial factor in the likelihood (Eq. 4.26).

The true and observed 1-D marginalized distributions of `D3` are shown in Figure 4.16. As expected, the observed set of SNe Ia are bluer (more negative values of c) and brighter (more positive values of x_1) than the population. The mean color shifts from 0.003 (true) to -0.023 (observed) and the mean stretch shifts from -0.039 (true) to 0.089 (observed).

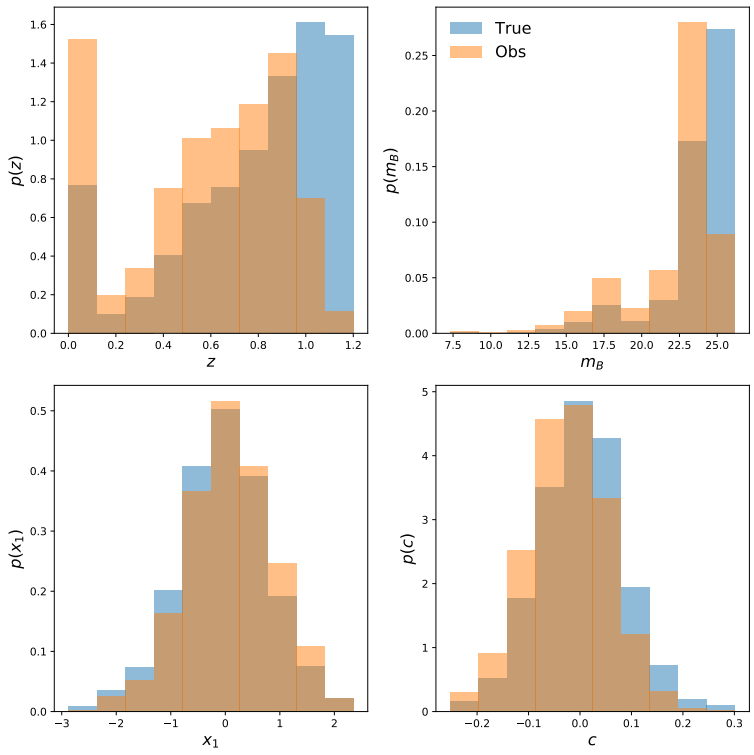

Figure 4.16: 1-D marginalized distributions of the true (blue) and observed (orange) SN Ia light-curve parameters and redshifts in D3. The selection function used to construct the observed sample is given in Table 4.8.

Table 4.9. Parameter Values for Mock Data

Parameter	Input Value
Ω_m	0.3
w_0	-1.0
γ	1.5
α	-0.14
β	3.2
ΔM_0	0.0
$\sigma_{\text{int}\,m_B}$	0.15
ξ_x	0.5
ξ_c	-0.05
ω_x	1.0
ω_c	0.1
ϕ_x	-1.0
ϕ_c	1.0

4.5.2 Results

As in Section 4.4.2.1, we adjust the `emcee` scale factor to $a = 1.2$ to ensure proper chain mixing near the peak of the posterior region. The simulation of 100,000 SNe Ia and evaluation of the log likelihood at each point proposed by the sampler takes ≈ 2s. We use 80 walkers, over 20 compute cores, and run the chains for ≈ 1.5 days. We find the MCMC chains take much longer to converge in this case, with typical autocorrelation times of $\tau \approx 80 - 100$ for the twelve parameters of interest. Convergence of the MCMC chain requires $\approx 250,000$ samples, including burn in.

Results using `D3` are presented in Figure 4.17 and Table 4.10. For this particular realization, we recover each of the parameters in θ and ψ_{skewnorm} within the 1σ uncertainty regions. Many of the recovered posteriors are roughly Gaussian, despite our use of wide uniform priors. Skewness of the color and stretch are particularly difficult to constrain; the c_s posterior is strongly non-Gaussian and skewed right. We recover $w_0 = -1.04^{+0.085}_{-0.080}$ and $\Omega_m = 0.303^{+0.024}_{-0.019}$. We remind the reader that as we are not including systematic

Table 4.10. Best Fit Parameter Estimates Using D3

Parameter	Prior	Input Value	Best Fit	σ_-	σ_+
w_0	$\mathcal{U}(-1.5,-0.6)$	-1.0	-1.04	0.08	0.085
Ω_m	$\mathcal{U}(0.1,0.6)$	0.3	0.303	0.024	0.019
${x_m}^*$	—	-0.064	-0.024	0.046	0.061
${x_v}^*$	—	0.682	0.642	0.049	0.056
${x_s}^*$	—	-0.137	-0.144	0.06	0.043
${c_m}^*$	—	0.006	0.009	0.006	0.005
${c_v}^*$	—	0.007	0.007	0.001	0.001
${c_s}^*$	—	0.137	0.088	0.081	0.112
ΔM_0	$\mathcal{U}(-0.1,0.1)$	0.0	-0.013	0.02	0.022
α	$\mathcal{U}(-0.25,-0.05)$	-0.14	-0.139	0.008	0.013
β	$\mathcal{U}(2,4)$	3.2	3.195	0.075	0.059
σ_{int}	$\mathcal{U}(0,0.25)$	0.15	0.156	0.007	0.006

*Note that priors are imposed on the hyperparameters and not the derived parameters presented here. We impose wide uniform priors on the width of the latent stretch and color distributions informed by the widths of the observed distributions: $\omega_x \sim \mathcal{U}(0, 2\sigma_{x_1^{\text{obs}}})$, $\omega_c \sim \mathcal{U}(0, 2\sigma_{c^{\text{obs}}})$.

uncertainties, errors on Ω_m and w_0 are idealized and should not be compared to previous measurements.

Given the observed parameter biases in Section 4.4.2, we expect to see parameter biases in the SN Ia cosmology model; how this bias will manifest, however, is unclear. We believe we must fully understand the source of bias presented in Section 4.4.2 before assessing biases in the cosmological model. Therefore, we present five realizations of the mock data as illustrative examples of cosmological parameter inference.

As we are primarily interested in cosmological parameter biases, w_0 and Ω_m contours inferred using each of the data realizations are displayed in Figure 4.18. We are able to recover both Ω_m and w_0 within their respective 1σ uncertainty regions in each of the re-

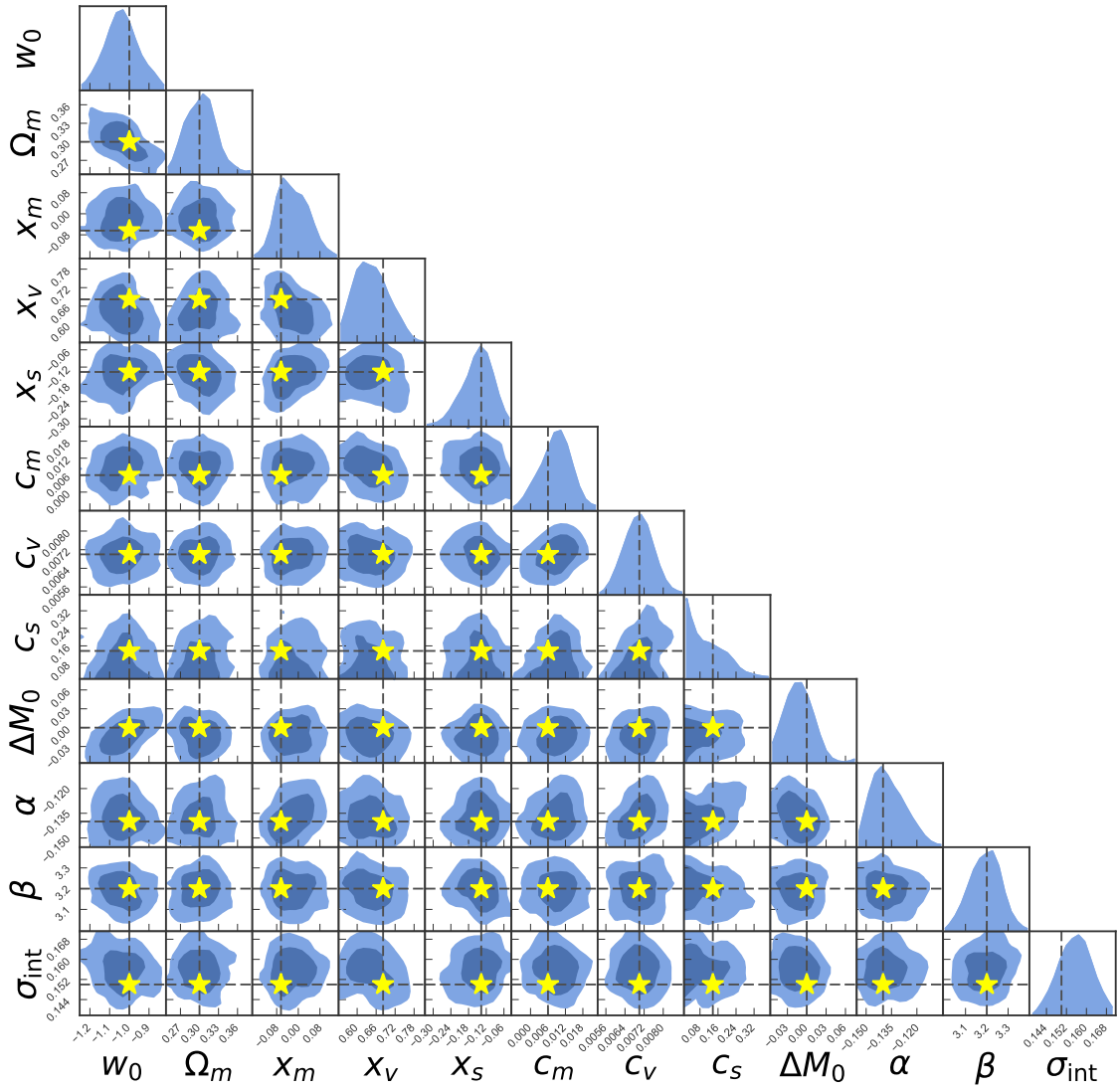

Figure 4.17: 1σ and 2σ uncertainty regions for the twelve parameters in θ and ψ_{skewnorm}. Yellow stars indicate the true values used in the simulation input. Priors and best fit results for each of the parameters are listed in Table 4.10.

alizations. However, it appears that the median of the 1-D marginalized w_0 posterior is systematically smaller than the true value and that the median of the 1-D marginalized Ω_m posterior is systematically larger than the true value. In a cursory analysis of the regression and hyperparameters, we find the skewness of the color and stretch distributions also appear to be systematically smaller than the truth, and that the intrinsic scatter is systematically larger than the truth. Of course, from these five realizations, we are unable to determine if these perceived biases are a manifestation of the bias exhibited in Section 4.4.2 or just random fluctuations from limited statistics.

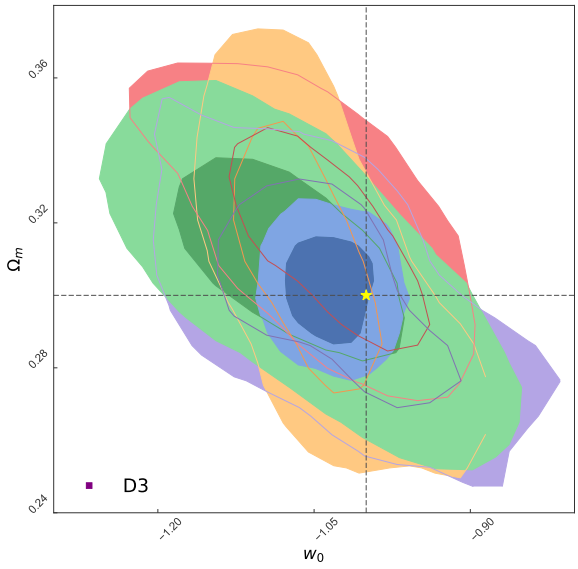

Figure 4.18: Contours of w_0 and Ω_m posteriors using five realizations of mock data. Filled contours represent 1σ and 2σ uncertainty regions; the yellow star indicates the true parameter values. Uncertainty regions inferred from `D3` are shown in purple.

4.5.3 Conclusions

Using a simple SN Ia regression model and a mock realization of 667 observed SNe Ia, we have shown that BAMBIS can recover the input simulation parameters within their 1σ uncertainties, where c_s and x_s are the most difficult parameters to constrain. As we

are aware of an inherent bias in the algorithm (demonstrated in Section 4.4.2), we only realize five sets of mock SN Ia data for illustrative purposes. In these realizations, there appears to be a systematic bias in w_0 in that the median of the inferred posterior is lower than the true value; a systematically larger values of Ω_m are also observed. However, we cannot assess the significance of these biases without further testing. As discussed in Section 4.4.2.2, we will investigate if such bias can be attributed to the non-parametric estimate of the PDF in each of the redshift bins in future work.

Despite potential parameter biases, we can utilize these simple simulations to compare the uncertainties on the inferred w_0 and Ω_m using the BAMBIS algorithm and a standard analytic χ^2 likelihood. We use a χ^2 based on the work of Kelly (2007) which models a BHM with Gaussian latent variable distributions:

$$\chi^2_i = \mathbf{D}_i^T V^{-1} \mathbf{D}_i \,, \tag{4.40}$$

where

$$\mathbf{D}_i = \begin{pmatrix} m_{Bi}^{\rm obs} - (M + \Delta M_0 + \mu(z_i) + \alpha x_m + \beta c_m) \\ x_{1i}^{\rm obs} - x_m \\ c_i^{\rm obs} - c_m \end{pmatrix} \tag{4.41}$$

and

$$V = \begin{pmatrix} \alpha^2 x_v + \beta^2 c_v + \sigma^2_{{\rm int}m_B} & \alpha x_v & \beta c_v \\ \alpha x_v & x_v & 0 \\ \beta c_v & 0 & c_v \end{pmatrix} . \tag{4.42}$$

We also assume a Gaussian likelihood such that

$$p(m_{Bi}^{\rm obs}, x_{1i}^{\rm obs}, c_i^{\rm obs} | \theta, \psi) = \frac{1}{2\pi |V|^{1/2}} \exp\left(-\frac{1}{2}\chi^2\right) . \tag{4.43}$$

Figure 4.19 shows the difference in the inferred w_0 and Ω_m posterior distributions between the two techniques using the `D3` data set. As we have not included any parameters in the analytic model to account for selection effects, we expect the posteriors obtained using this technique to be biased; therefore, we scale the posteriors in Figure 4.19 by their respective medians for better comparison. As shown in the figure, although BAMBIS includes a complex selection function, stochastic model, and non-parametric density estimates, it can more strongly constrain w_0 and Ω_m than this particular analytic approach.

The larger size of the uncertainty regions obtained using the analytic χ^2 is likely due to 1) the assumption of a Gaussian likelihood for the selected data and 2) the choice to model the latent distributions as Gaussians, which we know to be incorrect. This second point is particularly important, as the lack of explicit c_s and x_s model dependence is likely allowing too much freedom in the parameter sampling.

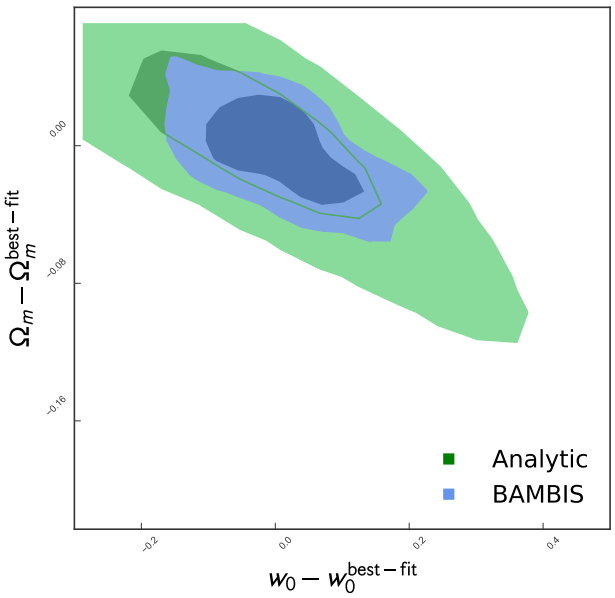

Figure 4.19: Comparison of w_0 and Ω_m posteriors inferred with BAMBIS (blue) and a standard analytic χ^2 used in a Gaussian likelihood (green). Contours represent 1σ and 2σ uncertainty regions; posteriors have been scaled by their respective median values.

While this comparison presents an interesting assessment of parameter uncertainties, it perhaps more clearly illuminates the dangers of incorrect analytic model and likelihood assumptions. Although the analytic χ^2 used in this example is not as sophisticated as those of other BHM analyses (Rubin et al., 2015; Shariff et al., 2016; Mandel et al., 2016), it illustrates how difficult it is to capture selection effects and non-Gaussian distributions in an analytic framework.

4.6 Summary and Future Work

In this chapter, we have introduced BAMBIS, a BHM likelihood and algorithm for cosmological parameter and SN Ia hyperparameter estimation. BAMBIS has two primary features that distinguish it from conventional BHM techniques: 1) the model is characterized by a sample of Monte-Carlo simulated SNe and 2) the likelihood of the observations under the model is evaluated using a non-parametric PDF produced by kernel density estimation of the simulation sample. These features allow us to incorporate correlations between observed variables and effects due to selection bias in a robust statistical framework. Using a non-parametric density estimate also allows us to avoid making incorrect assumptions about the analytic description of the model and the likelihood.

Using two toy examples, we demonstrated that BAMBIS can successfully recover the input simulation parameters. In the first simple Gaussian linear regression model, we generate 25 realizations of mock data and find that BAMBIS recovers all eleven model and hyperparameters within 0.43 times the 1σ uncertainty. When we include selection effects in the regression model, we find notable biases in the inferred σ_y (0.5σ), σ_x (1σ), and $\sigma_{\rm int}$ (0.8σ) over 25 realizations of the data. Determining the source of this bias requires further exploration of the non-parameteric density estimation, particularly when constructed in bins of an independent variable (i.e., redshift). This will be investigated in future work.

We also present results using a simplified SN Ia SALT2 regression model. Although we do not include systematics such as measurement uncertainty, we model a two-stage SN Ia survey with object detection and selection via a complex selection function. Using a mock data set of 667 low and high redshift SNe Ia, we recover w_0 and Ω_m within their respective 1σ uncertainty regions.. Our posterior distributions are roughly Gaussian, with c_s and x_s being the most difficult parameters to constrain. As with Toy Problem 2, we observe systematic biases in our recovered parameters; however, it is unclear if these biases are due to a feature of the algorithm or finite sample statistics.

To completely validate the BAMBIS algorithm, we need to explore BAMBIS' perfor-

mance when systematics, such as measurement and calibration uncertainties, are included in the model. We do not expect that including such effects will bias the algorithm results, as long as they are properly included in the forward-model simulations. A simple model including systematics could include building upon the model outlined in Section 4.5 by drawing a covariance matrix for each SN Ia from a Wishart distribution with scale matrix $\Sigma^2_{\rm meas}$ and three degrees of freedom, i.e.,

$$\mathcal{C}_i^{\rm obs} \sim \mathcal{W}(\Sigma^2_{\rm meas}, 3)\,. \tag{4.44}$$

However, rigorous treatment of survey-specific systematics would involve using a more sophisticated SN Ia simulation package such as `SNANA`.

Including such complex models raises concerns about MCMC run times and chain convergence. While the data simulation and likelihood evaluation in the examples shown in this chapter took $\approx 1-2$s per walker per MCMC proposal, it is likely that more complex models will require ≈ 30s - few minutes. This suggests that running BAMBIS using a more realistic SN Ia simulation package will require more computing time than was used in the demonstrations in this chapter. In each of the three demonstrations, no more than 20 compute cores were used for a given MCMC chain. We expect that parallelization on a much larger scale, perhaps $\sim 80-100$ cores, will be required to achieve realistic convergence times.

This computation issue could potentially be mitigated by using a more efficient sampling algorithm. As demonstrated throughout this chapter, using `emcee` required significant tuning in the cases which involved selection effects. We therefore intend to explore other sampling algorithms, including nested sampling and parallel-tempering ensemble sampling, which may improve the efficiency of chain convergence.

In addition to including experimental systematic uncertainties, within this framework there is also scope to expand the model in the likelihood to account for physical effects such as correlations with the host-galaxy mass, redshift evolution of color and stretch, and core-collapse contamination. As we enter the era of large-scale surveys, such as DES-SN and LSST, it is crucial to have analysis tools for sets of photometrically-classified SNe Ia.

Such samples will not only have biases from selection effects, but could potentially contain contamination from core-collapse (CC) SN. Analytic frameworks for cosmological parameter inference using photometrically-classified samples are in production and under development (e.g., Hlozek et al., 2012; Kunz et al., 2013; Kessler and Scolnic, 2017), but rely on many of the assumptions described in Chapter 2. While BAMBIS was designed for a set of spectroscopically-confirmed SNe Ia, its functionality could be extended to a photometric sample. For example, one could model the SNe Ia and CC SN as independent populations and fit for two distinct sets of model and hyperparameters. One could also include parameters of the photometric-classification software, i.e., Photometric SN IDentification (PSNID; Sako et al., 2011), in the model. Since BAMBIS relies on MC simulations of the data, we are not restricted by analytic descriptions of the model and can incorporate a wealth of options in the algorithm. However, before we incorporate more sophisticated elements in the algorithm, we must better understand any sources of parameter bias.

Chapter 5

Engaging the Public as a Scientist-Communicator

"Astronomy plays a special role within public science communication. It serves, most conspicuously, as a general science "catcher," not at least for young people. [...] Astronomy embraces core sciences such as mathematics, physics, chemistry, biology and geology, as well as technical disciplines including optics, observational techniques and data analysis. [...] To many people, however, rather than offering insights into the "mechanics" of nature, astronomy invites an emotional involvement in subjects like cosmology, the Solar System and the possibility of (finding) extraterrestrial life. In short, astronomy attracts a wide spectrum of people and may serve as a powerful vehicle for improving the public awareness and understanding of science." – Madsen and West (2003)

5.1 Introduction

The need for improved communication between scientists and the general public is recognized worldwide (Burns et al., 2003; National Research Council, 2010b). Life in the 21st century is motivated by advances in science and technology, and institutions ranging from

government agencies to scientific societies are calling for a transformation of the public perception of and appreciation for science. However, surveys suggest that the public does not know much about science, i.e. the scientific process and academic culture, and that scientists do not know much about the public (Miller, 1998; Lévy-Leblond, 1992). Furthermore, there is evidence for continued high levels of interest in science, but continuing low levels of accessible understanding of science (Miller, 2001). Such a paradox indicates that the relationship between science and the public will only improve if there are updated, innovative modes of communication.

For centuries, communication of science was almost exclusively reserved for intradisciplinary exchange (Madsen and West, 2003). As a result, knowledge of scientific progress and breakthroughs was confined to the sphere of professional scientists. While this remains a primary means of communication for many scientists, the research community is experiencing a shift from the "ivory tower" paradigm (Madsen and West, 2003). Scientists are now interacting with the public, and within their own communities, as public lecturers, in print and visual media, and through new avenues such as social media and science cafes. In this chapter, I summarize 1) why astronomy is an excellent subject for science communication; 2) reasons for scientists to participate in public engagement; 3) professional astronomers' opinions about science education and public outreach.

5.2 Astronomy: A Science to Captivate an Audience

Astronomy is one of the most popular sciences used to spur public interest (Heck and Madsen, 2013). Astronomical data often consist of spectacular images that can be both scientifically explained and admired for their beauty. Simulations of complex astrophysical systems can be used not only as scientific tools but as a dazzling displays of the power of modern computing. Questions such as "Are we alone in the Universe?" and "How did the Universe begin?" challenge imagination and moral philosophy. Unlike many other sciences, explaining fundamental astronomy concepts does not necessarily rely on under-

standing of complex mathematics or technical terminology. From countless perspectives, astronomy captures an audience.

Topics in astronomy translate well to a diverse array of education and public outreach (EPO) programming initiatives. For example, planetarium shows provide an immersive glimpse into the wonders of the night sky. Citizen science projects such as Galaxy Zoo[9] invite scientific collaboration between scientists and the public and demonstrate the importance of data science and computing. Written communication in popular magazines, websites, and blogs can be complemented by images and infographics and used to narrate stories of discovery. Public radio shows and podcasts can be used to communicate astronomy news, history, and notable astronomy events, such as eclipses and meteor showers, to a vast audience. Larger organized events such as science festivals, museum events, and star parties are venues where astronomers and the public can engage more personally and as a result, make impactful connections. On both smaller and grander scales, there is ample opportunity for astronomers to share their expertise and experience with the public.

5.3 Why Engage in Astronomy EPO?

Although measuring the success and impact of astronomy EPO programming is difficult, there are countless reasons to participate in astronomy EPO. According to the National Research Council, astronomers' most important contribution to society lies in the area of science education (National Research Council, 2001). This includes raising public awareness of science, translating science concepts to students and teachers, and contributing to educating a technically and technologically capable citizenry. In addition to the societal benefits of astronomy engagement, it can also be personally gratifying, and lead to new meaningful mentoring or collaborative networks and partnerships.

There is substantial statistical evidence that the public is interested in astronomy programming (National Research Council, 2001). There are approximately 1,100 planetaria

[9] `https://www.galaxyzoo.org/`

in North America, visited by nearly 28 million people yearly. Collectively, the Southwestern Consortium of Observatories attracts 500,000 visitors yearly, with the Visitor Center at Arecibo in Puerto Rico hosting an average of 120,000 people. Hundreds of thousands of people subscribe to magazines such as *Sky and Telescope* and *Astronomy* and radio shows such as "Stardate/Universo" have been reported to reach millions of listeners weekly. Astronomy-related websites and social media accounts are also incredibly popular, with the Hubble Space Telescope[10] and NASA[11] Twitter accounts having 2.4 million and 22 million followers, respectively.

Engaging the public is also critical for securing funding and updating policy for federally-sponsored astronomy programs. In the United States, taxpayer dollars allocated to agencies such as the National Science Foundation, the Department of Energy, and NASA provide most of the federal funding of astronomical research, with NASA contributing more than 85% of federal research grants.[12] Scientific societies such as The American Association for the Advancement of Science (AAAS) have recognized that scientists can and should play a significant role in securing research funding and are encouraging public engagement through public policy training and fellowships.

In addition to having societal benefits, engaging in science EPO furthers scientists' professional development. Translating technical aspects of research for both written and oral public engagement improves scientists' ability to communicate their work to their colleagues at conferences, in lectures, and in academic journals. In fact, studies have shown that scientists who participate in public engagement are more active academically (Jensen et al., 2008; Bauer et al., 2011). Participation in EPO also provides a unique opportunity to build a professional network outside the niche research environment and can lead to interdisciplinary scientific collaboration and better relationships with departmental colleagues.

[10] `https://twitter.com/NASA_Hubble`

[11] `https://twitter.com/NASA`

[12] `https://www.aaas.org/fy16budget/astronomy-and-astrophysics`

5.4 Astronomers' Attitudes Towards Education & Public Outreach

Generally, professional scientists are in favor of EPO (Ecklund et al., 2012; Andrews et al., 2005; Poliakoff and Webb, 2007). However, results from several studies find significant cultural and institutional barriers against public engagement (Thorley, 2016). Common concerns focus on reputation and academic career, with many early career scientists worried that EPO activity will be seen as superfluous by their advisors (Ecklund et al., 2012). There is also a wider perception that scientists who devote time to EPO spend less time and are less rigorous when conducting research (Jensen et al., 2008). The most significant reported barrier is time, as time spent on EPO is often viewed as time that should otherwise be spent on research (Thorley, 2016; Poliakoff and Webb, 2007).

Specific EPO attitudes and experience of professional astronomers is an emerging topic of study (Dang and Russo, 2015; Thorley, 2016). Although there are many studies in the literature regarding amateur astronomer's attitudes towards EPO and their effectiveness as science communicators (e.g. Gibbs and Berendsen, 2006; Berendsen et al., 2008; Sakimoto, 2008; Yocco et al., 2012), there are few analyses exploring the opinions and motivations of professional astronomers. Much astronomy EPO is organized and implemented by amateurs and EPO professionals rather than professional scientists (Raddick, 2008), and there are few public recordings of astronomers' individual efforts. Furthermore, large-scale EPO projects organized and implemented by professional researchers (e.g. graduate students, postdoctoral researchers, tenured faculty) are scarce.

In the first global study of astronomer's views on EPO, Dang and Russo (2015) analyzed survey responses from 155 professional astronomers at the 2012 International Astronomical Union General Assembly. In addition to the development of personal interest in astronomy, their survey explored views on participation, time constraints, and budget restrictions of EPO. Overall, 79% of respondents expressed belief that EPO initiatives are essential; 19% claimed they are important.

Figure 5.1 shows the distribution of work hours (blue) and free-time hours (yellow) respondents indicated they dedicate to EPO. Analysis of the data revealed no significant difference between the amount of free time and work time allocated for EPO activities. Furthermore, using a Spearman's rho correlation test, it was determined that astronomers who devote more work time to EPO activities also dedicate more free time to EPO ($\rho = 0.46, p < 0.05$).

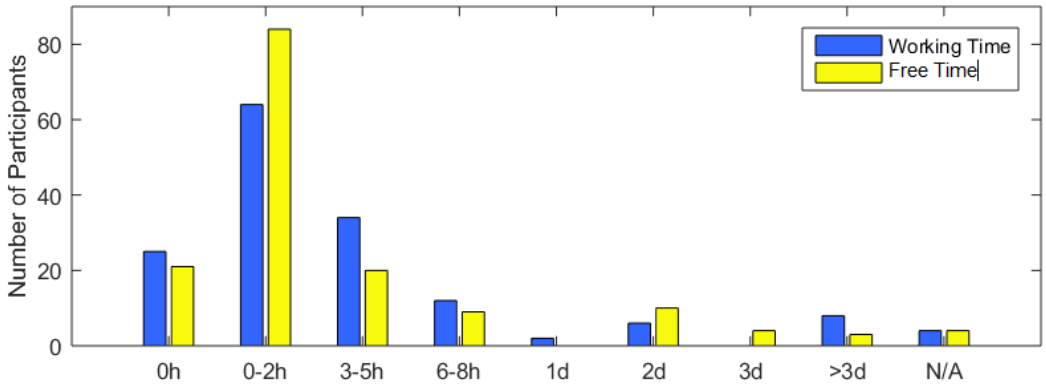

Figure 5.1: Number of working (blue) and free time (yellow) hours spent on average on EPO activities per week, reproduced from Dang and Russo (2015).

The survey also asked respondents about grant funding, specifically how much is allocated for EPO. Survey responses are summarized in Figure 5.2. Among those who responded to the particular question, 43% ($n = 116$) reported that 0% of their grant funds are used towards EPO. However, when asked how much of their grant funding *should* be allocated to EPO, however, astronomers reported that they believed 5-10% of research grants should be directed toward EPO programming on average. In general, astronomers reported that a higher portion of their grant funding should be allocated toward EPO, perhaps providing evidence for a change in grant policies and distribution.

Dang and Russo (2015) conclude that most astronomers have a positive attitude towards outreach. Astronomers sharing this view in positions of authority (e.g. mentors and supervisors) also tend to encourage their students to pursue EPO activities. However,

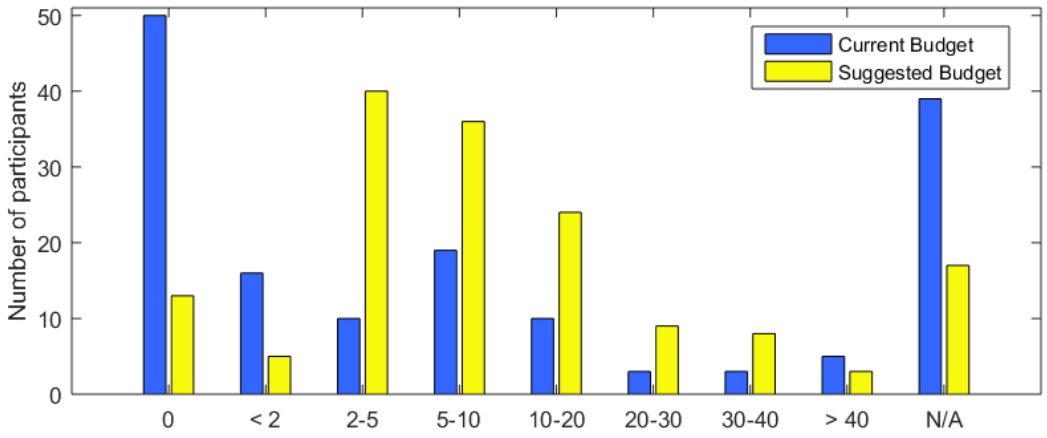

Figure 5.2: Percentage of research grants astronomers currently invest (blue) and suggest to allocate (yellow) into public outreach engagement, reproduced from Dang and Russo (2015).

motivating and inhibiting factors remain unclear. It is likely that these factors are dependent on the nature of the EPO project and that they are significantly affected by the EPO culture at a particular institution or within a particular project.

5.5 Summary

Astronomy is an exemplary field for science education and public outreach, as it naturally attracts and inspires scientific curiosity. Yet though there is clear public interest in astronomy, there remains a disconnect between the practicing scientists and general public. Despite the general support of EPO and many opportunities to be involved in EPO programming, astronomers' participation is often limited due to time constraints and institutional stigma. Exploring astronomers' involvement in EPO is an emerging field of study, and astronomy EPO programming will only improve upon critical analysis and reflection of the experiences of scientist-communicators.

Chapter 6

Education & Public Outreach in The Dark Energy Survey

6.1 Introduction

The landscape of professional astronomy has dramatically transformed over the past fifty years. While the field was once dominated by individuals or small, co-located teams (e.g., a professor and a graduate student), advances in technology have revolutionized the ways in which science is practiced and communicated (National Research Council, 2010b). International collaborations have emerged as the new standard, bringing about new research, administrative, and sociological opportunities and challenges. The primary charge of these large-scale astronomy surveys is to use evidence-based research to answer fundamental questions about our Universe. The drive to solve mysteries like the nature of dark matter and dark energy drive project commissioning, instrument development, project implementation, data products, and analysis (National Research Council, 2010b). Collaboration on such a large scale requires cooperation and respect amongst scientists from a diverse group of ages, genders, and cultures. In addition to the potential for groundbreaking science, this next generation of astronomy surveys also comes with a wealth of innovative material and experience that can be used to inspire and engage with

public interest in science (Borne et al., 2009).

Education and Public Outreach (EPO) programming has been a cornerstone of nationally sponsored agencies such as the National Aeronautics and Space Administration (NASA) in the USA for decades. The NASA Office of Education is dedicated to designing hands-on activities, creating teacher resources, developing opportunities for students, and inspiring students to pursue careers in the STEM disciplines (Rosendhal et al., 2004). Similarly, the multi-national European Space Agency (ESA) has a well developed and actively maintained EPO presence.[13] The NASA and ESA EPO efforts would not be possible without an agreed strategy, support from dedicated, well-trained staff, and an appropriate funding stream.

In the past ten years, many large-scale astronomy programs have devoted resources to EPO programming. For example, the Hubble Space Telescope (HST) and Sloan Digital Sky Survey created their own EPO initiatives (Griffin, 2003; Raddick, 2002), including Hubblesite[14] and SDSS Voyages[15], which encourage users to explore publicly available astronomy images, and data products, through a variety of online lesson plans and hands-on activities. In addition to more conventional avenues of astronomy EPO such as public lectures, science festivals, and planetarium shows, several innovative avenues for connecting science, and scientists, with the public have emerged. For example, *citizen science*, in which expert scientists collaborate with members of the public to complete a science project, is growing in popularity year-on-year (Borne et al., 2009; Haywood and Besley, 2014).

The importance of EPO activities to modern astronomy is demonstrated by the fact that several projects that are still in the development stage are already investing resources into public engagement. For example, the website for the James Webb Space Telescope (JWST, set to launch in 2018), already includes detailed EPO materials designed for K-12

[13] `http://www.esa.int/Education/ESA_at_the_forefront_of_space_education`

[14] `http://hubblesite.org/`

[15] `http://voyages.sdss.org/`

formal and informal education.[16] The Large Synoptic Survey Telescope (LSST), which will not begin taking data until the end of the decade, describes its EPO program as "as ambitious as the telescope itself."[17] The LSST EPO program includes plans for citizen science partnerships with The Zooniverse[18], and data visualization projects with several planetaria. Finally, The Wide-Field Infrared Survey Telescope (WFIRST, set to launch in the mid 2020's) outlines the internal organizational structure of the project and includes EPO as an element of its Science Operations Center.[19]

As the examples above demonstrate, EPO programming is now being put at forefront of collaboration structure well before any data have been taken. However, in the case of the Dark Energy Survey (DES, founded in 2004), EPO was not embedded during the development stage and had to be "shoehorned in" after survey operations were underway. The DES EPO program evolved from the grass-roots efforts of a small number of collaboration members who are passionate about science communication and outreach. This "bottom-up" approach has been positive in that it has resulted in a variety of innovative EPO projects. However, there have also been some unforeseen pitfalls and barriers. As such, our EPO experience in DES provides a unique perspective that can be used to inspire (and/or caution) teams developing EPO programs for the next generation of large astronomy projects.

In Section 6.2 we outline the internal structure of DES, specifically highlighting the benefits and challenges of including EPO within the official collaboration structure. In Section 6.3, we describe several of our EPO projects, including project goals, organization details, and project outputs. For each, we propose recommendations for similar future projects. Relevant DES project links are listed in Table 6.1 and references to this table are denoted in the text by an asterisk. Section 6.4 summarizes our strategy for internal EPO recording and describes scientists' reported methods of science communication. Finally,

[16] https://jwst.nasa.gov/teachers.html

[17] https://www.lsst.org/about/epo

[18] https://www.zooniverse.org/

[19] https://wfirst.gsfc.nasa.gov/science/

Table 6.1. List of Online DES EPO Resources

Web Address	Summary
http://www.darkenergysurvey.org	DES Website
http://www.darkenergysurvey.org/news-and-results/darchives/	DES DArchive Homepage
https://darkenergydetectives.org/	DES Dark Energy Detectives
http://www.darkenergysurvey.org/education/darkbites/	DES DarkBites Homepage
http://www.darkenergysurvey.org/education/scientist-of-the-week/	DES DEScientist of the Week Homepage
https://www.flickr.com/photos/129954880@N03	DES Flickr
https://www.youtube.com/channel/UCkAD7Un4aX-Y2ETTs_mImQ	DES YouTube Channel
https://www.facebook.com/darkenergysurvey/	DES Facebook Page
https://twitter.com/theDESurvey	DES Twitter Page

we conclude with a summary of the DES EPO experience in Section 6.5.

6.2 Survey Overview, Collaboration Structure, and the Evolution of the DES EPO Program

In this section we outline the underlying DES science (Section 6.2.1), describe how the grass-roots EPO effort was integrated into the larger, pre-existing collaboration structure (Section 6.2.2), and summarize how the dedication of a few scientists ultimately matured into an active DES EPO community (Section 6.2.3). We also outline the guiding principles driving the DES EPO effort (Section 6.2.4). Finally, we describe the DES social media strategy, as social media has been a primary vehicle for EPO product distribution (Section 6.2.5).

6.2.1 DES Project and Science

In the late 1990s, two teams of astronomers made the unexpected discovery that the Universe is expanding at an accelerating rate (Riess et al., 1998; Perlmutter et al., 1999). The mysterious agent of this acceleration, which acts against gravity's attractive force, has been named 'dark energy.' Understanding the nature of dark energy has become one of the greatest unsolved problems in modern cosmology (Hinshaw et al., 2013; Planck Collaboration et al., 2016). The goal of the international DES collaboration is to study this accelerating expansion with unprecedented precision and accuracy.

DES is surveying 5000 deg^2 of the southern sky, using the Dark Energy Camera (Flaugher et al., 2015, DECam) mounted on the 4-*m* Victor M. Blanco telescope at the Cerro-Tololo Inter-American Observatory. DES is scheduled to take data for five years (2013-2018), observing each year from August-February. Although much of the observing is computer-automated, DES collaboration members travel to the telescope site during the DES season to help take data. Once DES data is collected, the DES Data Management team stores and processes the data, preparing it for DES scientists all over the world to analyze. DES traces its origins as a project concept back to at least 2004. However, the first DES images were not taken until September 2012.

One of the unique strengths of DES is that it employs four complementary techniques to study the effects of dark energy, through observations of: Type Ia supernovae; gravitational lensing; galaxy clusters; and baryon acoustic oscillations. During the course of the survey, DES will observe thousands of supernovae, map millions of galaxies, and measure the growth of large-scale structure of our universe (The Dark Energy Survey Collaboration, 2005).

In addition to studying fundamental cosmological probes, DES makes important contributions to astronomy. DES scientists study the outer reaches of our solar system, finding new candidates for dwarf planets (Gerdes et al., 2017) and other trans-Neptunian objects. They identify galactic neighbors to our Milky Way (Li et al., 2016). They search for optical counterparts to newly discovered gravitational waves (Abbott et al., 2016).

DES is a collaboration of over 400 scientists from 25 institutions in seven countries around the world (a map of DES institutions is shown in Figure 6.1). University faculty and researchers, laboratory and observatory staff scientists, postdoctoral researchers, graduate students, and undergraduates are all working to answer unanswered questions about our Universe. The support staff, at the telescope and at DES institutions, enable DES scientists to travel for observing and to gather to discuss latest results at conferences at collaboration meetings. Together, members of the DES collaboration are at the cutting-edge of science and forging a new frontier for large-scale astronomy.

The various aspects of the survey highlighted in this Section are summarized in Figure 6.2. The DES EPO program draws inspiration from each of these components to design innovative EPO programming without necessary relying on published data products. Examples included in the Figure represent only a subset of the material available for EPO programming.

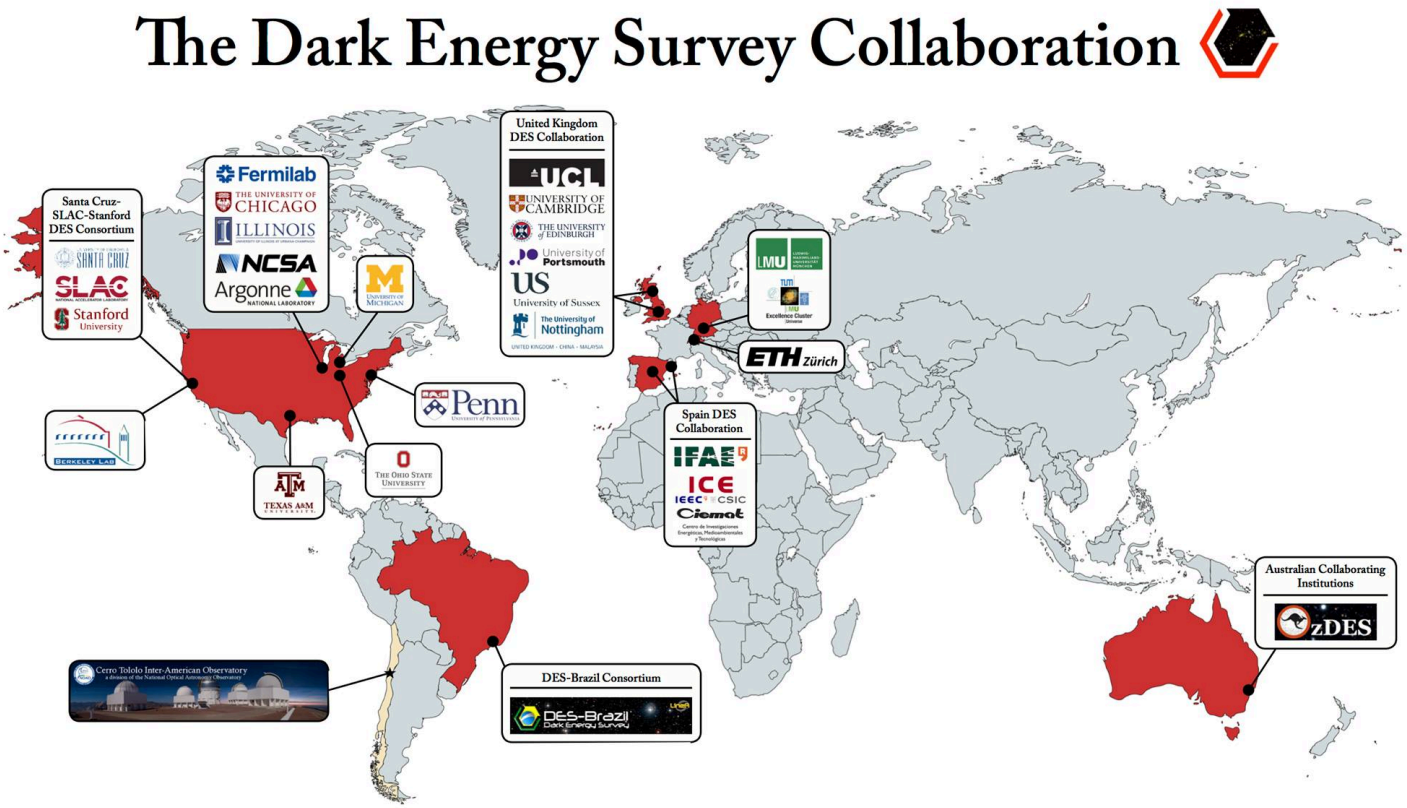

Figure 6.1: Map of DES collaborating institutions. Figure credit: Judit Prat, IFAE, DES-Spain.

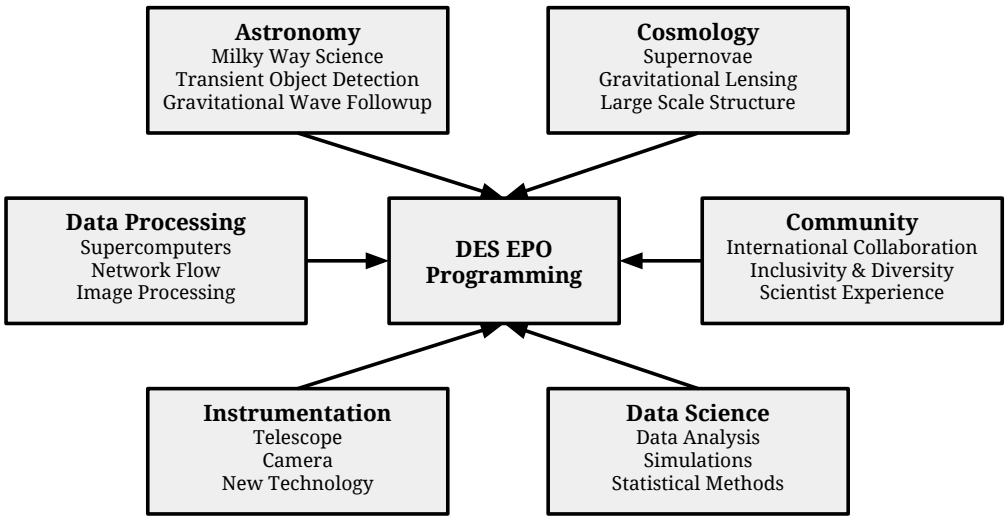

Figure 6.2: Schematic diagram illustrating various components of DES which provide inspiration for the EPO effort. Examples included here are merely a subset.

6.2.2 Organization and Management

The three signatory institutions of DES are the Fermi National Accelerator Laboratory (hereafter Fermilab), National Center for Supercomputing Applications (hereafter NCSA), and the National Optical Astronomy Observatory (hereafter NOAO). Support for DES is provided by grants from these respective institutions, primarily from the U.S. Department of Energy and the National Science Foundation. Members of the DES *Project Office* report directly to these agencies.

DES Scientists are categorized into *members*, *participants*, and *external collaborators*.[20] DES members are senior scientists, including faculty (tenured and tenure-track) and senior research associates, at official DES collaborating institutions. Participants are typically current postdoctoral researchers and graduates students of DES members. Members and participants have access to DES data and data products. External collaborators

[20]DES membership policies and infrastructure tasks are described in: `http://www.darkenergysurvey.org/wp-content/uploads/2016/05/membership_policy_revised-Dec-2011.pdf`

are senior scientists at non-DES institutions who provide resources that are otherwise unavailable to the collaboration, e.g., access to private telescopes. Participants can gain permanent access to DES data by working on DES infrastructure. Infrastructure activities include work on DES instrumentation, pipeline development, data calibration, and management activities. After one year of Full Time Equivalent (FTE) infrastructure work, participants can apply for data rights; after 2 FTE, participants can apply for Builder status, which includes data rights and optional authorship on DES papers. Throughout this work, we will refer to our DES colleagues as "collaboration members." This includes full DES members, participants, and external collaborators.

The internal organization of DES is divided into three main components: collaboration affairs, science, and operations. Collaboration affairs are overseen by the *Management Committee*, who are responsible for making collaboration-wide decisions including membership and publication policy. The *Science Committee* is responsible for managing the DES scientific program and ensuring all science requirements are met. Telescope operations, data management, and science releases are overseen by the *Executive Committee*. Each of these three committees is further subdivided into a variety of smaller groups, e.g., the Science Committee is comprised of science working groups and the Management Committee oversees the Publications Board (who review DES publications and enforce DES publication policy) and Speakers' Bureau (who recruit DES members to speak at conferences on behalf of the collaboration). Each subcommittee is governed by official protocol that dictates how collaboration members should work both within the respective committee, and with the collaboration as a whole.[21]

The DES EPO Committee (EPOC) became a part of the official DES organizational structure in the Fall of 2014 and was placed under the umbrella of collaboration affairs (for details regarding the creation and development of the EPO Committee, see Section 6.2.3). Prior to that time, DES did not have a centralized EPO effort nor official recognition of

[21] Further detail on DES policies and organization can be found in the DES Memorandum of Understanding: `https://www.darkenergysurvey.org/wp-content/uploads/2016/05/DES_MOU_as_executed.pdf`

EPO on a collaboration-wide scale. As such, once the EPOC formed, there were no policies in place for how the EPOC and its programming should interact and coordinate with the rest of the collaboration. For example, the EPOC is not invited to Management Committee meetings, although other committees responsible for collaboration affairs are included. A summary of the current DES organizational structure, including the EPOC, is presented in Figure 6.3.

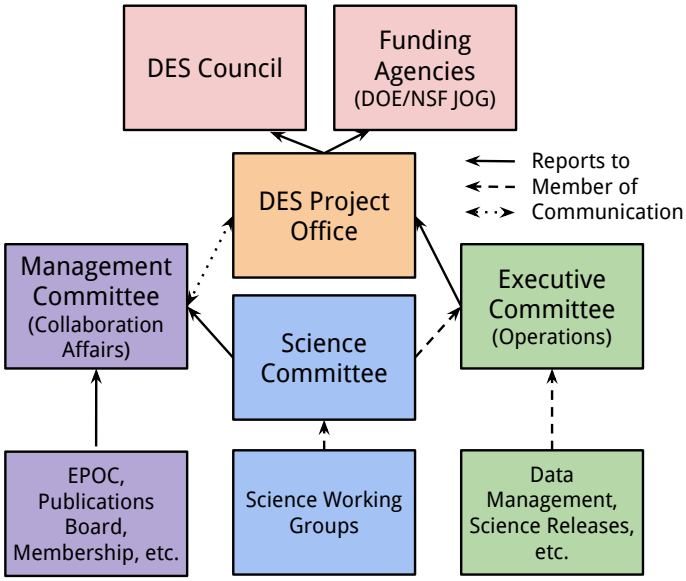

Figure 6.3: DES internal organization chart, including the EPOC (purple), adapted from the DES director's presentation at the Fall 2016 collaboration meeting. Solid arrows indicate a group that reports to and/or is appointed by the box to which it points. Dashed arrows indicate that the people named in that group are members of the higher-level Committee to which that box points (e.g., science working group coordinators are members of the Science Committee, and the Science Committee co-chairs are members of the Executive Committee). Dotted two-way arrows indicates a line of mutual communication.

The roles and responsibilities of the EPOC have evolved organically since its inception. As the sole organizers of EPO for the collaboration, the EPOC oversees and contributes to: updating and maintenance of the DES website, DES social media, creation of informal and formal educational materials, DES events with local communities (e.g.

museum events and science fairs), internal EPO reporting, public relations[22], and much more. The centralized DES EPO program has a limited, floating budget per the discretion of the DES director, which is jointly funded by the DES collaborating institutions. Details of how these funds have been allocated thus far are discussed in Section 6.3.

6.2.3 The Evolution of EPOC

Prior to the Fall 2014 collaboration meeting at the University of Sussex, no sessions dedicated to EPO had been scheduled by the scientific organizing committee (SOC). Kathy Romer (a faculty member at Sussex) was the chair of the Sussex SOC and decided to arrange two EPO sessions. This was done in consultation with Brian Nord (a postdoctoral researcher at Fermilab), who had been, by then, running – single handedly – a DES EPO initiative known as *The Dark Energy Detectives* blog.* Nord was not able to attend, because he was observing in Chile at the time, but recommended that Romer speak to Rachel Wolf (a graduate student at the University of Pennsylvania) about enhancing DES's social media presence (Romer's EPO focus to that date had been on working with school groups). And so began a grass-root effort to inspire coordinated EPO initiatives within DES. By the end of the Sussex collaboration meeting, Romer and Nord were asked by the DES director to lead an official EPO committee (the EPOC) for DES. They agreed to do so on the condition that Wolf was also included. Nord, Romer and Wolf (NRW hereafter) thus officially became the coordinators of the EPOC.

To discuss the organization and implementation necessary to get DES EPO off the ground, NRW established weekly (EPOC coordinator) telecons. NRW also created an internal DES EPO email listserv to communicate about EPO projects and opportunities with colleagues.

During the first year of the EPOC, most programming was organized and executed by NRW. Much of the effort was focused on updating, enhancing and maintaining the

[22]Note that this is distinct from official press releases which are organized through the Fermilab press office.

DES online presence. At the following semi-annual collaboration meeting (Spring 2015), NRW organized several EPO-specific sessions to present the work carried out so far, to receive feedback, and to generate new ideas. There were no shortage of new ideas and it became clear that more colleagues would need to be recruited to keep up with demand. Fortunately several DES members were eager to contribute, and even to lead, certain EPO projects, especially those that appealed to their particular interests (e.g. writing, artwork, or astrophotography). In addition to the weekly NRW coordinator meetings, monthly EPOC telecons were established to discuss the progress of the various projects. One of those projects is internal communication and has resulted in a monthly DES-EPO newsletter that is sent electronically to every registered scientist in the DES membership database.

6.2.4 DES EPO Guiding Principles

DES EPO efforts have been limited not by a lack of creative ideas, but by the lack of time that EPOC members could contribute, in addition to their regular duties (and to a lesser extent, the lack of a dedicated funding stream). Therefore, several underlying principles were established to help govern the distribution of resources (see below). However, we note that, in practice, the only DES Projects that actually took off were those that appealed to our colleagues' particular interests.

- GP1: Education and Public Outreach (EPO) is an important, worthwhile and enjoyable activity for individual scientists.
- GP2: EPO is an important and worthwhile activity for science collaborations (especially those that benefit from public funding).
- GP3: The public are interested in scientists as well as the science.
- GP4: It is possible to challenge the public's perception of scientists (as "old white males") through EPO.

- GP5: DES should have a strong social media presence.
- GP6: DES should have a professional website with high quality embedded content and resources.
- GP7: DES EPO should not be restricted to the English language.
- GP8: The EPO Committee (EPOC) will be able to motivate the broader DES membership to take part in EPO.
- GP9: The EPOC will manage, organize, and connect all DES EPO efforts.

These tenets laid the foundation for more than two years of DES EPO programming. They also informed interactions between the EPOC and other groups within the DES organizational structure. While the DES EPO program at large was motivated by GP1 and GP2, specific initiatives had more targeted goals. In Section 6.3, we detail specific projects and how, where relevant, these principles contributed to project development. We stress that these guiding principles stemmed from the previous experience of EPO by NRW, rather than being informed by the literature in the science communication field. In hindsight, it is clear that the EPOC would have benefited from some external guidance before launching into project work (see Section 6.5).

6.2.5 DES Social Media Strategy and User Summary

Social media has been one of the main vehicles for distribution of DES EPO content. The DES Facebook* account was created in November 2010; the Twitter account* followed in October 2013. Prior to the creation of the EPOC, social media posts were sparse, with updates roughly once per month. When the EPOC formed in October 2014, we decided to centralize the social media effort and make regular posts a priority (GP3, GP5 GP9). For this reason, most of the DES EPO projects have been driven by the need for a regular steam of social media content. Since early 2015, there have typically been Facebook (and

mirrored Twitter) posts at least five times per week: DEST4TD (Section 6.3.3) on Mondays, Tuesdays, and Thursdays, DarkBites (Section 6.3.4) on Wednesdays, DEScientist of the Week (Section 6.3.5) on Fridays, and MLDES (Section 6.3.6) on Sundays. We note that we opted to post content manually per platform, rather than use a social media management dashboard.

Since Fall 2014, the number of Facebook page "likes" has increased from ≈ 5100 to ≈ 8000 and the number of Twitter followers has increased from ≈ 30 to ≈ 1400. Figure 6.4 shows the growth in the DES Facebook following starting in April 2014[23]; the red star on Figure 6.4 indicates the formation of the EPOC.

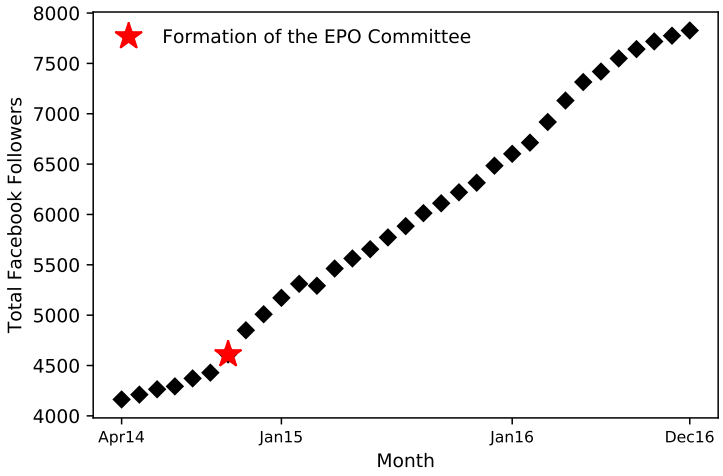

Figure 6.4: Total number of DES Facebook page followers per month. The red star signifies when the EPOC assumed control of the Facebook page and began posting content regularly.

Throughout this analysis, including in Figure 6.4, we present various metrics used to asses the social media strategy and reach of several DES EPO initiatives. Many of these metrics were obtained from Facebook Insights and Twitter Analytics, included metric services offered by the respective social media platforms. Any categorical information

[23]We begin our analysis in April 2014 as this is the earliest point from which we can retrieve data from Facebook.

used from these metrics is defined by the platforms. We have also conducted surveys within the collaboration (e.g. B.2) and extracted our own data from the social media sites.

Figures 6.5 and 6.6 present Facebook demographic information for our three primary social media user groups, based on level of engagement. We define users who have "liked" or "followed" the Facebook page as "Followers," users who are exposed to DES social media posts as "Reached," and users who actively engage with content as "Engaged."

In Figure 6.5 we analyze each user group by age and gender (as gathered by Facebook). The DES Facebook follower base is roughly 75% men and 25% women ($n = 7914$); however the engaged users are roughly 60% men and 40% women ($n \approx 500$). The largest user age group ($\approx 20\%$) is 25-34, for both men and women and across each of the three user groups. According to our Twitter metrics, most of our Twitter followers have self-identified an interest in science. 94% of our followers express an interest in "Science News" and 89% of our followers express an interest in "Space and Astronomy" ($n = 1402$).

Figure 6.6 displays the five most popular user-identified countries of origin and languages of the Facebook users in our three user groups. As shown in Figure 6.6, the majority of the Facebook users in each of the three primary user groups are located in the United States and speak English (US). Each user group also includes users from India, the UK, and Brazil. In addition to English (US), English (UK) and Spanish are both in the most popular languages for each user group. We note that the fifth most popular country for each user group is unique; the "Followers" are found in Mexico, the "Reached" in Turkey, and the "Engaged" in Australia.

We find our social media demographic information, for the most part, unsurprising. While the majority of Facebook users in general are young women (Duggan and Brenner, 2013), the fact that the majority of our followers are young men is consistent with the well-documented issue of the underrepresentation of women in astronomy and astrophysics (National Research Council, 2010a; Ceci et al., 2014; Ivie and Ray, 2005). We

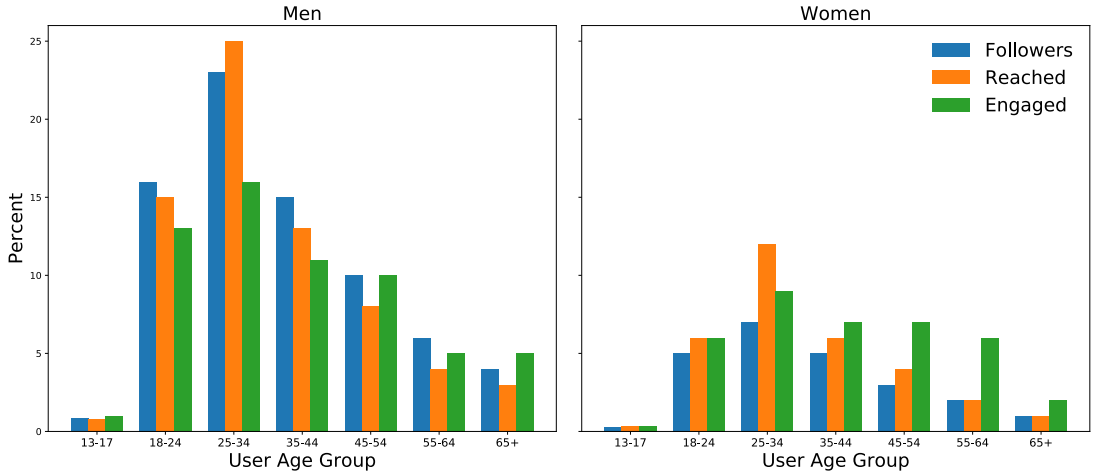

Figure 6.5: Percent of Facebook followers (blue), users reached (yellow), and engaged users (green) over various user ages. Information is also separated into men (left) and women (right) user groups. The 25-24 user age group is the most popular in each user group and for both men and women. While the men are roughly 75% of the total page followers ($n = 7914$), women make up nearly 40% of the total engaged users ($n \approx 500$).

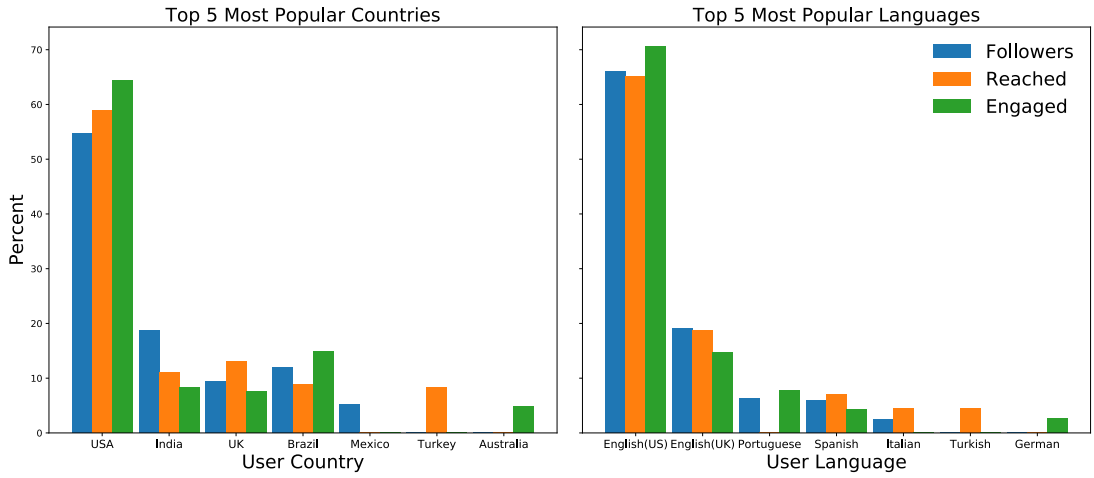

Figure 6.6: Percent of Facebook followers (blue, $n = 7914$), users reached (yellow, $n \approx 15000$) and engaged users (green, $n \approx 500$) in the five most popular user-identified countries and languages of origin.

are primarily reaching people predisposed to an interest in science, and not necessarily inspiring new interest. As expected, most of our followers are in the United States and English speakers. Perhaps the most puzzling demographics are those describing where our followers are located. We are unsure why one of primary locations of "Followers", Mexico, is not included in the primary locations of people "Reached" or "Engaged." We are also unsure why our posts are particularly popular in Turkey. Investigating these demographics in further detail will be explored in a later analysis.

As shown in Figure 6.6, Spanish-language speakers are in the top five of our Facebook "Follower", "Reached", and "Engaged" user groups. Combined with the fact that DECam is based in a Spanish-speaking country, this evidence suggests that translating DES content to Spanish is a valuable use of EPO resources (see Section 6.3.6 for more on EPO translations). Despite this international following, however, translated posts as part of the MLDES project (Section 6.3.6) reached only ≈ 200 users per post.

Based on these metrics, we find that although the number of people following DES on social media has increased, it has not increased at the rate we expected. We also conclude that although we may have increased awareness of the DES project, it appears our primary audience are those who already self-identify as having an interest in astronomy or science in general. It is unclear if these users are scientists themselves or enthusiastic members of the public. Unfortunately, it is unlikely that we have inspired new interest in astronomy. This suggests that 1) our social media strategy should be restructured and/or 2) the most effective methods of encouraging new interest in science are not via the web.

6.3 Programming for a Collaboration

In this section, we discuss some[24] of the primary DES EPO initiatives organized by the EPOC since Fall 2014. For each initiative, we present a summary of the project and

[24]The presented list of initiatives is not an exhaustive compilation of all DES EPO activities, but a representative sample of the DES EPO repertoire.

discuss its implementation and project strengths and challenges. We also offer recommendations for future large-scale astronomy (physics) EPO efforts. Corresponding logic models detailing the specific inputs (e.g., time, funding), outputs (e.g., online content, lesson plans), and outcomes (e.g., number of participants, public and scientists' reactions to projects) for many of the initiatives presented here can be found in Appendix B. In some cases where project products were distributed via social media, e.g., using Twitter and/or Facebook, we present analytics from the social media platforms over the 2016 calendar year. We compare these metrics to the global reach of all our products featured on social media (see Figure 6.7) as a benchmark for impact. We note that many of the projects described below are on-going, so the discussion presented here is limited to our experience to date.

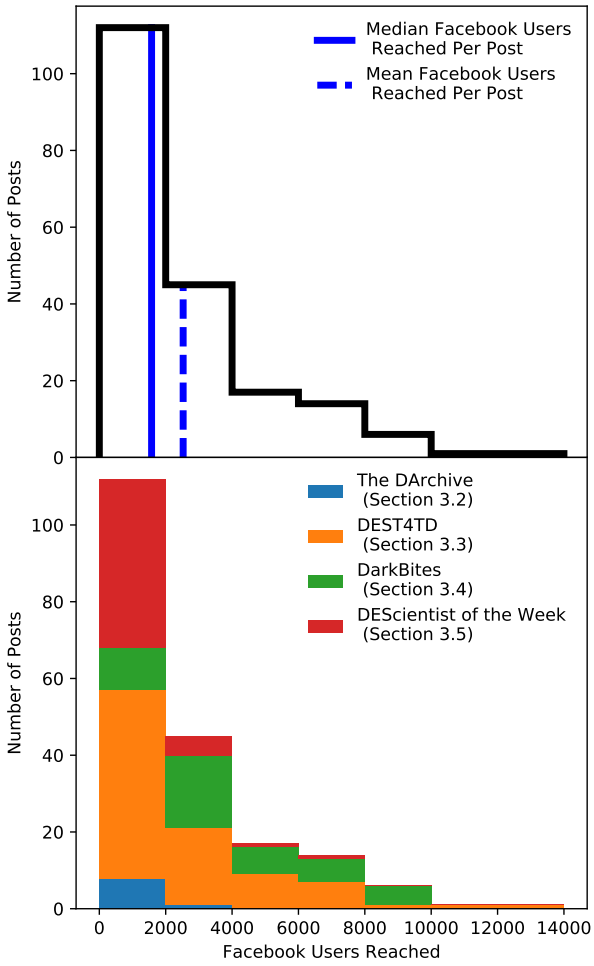

Figure 6.7: Global distribution of Facebook likes per post for DES EPO products featured on social media described in this work (DArchive – Section 6.3.2; DEST4TD – Section 6.3.3; DarkBites – Section 6.3.4; DEScientist of the Week 6.3.5) . Blue dashed and solid lines in the top panel indicate the mean and median, respectively. The bottom panel features a stacked histogram showing the number of posts per EPO product discussed in this section.

6.3.1 The `darkenergysurvey.org` Website

One of the first actions of the EPOC after it was founded in October 2014, was to take on the responsibility of updating the DES website. The aim was a modern, user-friendly, web site with integrated social media feeds (GP5, GP6).

Rather than update the content of the existing DES website, we decided to create a new website that would meet our aesthetic, content, and user-interface goals. This involved updating the "back-end" data access structure as well as the "front-end" publicly accessible presentation layer. This process, from development to public launch, included: 1) seeking out an external web development agency and obtaining their advice, 2) designing the layout, user experience, and information content, 3) organizing the back-end features necessary for page updates and maintenance, 4) creating, reviewing, and formatting content, and 5) designing a strategy for website maintenance.

Key choices for the front-end revolved around the user experience. We believed that if this element was appealing, simple and intuitive, the audience would be able to navigate easily to the online content, and want to return to it in the future. Our goal was to create a site that was easy to navigate, both on a computer and mobile device, for a variety of user groups (e.g., professional astronomers, educators, general public). After much internal discussion and research of existing science collaboration sites,[25] we opted for a compromise between a multi-page, hierarchical structure and one with more modern media-driven features. This allowed us to create a bridge between the past and present of science collaboration web pages; appealing to self-identified science enthusiasts who were already used to exploring well-organized and curated sites and new audience members who may be attracted by creative content and the multimedia-oriented main page.

Implementation of these front-end features relied on an understanding of back-end development. For reasons related to budget and site maintenance, we elected to utilize an existing template service[26] for the back-end of the new website. However, as the EPOC

[25] E.g., `hubblesite.org` and `sdss.org`

[26] `https://wordpress.com/`

coordinators did not have the necessary web developing experience, we contracted a professional website development team to adjust the back-end structure to suit our needs. Funding for this project was approved by the DES director and was drawn from contributions from the participating institutions. We worked with the development team for a year and a half and the cost ultimately came to $\approx$ \$5000. This was the largest single-project budget of any of our other EPO programs and greater than the sum of EPO funding allocated for all other DES-EPO projects.

Much of the developers' time was spent organizing the back-end structure so that site maintenance would be straightforward. For example, they created a slide interface for easy graphic uploading and multiple web forms for adding new content. Once the website was publicly launched, updating and adding content and other site maintenance was under the purview of the EPOC. Much of the content for the new site was transfered from the old; however, we devoted a substantial amount of time to updating and rewriting sections on a range of topics from DES science to collaboration structure.

Although we believe the current DES web page is a significant improvement from the previous public page (screenshots of the old and updated home pages are presented in Figure 6.8), development and maintenance required much more time and effort than we anticipated. In hindsight, we believe we devoted too much time to designing and creating the optimal aesthetic. This allocation of resources meant that we then did not have enough time to create and review static web page content or develop other EPO projects. In fact, several pages of written content had not been published at the time of writing because we lacked resources for editing.

6.3.1.1 Take-Home Messages

We strongly recommend that future projects devote whatever resources possible to contracting an external web development team who can lead back-end development and aesthetic design. This will clear time necessary for content writing, editing, and standardization.

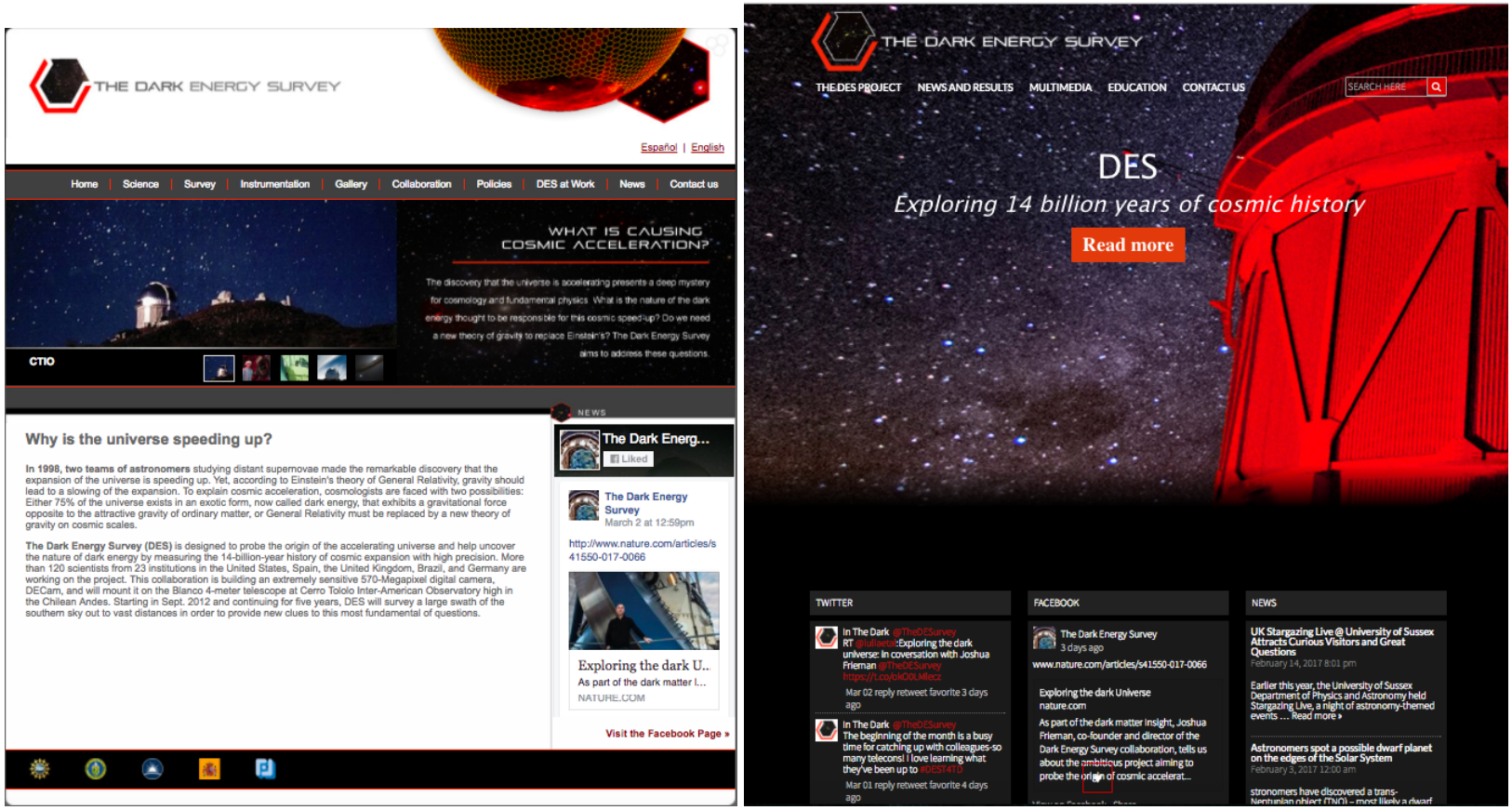

Figure 6.8: Screenshots of original (left) and updated (right) DES website home pages. Note that the screenshot of the new page does not capture the full screen as the template is widescreen.

6.3.2 The DArchive: DES Results in a Nutshell

The fundamental charge of DES is to conduct innovative, high-caliber research. As a large-scale science collaboration, DES scientists work together to produce new science results that are published in peer reviewed academic journals. While members of the academic community know how to access and interpret these results, refereed versions of these papers are not easily accessible to or digestible by the public due to the use of technical, scientific language. The "DArchive: DES Results in a Nutshell" project was designed with the goal of dissolving these barriers and making DES science more accessible to the public (GP3). Our intent was such that each DArchive would feature a summary of a DES paper, using language and analogies intended to connect a public audience with the science.

This was one of the first collaboration-wide projects organized by the EPOC. Our initial goal was to have a complementary DArchive featured with the release of each DES paper. In an internal collaboration-wide survey (see B.2 for survey details), 91% of respondents $(n = 69)$ indicated that they supported the DArchive project and believed it to be a worthwhile DES EPO effort. Between May 2015 and January 2017, there were 89 DES papers submitted to academic journals; yet there were only 15 published complementary DArchive articles.* Published DArchive posts were featured both on the DES website and on the DES social media platforms.

6.3.2.1 Project Organization and Implementation

Since its inception, the DArchive project has gone through three iterations of organization, which are summarized in Figure 6.9. A logic model describing the inputs for each iteration is presented in Figure B.1.

In Iteration 1, we expected the paper summaries would be primarily led by the paper authors (GP8). The EPO Committee created a DArchive template document, intended as a guide to help the authors draft their pieces, and sent this template, along with a request for a DArchive, to paper authors. Authors who responded to the request drafted a paper

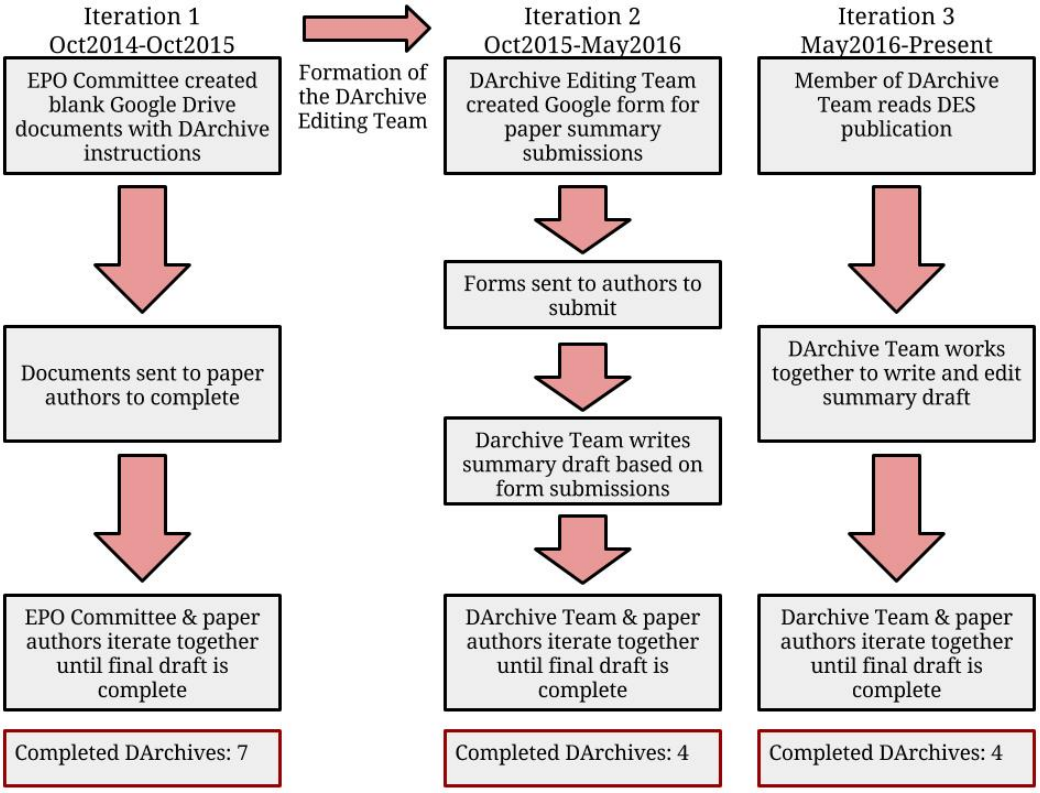

Figure 6.9: DArchive work flow for each of the three project organization iterations.

summary, and the EPO Committee worked with the authors to finalize the DArchive.

During this Iteration of the project, we encountered several key issues with author participation. Despite our efforts to get in contact with paper authors, the response rate, and willingness to participate was very low. We expected this might be due to when during the publication process we contacted the authors, i.e., once the paper had been submitted for internal collaboration-wide review or after it had been published in a journal, but found no correlation with request timing and response rate. Some authors found it particularly difficult to translate their work for a public audience, and therefore the EPOC often had to spend hours editing a particular piece to meet the DArchive communication goals. Additionally, some paper authors did not understand the importance of eliminating or rephrasing some scientific terminology, and would argue with the EPOC about how to best convey a topic, significantly lengthening the DArchive writing and editing process.

The goal of Iteration 2 was to decrease the amount of effort required by the paper authors. As part of this Iteration, we assembled the DArchive Team: a group of five authors (including NRW) and one editor-in-chief. The goal of this Iteration was to distribute the DArchive authorship and improve consistency and quality amongst posts. As part of Iteration 2, the DArchive team created a new DArchive submission form to help paper authors condense the most significant sections of their analyses. Questions on this form included:

- In one or two sentences describe the main hook of the paper.
- In three or four sentences, describe your conclusions, results, and the reasons why you are excited about this work.
- In a paragraph, describe how you came to these conclusions. Outline the main steps that lead to your results. Try to avoid too many technical details about systematic checks, etc.
- In a paragraph, describe how your conclusions contribute to the advancement of knowledge about dark energy, cosmology etc.

This form was sent to paper authors, and the DArchive Team drafted paper summaries based on authors' submissions. Unfortunately, the issues of Iteration 1 were also present in Iteration 2. The most significant problem was lack of participation from the paper authors. However, having a dedicated team of DArchive writers helped streamline the DArchive process and improved consistency between pieces.

To further reduce the need for author participation, the DArchive Team adopted Iteration 3. Summaries in this Iteration were driven primarily by the DArchive Team. A DArchive Team member would read a DES paper, write the paper summary, and then offer the DES paper author(s) a chance to include revisions. While the structure of this Iteration gave the DArchive Team more autonomy, DArchive writers had a difficult time balancing the time commitment necessary to complete a DArchive summary with the demands of their other duties (research, teaching, administration etc.). We found the total amount of time needed to complete a DArchive, from both the paper author(s) and the editing team, was roughly ten hours. This translated to the release of about one Darchive feature per month.

6.3.2.2 Social Media Reach: The DArchive

Figure 6.10 presents the Facebook reach of DArchive-related posts in 2016. Note that while most of the points correspond to an individual DArchive post, some may correspond to a general DArchive announcement, e.g., a general link to the DArchive page on the DES website. As shown in Figure 6.10, the number of people reached per DArchive-related post is highly variable. The mean number of people reached in 2016 is 1310 while the median is 907. Figure 6.10 also demonstrates that the majority of DArchive posts reach less than the median number of Facebook likes per post across all DES EPO products posted on social media.

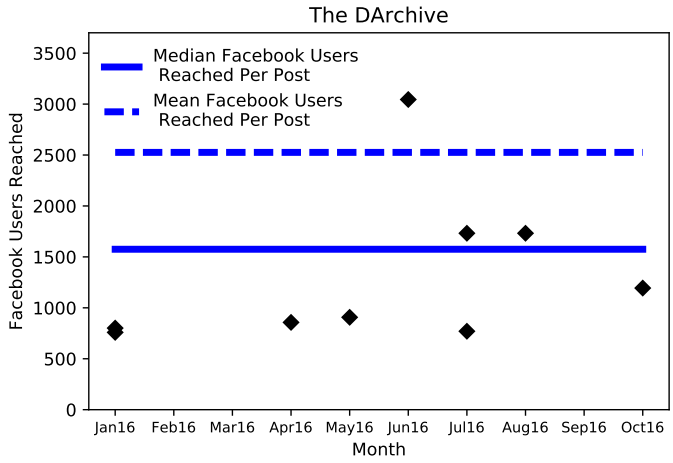

Figure 6.10: Number of people reached on Facebook by the DArchive posts each month in 2016. Points indicate an individual DArchive post or a reference to the DArchive catalog on the DES website. The mean and median number of Facebook users reached per post across all DES social media projects are shown in blue dashed and solid lines, respectively.

6.3.2.3 Discussion

As made evident during each Iteration of the DArchive structure, the time commitment was the biggest obstacle blocking the project's success. It was challenging to get paper authors, who had already written an academic paper, and DArchive writers, who enjoy written science communication, to devote the time necessary for each DArchive summary. Throughout the iterations, the EPOC tried various approaches to incentivize participation in the project, including:

- Asking the DES director to publicly support the project at collaboration meetings.
- Requesting that the DArchive process be streamlined into the official publication policy.
- Offering infrastructure credit towards data rights and DES Builder status for participation (see Section 6.2.2).

None of these approaches proved successful. While the director offered public support for the project, the lack of official policy made it difficult to encourage or mandate participation. We found the amount of time necessary to write and edit a polished piece was simply not realistic within the work demands of a full-time scientist.

6.3.2.4 Take-Home Messages

Although an efficient DArchive strategy has not yet been reached and we have not published DArchives at our goal rate, experiences in each Iteration were incredibly valuable. Overall, we learned that aiming for a DArchive summary for each DES paper was too ambitious, and likely unnecessary as occasionally papers would overlap with similar material (i.e., papers from an ongoing analysis would build upon one another). We also learned that the background information needed to provide context for the scientific analyses was repetitive from piece to piece. We began writing static background articles (i.e., about fundamental concepts like redshift or gravitational lensing) and intended to provide relevant links in each DArchive, but have not yet published them, due to lack of time. We found that having a "DArchive Editor-in-Chief" was essential, as it not only made the posts more consistent, but made the process easier for the writers and the paper authors.

In addition to providing an EPO output for the public, we also found the DArchive project had unexpected value for DES scientists. Writing these pieces gave their authors opportunity to improve upon their science communication skills. Moreover, DArchives make DES science results much more accessible to DES members who were not directly involved. Rather than having to read the whole of an academic papers, DES members can read a DArchive piece and learn the salient background and results. Furthermore, should those DES members be invited to give a general DES presentation to peers or to the public, the DArchives can be used to effectively convey the information in a given paper to the audience.

We believe that projects like the DArchive involving high-quality science writing would greatly benefit from professional experience and dedicated funding. Rather than

being written by full-time scientists, we recommend these pieces be written by a professional science writer. These pieces are important "legacy" content for DES, and are part of the static content on the DES website. We would also recommend finding a more impactful means of product distribution other than social media. The reach statistics presented in Figure 6.10 are lower than other DES EPO projects (e.g., Figures 6.14 and 6.11). A blog approach to dissemination would likely be more effective (the *Dark Energy Detectives* blog typically reached $45,000$ people on Tumblr).

6.3.3 DES Thought for the Day (DEST4TD)

One of the first priorities of the EPOC was to revitalize the DES social media presence and create a vehicle by which we could increase public awareness of the project (GP5). We hypothesized that providing a regular stream of social media content would be the best way to engage an audience that might otherwise be unaware of or uninterested in DES. However, as working researchers, we did not have the time to be the sole creators of daily original content. Therefore, we asked collaboration members to contribute by submitting a DES Thought for the Day (DEST4TD): a short statement about their work, science interests, or daily routine. In addition to providing the EPOC with social media content, i.e., to post on Facebook and Twitter, DEST4TD also provided the opportunity for collaboration members to engage with the public using a new, unconventional medium which would not require much time or preparation (GP8).

DEST4TD was also intended to serve as a channel through which we could share real-life experience of DES scientists with the public and contribute to our long-term goal of making science and scientists more accessible to those outside academia (GP3).

We anticipated that the project would be well received by the collaboration as it provided a means of reaching a large audience without requiring too much personal time or long-standing commitment. We also anticipated that collaboration members would respond to email requests for participation as they would be required to spend no more than five minutes on an individual DEST4TD. When asked about the project, 70% ($n = 30$)

of collaboration members responded that they believe DEST4TD was a worthwhile DES EPO project. Since the beginning of the project, 127 different collaboration members have contributed a DEST4TD; 13 members have contributed more than five unique submissions. By comparison, only 3 DES members had contributed to DES social media prior to the creation of the EPOC.

6.3.3.1 Project Organization and Implementation

Developing the most effective project strategy required substantial trial and error. Various iterations including sending batch emails to randomly selected collaboration members, requesting participation via form submission, and sending specific requests to DES observers at the telescope site proved to be inefficient and ineffective. Ultimately, we converged on a process where collaboration members were personally emailed at random (participants were drawn from the full collaboration member list and emails were automated via a Python script) and asked to respond to one of a list of prompts, which included:

- This week for DES, I'm working on ...
- The most exciting thing about working on DES is ...
- The most difficult / frustrating thing about working on DES is ...
- My favorite thing I've learned by working on this project is ...
- The biggest mystery in [your specialism in DES] is ...
- When I went observing for DES, I was surprised by ...
- When I went to [my first, the most recent etc] DES collaboration meeting, I was surprised by ...
- Submit a photo from observing or a public figure from your research

The response rate to DEST4TD email requests varied throughout the calendar year. Generally we received bursts of participation around the time of collaboration meetings and during the observing season (while scientists were at the telescope). To create a suitable content repository (in case we received no responses per set of requests) and increase the chance of response, we doubled the email request size from five to ten collaboration members per day in the summer of 2016 and pointedly asked for a specific response to one prompt. The full list of suggestions was also included in the email, in case the particular prompt did not inspire a response.

DEST4TD submissions were posted daily to the DES Facebook and Twitter accounts by EPOC founder Wolf. This required: vetting of the source material, i.e., ensuring any new science results were allowed to be publicly released; condensing posts to 140 characters for Twitter posting; finding related images and relevant article links. This process took $\sim 5-10$ minutes per day. Although we could have added further automation by utilizing a social media dashboard, we opted to post manually as it was more convenient to devote time at our convenience.

A full description of the final DEST4TD framework is presented in Figure B.2.

6.3.3.2 Social Media Reach: DEST4TD

Figure 6.11 presents the number of Facebook users reached by DEST4TD in 2016. Each black point represents an individual post; red points represent the monthly average. The average yearly reach in 2016 was 2649 and the median was 1567. We find that in the early months of the year, the average reach of DEST4TD posts is 1654; from August onwards, the average increases to 4706. We note that this spike in August occurs in the same month as the beginning of the DES observing season.

As shown in Figure 6.11, the average number of Facebook users reached by DEST4TD per month roughly follows the median across all the DES EPO products. This is unsurprising, as Figure 6.7 indicates that the majority of posts which reached $\lesssim 2000$ users were outputs of the DEST4TD project.

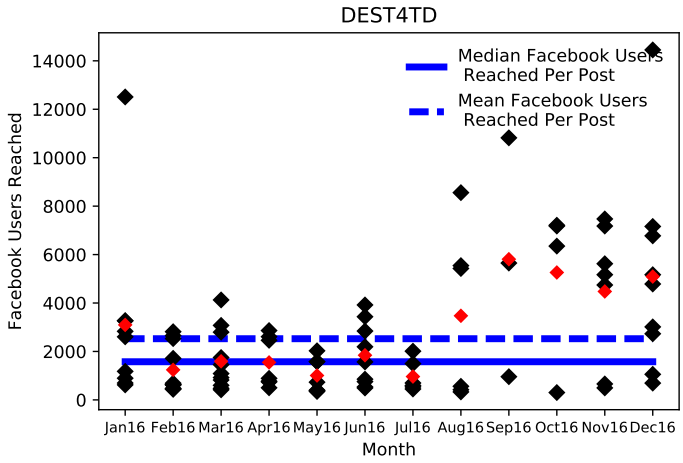

Figure 6.11: Number of Facebook users reached by DEST4TD posts in 2016. Each black point represents an individual DEST4TD post. Red points represent the average reach per month. The global mean and median number of Facebook users reached per post across our various social media projects are shown in blue dashed and solid lines, respectively.

The three most popular DEST4TD submissions of 2016, as determined by reach on social media, are presented in Figure 6.12. As displayed in Figure 6.12, there does not seem to be a unifying theme amongst these most popular posts. The most popular post of January 2016 featured a masked image of a Messier galaxy that was presented in the context of Pop art. The most popular post of September 2016 featured an image of the Blanco telescope and surrounding instruments. One of the last posts of the year, and the most popular of 2016, featured a photo-shopped HST lens image, and a whimsical play on the Christmas holiday and cosmological parameter inference.

6.3.3.3 Discussion

Overall, we found that the popularity of a particular DEST4TD was rather unpredictable. Photographs colleagues submitted during or after observing, e.g., of the telescope site or flora or fauna on the mountain, were generally the most popular and reached thousands of social media users. We have thus far been unable to assess if DEST4TD has made any

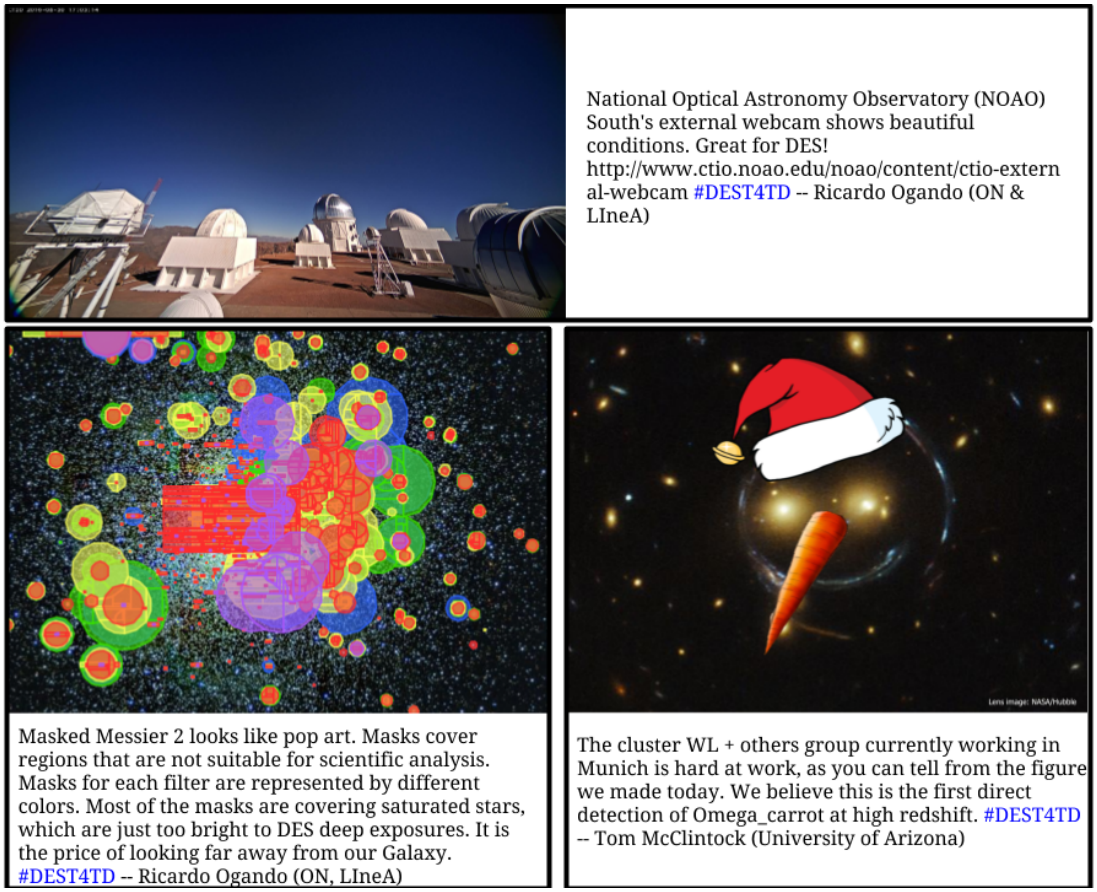

Figure 6.12: Three most popular DEST4TD posts of 2016 submitted by collaboration members as determined by social media reach. Posts were submitted in January 2016 (bottom left), September 2016 (top), and December 2016 (bottom right), respectively.

progress in better connecting DES science and scientists to the public.

Perhaps some of the most valuable information we learned from DEST4TD was not about developing and distributing social media content, but rather about how scientists perceive themselves and their ability to engage in outreach on social media. In a DEST4TD follow-up survey, we asked collaboration members about DEST4TD emails and responses to learn how to improve project participation. While only 6% responded that they reply to email requests right away, 20% responded that they submit a DEST4TD once they felt a bit more inspired, and 30% responded that they simply forget to respond to the request ($n = 59$). When asked why they did not respond to DEST4TD requests, 12% of collaboration members noted that they "did not have anything interesting to share." Unfortunately, despite our best efforts, our colleagues did not understand our role as the EPOC and our dedication and expertise in making science accessible and exciting for the public. Furthermore, our colleagues did not seem to understand that social media is a powerful tool for publicizing their work.

6.3.3.4 Take-Home Messages

Our experience developing and implementing DEST4TD illuminated two critical issues: 1) social media is an excellent tool by which scientists can engage with the public, but reaching a target demographic is nontrivial; and 2) scientists are generally quite shy, they need to be reminded that the public are fascinated by the process of doing science, not just the final results.

We advocate that "crowd sourced" social-media based initiatives such as DEST4TD are a net positive when it comes to increasing scientists' public engagement. However, specific social media strategies should be developed to ensure posts reach target user groups. As demonstrated in 6.2.5, the majority of social media users reached by DES EPO social media initiatives, including DEST4TD, self-identified as having an interest in science. This suggests that posts such as DEST4TD are not reaching new and underrepresented audiences. Although, on occasion, our posts do go "viral" and are presumably

reaching different audiences. For example, a post about an all-women observing team reached $\approx 11,000$ Facebook users.

In hindsight, it is clear that our DEST4TD efforts would have significantly benefited from feedback from focus groups and market research about social media audiences. However, these types of evaluation strategies were not realistic within our personnel and budgetary limits. Science projects that have more resources will likely be more successful in reaching a target audience through social media. On the other hand, our lack of resources meant that we were forced to tap into the creativity of 100's of active scientists (rather than develop content through an editorial team). As a result, the DEST4TD posts have been characterized by freshness, authenticity, and (often) quirky humor.

6.3.4 DarkBites

The DarkBites project was inspired by the popularity of short, astronomy-related media that include analogies or other ties to popular culture (GP3). In particular, we sought to emulate the post style of well-known astrophysicist Neil deGrasse Tyson[27] and, as a result, reach a different audience to those following DEST4TD (Section 6.3.3) or the DArchive (Section 6.3.2). The initial concept was to generate short (one or two sentences), astronomy and cosmology sound bites that would surprise and inspire the public. We envisioned that these would be written in such a way that they would be accessible to anyone over the age of 10. At the Fall 2015 collaboration meeting, we identified a DES colleague (a graduate student) who was excited by the concept and was never short of ideas. At about the same time, it came to NRW's attention that one of the DES postdoctoral researchers was a talented, and prolific artist. We approached her to ask if she would be interested in providing occasional illustrations for the DarkBites project. She was genuinely delighted to do so, and thus each of the 52 weekly DarkBites post was accompanied with original artwork. Two other artists joined the project in the latter stages.

[27] `https://twitter.com/neiltyson`

6.3.4.1 Projection Organization and Implementation

Participation in the DarkBites, which lasted roughly one year, was openly advertised to the entire collaboration. Throughout the duration of the project, the DarkBites team was comprised of two fact creators and three illustrators. The artistic decisions were made entirely based on the preferences of the project illustrators, there was no need for editorial input (which was fortunate as we were not resourced to provide that). DarkBites facts were composed on a shared online document and illustrations were kept in a shared online folder. A new DarkBite was posted on social media and the DES website roughly once a week for one year. Figure 6.13 features an example DarkBite image and caption.* A more complete description of the project inputs and outputs is presented in Figure B.3.

Figure 6.13: An example DarkBite image. The associated caption: If the lifetime of the universe were compressed to a single calendar year, the entirety of human history would occur in the last 15 seconds of December 31. Image Credit: Chihway Chang, University of Chicago; Fact Credit: Daniel Nagasawa, Texas A&M University.

6.3.4.2 Social Media Reach: DarkBites

Figure 6.14 presents the number of people reached on Facebook by DarkBites posts in 2016. Each black point on the Figure represents an individual DarkBites post; red points represent the average reach per month. As shown in the Figure, the average number of people reached increased fairly steadily from April 2016 to August 2016, and roughly plateaued for the remainder of the year. Over the course of the year, the mean number of people reached was 3843 and the median was 2873. If we consider only January-June 2016, the mean and median number of people reached were 2320 and 2202, respectively; for the latter half of the year, the mean and median number of people reached were 5800 and 6360, respectively.

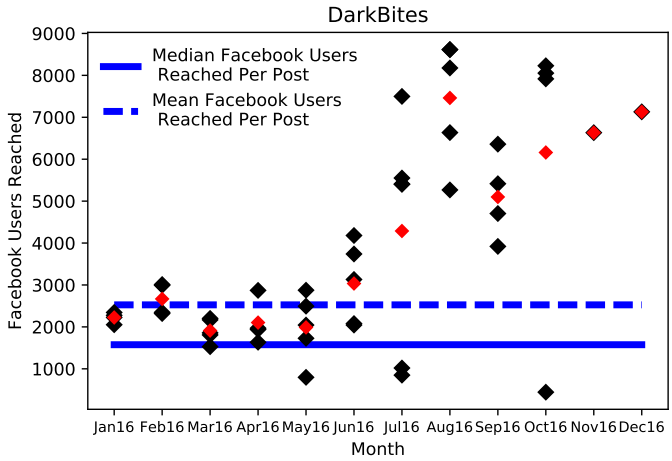

Figure 6.14: Number of people reached by DarkBites posts in 2016 on Facebook. Each black point represents an individual DarkBites post. Red points represent the average reach per month. The mean and median number of Facebook users reached per post across all the DES EPO social media projects are shown in blue dashed and solid lines, respectively.

We believe the increase in DarkBites reach after May 2015 could be attributed to two factors: 1) two new illustrators joined the project and 2) we began featuring images in color. As shown in Figure 6.14, the two most popular DarkBites of 2016 were featured

during the month of August. These two DarkBites were both related to sports, with the most popular referencing the Rio 2016 Olympics. Figure 6.14 clearly shows that DarkBites posts were some our most popular on social media. The average reach of a DarkBites post was roughly equivalent to or greater than the average EPO product reach across all the DES EPO social media initiatives.

6.3.4.3 Discussion

Perhaps the most valuable experience from the DarkBites project was witnessing the effect and impact of collaborative creativity. This project would never have succeeded without the artistic talents, creativity, and enthusiasm of our colleagues. We also observed how combining science with popular culture can be an effective tool for science communication. The most popular DarkBites posts of 2016 featured references to topical world events, suggesting that integrating science with "trending" topics may increase content reach.

6.3.4.4 Take-Home Messages

We found that a powerful way to inspire others to engage in EPO is to appeal to their personal hobbies or interests. We highly recommend that future EPO programs consider projects that capitalize on the talents of collaboration members.

Furthermore, the DarkBites project became a branching point for other EPO projects. Finished DarkBites were used by members of the EPOC to complement formal education curricula for elementary school children and in outreach events to inspire children to draw their own DarkBites images. We also designed a follow-up project, the "DarkBites Unplugged," as a vehicle to further explain and define the astronomical information included in the original DarkBites.

Through the organic evolution of the project came the surprising added benefit of its versatility. Products such as DarkBites which can be used in a variety of venues have become a valuable asset for our EPO repertoire. It has allowed us to develop additional ac-

tivities using the same content, thus leveraging the initial investment of the time involved to develop DarkBites. By comparison, the material generated for DEST4TD has not been used for other EPO activities. In hindsight, we would have designed more projects with this in mind and recommend other projects consider this in the future.

6.3.5 DEScientist of the Week

The DEScientist of the Week initiative was designed with the primary goal of making scientists more accessible to the general public (GP3, GP4). First and foremost, we sought to highlight the diversity in race, gender, and personality of collaboration members and scientists in general. We also wanted to provide our colleagues with a means of speaking openly and honestly about their experience as professional researchers (GP8).

6.3.5.1 Project Organization and Implementation

Each DEScientist of the Week piece featured a profile of a randomly selected DES collaboration member. This profile included a photograph (if desired), a small summary of research interests, and a short-form interview. Interviews were conducted using an online survey that included questions such as:

- What is your favorite part about being a scientist?
- When did you know you wanted to be a scientist?
- Do you have any hobbies or play any sports?
- What motivates/inspires you?
- If you weren't a scientist, what would your dream job be?
- Any advice for aspiring scientists?

The profiles were posted weekly on the DES website* and linked on social media. A complete description of the project inputs and outputs is presented in Figure B.4.

6.3.5.2 Social Media Reach: DEScientist of the Week

Figure 6.15 presents the Facebook reach of DEScientist of the Week posts in 2016. The average number of Facebook users reached in 2016 by DEScientist of the Week posts was 1285; the median number reached was 977. The post with the highest reach in 2016 was featured in January and highlighted a female collaboration member from a DES institution in the United Kingdom. This post was not the first of the year, not the first feature of a female scientist, and was posted on social media before the launch of the current DES website. This profile was however featured the day after one of our highest reaching DEST4TD posts (Section 6.3.3). As shown in Figure 6.15, most DEScientist of the Week posts reached less than the DES EPO global median and mean number of Facebook users.

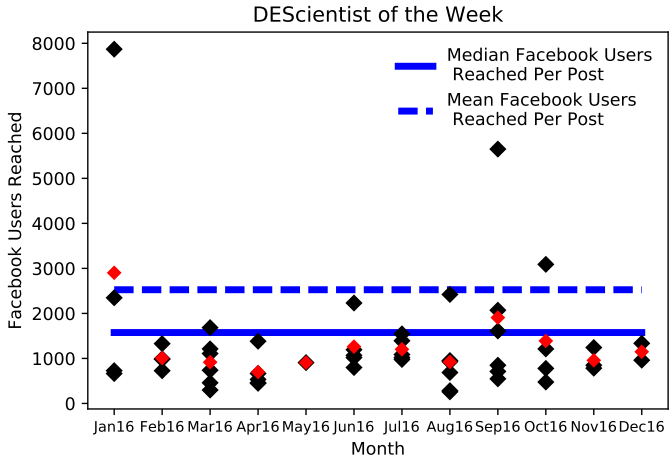

Figure 6.15: Facebook reach for DEScientist of the Week posts in 2016. Black points represent an individual post; red diamonds represent the monthly average. The global mean and median number of Facebook users reached per post across our various social media projects are shown in blue dashed and solid lines, respectively.

6.3.5.3 Discussion

Thus far, we have featured over 80 scientists as DEScientist of the Week. Initially, we asked only those signed up on the internal DES EPO listserv to participate and the re-

sponse rate was nearly 100%. After opening the project to the rest of the collaboration, the total response rate was 60% ($n = 149$), despite the fact that 82% ($n = 85$) of surveyed collaboration members responded that they believed project was a worthwhile EPO effort. This response rate is much higher than for DEST4TD (Section 6.3.3), which varies between 10% and 20% depending on the time of year. We believe this higher response rate is primarily due to the fact that scientists feel flattered to be asked to about themselves, whereas they feel nervous about taking about their research. Some collaboration members have even asked to be featured as DEScientist of the Week to coincide with job applications.

6.3.5.4 Take-Home Messages

As our colleagues generally have responded favorably to the project and as the project doesn't require a great amount of administrative effort, we recommend scientist profile/interview projects as they highlight the diversity in the scientific community and they have potential for significant long term-impact.

We continue to work toward the long-term goal of changing public opinion of science and scientists, which may ultimately include updating the structure of the project. As demonstrated in Figure 6.15, DEScientist of the Week posts did not reach as many followers as other DES EPO initiatives. This suggests that the current project structure may not be the most effective strategy for content distribution. However, interactions with our social media followers, including shares, likes, and comments, lead us to believe we are indeed making an impact, even if only on the smallest scales. For example, on the highest reaching piece of 2016, one social media follower commented that she found the post inspiring and that the post would help her on her path to becoming a particle physicist. To further this goal, we intend to make a compilation of the DEScientist of the Week pieces, either as a book or electronically, and distribute it to classrooms in our local communities.

6.3.6 Multilingual EPO

As DES is an international collaboration of scientists from seven different countries and a survey relying on data from the Blanco Telescope at CTIO, we sought to allocate EPOC resources towards projects that we believed would reach the broader, international community (GP7). Since we have been resource-limited, we have had to rely on our multilingual collaboration members to assist us in this goal. While there has been some original content created for our international audiences, most of this effort has focused on translating existing EPO content.

6.3.6.1 Project Organization and Implementation

The most ambitious of these projects has been a full translation of the DES website, including sub-page content, into Spanish. Per the approval of the DES director, we have dedicated $\approx$ \$1000 of to the development of a fully-functional Spanish version of the DES website. Translations are being done by a group of three native Spanish speakers in the collaboration who have volunteered to translate website content.

In addition to our Spanish-speaking user groups, we attempted to broaden the DES reach via the "Many Languages of DES", or MLDES, initiative. In this project, we asked multilingual members of the collaboration to translate DarkBites (Section 6.3.4), DEST4TD (Section 6.3.3), or other short-form, online DES EPO content on a weekly basis. Throughout the duration of the project, our translated languages included: Spanish, Portuguese, French, Italian, German, Chinese, Farsi, Russian, Greek, and Serbian. Translators were reminded weekly to submit any translations by Friday afternoon and translations were generally posted on social media on Sundays.

Several of our colleagues also contribute to the DES multilingual initiatives in other ways. Colleagues based in, or native to, non-English-speaking countries frequently post DES-related content in other languages (e.g., from local news articles or press releases) to their personal social media accounts; others participate in the spirit of MLDES and translate existing DES content online. Another small group of collaboration members

post and maintain an official DES account on Weibo, a Chinese hybrid of Twitter and Facebook. Posts on Weibo are roughly 40% original content (loosely based on existing DES posts) and 60% direct translations of DEST4TD or DarkBites. The Weibo page has roughly 2,000 followers and the average post reaches 1,000 users. The Weibo post with the largest reach ($\approx 30,000$) featured an image of an Einstein ring discovered by DES reminiscent of the logo for Youku (Chinese YouTube).

6.3.6.2 Discussion

As with many of our other projects, MLDES was difficult to sustain due to limited resources. We believe the translated posts did not have a large reach (≈ 200 users per post), perhaps due to the post schedule (on the weekends) or the chosen distribution platforms, and the EPOC was too time-constrained to justify continuing the project. The longer-term projects, such as the Spanish-language translations and maintenance of the DES Weibo profile, have been more successful. This is likely due to the fact that our multilingual colleagues who are passionate about these projects have taken leadership roles.

6.3.6.3 Take-Home Messages

These translation initiatives are an excellent example of designing projects that utilize skills and talents of collaboration members. The wealth of translated content which we have available is entirely due to the participation and leadership of our multilingual colleagues. Their efforts have undoubtedly helped foster an international DES audience.

6.3.7 Image & Video Curation and Creation

Images and figures are a vital component of DES science and DES EPO, and are used for science communication both within the scientific community and with the public. As part of our goal to centralize DES EPO effort and products, we attempted to consolidate image management for the collaboration as a whole (GP9). This was more successful for some types of images than others. In this section we discuss the creation and curation of

three main types of images: 1) analysis figures and plots, 2) false-color DECam images, and 3) photographs, infographics, etc. submitted for EPO initiatives and/or public talks.

6.3.7.1 Project Organization and Implementation

1. *Analysis Figures and Plots*

   The centralization of analysis figures and plots is under the jurisdiction of the DES Publication Board. Within DES, there exists a mechanism for submitting plots and figures featured in academic papers to a central database. Collaboration members are encouraged to submit any plots or figures to this "Figure Library" and are encouraged to use these figures in talks and presentations. As many of the figures that would be included in the Figure Library would also be useful for EPO products such as The DArchive, the EPOC proposed (without success) a joint image-management system for academic figures and EPO images to the Science Committee.

2. *False-Color DECam Images*

   False-color images are useful in several contexts and there is no single, DES pipeline for image processing. While some processing codes are made available in shared GitHub repositories, there is little communication between collaboration members working on image processing projects. We attempted to increase communication about these efforts through announcements at collaboration meetings and notices in the monthly EPO newsletter.

3. *Images & Videos Intended for EPO*

   A key component of our EPO image strategy involved consolidating images and videos designed for science education or as part of a science education program. For example, each of our online initiatives presented the opportunity to communicate science with visual media. In some cases this was an integral component to the project, e.g., DarkBites (Section 6.3.4). DEST4TD posts (Section 6.3.3) were often accompanied by some form of visual media - photograph, video, or infographic -

and DEScientist of the Week pieces (Section 6.3.5) almost always included photographs of the featured scientist. The variety of EPO initiatives, combined with content created by collaboration members for public presentations, led to a large pool of images that required regular maintenance and organization.

6.3.7.2 Discussion

Efforts to more officially integrate image processing and curation into official collaboration structure were not successful. The Figure Library remains the "official" image repository, although it is unclear if it is actually being used by the bulk of the collaboration. Despite our efforts to consolidate code and image-processing expertise, coordinating these multiple pipelines proved to be very challenging. We found that several members of the collaboration had their own codes to process images and did not communicate their efforts or resources with the rest of the collaboration. We found that this lack of communication often resulted in the duplication of effort and a poor allocation of time and resources. As a result of these infrastructure barriers, we refocused our energy on curating a separate EPO-focused image archive.

After much research, we opted to use *Flickr** as a repository for EPO-related images. A select sample of these images are embedded on the DES website. The DES *Flickr* account is now maintained by EPOC members, who label and sort images for public use. While there is an effort to automate this image curation process, it has been slow-going as those in charge must prioritize their research and have no additional incentive to maintain the image repository on a regular basis.

DES-related videos are hosted on the DES YouTube channel* and embedded on the DES website. Videos include public lectures, time-lapse videos created while observing, and other educational materials related to the study of dark energy. Although videos featured on social media (e.g., as part of DEST4TD) are generally very popular, maintenance of the YouTube channel has not been a priority of the EPOC as resources and effort are limited. An update of the DES Youtube channel is currently underway and is being led

by a member of the DES EPO community.

6.3.7.3 Take-Home Messages

Videos and images included in these three groups will likely be an important component of the legacy of DES and DES EPO. Moving forward, we will prioritize these efforts to ensure these media are made available to the public in an organized, user-friendly way. We recommend that future projects design an image organization scheme early on and advertise image and video repository structure clearly and consistently.

6.3.8 In-Person Outreach Activities

Although, most of the effort by the EPOC focused on developing materials that could be shared on-line (Sections 6.3.1-6.3.7), it was our initial intention to also develop materials for in-person DES EPO activities (GP3, GP4). In practice, we were severely resource limited and were only able to provide direct support to a small number of events. Two of these are described below: The Cosmic Kitchen (Section 6.3.8.1) and DES Adler After Dark (Section 6.3.8.2). The only other support provided by the EPOC to DES members was the collation of a sample of EPO talks that members could refer to when preparing their own presentations.

6.3.8.1 The Cosmic Kitchen

"The Cosmic Kitchen" (hereafter TCK) was an hour-long cosmology-themed evening public lecture delivered by NRW during a DES collaboration meeting in May 2015. The goal of TCK was to communicate fundamental concepts of cosmology and astrophysics. It differed from typical EPO lectures because it included multiple demonstrations. This approach was inspired by the Saturday Morning Physics series at the University of Michigan[28] – EPOC founder Nord had regularly participated in the series while a graduate student.

[28] `outreach.umich.edu/programs/saturday-morning-physics-public-lecture-series`

The tone and structure of TCK intended to mimic that of a televised cooking show. NRW assumed the personas of cosmology "chefs" and guided the audience through a "menu" of demonstrations based on ingredients and kitchen equipment. Each course was accompanied by a series of questions which were intended to spark the audience's interest and a demonstration to communicate a particular cosmology concept. For example, the "menu" included a cheese course during which wheels of cheese were used to demonstrate the proportions of matter and dark energy in the Universe. The cheese course then led into questions about dark energy and the accelerating expansion of the universe.

TCK logistics were organized by the local institution staff. While TCK theme and demonstrations were finalized before the collaboration meeting, the three EPOC "chefs" had to write scripts, collect materials, rehearse, develop evaluation strategies, and coordinate with the on-site staff during the meeting. This proved to be much more time-consuming and logistically difficult than expected, not least because the "chefs" were very busy with other duties during the meeting.

TCK was performed in a campus auditorium for an audience of ≈ 100 people of all ages. While the flow of the presentation would have improved with more time to prepare, TCK was generally well-received. The children in the audience particularly enjoyed the demonstrations; Figure 6.16 is a photograph from the event. Despite our asking the audience to participate in an online survey after the presentation, we received no responses.

6.3.8.2 DES Adler After Dark

Adler After Dark (hereafter AAD) is a monthly event hosted by Chicago's world-renowned Adler Planetarium.[29] Planetarium hours are extended and the event is only open to adults 21 years of age or older. Each event has a different theme, and tickets (priced at $\$20-\$25$) often sell out to a crowd of ~ 1000 visitors.

In June 2015, a DES collaboration member in the Chicago area approached the Adler

[29] `www.adlerplanetarium.org`

Figure 6.16: EPOC coordinator A.K. Romer interacting with a young audience member during TCK, May 2015. © Erika Martin

Planetarium about organizing a DES-themed AAD. As there are several DES institutions in the Chicago-area,[30] some of which already had established partnerships with the Adler through other EPO initiatives, an extension of DES EPO into the realm of museum programming and informal science education seemed natural. After several discussions, a DES and Halloween themed AAD event was scheduled for October 2015.

The AAD planning committee included the EPOC coordinators, several DES collaboration members in the Chicago area, and Fermilab Communications Office personnel. For four months the group had regular weekly meetings and telecons to brainstorm project ideas and develop materials for the event. The final suite of activities consisted of six different interactive demonstrations that covered cosmology and DES-specific topics ranging from the fate of the universe to differences between dark energy and dark matter. This included a "Cosmic Shuffleboard" (patent pending) used to teach about gravitational lensing and Tug-of-War to illustrate the combating forces of dark energy and gravity. The group also organized a question-and-answer panel and lecture featuring DES scientists.

According to DES participants and public patrons, the event itself was enjoyed by all who participated.[31] Tickets sold out to a crowd of roughly 1,000 visitors, most of whom were 20-35 years of age. At least 15 DES collaboration members from the Chicago area participated as scientist-volunteers. The most popular events were the lecture, Cosmic Shuffleboard, and Tug-of-War.

While the event was largely deemed a success, we had no means to evaluate whether or not the activities' learning goals were met. DES organizers at the event also commented that there was not enough time to properly set up everything that had been planned and that some activities were more well-organized and executed than others. Planning and implementing the six activities was perhaps too ambitious and resources may have been better spent focusing on a smaller number of activities.

[30] The University of Chicago, Fermi National Accelerator Laboratory, and Argonne National Laboratory all encompass "DES Chicagoland."

[31] As discussed in private communication with DES colleagues who attended the event.

6.3.8.3 Discussion

While we were generally pleased with these two events and the corresponding EPO product outputs, there was much room for improvement. One of the more flawed components of these projects was the evaluation strategy (or lack thereof). Although we wrote an evaluation survey for TCK, without proper incentive there was no reason for visitors to participate. We believed that creating an online survey which could be easily filled out on a smartphone would help us gather more responses than traditional pen-and-paper methods, but this proved to be false. In hindsight, it likely would have been more effective to hand out paper surveys and ask visitors to participate before leaving the venue, or to have set up a focus group.

Another issue with both TCK and AAD was the inability to effectively distribute associated EPO products throughout the collaboration after the event. We believed that the activities designed for both TCK and AAD would be useful for other collaboration members involved in their own EPO projects. We intended to offer TCK and AAD materials as packages that could be used at similar events, but believe the EPOC coordinators were the only ones to have used these materials in subsequent outreach events.

Whether or not developing materials for these events was an effective use of resources is clearly an important question. While only a small amount of funding ($\lesssim$ \$500 in total) was contributed to the projects, we estimate that at least 120 person-hours were spent planning the activities, organizing logistics, and carrying out the two events. Clearly, justifying this allocation of resources would be best supported with evaluation data for these initiatives and comparable data from other projects. However, we did not have the appropriate evaluation strategy or enough personnel to explore this issue. Therefore, we intend to more seriously consider evaluation strategies in the future and recommend future projects design EPO initiatives with project evaluation as a guiding principle.

6.4 Internal DES EPO Reporting

In the summer of 2015, we organized a recording system to archive collaboration members' engagement in EPO, including participation in internally organized EPO programming, outside EPO related to DES, and other STEM outreach not directly related to the survey. This effort was driven by: 1) our curiosity about the types of engagement in which our colleagues are involved and 2) an attempt to learn about EPO endeavors that our colleagues would not otherwise communicate with us. We note that while our archive is an incomplete catalog of the full breadth of our colleagues' EPO involvement, it provides some measure of EPO interest and activity.

To create this digital archive, we designed an online form that is now sent to the collaboration monthly and advertised in the EPO newsletter. The form has two submission options: the first requires a short summary of the project and the second provides options to submit answers to a longer, more detailed questionnaire about the type of activity and audience demographics. For both forms we require that the submitter indicate the project's "level of DES-ness," where "1" indicates no relevance to DES and "5" indicates the project is entirely dedicated to DES science.

Since the creation of this archival system, 98 unique DES members have submitted records of their EPO engagement. The current archive contains 209 individual activities, which include a mix of one-off events and on-going activities. We find the mean and median "DES-ness" of these projects are both 3. The total archive contains 60 "5," 22 "4," 52 "3," 42 "2," and 33 "1"-level projects.

Of these 209 projects, 87 include further description of the activity type, e.g., in-person lecture or online interview. We have 72 documented submissions that include "In-Person" and 15 that include "Remote" activities, where one submission may include activities from both categories. We have also divided these two activity types into subcategories. In Figure 6.17, we present the subcategories of the "In-Person" activity type and the percent of activities that fall under each subcategory. We note that one "In-Person" activity may include overlap of multiple subcategories.

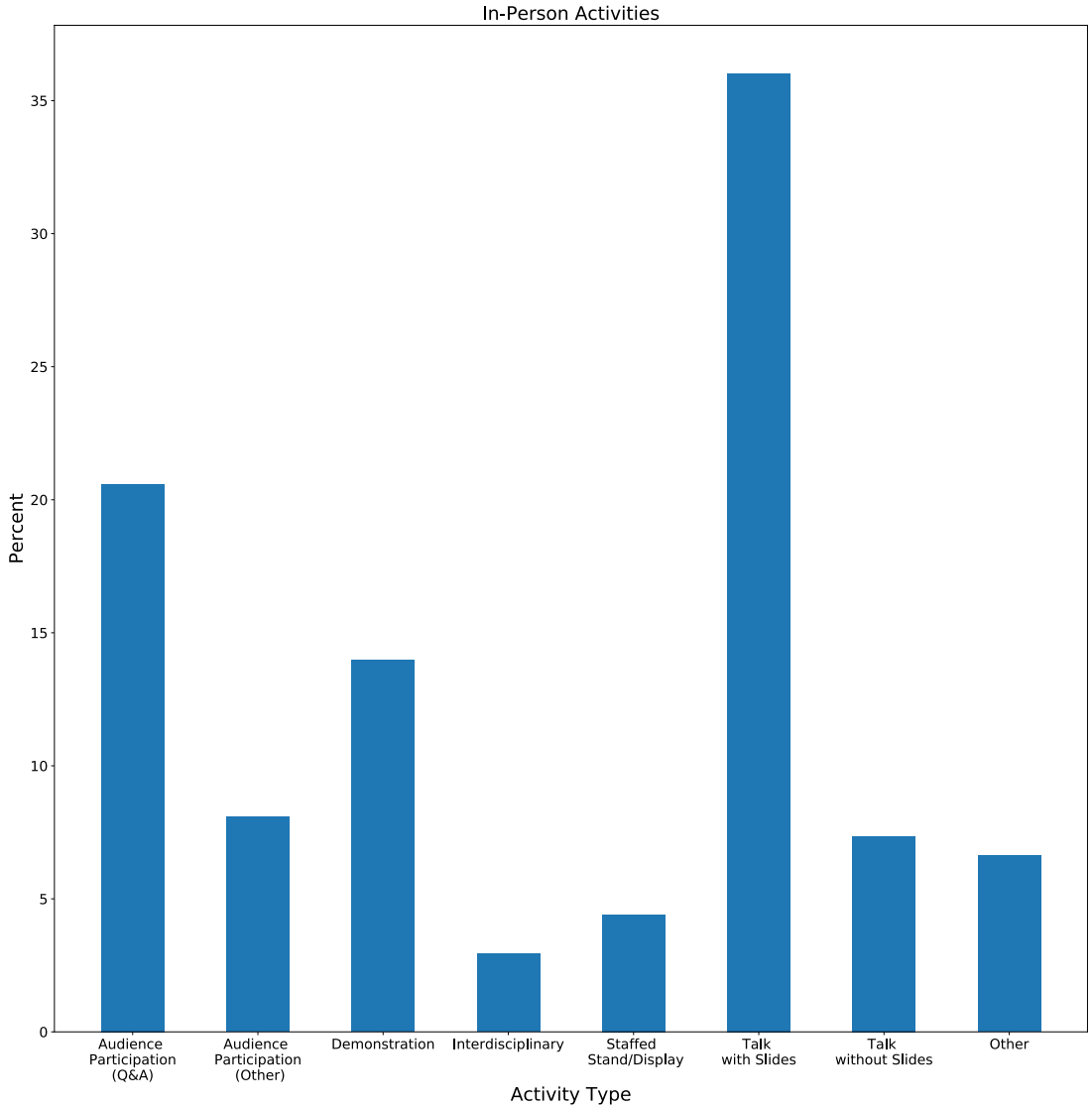

Figure 6.17: Activity types for EPO projects recorded with an "In-Person" component. Note that one "In-Person" activity might include overlap between several sub-categories, e.g., one activity may include a Talk with Slides and a Demonstration.

As shown in Figure 6.17, 36% of the "In-Person" activities include a public talk with slides and 20% of the activities include an audience question and answer session. We find that only 14% of the "In-Person" activities include an interactive live demonstration. Activities in the "Other" category include mentoring high school students and tutoring. We find the majority of "Remote" activities include printed articles or interviews, participation in radio shows, and participation in online videos.

We have observed three prominent trends when maintaining this activity archive. The first is that despite our efforts to send reminders, many collaboration members do not respond to reporting requests.[32] It is therefore difficult to make inferences about scientists attitudes towards EPO when our data are largely contributed by self-selecting participants. Secondly, we note that many of our colleagues engaged in EPO are regularly involved in a variety of EPO projects; roughly 45% $(n = 98)$ of the unique members submitting the form have submitted multiple activities. Finally, we note that public talks with slides seem to be a favored means of engaging with the public. This is consistent with the engagement trends of the larger scientific community, where public talks continue to be the favored means of filling the "deficit" in public knowledge (Andrews et al., 2005; Bubela et al., 2009; Besley and Tanner, 2011; Durant et al., 1989; Jensen and Holliman, 2016).

Recently, there has been evidence to support a transition from the "deficit" model of engagement, where public lack of knowledge or understanding is assumed, to one more focused on interactive dialogue between scientists and the public (Burns et al., 2003; Nisbet and Scheufele, 2009; Besley and Tanner, 2011). These studies find that in this model, participants not only learn about the technical aspects of the science, but the social, ethical, and economic components of the topic as well (Nisbet and Scheufele, 2009). DES scientists' reported engagement practices are further evidence of the disparity between scientists' communication methods and best-practices encouraged by communication professionals. We note, however, that this is not only indicative of an issue with

[32]From private communication we know of EPO engagement not recorded in the archive, including by senior DES members.

the practices of individual scientists, but of an issue with the greater institutional culture. Inviting scientists to give public lectures continues to be a popular method by which institutions pursue public engagement. A comparison of the internal EPO reporting data and suggested science communication strategies in the literature indicates that scientists would likely benefit from formal public engagement training.

6.5 Summary and Conclusions

In this work, we have described the evolution of education and public outreach programming in the Dark Energy Survey. Unlike many other large-scale astronomy EPO initiatives, DES EPO was not based on published data products, but rather inspired by the foundational science, data processing pipelines, and community of scientists that make up the DES collaboration. Throughout this work, we commented on the relationship between the EPOC and the rest of the collaboration, detailed specific EPO initiatives, and discussed collaboration members' public engagement practices.

One of the most significant obstacles faced by the DES EPO program was the lack of time the EPOC coordinators and community members could devote to DES EPO programming. Given the amount of time necessary to complete projects such as a DArchive summary (Section 6.3.2) and our lack of effective incentives, we perhaps should have expected lower overall participation rates from collaboration members. While many studies have shown that generally scientists are in favor of EPO (Ecklund et al., 2012; Andrews et al., 2005; Poliakoff and Webb, 2007), motives for and deterrents from participation in EPO, remain unclear. Dang and Russo (2015) assert that barriers to astronomers' participation in EPO are likely 1) the perceived academic cultural norm that one can only spend time on EPO after completing necessary academic duties (Ecklund et al., 2012) and 2) the lack of financial (institutional and grant) support for EPO. However, Dang and Russo (2015) also find that astronomers in particular are widely supportive of EPO. They find a positive correlation between the number of work hours and free-time hours astronomers

spend on EPO (i.e., the more time that they spend on EPO during office hours, the more they are likely to spend outside those hours). In theory, we should have been able to attract more collaboration members already involved in EPO to the project. However, competition for valuable EPO hours was likely a primary reason we could not recruit more volunteers.

Many of the DES EPO projects thus far have focused, at least in part, on changing the public perception of science and scientists. It is clear that this goal of changing the status quo is well-founded. Despite more recent integration of science into popular culture, e.g., books, television shows, movies, public perception of the "typical scientist" remains outdated. When asked to draw a scientist, elementary school students largely continue to depict a male with a lab coat and chemistry set (Barman et al., 1997; Tan et al., 2015). This limited perception is generally similar for many adults, as the media tends to give very little coverage to scientists or the scientific method, making scientists seem further removed from the general public (Losh, 2010). We hoped that by making scientists less "distant" from the public that we might positively affect perceptions of scientists and their careers (Losh, 2010). We leave a long-term assessment of this aspect of the DES EPO program for future work.

Reflecting on our experience holistically, we believe that many of our initial guiding principles were not realistic given the collaboration organization and structure when the EPOC was created. Although the EPOC coordinators and many of the EPOC community members share an enthusiasm for science education and outreach, it is clear that GP1 and GP2 have not been embedded into collaboration culture. Obviously we cannot expect that each collaboration member will share our goals, but perhaps officially integrating EPO into collaboration structure at the onset would have impacted general attitudes towards public engagement. Such structure may have also improved our experience trying to coordinate and incentivize EPO efforts (GP8, GP9).

We draw the following conclusions and make the following recommendations for other scientist-communicators looking to pursue similar EPO endeavors:

1. *It is critical that EPO is integrated into collaboration structure, policy, and culture.* As described throughout this work, we encountered several issues that could have been avoided had DES EPO been more well integrated into the DES collaboration structure. Although we received vocal support from the DES director, lack of official DES policy regarding EPO resulted in duplicated or inefficient EPO efforts, lack of respect for EPOC coordinators' time and expertise, and missed opportunities for targeted EPO projects for specific science results.

2. *Establish an EPO budget before program development.* We formed the EPOC under the assumption that DES EPO funds would be limited. However, we never explicitly established an annual budget. We asked for funding as opportunities arose, which included for development of the DES website and for supplies for smaller initiatives such as The Cosmic Kitchen. This system meant that we were never guaranteed funding for an EPO program. If we instead had firmly established a budget upfront, then we may have allocated resources differently and been able to fund projects that otherwise were not pursued.

3. *Collaboration members can only devote so much of their time to EPO. Designing, managing, and evaluating EPO programs requires a substantial amount of time. It difficult to incentivize scientists to participate in EPO programs if they are not already inclined to do so.* Unfortunately, EPO remains undervalued in the astronomy community. This is reflected not only in personal attitudes but in funding. While we have created many successful and innovative DES EPO programs, the list of projects we have not yet completed or did not have the time to start and/or complete is much longer. We believed we could incentivize participation by offering data rights to collaboration members, but this was not sufficient. Although we have successfully delegated projects to members of the DES EPO community, their personal time commitments have stalled the completion of projects as well. Without proper incentive, or encouraging people to devote time to EPO, it is incredibly

difficult to carry out an effective EPO program.

4. *Contract professionals if budget allows. If there is not adequate funding, set limits on how much time can be dedicated to a particular project.* Contracting web developers for the DES website was essential. Not only did the EPOC not have the necessary experience to build a website, we also did not have the time. The time we did allocate to website development was often misplaced, as we focused on aspects such as structure and aesthetics rather than content development, where our science expertise was most relevant. As a scientist-communicator developing an EPO project, we recommend reflecting on how your expertise will be utilized. If pieces of the project can be accomplished without your constant support, and if budget allows, consider external contractors for the task. If funding is unavailable, prioritize projects which balance time commitment and necessary experience.

5. *Identify a specific target audience and methods for reaching that audience for each program.* Many of the DES EPO projects discussed in this work were designed to inspire a general public interest in science. We hoped many of our online initiatives would reach people who might not otherwise be inclined towards the STEM disciplines. As our social media metrics revealed, we were not successful in reaching this target audience. In-person activities such as The Cosmic Kitchen and DES Adler After Dark reached a similar demographic (i.e., those already convinced that astronomy is interesting). We encourage future EPO efforts to think critically about content distribution and how to best interact with the desired audience. For example, the DES EPO effort may have been more successful if we had explored other social media platforms, e.g., Instagram and Snapchat.

6. *Inspire other scientists to participate in EPO by designing programs that utilize their personal interests and skills.* Some of the more innovative DES EPO projects, e.g., DarkBites, evolved from our colleagues' artistry and creativity. We also found that collaboration members were more inclined to participate in projects which ap-

pealed to their personal interests. This included projects centered around graphic design, astrophotography, video editing, and written science communication. We also believe these projects garnered more participation because colleagues could dedicate as much or as little time as they pleased, without feeling pressure to complete a project within a deadline.

7. *Consider science communication training sessions led by professionals.* Finally, we strongly recommend the organization of science communication workshops and trainings. We believe that DES collaboration members, including the coordinators of the EPOC, would significantly benefit from the professional experience of science communication experts. If scientists are expected to be at the forefront of knowledge, they should be cognizant of the most effective means to communicate that knowledge.

Chapter 7

Conclusions

7.1 Type Ia Supernova Luminosity and Host-Galaxy Correlations

In Chapter 3, we used 345 photometrically-classified and spectroscopically-confirmed SNe Ia from the SDSS-SNS to explore the dependence of the SN Ia absolute luminosity on host-galaxy properties. We find the strongest correlation (3.6σ) between Hubble residual and host-galaxy mass, confirming results in the literature and providing further support that light-curve calibration should include corrections for the SN Ia environment. We also find a significant difference in the standardization coefficients for the spectroscopically-confirmed and photometrically-classified samples. This discrepancy may allude to inhomogeneities in the combined sample or impurities in the photometric classification.

Current and future large-scale supernova surveys will provide a wealth of data which will be used to better explore the systematic uncertainties limiting SN Ia cosmology. The DES-SN, which will end its five-year observing run in 2018, is expected to detect a total of ~ 4000 SNe Ia in the redshift range $0.1 < z < 1.2$ (Bernstein et al., 2012). This will constitute the largest homogenous sample of SNe Ia to date. In the future, LSST expects to detect $\sim 50,000$ SNe Ia per year out to $z \sim 0.8$, with a mean redshift of $z \sim 0.45$ (LSST

Science Collaboration et al., 2009). Such large samples will be essential for future SN Ia host galaxy studies, as they will provide unprecedented statistical power for analyses. For example, subsamples of fixed host-galaxy mass, metallicity, or star-formation rate will have sufficient statistics to explore degeneracies between host-galaxy properties and can be used to investigate how a single host-galaxy property correlates with SN Ia magnitude. In these analyses, properly incorporating known correlations between host-galaxy mass, metallicity, and star formation rate, and correlations between their observational errors, will be essential (Mannucci et al., 2010). In addition, such samples will provide an excellent opportunity to improve photometric-classification software. As the demand for spectroscopic confirmation for these SNe Ia will be too great, the majority of SNe Ia will need to classified photometrically. While current techniques can achieve classification purity and efficiency of 91% and 94% respectively, classification of core-collapse SNe remains unreliable (Sako et al., 2014). Software improvements will be critical for cosmological parameter inference, and should significantly reduce the potential for inhomogeneities in combined samples of photometrically-classified and spectroscopically-confirmed SNe Ia.

7.2 Statistical Frameworks for SN Ia Cosmology

In Chapter 4, we introduced the BAyesian hierarchical Modeling with BIased Simulations (BAMBIS) algorithm, a novel statistical techqniue for cosmological parameter inference using SNe Ia. BAMBIS adds two new key features to the available suite of SN Ia cosmology tools. The algorithm employs forward modeling of the data at every proposed point in parameter space, allowing for treatment of any selection effects or other observational systematics that can be properly simulated, regardless of whether they can robustly be accounted for in analytic likelihoods. BAMBIS also estimates each model's probability distribution function (PDF) in the observational space using Kernel Density Estimation (KDE) of the simulated data; this provides a non-parametric estimate of the PDF that does not require analytically tractable likelihoods.

We explore the functionality of the BAMBIS algorithm using three models and corresponding simulated mock data sets. This includes: 1) Gaussian linear regression, 2) Gaussian linear regression with a complex selection process, and 3) a simplified SALT2 (Guy et al., 2010) SNa Ia regression model including data selection. Tests of the first model demonstrate that BAMBIS can recover the input model parameters within 0.43 times the 1σ uncertainty of the data. If we include a selection function, we observe a systematic bias in the latent width parameters. It is unclear if this bias is due to the inevitable smoothing and rounding of the estimated PDF or is perhaps a conflated effect of non-parametric density estimation in data bins (i.e. redshift bins). In our investigation of the simplified SN Ia cosmological model, we use a mock data sample of 667 SNe Ia and recover all cosmological and hyperparameters within their respective 1σ uncertainties. We find that over 5 realizations of SN Ia mock data, there appears to be a systematic bias in w_0 and Ω_m; however, it is unclear if this is a manifestation of the biases exhibited in the Gaussian linear model example or just fluctuations due to limited sample statistics. These parameter biases will be explored in future work using larger data sets and different regression models. It is possible that parameter bias is an inevitable consequence of using non-parametric density estimation, and the pros and cons of the BAMBIS algorithm will be weighed before applying the framework to real SN Ia data.

Ultimately, we would like to incorporate more sophisticated model systematics such as survey-specific measurement uncertainty and core-collapse contamination into the BAMBIS framework. However, we must first better understand sources of systematic bias in the algorithm. Using a more efficient sampler, or more computing resources, will also be critical when we use more sophisticated forward-modeling packages, as we expect the necessary time per likelihood evaluation to increase significantly. However, we are confident that BAMBIS can be used for cosmological parameter inference on SN Ia data on a realistic timescale, even with the current MCMC sampler implementation.

7.3 Astronomer Engagement in Education and Public Outreach

In Chapter 6, we analyzed the DES Education and Public Outreach (EPO) program, one of the first large-scale astronomy collaboration EPO efforts to be entirely led and organized by collaboration scientists. We found that although the organic evolution of the EPO program inspired a variety of innovative projects, it was difficult to integrate EPO into the pre-existing organizational structure of the collaboration. Many of the DES EPO products distributed online via the collaboration website and social media reached thousands of users; however, we discovered that rather than attracting a new, and perhaps underrepresented audience to astronomy, $\approx 75\%$ of our audience were male and $\approx 90\%$ of our audience indicated a self-identified interest in and predisposition to science. As full-time scientists, we found the most significant barrier to completing EPO projects was lack of time, which was often linked to lack of personnel or funding. Finally, we observed that many of our colleagues continue to participate in modes of science communication which favor the "deficit" model, with $\approx 36\%$ of reported "in-person" activities including some type of lecture with slides.

Data presented in Chapter 6 provided only a cursory glance into the abundance of material available for EPO and astronomy education research available from the DES EPO experience. A detailed study of social media analytics and website traffic could provide further insight into key audience demographics such as education, occupation, and socioeconomic status, and be used to evaluate the overall impact of social media programming. Further analysis of our colleagues' EPO reporting will illuminate correlations between variables such as scientist age, position (e.g. graduate student, postdoctoral researcher, tenured professor), and institution (i.e. university, national laboratory) and EPO practices. Through this assessment we can better understand how astronomers value different types of EPO and how much time they feel is appropriate to dedicate to outreach. We have also begun an analysis of DES collaborators' attitudes towards EPO. Preliminary

results indicate that many of our colleagues who were instrumental contributors to DES EPO programming did not participate in EPO prior to their involvement in DES. We have also found that establishing a DES-wide culture of EPO was a primary motivating factor to their continued participation in outreach, both within and outside the collaboration.

7.4 Scientific Acknowledgements

Work in Chapter 3 of this thesis makes use of data from the Sloan Digital Sky Survey (SDSS). Supernovae were obtained from the SDSS-II SN survey and host-galaxy spectroscopy was obtained from the ancillary program of the SDSS-III Baryon Oscillation Spectroscopic Survey (BOSS). Funding for the SDSS and SDSS-II has been provided by the Alfred P. Sloan Foundation, the Participating Institutions, the National Science Foundation, the U.S. Department of Energy, the National Aeronautics and Space Administration, the Japanese Monbukagakusho, the Max Planck Society, and the Higher Education Funding Council for England. The SDSS Web Site is http://www.sdss.org/. The SDSS is managed by the Astrophysical Research Consortium for the Participating Institutions. The Participating Institutions are the American Museum of Natural History, Astrophysical Institute Potsdam, University of Basel, University of Cambridge, Case Western Reserve University, University of Chicago, Drexel University, Fermilab, the Institute for Advanced Study, the Japan Participation Group, Johns Hopkins University, the Joint Institute for Nuclear Astrophysics, the Kavli Institute for Particle Astrophysics and Cosmology, the Korean Scientist Group, the Chinese Academy of Sciences (LAMOST), Los Alamos National Laboratory, the Max-Planck-Institute for Astronomy (MPIA), the Max-Planck-Institute for Astrophysics (MPA), New Mexico State University, Ohio State University, University of Pittsburgh, University of Portsmouth, Princeton University, the United States Naval Observatory, and the University of Washington.

Funding for SDSS-III has been provided by the Alfred P. Sloan Foundation, the Participating Institutions, the National Science Foundation, and the U.S. Department of Energy.

The SDSS-III web site is http://www.sdss3.org/. SDSS-III is managed by the Astrophysical Research Consortium for the Participating Institutions of the SDSS-III Collaboration including the University of Arizona, the Brazilian Participation Group, Brookhaven National Laboratory, University of Cambridge, University of Florida, the French Participation Group, the German Participation Group, the Instituto de Astrofisica de Canarias, the Michigan State/Notre Dame/JINA Participation Group, Johns Hopkins University, Lawrence Berkeley National Laboratory, Max Planck Institute for Astrophysics, New Mexico State University, New York University, Ohio State University, Pennsylvania State University, University of Portsmouth, Princeton University, the Spanish Participation Group, University of Tokyo, University of Utah, Vanderbilt University, University of Virginia, University of Washington, and Yale University.

Work in Chapters 4 and 6 of this thesis uses data from The Dark Energy Survey (DES). Simulations in Chapter 4 are based on SNe Ia observations of the DES Supernova Program. Education and public outreach (EPO) metrics presented in Chapter 6 were obtained from the DES social media platforms. Survey responses and EPO reporting information were provided by DES collaboration members.

Funding for the DES Projects has been provided by the U.S. Department of Energy, the U.S. National Science Foundation, the Ministry of Science and Education of Spain, the Science and Technology Facilities Council of the United Kingdom, the Higher Education Funding Council for England, the National Center for Supercomputing Applications at the University of Illinois at Urbana-Champaign, the Kavli Institute of Cosmological Physics at the University of Chicago, the Center for Cosmology and Astro-Particle Physics at the Ohio State University, the Mitchell Institute for Fundamental Physics and Astronomy at Texas A&M University, Financiadora de Estudos e Projetos, Fundação Carlos Chagas Filho de Amparo à Pesquisa do Estado do Rio de Janeiro, Conselho Nacional de Desenvolvimento Científico e Tecnológico and the Ministério da Ciência, Tecnologia e Inovação, the Deutsche Forschungsgemeinschaft and the Collaborating Institutions in the Dark Energy Survey.

The Collaborating Institutions are Argonne National Laboratory, the University of California at Santa Cruz, the University of Cambridge, Centro de Investigaciones Energéticas, Medioambientales y Tecnológicas-Madrid, the University of Chicago, University College London, the DES-Brazil Consortium, the University of Edinburgh, the Eidgenössische Technische Hochschule (ETH) Zürich, Fermi National Accelerator Laboratory, the University of Illinois at Urbana-Champaign, the Institut de Ciències de l'Espai (IEEC/CSIC), the Institut de Física d'Altes Energies, Lawrence Berkeley National Laboratory, the Ludwig-Maximilians Universität München and the associated Excellence Cluster Universe, the University of Michigan, the National Optical Astronomy Observatory, the University of Nottingham, The Ohio State University, the University of Pennsylvania, the University of Portsmouth, SLAC National Accelerator Laboratory, Stanford University, the University of Sussex, Texas A&M University, and the OzDES Membership Consortium.

This work was also funded in part by:

- the National Science Foundation Graduate Research Fellowship under Grant No. DGE-1321851. Any opinion, findings, and conclusions or recommendations expressed in this material are those of the authors(s) and do not necessarily reflect the views of the National Science Foundation.
- DOE grant DE-FOA-0001358 and NSF grant AST-1517742.
- the Visiting Scholars Award Program of the Universities Research Association.

Computational resources necessary for the analyses in Chapter 4 were provided by the University of Chicago Research Computing Center, the University of Pennsylvania, and the National Energy Research Scientific Center.

Appendix A

SDSS-SNS Supplemental Data and Analysis

A.1 Comparison to DR10

As described in Section 3.4, the spectroscopic host properties used in this analysis are derived from emission-line fluxes measured using our own modified version of GANDALF. We detail our reasons for this reanalysis there, but note that the primary motivation is to optimize the emission-line flux measurement to the redshift range of our sample. Therefore, the host properties published in the SDSS DR10 may differ from those used in this work.

In this Appendix we use 3787 overlapping spectra to compare results, specifically measured emission-line fluxes, A/N ratios, and host-galaxy extinction. We also show how these results would contribute to differences in derived host-properties, namely gas-phase metallicity. For clarity, parameters derived in DR10 are denoted by the subscript "DR10." Some comparisons are best made using the subset of overlapping spectra with Hα and Hβ $A/N > 2$, consistent with the quality requirements imposed on the host spectra in our analysis. This A/N requirement leaves 2118 spectra in common.

In Figure A.1 we compare the A/N values used in this work and those reported in

DR10 for the four emission lines needed for the BPT diagnostic (Hα, Hβ, [N II], [O III]). Generally, our A/N values are slightly higher than those in DR10, with the [N II] line showing the closest agreement. This behavior is expected, as constraining the Balmer and forbidden lines to have the same width and velocity as Hα and [N II] respectively, reduces the number of free parameters being fit (see Table 3.2). This effect is particularly strong at low A/N. We find that 96.0% of the spectra for which we measure $A/N > 2$ in both Hα and Hβ pass the same cuts in DR10, and that only 3.4% of the full overlapping sample pass those cuts in DR10 but not in our sample. The majority of the disagreement comes from just one of these two Balmer lines failing the cut (87.4%).

This analysis and Thomas et al. (2013, hereafter T13) (for $z < 0.45$) both use BPT diagnostics to separate star-forming galaxies from those dominated by other physical processes (i.e., AGNs). In this analysis we use those galaxies that are classified as either "star-forming" or "composite" (SFC) based on this diagnostic. We find that 6.1% of the galaxies we classify as SFC are otherwise labelled by T13, while 8.3% of the full overlapping sample are labelled SFC by DR10 but not in this work. Clearly, there is a discrepancy between the SFC classifications of the two samples. Upon visual inspection of the spectra DR10 classifies as SFC and we do not, we observe that most of the DR10 spectra look like passive galaxies with very weak Balmer lines, which are unlikely to pass our A/N cuts for inclusion in our analysis. This confirms the need for a good indicator of emission-line strength and spectral quality, such as A/N, to ensure a more pure sample of emission-line galaxies.

In Figure A.2 we compare the observed emission-line fluxes used for the BPT diagnostic between this work and DR10, where we have imposed Hα and Hβ $A/N > 2$. We make the comparison in observed flux, rather than intrinsic, as the latter quantity includes corrections for measured extinction and thus doesn't lend itself to a direct comparison. While we can use the direct `GANDALF` output parameters from our analysis, for DR10 we redden the published intrinsic fluxes via the Calzetti (2001) law using the published $E(B-V)$ values. We find for all four lines that our measured fluxes are on average higher

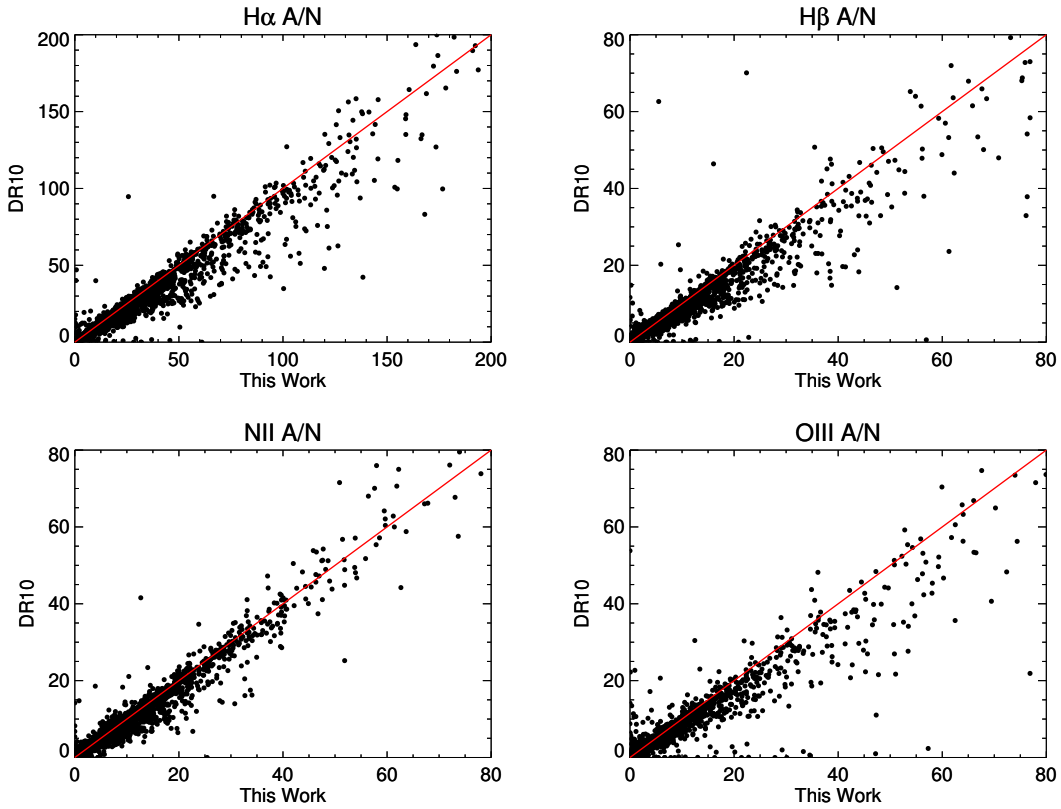

Figure A.1: Comparison of output A/N values between this work and DR10. The line $y = x$ is shown in red. The ranges in both directions have been limited to focus on the bulk of the data; 91%, 84%, 91% and 87% of the data in the Hα, Hβ, [N II], and [O III] lines are shown, respectively. For all emission lines, we find that our A/N values are systematically higher than those reported in DR10.

than those in DR10 by $\approx 10-15\%$, with no apparent dependence on flux. However, we do expect to find higher observed fluxes than DR10 due to the fact that we, unlike T13, correct the observed spectra for MW extinction before measuring fluxes.

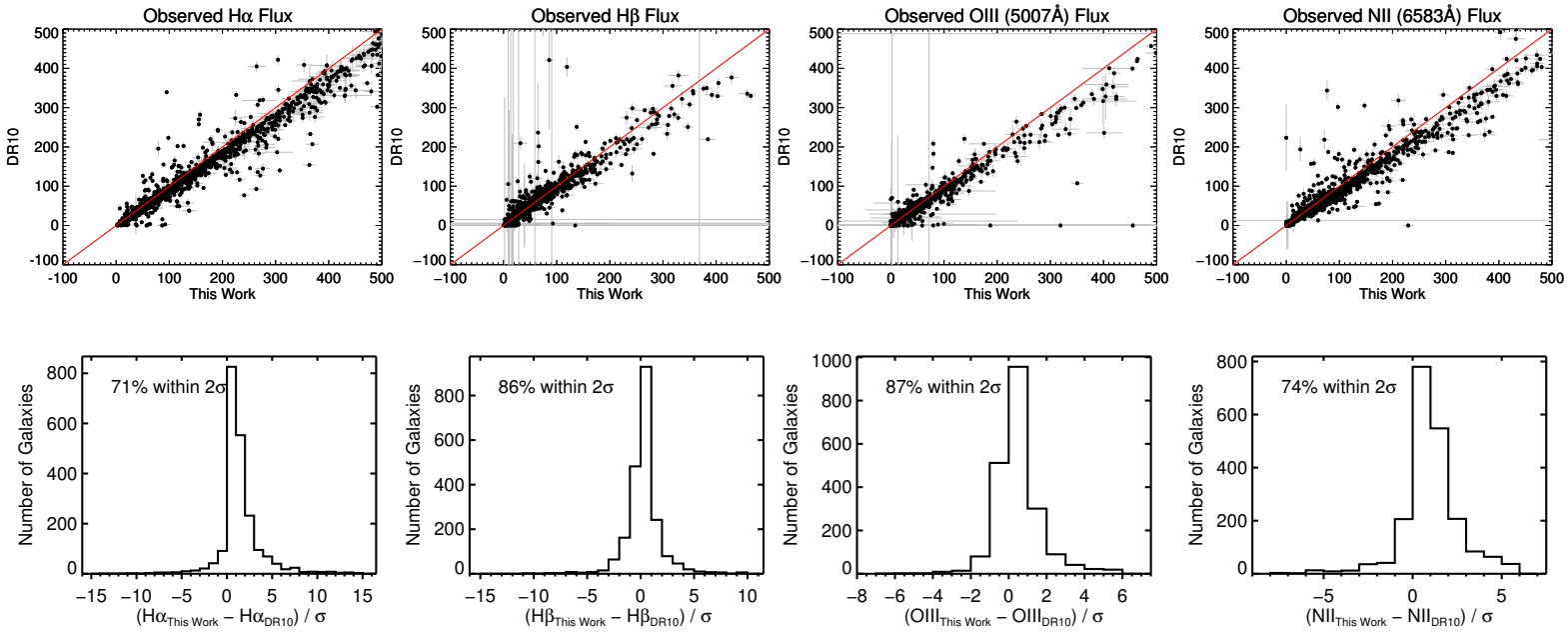

Figure A.2: Comparison of the observed emission-line flux measurements between this work and DR10 where Hα and Hβ $A/N > 2$. All figure axes have been truncated to focus on the bulk of the data; 90%, 97%, 96%, and 95% of the data points in the Hα, Hβ, [O III], and [N II] lines are shown, respectively. The top row shows a direct comparison of line flux with the line $y = x$ shown in red. The corresponding distributions in the bottom row present the difference between the DR10 measurements and those in this work. The σ value used is the uncertainties from each work added in quadrature.

Using these observed fluxes and measured extinction, we can compute the intrinsic line fluxes necessary to estimate host-galaxy properties. While DR10 uses the extinction output by GANDALF, measured from the continuum, we employ Case B recombination, which assumes a set ratio of intrinsic Hα and Hβ fluxes. The difference in measured extinction values between the two methods is shown in Figure A.3. As expected, our decision to use Case B recombination produces a much wider range of extinction values than what is reported in DR10. This difference in extinction values translates to a difference in intrinsic flux measurements between the two works: those reported in DR10 are systematically lower than those used here.

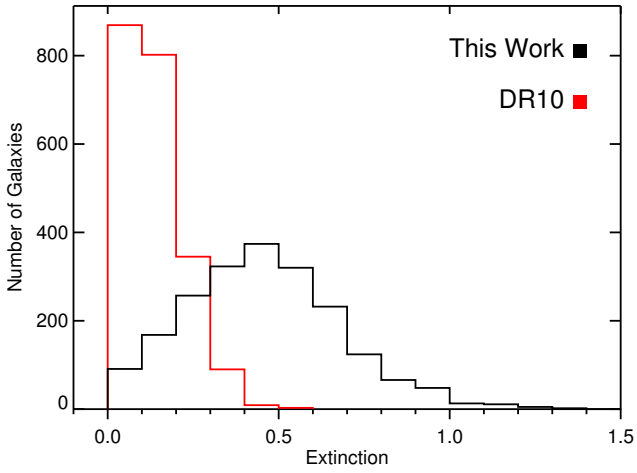

Figure A.3: Comparison of extinction values used in this work (black) and in DR10 (red). While this work uses Case B recombination to calculate the extinction, DR10 relies on the GANDALF output as measured using the spectral continuum fit.

This difference in intrinsic flux measurements does not seem to translate to significant differences in computed host-galaxy gas-phase metallicity. We compute the KD02 gas-phase metallicity (detailed in Section 3.5) using the intrinsic fluxes from DR10 and this work, and present a comparison in Figure A.4. A physical metallicity measurement is computed for 77% of the overlapping spectra; 54% have a physical metallicity measurement and meet the A/N requirement. As displayed in the figure, the metallicities derived

using the fluxes from this work slightly overestimate those obtained using the fluxes from DR10; yet, 98% of the metallicities agree within 2σ.

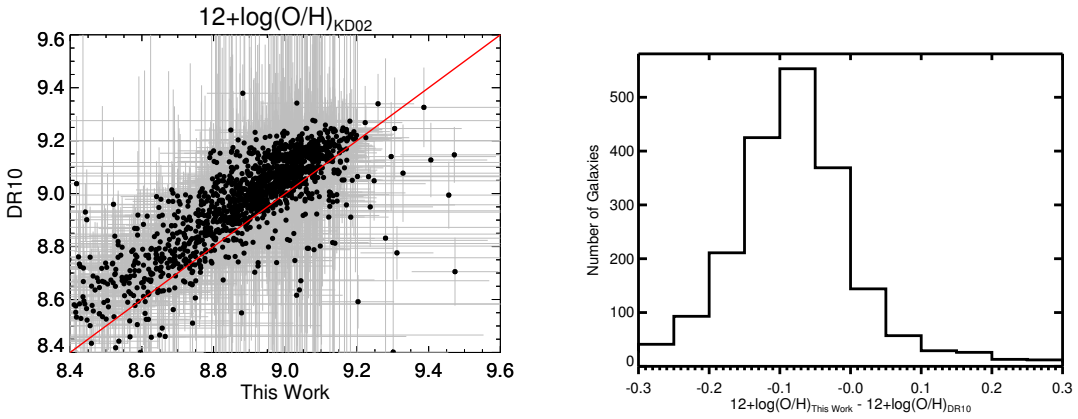

Figure A.4: Comparison of KD02 gas-phase metallicities derived using emission-line fluxes from this work and DR10, where Hα and Hβ $A/N > 2$. Figure axes have been truncated to focus on the bulk of the data; 96.7% of the data points are shown here. A direct comparison of metallicity measurements is shown on the left (the line $y = x$ is plotted in red for comparison); the difference in metallicities is shown on the right. The median and standard deviation of the difference, including outliers which are not displayed, are -0.08 dex and 3.73 dex, respectively.

Because spectroscopic SFR is directly proportional to intrinsic Hα emission-line flux, and thus affected by choice of extinction correction, we would not expect such close agreement between the SFRs found in this work and those in DR10 (note Figure A.2 only compares observed fluxes). However, we would not expect that these differences in computing SFR would significantly affect observed HR–SFR or HR–sSFR correlations.

This appendix illustrates that the decision to optimize our analysis of emission-line spectra for our redshift range does not significantly affect the observed emission lines extracted from `GANDALF`. Rather, the more important difference between this analysis and that of DR10 is the treatment of extinction. The decision to use Case B recombination when computing extinction affects the intrinsic emission-line flux measurements and thus

creates an offset in host-property measurements. However, this is not concerning as any true correlations between SN Ia properties and host-galaxy properties should be observed independent of choice of extinction correction.

A.2 Correcting For Residual Trends with SN Color

An analysis of our measured HR as a function of SN Ia properties reveals correlations between SN Ia luminosity and the SALT2 light-curve parameters c and x_1. The trend with x_1 is not very strong but the trend with c is significant and shows evidence that bluer SNe prefer a lower value of β, the slope of the color–luminosity relation (see Equation 3.1). In Figure A.5 we show HR as a function of c and x_1 for our PM sample.

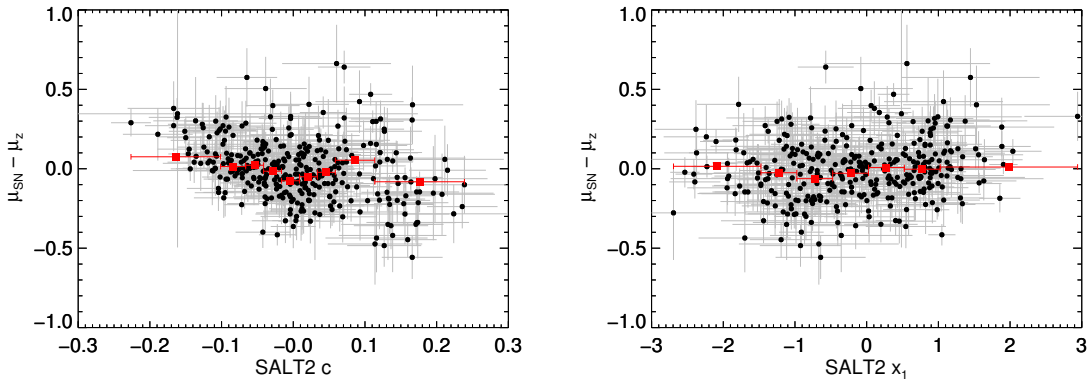

Figure A.5: HR as a function of SALT2 color (left panel) and stretch (right panel) for the PM sample. Inverse-variance weighted average bins of width 0.025 dex and 0.5 dex, for c and x_1 respectively, are displayed in red; each bin contains at least 30 SNe Ia.

Scolnic et al. (2014b) showed that nonlinear correlations between color and HR should be expected due to the asymmetric and narrow underlying distribution of color that correlates with luminosity. They also predict similar relations between HR and color for models of varying intrinsic scatter and reddening components; namely one model in which intrinsic scatter is dominated by color variation (Chotard et al., 2011) and a color-luminosity

relation following a Milky Way reddening law ($\beta = 4.1$) and a second model with scatter dominated by luminosity variation and a color-luminosity relation following $\beta = 3.1$. In particular, two distinct color–luminosity relations are observed for $c < 0$ and $c > 0$. This effect is displayed in Figure A.5.

To examine this color effect on our HR–host-galaxy correlations, we recompute the trends fitting for SN Ia color and host properties simultaneously using LINMIX. We expect that correcting for this correlation with c may weaken our host-galaxy correlations slightly; but, as discussed in Scolnic et al. (2014b), accounting for this color variation is not enough to explain the HR trend with host mass. When fitting for the HR–mass-color relation using the PM sample, the slope of the mass term (-0.054 ± 0.015) is within 0.05σ of the slope recovered when fitting for the HR–mass relation only. We also recover the sSFR slope of the HR–sSFR-color relation for the MZS sample within 0.05σ (0.015 ± 0.046) of the slope measured fitting only HR–sSFR. Interestingly, while the posterior distributions of the mass (and sSFR) and color fit coefficients are Gaussian, the distributions of the metallicity and color coefficients for the HR-metallicity-color relation are clearly skewed. Despite this skewness, we recover the metallicity coefficient (-1.299 ± 0.860) within 1σ of the slope reported fitting the HR–metallicity relation for the MZS sample. In all cases, we find the slope of the color term to be within 1σ of -0.705 ± 0.136.

It seems that including the HR–color correlation in our host-galaxy analysis does not have much of an effect on the observed results. This analysis, however, is only a crude estimate of these effects. LINMIX assumes a linear relation between HR and color, yet in Figure A.5 it is apparent that the HR-color relation varies for low and high values of c. Future works should consider a more robust statistical treatment of this effect.

A.3 PM Sample SN Ia and Host-Galaxy Data

Table A.1. Properties of SNe Ia and their Host Galaxies

CID	IAU Name*	Type*,[a]	Redshift*	SALT2 c	SALT2 x_1	HR[b](mag)	DR8 HostID*	BPT[c]	log(M/$M_\odot$)*,†	12 + log(O/H)†	log(sSFR)†	gFF[d]	Source
703	...	P	0.30	-0.01 ± 0.05	0.66 ± 0.65	-0.15 ± 0.17	1237663544222483004	1	9.96 ± 0.13	8.92 ± 0.05	-9.82 ± 0.13	0.46	BOSS
762	2005eg	S	0.19	-0.04 ± 0.03	1.13 ± 0.27	0.16 ± 0.09	1237666338114765068	1	11.24 ± 0.08	8.92 ± 0.08	-10.16 ± 0.09	0.21	SDSS
779	...	P	0.24	0.02 ± 0.04	0.41 ± 0.39	-0.10 ± 0.12	1237657069548208337	3	10.10 ± 0.09	$-999. \pm -999.$	$-999. \pm -999.$	0.30	BOSS
822	...	P	0.24	-0.09 ± 0.05	-0.58 ± 0.58	0.24 ± 0.16	1237657584950379049	3	10.02 ± 0.15	$-999. \pm -999.$	$-999. \pm -999.$	0.32	BOSS
859	...	P	0.28	0.02 ± 0.04	0.46 ± 0.51	-0.33 ± 0.14	1237666408438301119	1	9.64 ± 0.13	8.80 ± 0.06	-8.91 ± 0.13	0.42	BOSS
911	...	P	0.21	0.24 ± 0.06	-0.48 ± 0.73	-0.10 ± 0.18	1237666407922467526	1	10.14 ± 0.09	8.75 ± 0.05	-9.13 ± 0.09	0.18	BOSS
986	...	P	0.28	0.01 ± 0.06	-0.21 ± 1.09	0.09 ± 0.25	1237663463145079009	1	10.26 ± 0.10	8.61 ± 0.17	-9.21 ± 0.12	0.27	BOSS
1008	2005il	P	0.23	-0.02 ± 0.04	0.46 ± 0.48	-0.11 ± 0.11	1237678617430197147	2	10.61 ± 0.14	9.00 ± 0.11	-11.62 ± 0.31	0.28	BOSS
1032	2005ez	S	0.13	0.05 ± 0.04	-2.54 ± 0.20	-0.02 ± 0.10	1237666302164664434	2	10.68 ± 0.07	9.10 ± 0.06	-11.38 ± 0.09	0.46	SDSS
1112	2005fg	S	0.26	-0.04 ± 0.05	-0.53 ± 0.71	0.10 ± 0.18	1237663478724428434	10	11.35 ± 0.06	8.93 ± 0.09	-9.42 ± 0.07	0.13	SDSS
1119	2005fc	S	0.30	-0.14 ± 0.06	0.86 ± 1.38	0.30 ± 0.28	1237663458851619714	0	10.80 ± 0.07	8.99 ± 0.02	-9.25 ± 0.07	0.29	BOSS
1241	2005ff	S	0.09	0.05 ± 0.02	-0.54 ± 0.08	-0.09 ± 0.06	1237656567586226517	2	10.70 ± 0.11	8.78 ± 0.05	-9.33 ± 0.11	0.13	BOSS
1253	2005fd	S	0.26	-0.10 ± 0.04	-0.93 ± 0.47	-0.12 ± 0.14	1237663457779384632	2	11.15 ± 0.09	9.15 ± 0.05	-11.55 ± 0.12	0.22	BOSS
1354	...	P	0.25	0.20 ± 0.08	-1.12 ± 1.22	-0.15 ± 0.30	1237663784195129684	1	10.63 ± 0.08	8.88 ± 0.02	-8.71 ± 0.09	0.21	BOSS
1371	2005fh	S	0.12	-0.10 ± 0.02	0.79 ± 0.10	-0.15 ± 0.06	1237663277923106978	3	10.89 ± 0.08	$-999. \pm -999.$	$-999. \pm -999.$	0.45	SDSS
1415	...	P	0.21	0.17 ± 0.04	0.92 ± 0.50	-0.21 ± 0.13	1237663716016980100	0	11.64 ± 0.13	9.08 ± 0.07	-11.34 ± 0.16	0.29	SDSS
1658	...	P	0.28	0.00 ± 0.05	0.43 ± 0.47	0.06 ± 0.15	1237657191977845356	1	9.73 ± 0.12	8.57 ± 0.95	-9.51 ± 0.18	0.27	BOSS
1794	2005fj	S	0.14	0.03 ± 0.03	1.17 ± 0.32	0.11 ± 0.08	1237663542603809147	3	9.27 ± 0.08	$-999. \pm -999.$	$-999. \pm -999.$	0.21	BOSS
1979	...	P	0.29	0.01 ± 0.06	-1.28 ± 1.08	-0.16 ± 0.26	1237678617406604390	1	9.74 ± 0.17	8.78 ± 0.16	-10.09 ± 0.21	0.33	BOSS
2017	2005fo	S	0.26	-0.11 ± 0.04	1.37 ± 0.56	0.30 ± 0.16	1237663479793714269	1	10.55 ± 0.08	9.09 ± 0.03	-9.73 ± 0.09	0.32	BOSS
2081	...	P	0.25	-0.10 ± 0.05	-0.43 ± 0.82	0.25 ± 0.18	1237660024493834637	1	10.09 ± 0.09	8.86 ± 0.07	-9.43 ± 0.10	0.53	SDSS
2149	...	P	0.30	-0.09 ± 0.06	0.29 ± 0.73	0.33 ± 0.20	1237666338652487684	3	10.49 ± 0.16	$-999. \pm -999.$	$-999. \pm -999.$	0.35	BOSS
2330	2005fp	S	0.21	0.02 ± 0.06	-1.79 ± 0.58	0.41 ± 0.17	1237678434328183252	1	9.87 ± 0.10	9.14 ± 0.05	-10.42 ± 0.13	0.28	BOSS
2372	2005ft	S	0.18	0.03 ± 0.03	0.31 ± 0.22	-0.09 ± 0.08	1237657070091108996	1	10.60 ± 0.08	9.02 ± 0.05	-9.90 ± 0.08	0.31	BOSS
2440	2005fu	S	0.19	-0.08 ± 0.03	0.43 ± 0.29	0.21 ± 0.09	1237678617436487971	1	10.32 ± 0.08	8.86 ± 0.02	-8.82 ± 0.08	0.28	BOSS
2532	...	P	0.27	0.00 ± 0.05	0.89 ± 0.63	0.21 ± 0.19	1237663783672676591	20	11.44 ± 0.10	9.06 ± 0.13	-11.42 ± 0.19	0.14	BOSS
2561	2005fv	S	0.12	0.04 ± 0.03	-0.08 ± 0.11	0.04 ± 0.06	1237678437019287600	1	10.76 ± 0.06	8.78 ± 0.07	-10.36 ± 0.07	0.20	SDSS
2639	...	P	0.22	0.00 ± 0.03	0.40 ± 0.28	-0.33 ± 0.10	1237663544219926794	0	10.92 ± 0.07	9.55 ± 0.05	-14.40 ± 0.61	0.39	BOSS
2766	...	P	0.15	-0.05 ± 0.03	-0.05 ± 0.40	-0.06 ± 0.09	1237666300019802272	0	11.25 ± 0.11	8.98 ± 0.05	-10.57 ± 0.12	0.34	SDSS
2789	2005fx	S	0.29	-0.11 ± 0.05	-0.77 ± 0.55	0.00 ± 0.17	1237663444906017256	3	11.22 ± 0.17	$-999. \pm -999.$	$-999. \pm -999.$	0.25	BOSS
2855	...	P	0.25	-0.04 ± 0.04	0.66 ± 0.43	-0.01 ± 0.15	1237663783667630515	1	9.71 ± 0.11	8.95 ± 0.06	-9.34 ± 0.12	0.38	BOSS
2871	...	P	0.29	-0.04 ± 0.02	-0.77 ± 0.96	0.14 ± 0.21	1237663782590873812	0	11.30 ± 0.11	9.20 ± 11.14	-10.04 ± 0.31	0.27	BOSS
2992	2005gp	S	0.13	0.10 ± 0.03	-0.96 ± 0.14	-0.20 ± 0.07	1237663237667553616	1	10.23 ± 0.06	8.83 ± 0.06	-9.85 ± 0.06	0.29	SDSS
3080	2005ga	S	0.17	-0.05 ± 0.02	0.11 ± 0.19	-0.13 ± 0.07	1237666338115354816	2	10.96 ± 0.11	8.91 ± 0.04	-9.91 ± 0.11	0.26	BOSS
3087	2005gc	S	0.17	0.01 ± 0.02	0.53 ± 0.19	-0.09 ± 0.07	1237666338116927817	1	9.66 ± 0.09	8.61 ± 0.09	-9.49 ± 0.10	0.20	BOSS
3317	2005gd	S	0.16	0.02 ± 0.03	-0.51 ± 0.19	-0.14 ± 0.07	1237657071695823233	1	10.05 ± 0.07	8.96 ± 0.05	-9.72 ± 0.08	0.20	BOSS
3426	...	P	0.23	-0.15 ± 0.03	-0.28 ± 0.44	0.20 ± 0.12	1237663479799415139	0	11.04 ± 0.09	8.87 ± 0.04	-9.22 ± 0.09	0.26	BOSS
3451	2005gf	S	0.25	-0.07 ± 0.03	0.75 ± 0.33	-0.14 ± 0.11	1237663544221499805	0	10.84 ± 0.12	8.96 ± 0.05	-10.35 ± 0.14	0.31	BOSS
3452	2005gg	S	0.23	-0.08 ± 0.03	0.89 ± 0.27	-0.03 ± 0.09	1237663544221762366	1	9.23 ± 0.09	8.73 ± 0.82	-8.99 ± 0.12	0.33	BOSS
3565	...	P	0.29	-0.19 ± 0.05	-1.15 ± 0.49	0.22 ± 0.17	1237657191980073195	2	11.95 ± 0.13	9.03 ± 0.16	-10.46 ± 0.19	0.21	SDSS
3592	2005gb	S	0.09	-0.04 ± 0.02	-0.14 ± 0.07	-0.02 ± 0.06	1237663204922491010	2	10.74 ± 0.07	9.00 ± 0.03	-9.53 ± 0.07	0.21	SDSS
3887	...	P	0.30	0.03 ± 0.08	-2.69 ± 1.01	-0.28 ± 0.30	1237663784202207497	0	10.86 ± 0.11	$-999. \pm -999.$	-9.05 ± 0.12	0.37	BOSS
3945	...	P	0.26	-0.16 ± 0.34	0.49 ± 0.09	0.35 ± 0.84	1237663783654392436	2	9.76 ± 0.11	8.74 ± 0.07	-9.31 ± 0.12	0.40	BOSS
4000	2005gt	S	0.28	-0.01 ± 0.06	-1.04 ± 0.61	0.10 ± 0.21	1237663783674118396	10	10.92 ± 0.08	8.88 ± 0.16	-10.49 ± 0.18	0.21	BOSS
4019	...	P	0.18	0.16 ± 0.04	0.51 ± 0.28	-0.08 ± 0.09	1237657192516354264	1	11.04 ± 0.07	9.05 ± 0.05	-9.80 ± 0.08	0.30	SDSS
4046	2005gw	S	0.28	-0.01 ± 0.04	0.81 ± 0.52	0.01 ± 0.16	1237657191976534239	1	9.36 ± 0.31	8.99 ± 0.03	-7.81 ± 0.31	0.56	BOSS
4181	...	P	0.29	-0.09 ± 0.04	1.88 ± 0.73	0.26 ± 0.18	1237663782603325756	3	10.44 ± 0.08	$-999. \pm -999.$	$-999. \pm -999.$	0.31	BOSS
4206	...	P	0.29	0.03 ± 0.07	-1.52 ± 0.64	-0.06 ± 0.21	1237666407366328709	1	11.01 ± 0.15	8.91 ± 0.07	-9.68 ± 0.15	0.33	BOSS
4311	...	P	0.30	-0.02 ± 0.05	0.09 ± 0.52	-0.17 ± 0.18	1237678617431900508	3	10.48 ± 0.08	$-999. \pm -999.$	$-999. \pm -999.$	0.34	BOSS

Table A.1 (cont'd)

CID	IAU Name*	Type^{*,a}	Redshift*	SALT2 c	SALT2 x_1	HR^{b}(mag)	DR8 HostID*	BPT^{c}	log(M/$M_{\odot}$)*,†	12 + log(O/H)†	log(sSFR)†	gFF^{d}	Source
4676	...	P	0.25	-0.09 ± 0.03	0.60 ± 0.11	0.06 ± 0.09	1237663204922425799	1	10.27 ± 0.12	8.80 ± 0.11	-9.07 ± 0.12	0.35	BOSS
5103	2005gx	S	0.16	0.02 ± 0.03	-0.23 ± 0.15	-0.09 ± 0.07	1237657191978893955	1	9.09 ± 0.08	8.43 ± 0.33	-8.47 ± 0.10	0.34	BOSS
5199	...	P	0.22	0.13 ± 0.05	0.77 ± 0.56	0.24 ± 0.15	1237656906350199183	1	9.54 ± 0.11	8.78 ± 0.10	-9.43 ± 0.14	0.41	BOSS
5235	...	P	0.25	0.01 ± 0.05	-0.47 ± 0.40	-0.03 ± 0.14	1237663544222876100	1	9.01 ± 0.18	8.47 ± 0.39	-9.30 ± 0.30	0.83	BOSS
5473	...	P	0.28	-0.07 ± 0.05	-1.07 ± 0.43	0.08 ± 0.16	1237666408440135898	0	11.29 ± 0.14	9.19 ± 0.06	-12.08 ± 0.33	0.23	BOSS
5486	...	P	0.23	0.06 ± 0.05	1.27 ± 0.60	0.13 ± 0.15	1237663478721872641	1	10.22 ± 0.08	8.79 ± 0.04	-9.23 ± 0.09	0.23	BOSS
5533	2005hu	S	0.22	0.02 ± 0.03	-0.06 ± 0.28	-0.01 ± 0.08	1237663543682270143	1	9.96 ± 0.09	8.52 ± 0.11	-9.47 ± 0.10	0.17	BOSS
5549	2005hx	S	0.12	0.00 ± 0.02	0.25 ± 0.10	0.00 ± 0.05	1237657191443530063	1	8.72 ± 0.10	8.50 ± 0.18	-9.40 ± 0.14	0.52	BOSS
5550	2005hy	S	0.16	-0.05 ± 0.02	1.91 ± 0.20	0.03 ± 0.06	1237657191443661086	1	9.56 ± 0.10	8.64 ± 0.04	-8.98 ± 0.10	0.26	BOSS
5635	2005hv	S	0.18	-0.03 ± 0.04	0.06 ± 0.41	0.40 ± 0.10	1237663543147364468	3	9.48 ± 0.07	$-999. \pm -999.$	$-999. \pm -999.$	0.41	BOSS
5751	2005hz	S	0.13	0.15 ± 0.02	0.65 ± 0.11	-0.09 ± 0.05	1237663204919279814	1	10.78 ± 0.10	9.06 ± 0.04	-9.61 ± 0.10	0.18	BOSS
5776	...	P	0.24	-0.17 ± 0.06	0.11 ± 0.51	0.38 ± 0.17	1237656568119099748	0	11.18 ± 0.09	8.88 ± 0.06	-10.76 ± 0.13	0.24	BOSS
5890	...	P	0.18	-0.01 ± 0.04	0.11 ± 0.31	0.05 ± 0.09	1237663479795286373	2	10.74 ± 0.09	8.97 ± 0.02	-9.76 ± 0.10	0.30	BOSS
5917	...	P	0.30	-0.10 ± 0.04	0.35 ± 0.49	-0.18 ± 0.13	1237663783663174738	3	9.88 ± 0.19	$-999. \pm -999.$	$-999. \pm -999.$	0.21	BOSS
5957	2005ie	S	0.28	-0.11 ± 0.04	-0.11 ± 0.44	0.08 ± 0.12	1237663783675756839	1	10.46 ± 0.09	9.05 ± 0.03	-9.39 ± 0.09	0.40	BOSS
5959	...	P	0.21	-0.07 ± 0.03	-0.17 ± 0.26	0.07 ± 0.08	1237663783677198401	2	11.16 ± 0.14	9.04 ± 0.10	-9.97 ± 0.15	0.12	BOSS
5963	...	P	0.24	0.00 ± 0.04	-0.07 ± 0.37	-0.18 ± 0.10	1237663716019208746	1	10.36 ± 0.09	8.88 ± 0.05	-9.58 ± 0.10	0.23	BOSS
6192	2005jy	S	0.27	-0.05 ± 0.05	-1.94 ± 0.79	-0.06 ± 0.17	1237678617412764350	1	9.64 ± 0.12	8.22 ± 1.19	-9.45 ± 0.18	0.24	BOSS
6196	2005ig	S	0.28	-0.01 ± 0.05	-1.44 ± 0.59	-0.33 ± 0.14	1237663542612460262	3	11.41 ± 0.15	$-999. \pm -999.$	$-999. \pm -999.$	0.26	BOSS
6249	2005ii	S	0.30	0.03 ± 0.05	0.60 ± 0.70	-0.04 ± 0.16	1237657190369788342	1	10.05 ± 0.12	$10.68 \pm -999.$	$-999. \pm -999.$	0.28	BOSS
6275	...	P	0.27	0.14 ± 0.05	-0.15 ± 0.67	-0.36 ± 0.15	1237663784212562431	1	11.07 ± 0.12	8.85 ± 0.07	-9.45 ± 0.13	0.33	BOSS
6304	2005jk	S	0.19	0.07 ± 0.03	-0.49 ± 0.39	-0.09 ± 0.09	1237678617429410146	1	10.66 ± 0.06	8.84 ± 0.07	-9.51 ± 0.07	0.14	BOSS
6406	2005ij	S	0.12	0.00 ± 0.02	0.13 ± 0.13	-0.10 ± 0.06	1237660024523915530	1	10.55 ± 0.06	8.85 ± 0.05	-9.71 ± 0.07	0.23	SDSS
6422	2005id	S	0.19	-0.11 ± 0.02	0.82 ± 0.22	0.04 ± 0.07	1237663783118897693	1	9.77 ± 0.09	8.79 ± 0.07	-9.52 ± 0.11	0.28	BOSS
6431	...	P	0.26	-0.12 ± 0.07	-2.24 ± 0.60	0.20 ± 0.20	1237663783126958311	0	11.20 ± 0.11	8.54 ± 0.20	-10.39 ± 0.22	0.26	BOSS
6479	...	P	0.23	0.00 ± 0.03	-0.72 ± 0.45	-0.19 ± 0.11	1237678617400509664	2	10.35 ± 0.09	8.81 ± 0.04	-9.52 ± 0.09	0.38	BOSS
6530	...	P	0.19	-0.09 ± 0.04	-1.53 ± 0.03	0.04 ± 0.09	1237663784203649195	3	10.34 ± 0.10	$-999. \pm -999.$	$-999. \pm -999.$	0.51	BOSS
6556	...	P	0.26	0.13 ± 0.05	-0.92 ± 0.57	-0.48 ± 0.13	1237663782589825292	0	11.15 ± 0.07	9.03 ± 0.03	-9.66 ± 0.07	0.21	BOSS
6560	...	P	0.27	-0.02 ± 0.08	-1.12 ± 1.06	0.14 ± 0.22	1237663458852078081	1	9.70 ± 0.09	8.64 ± 0.11	-9.03 ± 0.12	0.37	BOSS
6709	...	P	0.28	0.05 ± 0.09	-1.22 ± 1.06	0.18 ± 0.26	1237663277925139062	2	11.60 ± 0.10	8.78 ± 0.11	-9.09 ± 0.11	0.16	BOSS
6780	2005iz	S	0.20	-0.04 ± 0.04	-1.77 ± 0.38	-0.11 ± 0.11	1237663543682007593	10	11.27 ± 0.09	9.13 ± 0.19	-13.59 ± 0.36	0.21	BOSS
6895	...	P	0.22	0.17 ± 0.04	0.20 ± 0.51	-0.35 ± 0.11	1237678617404768743	2	11.29 ± 0.11	9.26 ± 0.08	-11.44 ± 0.18	0.10	BOSS
6903	...	P	0.25	0.00 ± 0.05	-1.44 ± 0.60	-0.21 ± 0.15	1237678617407062453	0	11.45 ± 0.09	8.67 ± 0.10	-10.33 ± 0.12	0.25	BOSS
6936	2005jl	S	0.18	-0.02 ± 0.03	0.03 ± 0.31	0.02 ± 0.08	1237656567579870979	1	10.26 ± 0.08	8.90 ± 0.05	-9.44 ± 0.08	0.17	BOSS
7099	...	P	0.22	-0.03 ± 0.03	1.31 ± 0.32	-0.18 ± 0.09	1237678617410338948	1	10.80 ± 0.05	9.18 ± 0.13	-12.03 ± 0.13	0.19	BOSS
7147	2005jh	S	0.11	-0.10 ± 0.02	-1.94 ± 0.14	0.03 ± 0.06	1237657190900826305	0	10.56 ± 0.06	$-999. \pm -999.$	-9.45 ± 0.23	0.25	BOSS
7243	2005jm	S	0.20	-0.02 ± 0.04	0.68 ± 0.39	0.01 ± 0.11	1237663479793386066	1	9.22 ± 0.13	8.20 ± 0.30	-9.11 ± 0.14	0.33	BOSS
7258	...	P	0.25	-0.06 ± 0.04	1.45 ± 0.96	0.57 ± 0.18	1237657189814501509	1	11.19 ± 0.11	11.71 ± 57.26	-8.99 ± 0.60	0.28	BOSS
7373	...	P	0.28	-0.07 ± 0.04	1.52 ± 0.52	0.13 ± 0.13	1237663277924614415	1	10.55 ± 0.07	9.03 ± 0.02	-9.13 ± 0.08	0.33	BOSS
7444	...	P	0.25	0.00 ± 0.04	0.95 ± 0.54	0.32 ± 0.15	1237663784746418640	1	9.95 ± 0.11	8.79 ± 0.07	-9.47 ± 0.12	0.33	BOSS
7600	...	P	0.19	0.00 ± 0.04	-2.40 ± 0.36	-0.08 ± 0.10	1237663275774836989	0	11.08 ± 0.09	9.18 ± 0.09	-11.74 ± 0.20	0.25	BOSS
7847	2005jp	S	0.21	0.12 ± 0.03	0.14 ± 0.40	-0.16 ± 0.10	1237666407919780198	3	10.70 ± 0.14	$-999. \pm -999.$	$-999. \pm -999.$	0.33	BOSS
8046	2005ju	S	0.26	0.05 ± 0.05	0.23 ± 0.49	0.00 ± 0.14	1237663784751399105	20	11.33 ± 0.09	$-999. \pm -999.$	-8.67 ± 0.12	0.21	BOSS
8195	...	P	0.27	0.14 ± 0.06	1.27 ± 0.94	-0.05 ± 0.23	1237657189818761524	2	11.79 ± 0.13	8.89 ± 0.13	-10.07 ± 0.14	0.29	SDSS
8213	2005ko	S	0.19	0.16 ± 0.04	-0.66 ± 0.34	-0.17 ± 0.10	1237656906354000314	2	10.52 ± 0.17	9.12 ± 0.07	-10.52 ± 0.18	0.26	BOSS
8216	...	P	0.29	0.06 ± 0.06	-0.69 ± 0.63	-0.09 ± 0.19	1237663543146513432	1	9.78 ± 0.12	8.89 ± 0.09	-9.42 ± 0.13	0.38	BOSS
8254	...	P	0.19	0.05 ± 0.05	-0.89 ± 0.42	0.11 ± 0.12	1237663462607487236	1	9.72 ± 0.08	8.64 ± 0.04	-9.30 ± 0.08	0.37	BOSS
8495	2005mi	S	0.22	-0.02 ± 0.04	0.73 ± 0.46	-0.05 ± 0.11	1237656567585177898	2	11.03 ± 0.06	9.02 ± 0.02	-9.66 ± 0.07	0.19	BOSS
8555	...	P	0.20	0.12 ± 0.04	-1.19 ± 0.39	0.31 ± 0.12	1237663783661797768	1	9.97 ± 0.08	8.96 ± 0.05	-9.21 ± 0.09	0.62	SDSS

Table A.1 (cont'd)

CID	IAU Name⋆	Type⋆,[a]	Redshift⋆	SALT2 c	SALT2 x_1	HR[b](mag)	DR8 HostID⋆	BPT[c]	log(M/$M_\odot$)⋆,†	12 + log(O/H)†	log(sSFR)†	gFF[d]	Source
8719	2005kp	S	0.12	-0.06 ± 0.02	0.01 ± 0.17	0.02 ± 0.06	1237663783127023965	1	9.31 ± 0.07	8.19 ± 0.27	-8.63 ± 0.09	0.22	BOSS
8921	2005ld	S	0.15	-0.02 ± 0.03	0.79 ± 0.25	0.03 ± 0.07	1237663543143825907	1	10.22 ± 0.06	8.70 ± 0.03	-9.02 ± 0.06	0.16	BOSS
9109	...	P	0.28	-0.14 ± 0.04	0.38 ± 0.42	0.04 ± 0.13	1237663785282699688	1	9.36 ± 0.17	9.29 ± 7.57	-8.86 ± 0.22	0.46	BOSS
9457	2005li	S	0.26	-0.01 ± 0.06	-0.34 ± 0.60	-0.06 ± 0.17	1237663543685415622	20	11.13 ± 0.15	8.89 ± 0.08	-10.68 ± 0.17	0.25	BOSS
9467	2005lh	S	0.22	-0.15 ± 0.02	-1.37 ± 0.01	0.24 ± 0.08	1237678595929407536	0	10.93 ± 0.08	8.66 ± 0.10	-9.67 ± 0.09	0.19	BOSS
9594	...	P	0.30	0.14 ± 0.08	-0.35 ± 0.99	-0.42 ± 0.23	1237663784205156941	0	11.03 ± 0.11	8.96 ± 0.08	-11.35 ± 0.25	0.29	BOSS
10037	...	P	0.25	0.02 ± 0.08	-1.00 ± 0.62	0.09 ± 0.23	1237678617936986968	0	11.11 ± 0.14	8.64 ± 0.07	-10.17 ± 0.16	0.31	BOSS
10299	...	P	0.26	-0.03 ± 0.07	0.99 ± 1.17	0.33 ± 0.24	1237663480336417538	1	9.68 ± 0.13	8.64 ± 0.07	-9.11 ± 0.13	0.31	BOSS
10559	...	P	0.28	0.02 ± 0.06	1.18 ± 0.62	0.00 ± 0.18	1237663275777720792	0	10.76 ± 0.10	8.87 ± 0.06	-9.58 ± 0.12	0.28	BOSS
11306	...	P	0.27	-0.04 ± 0.07	0.56 ± 0.79	-0.04 ± 0.20	1237666300021506130	2	11.30 ± 0.13	9.11 ± 0.16	-10.33 ± 0.15	0.31	SDSS
12781	2006er	S	0.08	0.04 ± 0.03	-1.83 ± 0.19	0.18 ± 0.08	1237657189833834706	0	10.94 ± 0.08	9.08 ± 0.07	-11.65 ± 0.15	0.24	SDSS
12804	...	P	0.13	0.03 ± 0.03	0.41 ± 0.32	0.06 ± 0.08	1237663278472626412	1	9.57 ± 0.07	8.72 ± 0.02	-9.26 ± 0.07	0.33	BOSS
12841	2006gk	S	0.29	-0.11 ± 0.11	-0.69 ± 1.08	-0.01 ± 0.22	1237657189814567778	1	10.12 ± 0.13	9.08 ± 0.04	-10.16 ± 0.14	0.20	BOSS
12843	2006fa	S	0.17	0.04 ± 0.04	-1.01 ± 0.30	-0.29 ± 0.09	1237657189815681386	0	11.26 ± 0.09	9.19 ± 0.05	-12.67 ± 0.34	0.30	SDSS
12856	2006fl	S	0.17	-0.09 ± 0.02	0.87 ± 0.20	0.04 ± 0.07	1237663544220975551	1	10.35 ± 0.05	8.95 ± 0.06	-9.60 ± 0.07	0.23	SDSS
12860	2006fc	S	0.12	0.14 ± 0.03	-0.30 ± 0.20	0.05 ± 0.07	1237678617938821532	1	10.61 ± 0.05	8.83 ± 0.04	-9.31 ± 0.06	0.15	BOSS
12875	...	P	0.26	0.02 ± 0.09	-1.04 ± 0.63	0.13 ± 0.23	1237657190903972226	0	10.06 ± 0.15	8.93 ± 0.06	-9.91 ± 0.17	0.49	BOSS
12881	2006gu	S	0.24	0.02 ± 0.03	0.88 ± 0.54	-0.12 ± 0.13	1237657190909673909	1	9.68 ± 0.11	8.92 ± 0.10	-9.36 ± 0.14	0.44	BOSS
12898	2006fw	S	0.08	0.06 ± 0.02	-0.05 ± 0.09	0.01 ± 0.06	1237666407917289559	3	9.95 ± 0.05	$-999. \pm -999.$	$-999. \pm -999.$	0.25	BOSS
12930	2006ex	S	0.15	0.02 ± 0.03	1.89 ± 0.40	0.14 ± 0.10	1237663542600205560	1	10.90 ± 0.06	$10.68 \pm -999.$	$-999. \pm -999.$	0.16	SDSS
12971	2006ff	S	0.24	-0.08 ± 0.03	1.12 ± 0.53	-0.05 ± 0.13	1237663783663436008	3	11.60 ± 0.10	$-999. \pm -999.$	$-999. \pm -999.$	0.29	SDSS
12977	2006gh	S	0.25	-0.04 ± 0.04	0.06 ± 0.51	-0.10 ± 0.13	1237663783666516561	1	9.61 ± 0.10	8.54 ± 0.14	-9.23 ± 0.12	0.29	BOSS
13016	...	P	0.25	-0.10 ± 0.05	-0.05 ± 0.51	0.24 ± 0.15	1237663785282306656	1	9.53 ± 0.23	8.66 ± 1.24	-9.43 ± 0.28	0.33	BOSS
13025	2006fx	S	0.22	0.04 ± 0.03	0.73 ± 0.31	0.08 ± 0.09	1237663543687905672	1	10.84 ± 0.05	9.03 ± 0.03	-9.61 ± 0.06	0.16	BOSS
13044	2006fm	S	0.13	-0.07 ± 0.02	-0.02 ± 0.13	0.04 ± 0.06	1237663479795287086	1	9.91 ± 0.07	8.90 ± 0.04	-9.81 ± 0.08	0.09	BOSS
13070	2006fu	S	0.20	-0.15 ± 0.03	0.96 ± 0.28	0.09 ± 0.08	1237663783122698517	1	10.27 ± 0.06	8.86 ± 0.06	-9.37 ± 0.08	0.37	SDSS
13099	2006gb	S	0.27	-0.01 ± 0.04	0.31 ± 0.58	0.06 ± 0.15	1237663275780210858	1	10.86 ± 0.08	9.05 ± 0.04	-9.50 ± 0.09	0.34	SDSS
13135	2006fz	S	0.10	-0.06 ± 0.02	-1.40 ± 0.07	0.01 ± 0.05	1237657190370181351	3	11.13 ± 0.08	$-999. \pm -999.$	$-999. \pm -999.$	0.30	SDSS
13152	2006gg	S	0.20	-0.01 ± 0.02	0.30 ± 0.25	-0.18 ± 0.07	1237663784200503825	1	9.39 ± 0.10	8.54 ± 0.09	-9.10 ± 0.10	0.41	BOSS
13305	2006he	S	0.21	-0.02 ± 0.03	1.01 ± 0.30	0.00 ± 0.09	1237663544220189296	1	10.05 ± 0.08	8.60 ± 0.07	-8.66 ± 0.09	0.24	BOSS
13323	...	P	0.23	0.02 ± 0.04	0.36 ± 0.47	0.16 ± 0.12	1237663543142974216	1	10.08 ± 0.08	8.77 ± 0.05	-9.02 ± 0.08	0.25	BOSS
13334	...	P	0.25	0.21 ± 0.08	-0.75 ± 0.74	0.06 ± 0.21	1237663543679190385	1	10.02 ± 0.17	9.05 ± 0.08	-10.14 ± 0.18	0.56	BOSS
13354	2006hr	S	0.16	0.09 ± 0.03	1.05 ± 0.17	-0.11 ± 0.07	1237657069548601421	1	10.47 ± 0.08	8.98 ± 0.03	-9.28 ± 0.08	0.36	SDSS
13432	...	P	0.23	0.07 ± 0.09	-1.36 ± 1.00	-0.03 ± 0.26	1237656567040902467	3	10.38 ± 0.07	$-999. \pm -999.$	$-999. \pm -999.$	0.35	BOSS
13441	...	P	0.29	0.03 ± 0.05	0.43 ± 0.88	-0.05 ± 0.19	1237663783654785302	3	11.13 ± 0.11	8.69 ± 0.12	-10.19 ± 0.21	0.11	BOSS
13465	...	P	0.29	0.07 ± 0.09	-0.96 ± 0.92	0.12 ± 0.26	1237663784192508693	1	9.65 ± 0.11	8.69 ± 0.10	-9.08 ± 0.13	0.42	BOSS
13476	...	P	0.28	0.12 ± 0.05	0.81 ± 0.79	0.15 ± 0.17	1237663783121912302	1	9.96 ± 0.14	8.82 ± 0.14	-9.95 ± 0.16	0.34	BOSS
13487	...	P	0.29	0.03 ± 0.06	-1.25 ± 0.48	-0.04 ± 0.17	1237663784212759337	3	11.10 ± 0.17	$-999. \pm -999.$	$-999. \pm -999.$	0.20	BOSS
13506	2006hg	S	0.24	0.12 ± 0.05	-0.10 ± 0.65	0.04 ± 0.15	1237663783134691657	3	10.19 ± 0.08	$-999. \pm -999.$	$-999. \pm -999.$	0.38	BOSS
13511	2006hh	S	0.24	-0.10 ± 0.04	-1.42 ± 0.46	0.27 ± 0.12	1237663783141441728	2	11.41 ± 0.13	8.93 ± 0.12	-10.38 ± 0.15	0.32	SDSS
13520	...	P	0.27	0.07 ± 0.05	0.03 ± 0.63	-0.30 ± 0.16	1237666339189227760	0	10.49 ± 0.09	8.89 ± 0.08	-10.58 ± 0.12	0.45	BOSS
13610	2006hd	S	0.30	-0.10 ± 0.04	0.16 ± 0.54	-0.15 ± 0.15	1237678617402933784	1	10.47 ± 0.10	8.88 ± 0.03	-8.86 ± 0.11	0.59	SDSS
13647	...	P	0.25	-0.02 ± 0.06	-1.09 ± 0.70	-0.10 ± 0.18	1237657189831606432	0	11.21 ± 0.11	8.98 ± 0.12	-11.65 ± 0.41	0.21	BOSS
13689	...	S	0.25	-0.12 ± 0.01	1.18 ± 0.39	0.11 ± 0.08	1237657191980728518	1	10.45 ± 0.07	8.98 ± 0.02	-8.96 ± 0.08	0.22	BOSS
13703	...	P	0.24	-0.02 ± 0.03	-0.15 ± 0.27	-0.07 ± 0.09	1237678617971785824	2	11.30 ± 0.12	8.90 ± 0.03	-9.65 ± 0.12	0.24	BOSS
13727	2006hj	S	0.23	-0.03 ± 0.03	1.32 ± 0.35	0.00 ± 0.10	1237678617936135644	1	9.95 ± 0.09	8.72 ± 0.08	-9.36 ± 0.10	0.18	BOSS
13736	2006hv	S	0.15	-0.03 ± 0.02	1.12 ± 0.17	0.04 ± 0.06	1237678617407717964	1	9.68 ± 0.08	8.81 ± 0.06	-9.97 ± 0.09	0.22	BOSS
13796	2006hl	S	0.15	-0.02 ± 0.02	0.80 ± 0.12	-0.13 ± 0.06	1237663277923696964	3	10.33 ± 0.06	$-999. \pm -999.$	$-999. \pm -999.$	0.15	BOSS
13835	2006hp	S	0.25	-0.05 ± 0.03	0.61 ± 0.26	-0.06 ± 0.09	1237663783663173820	1	10.51 ± 0.06	8.96 ± 0.02	-9.43 ± 0.07	0.27	BOSS

Table A.1 (cont'd)

CID	IAU Name*	Type^{*,a}	Redshift*	SALT2 c	SALT2 x_1	HR^{b}(mag)	DR8 HostID*	BPT^{c}	log(M/$M_{\odot}$)*,†	12 + log(O/H)†	log(sSFR)†	gFF^{d}	Source
13896	...	P	0.16	0.07 ± 0.04	-0.57 ± 0.39	0.64 ± 0.10	1237657190906397233	2	8.95 ± 0.13	8.80 ± 0.08	-9.79 ± 0.15	0.43	BOSS
13897	...	P	0.23	0.08 ± 0.04	0.54 ± 0.53	0.08 ± 0.14	1237657190907904102	1	10.54 ± 0.06	8.93 ± 0.02	-9.39 ± 0.06	0.38	BOSS
13907	...	P	0.20	0.13 ± 0.04	-0.21 ± 0.30	-0.15 ± 0.10	1237666339724788003	2	11.16 ± 0.15	9.07 ± 0.07	-10.82 ± 0.17	0.23	BOSS
13909	...	P	0.29	-0.11 ± 0.04	0.88 ± 0.39	0.23 ± 0.13	1237666339725771307	3	9.76 ± 0.15	$-999. \pm -999.$	$-999. \pm -999.$	0.18	BOSS
13971	...	P	0.26	0.00 ± 0.06	-0.34 ± 0.68	0.21 ± 0.19	1237678617428165272	1	10.22 ± 0.13	8.42 ± 0.16	-8.95 ± 0.17	0.24	BOSS
14024	2006ht	S	0.15	0.04 ± 0.04	-1.92 ± 0.20	-0.05 ± 0.12	1237678617936396489	3	8.93 ± 0.21	$-999. \pm -999.$	$-999. \pm -999.$	1.13	BOSS
14074	...	P	0.26	0.12 ± 0.06	0.72 ± 0.65	0.10 ± 0.17	1237660025032802799	1	9.82 ± 0.10	8.50 ± 0.12	-9.12 ± 0.13	0.25	BOSS
14113	...	P	0.24	0.17 ± 0.04	-0.64 ± 0.63	-0.56 ± 0.14	1237663783136067815	1	10.27 ± 0.08	9.13 ± 0.07	-9.61 ± 0.09	0.36	BOSS
14212	2006iy	S	0.20	-0.04 ± 0.03	-0.31 ± 0.18	0.06 ± 0.08	1237678595930063495	1	10.50 ± 0.11	8.93 ± 0.12	-10.72 ± 0.12	0.31	BOSS
14261	2006jk	S	0.29	-0.04 ± 0.05	0.68 ± 0.49	-0.19 ± 0.13	1237663543682073622	2	9.13 ± 0.09	9.03 ± 0.07	-9.43 ± 0.11	0.58	BOSS
14284	2006ib	S	0.18	-0.07 ± 0.02	-0.29 ± 0.17	-0.23 ± 0.06	1237666300018163914	-999	10.57 ± 0.12	$-999. \pm -999.$	$-999. \pm -999.$	$-999.$	SDSS
14331	2006kl	S	0.22	0.01 ± 0.04	0.17 ± 0.30	0.14 ± 0.11	1237657190908690822	1	9.70 ± 0.10	8.42 ± 0.47	-8.90 ± 0.13	0.24	BOSS
14333	...	P	0.27	-0.12 ± 0.04	-0.47 ± 0.40	0.14 ± 0.13	1237666339188834503	3	11.00 ± 0.10	$-999. \pm -999.$	$-999. \pm -999.$	0.38	BOSS
14340	...	P	0.28	0.02 ± 0.05	-0.77 ± 0.57	-0.20 ± 0.17	1237656906348888177	3	11.53 ± 0.11	$-999. \pm -999.$	$-999. \pm -999.$	0.41	SDSS
14403	...	P	0.29	-0.13 ± 0.05	-0.77 ± 0.47	0.26 ± 0.16	1237663204921508635	10	10.17 ± 0.13	8.81 ± 0.11	-9.51 ± 0.15	0.40	BOSS
14421	2006ia	S	0.17	-0.09 ± 0.03	-0.68 ± 0.19	0.10 ± 0.08	1237680099167109192	2	11.56 ± 0.08	8.97 ± 0.07	-11.13 ± 0.15	0.16	SDSS
14437	2006hy	S	0.15	-0.10 ± 0.03	0.62 ± 0.12	-0.05 ± 0.06	1237656567046865251	2	10.19 ± 0.13	8.83 ± 0.09	-10.12 ± 0.14	0.44	BOSS
14438	...	P	0.30	-0.09 ± 0.04	1.56 ± 0.62	0.09 ± 0.15	1237660024495014189	3	9.68 ± 0.08	$-999. \pm -999.$	$-999. \pm -999.$	0.44	BOSS
14444	...	P	0.25	-0.16 ± 0.04	-1.08 ± 0.35	0.32 ± 0.12	1237656567585768071	3	10.95 ± 0.10	$-999. \pm -999.$	$-999. \pm -999.$	0.24	BOSS
14445	...	P	0.24	0.01 ± 0.06	-2.37 ± 0.45	0.10 ± 0.17	1237660025032278372	10	11.40 ± 0.11	$-999. \pm -999.$	-10.46 ± 0.24	0.28	BOSS
14470	...	P	0.20	-0.01 ± 0.02	-0.31 ± 0.22	-0.15 ± 0.07	1237663783679885795	3	10.15 ± 0.16	$-999. \pm -999.$	$-999. \pm -999.$	0.33	BOSS
14481	2006lj	S	0.24	-0.13 ± 0.05	-1.06 ± 0.40	0.28 ± 0.14	1237663784198537430	0	11.21 ± 0.12	8.93 ± 0.03	-10.18 ± 0.12	0.23	BOSS
14524	...	P	0.27	0.07 ± 0.05	-0.22 ± 0.50	0.04 ± 0.15	1237663783141835725	10	10.78 ± 0.06	9.00 ± 0.03	-9.05 ± 0.07	0.33	BOSS
14784	...	P	0.19	0.11 ± 0.04	0.66 ± 0.38	0.16 ± 0.11	1237663457242514193	2	10.72 ± 0.10	8.89 ± 0.04	-9.73 ± 0.10	0.28	BOSS
14846	2006jn	S	0.22	-0.05 ± 0.03	0.65 ± 0.29	0.04 ± 0.10	1237663784200765533	1	11.08 ± 0.07	9.04 ± 0.03	-9.58 ± 0.07	0.21	BOSS
14965	...	P	0.28	0.01 ± 0.05	0.03 ± 0.52	-0.27 ± 0.14	1237663785279422932	1	10.01 ± 0.11	8.50 ± 0.17	-9.17 ± 0.12	0.24	BOSS
15033	...	P	0.22	0.07 ± 0.06	-1.67 ± 0.49	0.04 ± 0.18	1237666339188637777	0	11.37 ± 0.08	9.68 ± 0.08	$-999. \pm -999.$	0.22	BOSS
15057	2006md	P	0.25	-0.03 ± 0.06	-2.38 ± 0.58	0.25 ± 0.18	1237666339726426556	1	9.59 ± 0.11	8.36 ± 0.26	-9.10 ± 0.12	0.40	BOSS
15129	2006kq	S	0.20	-0.07 ± 0.03	-0.69 ± 0.23	-0.03 ± 0.09	1237663457240351218	1	10.97 ± 0.08	8.98 ± 0.04	-9.82 ± 0.08	0.29	SDSS
15137	...	P	0.28	-0.08 ± 0.05	-0.69 ± 0.47	0.08 ± 0.14	1237663783121912544	2	10.42 ± 0.13	8.72 ± 0.07	-9.53 ± 0.14	0.40	BOSS
15160	...	P	0.25	0.13 ± 0.05	-0.76 ± 0.43	-0.19 ± 0.14	1237657190367625928	1	10.24 ± 0.09	9.00 ± 0.04	-9.33 ± 0.10	0.25	BOSS
15161	2006jw	S	0.25	-0.08 ± 0.04	-0.26 ± 0.25	0.00 ± 0.10	1237657587095765661	1	11.06 ± 0.08	9.02 ± 0.12	-9.91 ± 0.10	0.14	SDSS
15198	...	P	0.29	-0.07 ± 0.03	0.28 ± 0.35	0.00 ± 0.11	1237663783675691751	1	9.57 ± 0.14	8.77 ± 0.20	-9.68 ± 0.21	0.29	BOSS
15201	2006ks	S	0.21	0.12 ± 0.04	-1.25 ± 0.48	0.30 ± 0.12	1237663479260643634	0	11.31 ± 0.10	8.86 ± 0.31	-11.53 ± 0.53	0.16	BOSS
15203	2006jy	S	0.20	-0.01 ± 0.03	1.16 ± 0.28	0.01 ± 0.08	1237663784204304772	3	10.22 ± 0.08	$-999. \pm -999.$	$-999. \pm -999.$	0.45	BOSS
15219	2006ka	S	0.25	-0.14 ± 0.03	-0.15 ± 0.39	0.08 ± 0.10	1237666408457568503	2	11.08 ± 0.09	8.85 ± 0.04	-9.63 ± 0.09	0.30	BOSS
15222	2006jz	S	0.20	0.01 ± 0.03	-1.33 ± 0.29	-0.14 ± 0.10	1237657191980204184	3	11.57 ± 0.12	$-999. \pm -999.$	$-999. \pm -999.$	0.21	SDSS
15226	...	P	0.29	0.09 ± 0.07	-1.16 ± 0.53	-0.27 ± 0.18	1237657071698707180	3	10.68 ± 0.12	$-999. \pm -999.$	$-999. \pm -999.$	0.45	BOSS
15234	2006kd	S	0.14	0.13 ± 0.03	0.90 ± 0.21	0.25 ± 0.07	1237663204921573628	1	10.52 ± 0.07	9.08 ± 0.05	-10.00 ± 0.08	0.29	SDSS
15260	...	P	0.25	0.15 ± 0.04	1.33 ± 0.45	-0.22 ± 0.13	1237663478724494011	1	10.44 ± 0.13	9.00 ± 0.04	-9.65 ± 0.13	0.32	BOSS
15268	...	P	0.30	-0.11 ± 0.04	0.51 ± 0.67	0.09 ± 0.16	1237663479261037240	1	9.51 ± 0.07	8.53 ± 0.12	-8.72 ± 0.10	0.38	BOSS
15272	...	P	0.28	0.00 ± 0.05	-1.10 ± 0.60	-0.29 ± 0.15	1237663784193360056	0	11.66 ± 0.09	8.97 ± 0.03	-9.90 ± 0.10	0.17	BOSS
15287	2006kt	S	0.24	-0.03 ± 0.03	1.09 ± 0.31	0.11 ± 0.09	1237656567043327064	3	10.62 ± 0.17	$-999. \pm -999.$	$-999. \pm -999.$	0.35	BOSS
15301	2006lo	P	0.18	-0.02 ± 0.03	-0.33 ± 0.23	0.05 ± 0.08	1237663458316125530	1	10.12 ± 0.09	9.00 ± 0.05	-10.24 ± 0.10	0.33	BOSS
15325	...	P	0.21	0.04 ± 0.04	-0.36 ± 0.35	-0.04 ± 0.10	1237663783137771858	0	10.95 ± 0.10	9.80 ± 0.08	-15.29 ± 4059.13	0.33	BOSS
15347	...	P	0.27	0.00 ± 0.05	-0.85 ± 0.44	-0.30 ± 0.15	1237678617939543280	0	10.74 ± 0.15	9.04 ± 0.05	-10.51 ± 0.16	0.38	BOSS
15356	2006lm	S	0.27	-0.04 ± 0.04	-0.64 ± 0.50	-0.18 ± 0.14	1237663543685087893	0	10.74 ± 0.19	8.95 ± 0.18	-11.34 ± 0.60	0.38	BOSS
15365	2006ku	S	0.19	-0.06 ± 0.03	0.79 ± 0.23	0.08 ± 0.08	1237678617415450837	2	11.18 ± 0.09	9.00 ± 0.03	-9.70 ± 0.09	0.19	BOSS
15419	...	P	0.28	-0.07 ± 0.04	-0.37 ± 0.48	-0.03 ± 0.13	1237663785279816317	3	9.74 ± 0.18	$-999. \pm -999.$	$-999. \pm -999.$	0.52	BOSS

Table A.1 (cont'd)

CID	IAU Name⋆	Type⋆,[a]	Redshift⋆	SALT2 c	SALT2 x_1	HR[b](mag)	DR8 HostID⋆	BPT[c]	log(M/$M_\odot$)⋆,†	12 + log(O/H)†	log(sSFR)†	gFF[d]	Source
15421	2006kw	S	0.19	-0.04 ± 0.03	0.20 ± 0.26	0.13 ± 0.07	1237663784749039900	1	10.17 ± 0.07	8.85 ± 0.05	-9.66 ± 0.08	0.35	SDSS
15425	2006kx	S	0.16	0.00 ± 0.03	0.98 ± 0.17	-0.26 ± 0.06	1237663239278231823	0	10.53 ± 0.07	9.00 ± 0.05	-11.14 ± 0.19	0.60	SDSS
15433	2006mt	S	0.22	-0.06 ± 0.03	-0.06 ± 0.27	0.01 ± 0.09	1237663783667040480	2	10.81 ± 0.09	8.82 ± 0.07	-9.71 ± 0.10	0.30	BOSS
15440	2006lr	S	0.26	0.06 ± 0.04	-0.56 ± 0.53	-0.21 ± 0.13	1237663784214790662	2	10.85 ± 0.14	8.88 ± 0.07	-10.18 ± 0.16	0.30	BOSS
15443	2006lb	S	0.18	-0.04 ± 0.02	1.57 ± 0.18	-0.09 ± 0.06	1237660240313581839	1	10.34 ± 0.06	8.92 ± 0.04	-9.69 ± 0.08	0.41	SDSS
15459	2006la	S	0.13	0.11 ± 0.03	0.38 ± 0.22	0.47 ± 0.07	1237656906346660220	1	9.08 ± 0.07	8.55 ± 0.07	-9.44 ± 0.07	0.36	BOSS
15461	2006kz	S	0.19	-0.11 ± 0.03	-0.18 ± 0.21	-0.01 ± 0.07	1237663542607741904	1	10.52 ± 0.08	9.05 ± 0.06	-10.08 ± 0.09	0.15	BOSS
15466	2006mz	S	0.25	0.01 ± 0.05	-1.05 ± 0.40	-0.25 ± 0.13	1237663543140550186	3	10.62 ± 0.07	$-999. \pm -999.$	$-999. \pm -999.$	0.29	BOSS
15467	...	S	0.21	-0.09 ± 0.03	0.81 ± 0.26	-0.02 ± 0.08	1237663543141597901	1	10.43 ± 0.05	9.00 ± 0.03	-9.48 ± 0.06	0.39	SDSS
15496	...	P	0.23	-0.05 ± 0.03	1.01 ± 0.28	0.05 ± 0.09	1237657191445627367	0	8.86 ± 0.17	9.55 ± 0.08	-13.50 ± 1.31	0.30	BOSS
15508	2006ls	S	0.13	-0.06 ± 0.02	0.88 ± 0.11	0.00 ± 0.06	1237666407380549827	3	9.96 ± 0.07	$-999. \pm -999.$	$-999. \pm -999.$	0.10	BOSS
15535	...	P	0.20	0.04 ± 0.04	-1.82 ± 0.58	0.12 ± 0.13	1237663783661339126	3	10.49 ± 0.15	$-999. \pm -999.$	$-999. \pm -999.$	0.35	BOSS
15584	2006nt	S	0.28	-0.05 ± 0.04	0.39 ± 0.42	-0.08 ± 0.13	1237678437018042944	2	10.90 ± 0.13	9.01 ± 0.08	-9.05 ± 0.15	0.19	BOSS
15587	...	P	0.22	-0.01 ± 0.04	-0.01 ± 0.27	-0.04 ± 0.09	1237660241926226266	2	10.70 ± 0.07	8.97 ± 0.03	-9.74 ± 0.07	0.35	SDSS
15603	...	P	0.26	0.12 ± 0.06	-0.99 ± 0.68	-0.20 ± 0.18	1237663275778507207	2	10.49 ± 0.15	8.79 ± 0.10	-9.53 ± 0.17	0.33	BOSS
15648	2006ni	S	0.17	0.11 ± 0.05	-1.38 ± 0.35	-0.06 ± 0.11	1237663543138845573	2	11.34 ± 0.09	9.15 ± 0.07	-12.74 ± 0.26	0.37	SDSS
15663	...	P	0.29	-0.04 ± 0.05	-0.75 ± 0.61	-0.22 ± 0.17	1237678595932684553	1	10.55 ± 0.14	9.05 ± 0.06	-10.30 ± 0.14	0.34	BOSS
15675	...	P	0.23	-0.05 ± 0.05	-0.65 ± 0.44	0.09 ± 0.13	1237663444905558636	0	10.94 ± 0.12	8.70 ± 0.27	-10.86 ± 0.18	0.27	BOSS
15719	...	P	0.27	-0.06 ± 0.04	-0.65 ± 0.44	-0.05 ± 0.13	1237678437015487028	1	10.33 ± 0.15	8.93 ± 0.09	-9.60 ± 0.16	0.37	BOSS
15755	...	P	0.28	-0.02 ± 0.04	-0.82 ± 0.44	-0.17 ± 0.14	1237666408441708761	2	10.34 ± 0.10	8.93 ± 0.02	-8.51 ± 0.10	0.35	BOSS
15779	...	P	0.26	-0.04 ± 0.06	-0.08 ± 0.73	0.50 ± 0.20	1237666407362396769	1	10.51 ± 0.09	9.02 ± 0.06	-9.52 ± 0.10	0.32	BOSS
15784	...	P	0.28	0.02 ± 0.05	0.00 ± 0.48	-0.20 ± 0.14	1237657190366904466	1	10.56 ± 0.07	8.86 ± 0.02	-9.83 ± 0.08	0.24	BOSS
15806	...	P	0.25	0.02 ± 0.05	-1.95 ± 0.56	-0.12 ± 0.16	1237663783134167750	2	11.10 ± 0.15	$-999. \pm -999.$	-9.25 ± 0.16	0.27	BOSS
15829	...	P	0.25	0.09 ± 0.06	1.07 ± 0.83	0.42 ± 0.20	1237663456705316065	1	9.17 ± 0.13	8.50 ± 0.62	-8.59 ± 0.16	0.47	BOSS
15850	...	P	0.25	-0.07 ± 0.05	-1.19 ± 0.35	0.00 ± 0.13	1237663275780538659	0	11.18 ± 0.10	8.68 ± 0.12	-10.55 ± 0.20	0.27	BOSS
15866	...	P	0.19	0.00 ± 0.04	-0.93 ± 0.31	-0.03 ± 0.11	1237663480334909517	0	11.24 ± 0.08	8.83 ± 0.09	-10.78 ± 0.13	0.19	BOSS
15868	2006pa	S	0.25	-0.23 ± 0.03	0.31 ± 0.24	0.29 ± 0.09	1237663783140328086	1	10.39 ± 0.10	8.89 ± 0.07	-9.17 ± 0.12	0.14	BOSS
15872	2006nb	S	0.21	-0.07 ± 0.04	0.75 ± 0.31	-0.06 ± 0.09	1237663783676609084	1	9.66 ± 0.09	8.92 ± 0.04	-10.17 ± 0.10	0.42	BOSS
15892	...	P	0.18	0.18 ± 0.06	-1.70 ± 0.42	-0.15 ± 0.13	1237678617401688873	1	10.83 ± 0.06	8.96 ± 0.03	-9.26 ± 0.06	0.17	BOSS
15897	2006pb	S	0.17	0.01 ± 0.04	-2.41 ± 0.26	-0.03 ± 0.10	1237657189836587309	3	10.82 ± 0.10	$-999. \pm -999.$	$-999. \pm -999.$	0.33	BOSS
15901	2006od	S	0.20	-0.05 ± 0.03	0.01 ± 0.26	0.01 ± 0.08	1237666407382647396	0	9.97 ± 0.09	8.14 ± 108.08	-4.62 ± 0.56	0.20	BOSS
15909	...	P	0.22	0.05 ± 0.04	-1.09 ± 0.33	-0.17 ± 0.12	1237663204919148757	3	11.21 ± 0.09	$-999. \pm -999.$	$-999. \pm -999.$	0.29	BOSS
15950	...	P	0.22	0.05 ± 0.05	-1.27 ± 0.47	-0.23 ± 0.14	1237663278467317915	2	11.34 ± 0.05	9.00 ± 0.03	-9.81 ± 0.06	0.23	SDSS
16021	2006nc	S	0.12	-0.04 ± 0.02	-0.34 ± 0.13	-0.05 ± 0.06	1237663783666581814	1	10.14 ± 0.07	8.99 ± 0.03	-9.98 ± 0.07	0.15	BOSS
16069	2006nd	S	0.13	0.16 ± 0.03	0.89 ± 0.22	-0.06 ± 0.06	1237656906346856638	1	10.84 ± 0.05	8.98 ± 0.03	-9.23 ± 0.06	0.32	SDSS
16073	2006of	S	0.15	-0.02 ± 0.02	0.74 ± 0.14	0.18 ± 0.06	1237663782590349551	1	9.75 ± 0.09	8.82 ± 0.06	-9.34 ± 0.09	0.28	BOSS
16099	2006nn	S	0.20	0.02 ± 0.02	2.04 ± 0.40	0.11 ± 0.08	1237663782598345186	1	10.66 ± 0.09	8.53 ± 0.33	-10.84 ± 0.20	0.32	SDSS
16172	...	P	0.22	0.10 ± 0.06	0.81 ± 0.59	0.15 ± 0.16	1237663238205407778	1	11.06 ± 0.08	8.95 ± 0.07	-9.91 ± 0.08	0.27	SDSS
16185	2006ok	S	0.10	0.06 ± 0.03	-2.23 ± 0.21	0.01 ± 0.07	1237663783667893113	0	9.72 ± 0.09	8.48 ± 0.20	-10.46 ± 0.40	0.39	BOSS
16199	...	P	0.28	0.06 ± 0.06	0.33 ± 0.74	-0.23 ± 0.16	1237678595931177552	1	10.07 ± 0.13	9.03 ± 0.06	-9.94 ± 0.15	0.33	BOSS
16219	...	P	0.26	0.01 ± 0.06	-0.90 ± 0.61	0.02 ± 0.18	1237663204916789403	2	11.17 ± 0.11	$-999. \pm -999.$	-9.49 ± 0.28	0.31	BOSS
16410	...	P	0.29	-0.10 ± 0.07	0.05 ± 1.04	0.18 ± 0.19	1237678617400181873	1	11.05 ± 0.09	9.08 ± 0.07	-10.20 ± 0.11	0.28	BOSS
16462	...	P	0.24	0.01 ± 0.05	-1.38 ± 0.44	-0.22 ± 0.13	1237663783667957998	0	11.58 ± 0.09	$-999. \pm -999.$	-8.30 ± 0.30	0.29	SDSS
16467	...	P	0.22	0.02 ± 0.05	-1.83 ± 0.47	-0.16 ± 0.14	1237663479256711274	3	11.06 ± 0.08	$-999. \pm -999.$	$-999. \pm -999.$	0.30	BOSS
16606	...	P	0.23	0.16 ± 0.08	-0.80 ± 0.82	0.07 ± 0.20	1237678617410208604	3	10.41 ± 0.17	$-999. \pm -999.$	$-999. \pm -999.$	0.32	BOSS
16739	...	P	0.27	-0.01 ± 0.04	0.93 ± 0.62	0.26 ± 0.14	1237656567042277752	1	10.28 ± 0.10	9.04 ± 0.04	-9.50 ± 0.11	0.42	BOSS
17168	2007ik	S	0.19	-0.04 ± 0.03	0.54 ± 0.31	0.13 ± 0.10	1237660024494883496	1	9.76 ± 0.09	8.55 ± 0.08	-9.21 ± 0.10	0.23	BOSS
17186	2007hx	S	0.08	0.11 ± 0.02	0.65 ± 0.15	0.30 ± 0.07	1237666406845644893	2	10.77 ± 0.06	8.62 ± 0.07	-9.54 ± 0.07	0.10	SDSS
17206	...	P	0.16	0.11 ± 0.04	-0.93 ± 0.42	0.02 ± 0.12	1237666301627465999	2	10.79 ± 0.12	8.95 ± 0.06	-9.75 ± 0.13	0.34	SDSS

Table A.1 (cont'd)

CID	IAU Name*	Type^{*,a}	Redshift*	SALT2 c	SALT2 x_1	HR^{b}(mag)	DR8 HostID*	BPT^{c}	log(M/$M_{\odot}$)*,†	12 + log(O/H)†	log(sSFR)†	gFF^{d}	Source
17215	2007hy	S	0.18	0.02 ± 0.04	0.30 ± 0.42	-0.06 ± 0.11	1237666302168203468	3	11.33 ± 0.08	$-999. \pm -999.$	-9.30 ± 0.15	0.14	SDSS
17218	2007jp	S	0.18	-0.08 ± 0.03	-0.79 ± 0.41	-0.02 ± 0.10	1237657190903513358	1	10.16 ± 0.07	8.98 ± 0.03	-9.51 ± 0.07	0.35	BOSS
17220	2007ji	S	0.18	0.13 ± 0.03	1.86 ± 0.29	-0.19 ± 0.09	1237657190909476940	2	10.86 ± 0.13	9.10 ± 0.04	-10.25 ± 0.14	0.32	BOSS
17332	2007jk	S	0.18	0.04 ± 0.03	-0.21 ± 0.28	-0.12 ± 0.10	1237660339089899929	2	10.60 ± 0.12	9.11 ± 0.12	-10.22 ± 0.13	0.34	SDSS
17340	2007kl	S	0.26	-0.01 ± 0.04	-0.10 ± 0.44	-0.17 ± 0.14	1237666408460452080	0	11.44 ± 0.11	8.99 ± 0.10	-10.54 ± 0.12	0.21	SDSS
17366	2007hz	S	0.14	-0.09 ± 0.03	0.57 ± 0.17	-0.07 ± 0.07	1237663542066020598	10	10.97 ± 0.06	8.98 ± 0.06	-9.95 ± 0.06	0.19	SDSS
17374	...	P	0.25	-0.07 ± 0.04	0.25 ± 0.66	-0.01 ± 0.16	1237663542067659081	3	11.07 ± 0.14	$-999. \pm -999.$	$-999. \pm -999.$	0.15	BOSS
17389	2007ih	S	0.17	0.06 ± 0.03	1.13 ± 0.38	0.27 ± 0.10	1237666185626256736	1	9.89 ± 0.08	8.81 ± 0.05	-9.36 ± 0.09	0.26	BOSS
17393	...	P	0.22	0.01 ± 0.06	-0.84 ± 1.01	0.10 ± 0.23	1237657189818041289	1	9.65 ± 0.12	8.69 ± 0.14	-9.35 ± 0.15	0.25	BOSS
17408	...	P	0.24	-0.03 ± 0.05	0.33 ± 0.74	0.03 ± 0.19	1237663544214160228	2	11.20 ± 0.09	8.91 ± 0.13	-11.04 ± 0.20	0.19	BOSS
17423	...	P	0.27	-0.17 ± 0.04	-0.21 ± 0.71	0.27 ± 0.16	1237663783117390131	0	10.97 ± 0.13	9.09 ± 0.04	-9.86 ± 0.13	0.35	BOSS
17433	...	P	0.29	0.06 ± 0.06	1.04 ± 0.87	-0.04 ± 0.23	1237657190906593911	1	9.50 ± 0.17	8.58 ± 0.18	-9.47 ± 0.21	0.39	BOSS
17497	2007jt	S	0.14	0.04 ± 0.02	0.91 ± 0.13	-0.03 ± 0.06	1237663237122687153	1	10.43 ± 0.05	9.00 ± 0.04	-9.47 ± 0.07	0.23	SDSS
17552	2007jl	S	0.25	-0.01 ± 0.04	1.34 ± 0.42	0.08 ± 0.13	1237657189814960898	2	10.69 ± 0.11	8.84 ± 0.04	-9.56 ± 0.11	0.25	BOSS
17586	...	P	0.27	0.11 ± 0.07	-0.67 ± 1.11	-0.47 ± 0.26	1237656567582819018	3	10.51 ± 0.09	$-999. \pm -999.$	$-999. \pm -999.$	0.22	BOSS
17605	2007js	S	0.15	0.02 ± 0.04	0.81 ± 0.36	0.01 ± 0.10	1237663479248192988	3	10.84 ± 0.05	$-999. \pm -999.$	$-999. \pm -999.$	0.44	SDSS
17629	2007jw	S	0.14	0.06 ± 0.03	-0.35 ± 0.15	-0.15 ± 0.07	1237663782600180017	2	11.20 ± 0.06	9.06 ± 0.03	-10.02 ± 0.07	0.24	SDSS
17748	...	P	0.18	0.17 ± 0.04	1.17 ± 0.55	0.31 ± 0.14	1237663783664812351	1	9.99 ± 0.07	8.82 ± 0.06	-9.19 ± 0.09	0.18	BOSS
17773	...	P	0.29	-0.13 ± 0.05	-1.02 ± 0.66	0.03 ± 0.17	1237663783675101438	1	9.84 ± 0.11	8.94 ± 0.08	-8.95 ± 0.13	0.36	BOSS
17809	2007kr	S	0.29	0.01 ± 0.03	1.63 ± 0.45	-0.08 ± 0.12	1237663783126434560	1	9.84 ± 0.12	8.78 ± 0.11	-8.96 ± 0.15	0.32	BOSS
17884	2007kt	S	0.24	-0.12 ± 0.03	0.71 ± 0.28	0.04 ± 0.10	1237678617429934631	1	10.45 ± 0.08	9.12 ± 0.05	-9.89 ± 0.09	0.19	BOSS
17899	...	P	0.29	0.02 ± 0.05	1.07 ± 0.50	-0.20 ± 0.17	1237657190902464955	1	9.84 ± 0.12	8.56 ± 0.13	-9.18 ± 0.14	0.43	BOSS
17908	...	P	0.23	0.04 ± 0.06	-1.11 ± 0.58	0.21 ± 0.19	1237663543678992867	0	10.98 ± 0.10	9.17 ± 0.08	-12.24 ± 0.26	0.32	BOSS
17928	...	P	0.20	0.24 ± 0.05	-0.42 ± 0.45	-0.24 ± 0.14	1237657192515174577	0	11.09 ± 0.09	8.86 ± 0.04	-9.65 ± 0.10	0.26	BOSS
17949	...	P	0.26	0.06 ± 0.05	-0.33 ± 0.70	0.04 ± 0.20	1237663783673332230	10	10.30 ± 0.12	$-999. \pm -999.$	-11.08 ± 0.27	0.33	BOSS
17958	...	P	0.28	-0.07 ± 0.04	1.12 ± 0.61	0.27 ± 0.16	1237663783138755068	10	9.67 ± 0.15	$-999. \pm -999.$	-9.65 ± 0.39	0.51	SDSS
18011	...	P	0.28	0.21 ± 0.07	0.58 ± 1.01	-0.16 ± 0.26	1237663784191525831	2	10.62 ± 0.08	9.02 ± 0.04	-10.05 ± 0.09	0.26	BOSS
18030	2007kq	S	0.16	-0.05 ± 0.03	-0.58 ± 0.25	0.18 ± 0.08	1237663783662649523	1	9.66 ± 0.05	8.52 ± 0.05	-8.97 ± 0.05	0.53	SDSS
18049	...	P	0.29	-0.06 ± 0.06	1.07 ± 0.85	0.10 ± 0.21	1237663783663305098	1	10.12 ± 0.11	8.83 ± 0.07	-9.14 ± 0.12	0.33	BOSS
18083	...	P	0.29	0.13 ± 0.07	-1.12 ± 0.76	-0.35 ± 0.22	1237663782602670523	3	9.61 ± 0.15	$-999. \pm -999.$	$-999. \pm -999.$	0.53	BOSS
18189	...	P	0.29	0.17 ± 0.07	-0.77 ± 0.82	-0.34 ± 0.23	1237663783677133016	1	11.09 ± 0.07	8.97 ± 0.03	-9.40 ± 0.07	0.26	BOSS
18201	...	P	0.29	0.04 ± 0.06	1.00 ± 0.89	-0.09 ± 0.21	1237663783144390824	1	10.98 ± 0.08	8.87 ± 0.06	-9.10 ± 0.09	0.28	SDSS
18253	...	P	0.28	0.03 ± 0.08	-1.48 ± 0.65	-0.11 ± 0.22	1237656906348757528	1	10.34 ± 0.10	9.08 ± 0.06	-9.38 ± 0.11	0.37	BOSS
18276	...	P	0.28	0.13 ± 0.06	0.82 ± 0.70	-0.22 ± 0.19	1237666407363117882	1	9.95 ± 0.13	8.84 ± 0.10	-9.07 ± 0.15	0.29	BOSS
18283	...	P	0.30	0.12 ± 0.07	-1.70 ± 0.65	-0.44 ± 0.22	1237657070090781290	2	11.03 ± 0.07	9.13 ± 0.03	-9.44 ± 0.07	0.28	BOSS
18323	2007kx	S	0.15	-0.04 ± 0.03	0.21 ± 0.22	0.16 ± 0.08	1237657191980466833	1	9.36 ± 0.09	8.62 ± 0.11	-9.36 ± 0.11	0.35	BOSS
18324	...	P	0.27	0.08 ± 0.06	-0.45 ± 0.61	-0.11 ± 0.20	1237678434327921353	0	9.78 ± 0.16	251.83 ± 341.32	-10.68 ± 0.80	0.44	BOSS
18325	2007mv	S	0.26	-0.07 ± 0.04	0.41 ± 0.39	0.05 ± 0.13	1237657191445954792	10	11.51 ± 0.15	8.79 ± 0.08	-9.74 ± 0.15	0.18	BOSS
18333	...	P	0.25	0.16 ± 0.06	-0.87 ± 0.60	-0.28 ± 0.19	1237666340800823625	1	10.49 ± 0.08	8.94 ± 0.03	-9.32 ± 0.09	0.28	BOSS
18362	...	P	0.24	0.02 ± 0.05	-1.04 ± 0.42	-0.06 ± 0.15	1237657190909673715	1	10.72 ± 0.09	8.93 ± 0.06	-9.84 ± 0.10	0.32	BOSS
18415	2007la	S	0.13	-0.09 ± 0.03	-1.63 ± 0.17	0.04 ± 0.07	1237678617407979650	3	10.99 ± 0.09	$-999. \pm -999.$	$-999. \pm -999.$	0.43	SDSS
18456	2007lk	S	0.22	0.05 ± 0.03	0.56 ± 0.33	-0.26 ± 0.10	1237663783673397409	10	10.79 ± 0.12	8.96 ± 0.07	-10.82 ± 0.14	0.35	BOSS
18463	2007kv	S	0.27	-0.03 ± 0.04	0.97 ± 0.42	-0.02 ± 0.14	1237663784741961992	1	10.24 ± 0.10	9.02 ± 0.04	-9.47 ± 0.11	0.33	BOSS
18588	...	P	0.25	0.17 ± 0.07	1.53 ± 1.02	0.40 ± 0.25	1237660024494358839	1	9.59 ± 0.08	8.64 ± 0.08	-8.51 ± 0.09	0.36	BOSS
18602	2007lo	S	0.14	0.06 ± 0.03	0.91 ± 0.19	0.06 ± 0.07	1237663479798104844	3	9.30 ± 0.11	$-999. \pm -999.$	$-999. \pm -999.$	0.31	BOSS
18604	2007lp	S	0.18	-0.04 ± 0.03	-2.10 ± 0.22	0.17 ± 0.07	1237663479798956397	3	11.05 ± 0.08	$-999. \pm -999.$	$-999. \pm -999.$	0.32	BOSS
18650	2007lt	S	0.11	-0.04 ± 0.02	0.89 ± 0.12	0.15 ± 0.06	1237663479256646245	0	8.91 ± 0.08	8.53 ± 0.12	-9.41 ± 0.09	0.38	BOSS
18697	2007ma	S	0.11	0.00 ± 0.02	0.75 ± 0.12	-0.05 ± 0.06	1237657189836390529	1	10.52 ± 0.05	8.97 ± 0.03	-9.58 ± 0.05	0.26	SDSS
18740	2007mc	S	0.15	0.03 ± 0.02	-0.04 ± 0.13	-0.16 ± 0.06	1237663785278505244	1	10.66 ± 0.09	8.92 ± 0.07	-9.67 ± 0.09	0.19	BOSS

Table A.1 (cont'd)

CID	IAU Name*	Type^{*,a}	Redshift*	SALT2 c	SALT2 x_1	HR^{b}(mag)	DR8 HostID*	BPT^{c}	log(M/$M_{\odot}$)*,†	12 + log(O/H)†	log(sSFR)†	gFF^{d}	Source
18749	2007mb	S	0.19	0.06 ± 0.03	-1.41 ± 0.39	-0.07 ± 0.10	1237663204919672933	3	11.17 ± 0.08	$-999. \pm -999.$	$-999. \pm -999.$	0.24	BOSS
18787	2007mf	S	0.19	0.04 ± 0.03	0.18 ± 0.45	0.35 ± 0.10	1237657069549519104	2	11.07 ± 0.13	8.96 ± 0.10	-10.22 ± 0.15	0.17	BOSS
18804	2007me	S	0.20	-0.06 ± 0.02	0.91 ± 0.20	-0.11 ± 0.07	1237666407379763650	3	10.30 ± 0.08	$-999. \pm -999.$	$-999. \pm -999.$	0.14	BOSS
18809	2007mi	S	0.13	-0.08 ± 0.03	-1.17 ± 0.18	-0.01 ± 0.11	1237666301629563188	10	11.14 ± 0.09	$-999. \pm -999.$	-11.17 ± 0.34	0.38	SDSS
18835	2007mj	S	0.12	-0.01 ± 0.03	0.76 ± 0.11	-0.05 ± 0.06	1237666301093937304	3	10.79 ± 0.10	$-999. \pm -999.$	$-999. \pm -999.$	0.31	SDSS
18855	2007mh	S	0.13	-0.03 ± 0.03	0.25 ± 0.15	0.02 ± 0.06	1237666301091709356	2	10.37 ± 0.06	9.09 ± 0.08	-9.98 ± 0.07	0.29	SDSS
18940	2007sb	S	0.21	-0.02 ± 0.03	-0.88 ± 0.23	-0.10 ± 0.08	1237657191446610208	1	10.23 ± 0.08	8.98 ± 0.06	-9.82 ± 0.09	0.16	BOSS
18965	2007ne	S	0.21	-0.12 ± 0.03	-0.61 ± 0.23	0.05 ± 0.09	1237666340798202045	3	10.63 ± 0.12	9.12 ± 0.04	-9.96 ± 0.13	0.27	BOSS
18971	...	P	0.27	0.05 ± 0.06	-1.51 ± 0.62	-0.03 ± 0.18	1237680099166912698	0	11.19 ± 0.16	9.09 ± 0.08	-10.44 ± 0.22	0.28	BOSS
19000	...	P	0.29	-0.06 ± 0.04	0.86 ± 0.38	-0.09 ± 0.12	1237657070089994814	10	9.89 ± 0.13	$-999. \pm -999.$	-9.11 ± 0.14	0.40	BOSS
19002	2007nh	S	0.27	-0.09 ± 0.03	0.34 ± 0.32	-0.07 ± 0.10	1237657070092025931	3	10.72 ± 0.09	$-999. \pm -999.$	$-999. \pm -999.$	0.43	BOSS
19027	2007my	S	0.29	0.00 ± 0.03	0.55 ± 0.56	-0.36 ± 0.14	1237656568119231185	1	9.59 ± 0.14	8.37 ± 0.27	-9.01 ± 0.15	0.37	BOSS
19051	2007nb	S	0.28	-0.04 ± 0.03	0.73 ± 0.30	-0.06 ± 0.09	1237663277923959057	3	11.29 ± 0.11	$-999. \pm -999.$	$-999. \pm -999.$	0.30	BOSS
19052	...	P	0.29	-0.06 ± 0.08	-1.71 ± 0.76	0.10 ± 0.25	1237663277924811375	3	10.13 ± 0.15	$-999. \pm -999.$	$-999. \pm -999.$	0.20	BOSS
19149	2007ni	S	0.21	-0.02 ± 0.03	1.05 ± 0.19	-0.42 ± 0.07	1237663783674315119	1	9.61 ± 0.10	8.71 ± 0.08	-8.97 ± 0.11	0.33	BOSS
19274	...	P	0.25	0.07 ± 0.05	-0.42 ± 0.81	0.17 ± 0.18	1237666407366001228	1	10.05 ± 0.12	9.07 ± 0.06	-9.59 ± 0.13	0.39	BOSS
19341	2007nf	S	0.24	0.01 ± 0.04	-1.48 ± 0.36	-0.10 ± 0.13	1237666339725508846	3	11.02 ± 0.09	9.65 ± 0.09	-15.10 ± 2.03	0.34	BOSS
19347	...	P	0.26	-0.01 ± 0.04	-0.28 ± 0.51	0.14 ± 0.13	1237657071160590831	10	9.71 ± 0.14	8.33 ± 0.47	-9.23 ± 0.17	0.21	BOSS
19353	2007nj	S	0.15	0.04 ± 0.03	0.91 ± 0.21	-0.01 ± 0.07	1237657586562105551	1	11.00 ± 0.06	8.88 ± 0.06	-9.61 ± 0.07	0.20	SDSS
19414	...	P	0.29	0.20 ± 0.07	1.31 ± 1.15	-0.06 ± 0.28	1237663479258022833	2	11.19 ± 0.14	9.24 ± 0.10	-12.14 ± 0.19	0.25	BOSS
19616	2007ok	S	0.17	-0.03 ± 0.03	0.14 ± 0.19	-0.07 ± 0.06	1237663784213610757	1	11.04 ± 0.05	8.99 ± 0.02	-9.17 ± 0.05	0.35	SDSS
19652	...	P	0.25	0.22 ± 0.07	-0.99 ± 0.67	-0.28 ± 0.18	1237663278459322853	1	10.15 ± 0.10	8.79 ± 0.08	-9.31 ± 0.11	0.20	BOSS
19708	...	P	0.24	-0.04 ± 0.04	-0.91 ± 0.31	-0.40 ± 0.10	1237657587098583274	3	10.91 ± 0.09	$-999. \pm -999.$	$-999. \pm -999.$	0.42	BOSS
19723	...	P	0.26	-0.02 ± 0.04	-0.44 ± 0.37	0.03 ± 0.11	1237663543686725995	1	10.16 ± 0.09	9.00 ± 0.03	-8.56 ± 0.10	0.36	BOSS
19769	...	P	0.25	0.17 ± 0.05	-0.40 ± 0.62	-0.34 ± 0.15	1237656906350920059	1	10.28 ± 0.12	8.95 ± 0.05	-9.71 ± 0.13	0.27	BOSS
19775	2007pc	S	0.14	0.09 ± 0.03	-0.22 ± 0.20	-0.03 ± 0.07	1237678617399853623	0	10.49 ± 0.11	8.90 ± 0.05	-10.09 ± 0.12	0.35	BOSS
19821	...	P	0.27	-0.10 ± 0.05	-0.91 ± 0.43	0.15 ± 0.16	1237663278463189658	2	10.54 ± 0.12	9.01 ± 0.10	-10.31 ± 0.15	0.40	BOSS
19969	2007pt	S	0.18	0.02 ± 0.03	0.06 ± 0.25	-0.08 ± 0.07	1237663783674511434	1	10.37 ± 0.07	9.02 ± 0.03	-9.11 ± 0.08	0.49	SDSS
19990	2007ps	S	0.25	-0.09 ± 0.04	-1.28 ± 0.35	0.05 ± 0.12	1237663783675757163	0	10.63 ± 0.18	9.24 ± 0.14	-12.23 ± 0.32	0.39	BOSS
20033	...	P	0.25	0.08 ± 0.04	-0.85 ± 0.54	-0.20 ± 0.13	1237663783133708698	0	10.62 ± 0.09	9.11 ± 0.17	-11.31 ± 0.15	0.38	BOSS
20040	2007rf	S	0.29	-0.11 ± 0.05	1.14 ± 0.73	0.00 ± 0.16	1237678617404179648	3	10.26 ± 0.14	$-999. \pm -999.$	$-999. \pm -999.$	0.46	BOSS
20046	...	P	0.26	0.01 ± 0.04	1.64 ± 0.53	0.06 ± 0.13	1237663544215995236	1	10.03 ± 0.10	8.97 ± 0.05	-9.00 ± 0.12	0.44	BOSS
20048	2007pq	S	0.19	0.01 ± 0.04	-0.68 ± 0.52	0.07 ± 0.12	1237663544223793475	1	10.86 ± 0.09	9.30 ± 0.13	-13.66 ± 0.53	0.37	BOSS
20051	2007pv	S	0.24	0.00 ± 0.04	2.94 ± 0.74	0.33 ± 0.15	1237678595929801315	1	9.95 ± 0.08	8.82 ± 0.04	-9.19 ± 0.08	0.32	BOSS
20084	2007pd	S	0.14	0.14 ± 0.03	0.07 ± 0.29	0.10 ± 0.08	1237666407363444800	1	9.19 ± 0.10	8.71 ± 0.05	-9.30 ± 0.10	1.93	BOSS
20088	...	S	0.24	-0.14 ± 0.03	-0.22 ± 0.22	0.00 ± 0.08	1237663204919935202	2	11.38 ± 0.11	9.05 ± 0.06	-10.47 ± 0.11	0.22	BOSS
20111	2007pw	S	0.24	0.01 ± 0.04	0.00 ± 0.61	0.03 ± 0.14	1237666408439940055	0	10.93 ± 0.12	8.92 ± 0.10	-11.02 ± 0.18	0.23	BOSS
20125	...	P	0.17	0.05 ± 0.03	-0.74 ± 0.22	-0.18 ± 0.08	1237663785282371709	3	11.03 ± 0.06	$-999. \pm -999.$	$-999. \pm -999.$	0.30	BOSS
20185	...	P	0.25	0.06 ± 0.08	0.56 ± 1.16	0.66 ± 0.24	1237678617419186293	1	10.55 ± 0.08	8.94 ± 0.04	-8.97 ± 0.09	0.34	BOSS
20227	2007qi	S	0.28	-0.15 ± 0.04	-1.15 ± 0.55	0.12 ± 0.15	1237657190900433560	2	11.05 ± 0.17	9.05 ± 0.09	-10.23 ± 0.19	0.16	BOSS
20232	...	P	0.22	0.01 ± 0.04	-1.05 ± 0.56	-0.23 ± 0.12	1237657190908297506	0	11.21 ± 0.11	9.27 ± 16.43	-8.71 ± 0.12	0.28	BOSS
20364	2007qo	S	0.22	0.04 ± 0.02	0.31 ± 0.74	-0.05 ± 0.13	1237657069547815314	3	10.39 ± 0.08	$-999. \pm -999.$	$-999. \pm -999.$	0.36	BOSS
20376	2007re	S	0.21	0.16 ± 0.04	-1.19 ± 0.44	-0.45 ± 0.11	1237663542604465540	3	10.72 ± 0.14	$-999. \pm -999.$	$-999. \pm -999.$	0.33	BOSS
20467	...	P	0.27	-0.07 ± 0.04	0.96 ± 0.54	0.29 ± 0.14	1237663785279881489	10	9.91 ± 0.11	8.84 ± 0.08	-9.59 ± 0.13	0.40	BOSS
20545	...	P	0.19	0.17 ± 0.03	-1.66 ± 0.50	-0.15 ± 0.10	1237663542609248694	3	10.52 ± 0.08	$-999. \pm -999.$	$-999. \pm -999.$	0.22	BOSS
20663	...	P	0.30	-0.06 ± 0.06	-0.10 ± 0.46	0.02 ± 0.19	1237663204921377321	1	10.81 ± 0.13	8.85 ± 0.06	-9.22 ± 0.14	0.29	BOSS
20687	2007ri	S	0.19	0.14 ± 0.05	-0.65 ± 0.74	-0.20 ± 0.14	1237666340799643790	1	10.98 ± 0.07	9.12 ± 0.03	-9.89 ± 0.07	0.20	BOSS
20721	...	P	0.21	0.22 ± 0.05	-0.50 ± 0.82	-0.01 ± 0.16	1237663542606103297	1	10.47 ± 0.08	9.01 ± 0.02	-9.28 ± 0.08	0.33	SDSS
20744	...	P	0.28	0.01 ± 0.05	-0.41 ± 0.89	-0.27 ± 0.19	1237666408436531439	3	11.03 ± 0.12	$-999. \pm -999.$	$-999. \pm -999.$	0.33	BOSS

Table A.1 (cont'd)

CID	IAU Name*	Type^{*,a}	Redshift*	SALT2 c	SALT2 x_1	HR^{b}(mag)	DR8 HostID*	BPT^{c}	log(M/$M_{\odot}$)*,†	12 + log(O/H)†	log(sSFR)†	gFF^{d}	Source
20768	2007qq	S	0.24	0.07 ± 0.06	-0.78 ± 1.17	0.32 ± 0.20	1237657584950379205	0	11.02 ± 0.09	$-999. \pm -999.$	-10.12 ± 0.14	0.12	BOSS
21858	...	P	0.27	0.13 ± 0.08	-1.58 ± 1.43	0.06 ± 0.32	1237657192516419782	3	11.14 ± 0.10	$-999. \pm -999.$	$-999. \pm -999.$	0.24	BOSS

*As specified in S14.

†Measurement errors on derived host-galaxy properties do not include systematic uncertainties; -999 indicates no measurement could be made.

[a]Denotes if the SN Ia is spectroscopically confirmed (S) or photometrically typed (P).

[b]Uncertainties on HR do not include the intrinsic ~ 0.1 mag scatter.

[c]BPT diagnostic flag that indicates a star-forming (1), composite (2) galaxy, or AGN (0). Star-forming (10) and composite (20) hosts as determined by the BPT diagnostic where some line fluxes are measured to be zero are also included. In some cases we cannot measure the necessary line fluxes for the BPT diagnostic (3).

[d]g-band fiber fraction.

Appendix B

Supplemental DES Education and Public Outreach Materials and Analysis

B.1 Program Logic Models

In this Appendix we present logic models for The Darchive, DEST4TD, DarkBites, and DEScientist of the Week EPO Initiatives. In each model, we describe the inputs, actions, and product outputs created by the EPO coordinators and participating scientists. We also present the DES-specific outcomes, as well as the predicted short-term, medium-term, and long-term outcomes. We encourage readers to treat these logic models as planning outlines for the respective projects and leave details on project evaluation for future work.

B.2 Internal Survey of EPO Projects

Approximately one year after the formation of the EPOC, we conducted a survey to gauge collaboration members' awareness of and attitudes towards the DES EPO program in general as well as four specific EPO initiatives. We created an online survey and emailed it to the entire collaboration, asking all collaboration members to participate. We also advertised the survey at the Fall 2015 collaboration meeting. Small incentives were offered for

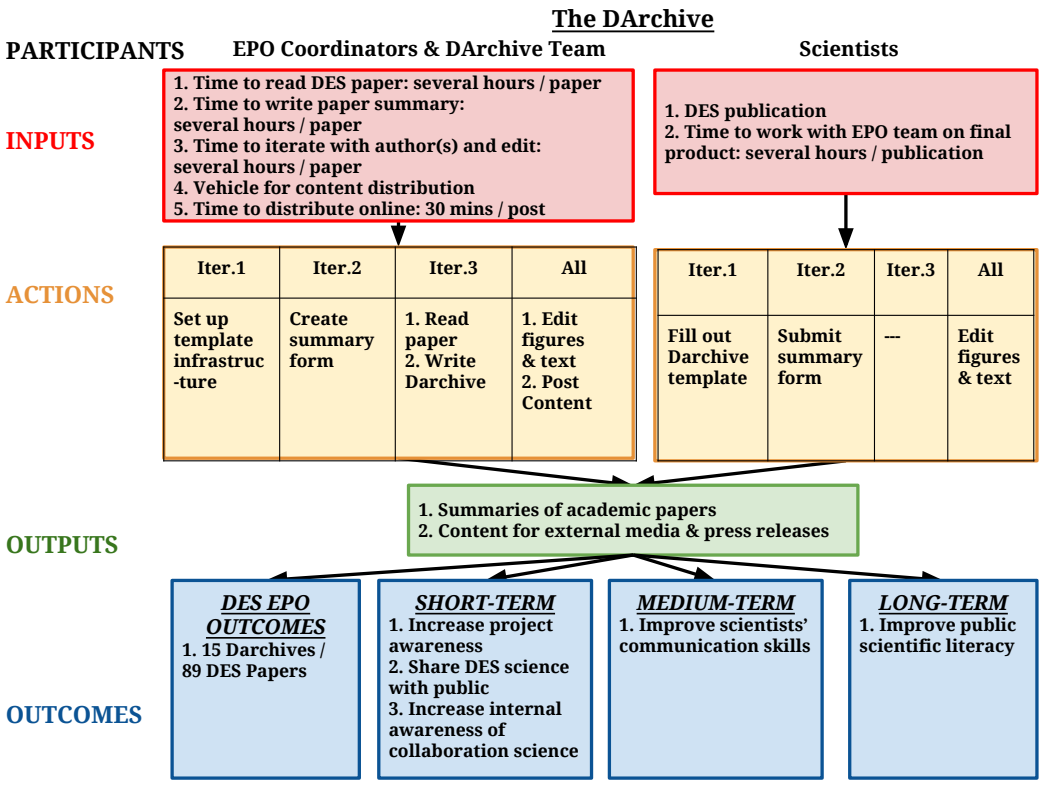

Figure B.1: Logic model describing The DArchive project structure and outcomes.

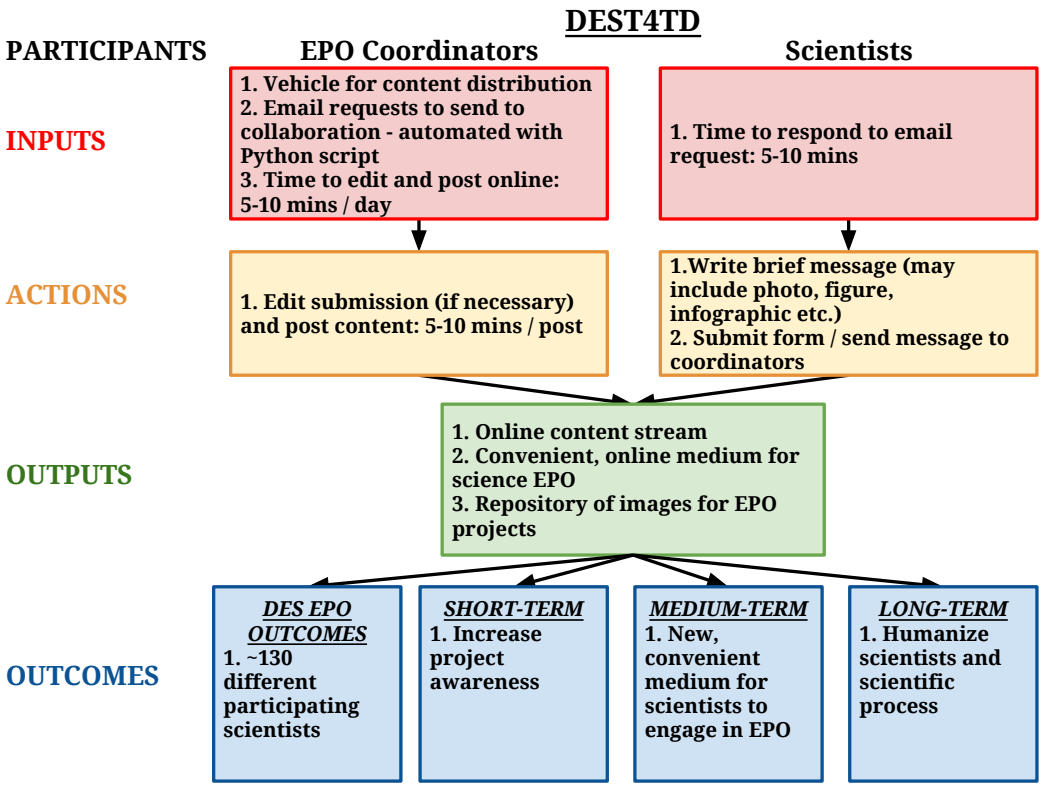

Figure B.2: Logic model describing DEST4TD project structure and outcomes.

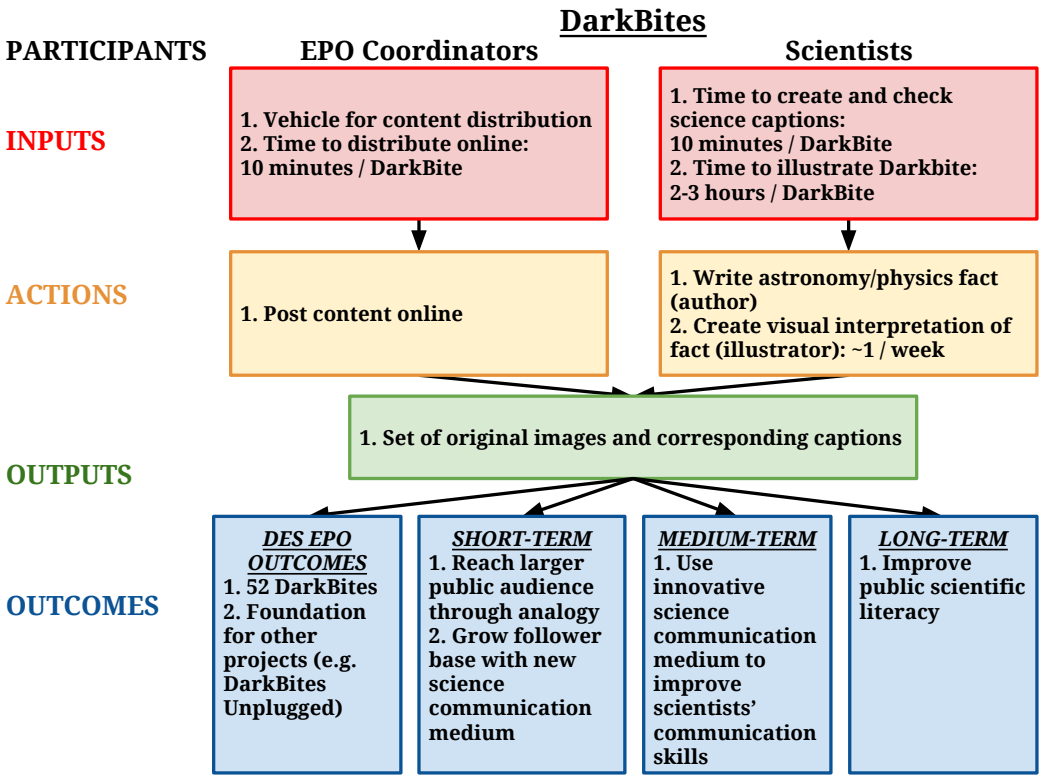

Figure B.3: Logic model describing DarkBites project structure and outcomes.

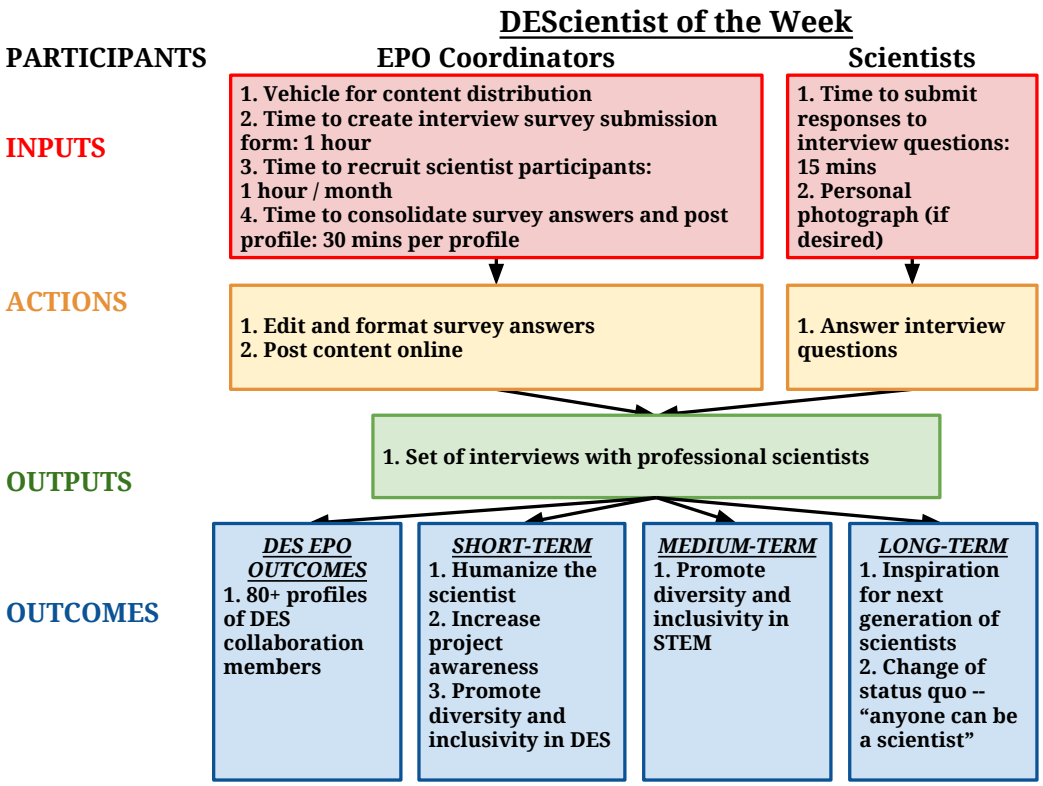

Figure B.4: Logic model describing DEScientist of the Week project structure and outcomes.

those who participated in the survey. A total of 90 collaboration members participated.

Here we include a transcribed copy of the survey. Asterisks indicate questions which required a response. Participants were offered the opportunity to exit the survey after a few key sections; these are indicated with investigator notes. The online version of the survey included examples of the particular EPO initiatives for those who indicated they were unfamiliar with a particular project. We do not include these examples here.

DES Education & Public Outreach (EPO) Feedback Form

Thanks for checking out the EPO evaluation form! We'd very much like to know your thoughts about DES EPO projects.

The form is divided into several sections. There are four sections about specific outreach projects and some general questions at the end. The questionnaire is a bit long (filling out the whole form may take 20 minutes), but you don't have to complete the entire thing!

Thanks for your participation!
The EPO Committee

***Name:**_____

***Institution:**_____

***Email Address:**_____

***Current Position**
☐ Graduate Student ☐ Postdoc ☐ Faculty/Professor ☐ Staff Scientist ☐ Other:

DES SOCIAL MEDIA (SM) PROJECTS

***What social media platforms do you use?**
Please select any that apply
☐ Facebook ☐ Twitter ☐ Instagram ☐ Snapchat ☐ None ☐ Other:

***Do you know where to find DES social media posts?**
☐ Yes ☐ No ☐ What's social media??

DES Thought for the Day (DEST4TD)
***Are you familiar with the DES Thought for the Day (DEST4TD) project?**
☐ Yes ☐ No ☐ Yes, but I could use a refresher
Investigator Note: If the participant indicated anything other than "Yes", he/she was sent to an example DEST4TD.

Check all that apply
☐ I have contributed a DEST4TD ☐ I would contribute a DEST4TD
☐ I think DEST4TD is a worthwhile EPO initiative ☐ I think DEST4TD can be improved

T4TD Feedback
Looking for inspiration - What do you think of the T4TD posts? Have you been asked to submit a T4TD? What would encourage you to participate in T4TD?_____

DEScientist of the Week
***Are you familiar with the DEScientist of the Week project?**
☐ Yes ☐ No ☐ Yes, but I could use a refresher
Investigator Note: If the participant indicated anything other than "Yes", he/she was sent to an example DEScientist of the Week.

Check all that apply
☐ I have participated in DEScientist of the Week ☐ I would participate in DEScientist of the Week
☐ I think DEScientist of the Week is a worthwhile EPO project ☐ I think DEScientist of the Week can be improved

DEScientist of the Week (SoW) Feedback
Looking for inspiration - What do you think of SoW? Would you be willing to participate in SoW?
_____

Would you like to continue to questions about The DArchive?

☐ Sure! ☐ No thanks, I'd like to go to the final page.

Investigator Note: As the DArchive is a longer project, we gave participants the opportunity to end the survey at this point.

The DArchive

Are you familiar with The DArchive project?

☐ Yes, and I've read a post recently ☐ Yes, but I haven't read a post before

☐ No ☐ Yes, but I could use a refresher

Investigator Note: If the participant indicated anything other than "Yes, and I've read a post recently", he/she was sent to an example DArchive Post.

Check all that apply

☐ I have submitted a DArchive summary ☐ I would be willing to write a DArchive summary

☐ I think the DArchive is a worthwhile EPO project ☐ I think the DArchive can be improved

The DArchive Feedback

Looking for inspiration - What do you think of The DArchive? Do you think the posted DArchives summarized the DES papers well? Would you be willing to write a DArchive summary?

_____

Would you like to continue to questions about Dark Energy Detectives?

☐ Sure! ☐ No thanks, I'd like to go to the final page.

Investigator Note: As Dark Energy Detectives is a longer project, we gave participants the opportunity to end the survey at this point.

Dark Energy Detectives (DED)

Are you familiar with The Dark Energy Detectives project?

☐ Yes ☐ No ☐ Yes, but I could use a refresher

Investigator Note: If the participant indicated anything other than "Yes", he/she was sent to an example Dark Energy Detectives.

Check all that apply

☐ I have written a DED post ☐ I would be willing to write a DED post

☐ I think the DED is a worthwhile DES project ☐ I think DED can be improved

Dark Energy Detectives Feedback

Looking for inspiration - What would encourage you to write a post? Do you like the theme of the blog?

_____

Last Few General Questions

You're almost done!

***Have you received an email to participate in a DES EPO project? Did you participate? If not, what would inspire you to get involved?** You can answer for one project in particular or several.

_____

***Do you read the monthly EPO Newsletter? Do you find it useful? Do you think it can be improved?**

_____

***The EPO Committee is working to maintain a record of all DES EPO activity. Did you know you can record non-DES STEM outreach activity?**

☐ Yes, and I have submitted a form ☐ Yes, but I have not submitted the form

☐ No ☐ No, I thought it was for only DES-specific events

Bibliography

Abazajian, K. N., Adelman-McCarthy, J. K., Agüeros, M. A., et al.: 2009, *ApJS* **182**, 543

Abbott, B. P., Abbott, R., Abbott, T. D., et al.: 2016, *ApJL* **826**, L13

Ahn, C. P., Alexandroff, R., Allende Prieto, C., et al.: 2014, *ApJS* **211**, 17

Ahn, C. P., Alexandroff, R., Allende Prieto, C., et al.: 2012, *ApJS* **203**, 21

Aihara, H., Allende Prieto, C., An, D., et al.: 2011, *ApJS* **193**, 29

Andrews, E., Weavpolir, A., Hanley, D., Shamatha, J., and Melton, G.: 2005, *Journal of Geoscience Education* **53(3)**, 281

Andrieu, C. and Roberts, G. O.: 2009, *Ann. Statist.* **37(2)**, 697

Annis, J., Soares-Santos, M., Strauss, M. A., et al.: 2014, *ApJ* **794**, 120

Astier, P., El Hage, P., Guy, J., et al.: 2013, *A&A* **557**, A55

Astier, P., Guy, J., Regnault, N., et al.: 2006, *A&A* **447**, 31

Baade, W. and Zwicky, F.: 1934, *Proceedings of the National Academy of Science* **20**, 254

Baldwin, J. A., Phillips, M. M., and Terlevich, R.: 1981, *PASP* **93**, 5

Barman, C. R., Ostlund, K. L., Gatto, C. C., and Halferty, M.: 1997, in *1997 AETS Conference papers and summaries of presentations*, Fifth grade student's perceptions about scientists and how they study and use science, p. 711

Bauer, M. W., Jensen, P., and Jensen, P.: 2011, *Public Understanding of Science* **20(1)**, 26

Beaumont, M. A.: 2003, *Genetics* **164(3)**, 1139

Beaumont, M. A., Cornuet, J.-M., Marin, J.-M., and Robert, C. P.: 2008, arXiv:0805.2256

Berendsen, M., White, V., Devore, E., and Reynolds, M.: 2008, in *EPO and a Changing World: Creating Linkages and Expanding Partnerships*, Vol. 389, p. 43

Bernstein, J. P., Kessler, R., Kuhlmann, S., et al.: 2012, *ApJ* **753**, 152

Besley, J. C. and Tanner, A. H.: 2011, *Science Communication* **33(2)**, 239

Betoule, M., Kessler, R., Guy, J., et al.: 2014, *A&A* **568**, A22

Bonvin, V., Courbin, F., Suyu, S. H., et al.: 2017, *MNRAS* **465**, 4914

Borne, K. D., Jacoby, S., Carney, K., et al.: 2009, in *Astro2010: The Astronomy and Astrophysics Decadal Survey*

Brinchmann, J., Charlot, S., White, S. D. M., et al.: 2004, *MNRAS* **351**, 1151

Bubela, T., Nisbet, M. C., Borchelt, R., et al.: 2009, *Nature biotechnology* **27(6)**, 514

Bulla, M., Sim, S. A., Pakmor, R., et al.: 2016, *MNRAS* **455**, 1060

Burns, T. W., O'Connor, D. J., and Stocklmayer, S. M.: 2003, *Public Understanding of Science* **12(2)**, 183

Calzetti, D.: 2001, *PASP* **113**, 1449

Campbell, H., D'Andrea, C. B., Nichol, R. C., et al.: 2013, *ApJ* **763**, 88

Campbell, H., Fraser, M., and Gilmore, G.: 2016, *MNRAS* **457**, 3470

Cao, Y., Kulkarni, S. R., Howell, D. A., et al.: 2015, *Nature* **521**, 328

Cappellari, M. and Emsellem, E.: 2004, *PASP* **116**, 138

Cardelli, J. A., Clayton, G. C., and Mathis, J. S.: 1989, *ApJ* **345**, 245

Ceci, S. J., Ginther, D. K., Kahn, S., and Williams, W. M.: 2014, *Psychological Science in the Public Interest* **15(3)**, 75, PMID: 26172066

Chabrier, G.: 2003, *PASP* **115**, 763

Childress, M., Aldering, G., Antilogus, P., et al.: 2013, *ApJ* **770**, 108

Childress, M. J., Wolf, C., and Zahid, H. J.: 2014, *MNRAS* **445**, 1898

Chotard, N., Gangler, E., Aldering, G., et al.: 2011, *A&A* **529**, L4

Cleveland, W. S., Gross, E., and Shyu, W. M.: 1992, *Local regression models. Chapter 8 of Statistical Models in S eds J.M Chambers and T.J. Hastie*, Wadsworth & Brooks/Cole

Colgate, S. A. and McKee, C.: 1969, *ApJ* **157**, 623

Conley, A., Guy, J., Sullivan, M., et al.: 2011, *ApJS* **192**, 1

Conroy, C.: 2013, *ARA&A* **51**, 393

Conroy, C. and Gunn, J. E.: 2010, *ApJ* **712**, 833

Conroy, C., Gunn, J. E., and White, M.: 2009, *ApJ* **699**, 486

D'Agostini, G.: 1995, arXiv:hep-ph/9512295

D'Andrea, C. B., Gupta, R. R., Sako, M., et al.: 2011, *ApJ* **743**, 172

Dang, L. and Russo, P.: 2015, *Communicating Astronomy with the Public Journal* **18**, 16

Dawson, K. S., Schlegel, D. J., Ahn, C. P., et al.: 2013, *AJ* **145**, 10

Dilday, B., Howell, D. A., Cenko, S. B., et al.: 2012, *Science* **337(6097)**, 942

Dodelson, S. and Schneider, M. D.: 2013, *Phys. Rev. D* **88(6)**, 063537

Duggan, M. and Brenner, J.: 2013, *The demographics of social media users, 2012*, Vol. 14, Pew Research Center's Internet & American Life Project Washington, DC

Durant, J. R., Evans, G. A., and Thomas, G. P.: 1989, *Nature* **340(6228)**, 11

Ecklund, E. H., James, S. A., and Lincoln, A. E.: 2012, *PLOS ONE* **7(5)**, 1

Eisenstein, D. J., Weinberg, D. H., Agol, E., et al.: 2011, *AJ* **142**, 72

Ferland, G. J., Korista, K. T., Verner, D. A., et al.: 1998, *PASP* **110**, 761

Filippenko, A. V.: 1997, *ARA&A* **35**, 309

Flaugher, B., Diehl, H. T., Honscheid, K., et al.: 2015, *AJ* **150**, 150

Foreman-Mackey, D., Hogg, D. W., Lang, D., and Goodman, J.: 2013, *PASP* **125**, 306

Frieman, J. A., Bassett, B., Becker, A., et al.: 2008, *AJ* **135**, 338

Fukugita, M., Ichikawa, T., Gunn, J. E., et al.: 1996, *AJ* **111**, 1748

Gallagher, J. S., Garnavich, P. M., Berlind, P., et al.: 2005, *ApJ* **634**, 210

Gallagher, J. S., Garnavich, P. M., Caldwell, N., et al.: 2008, *ApJ* **685**, 752

Ganeshalingam, M., Li, W., and Filippenko, A. V.: 2013, *MNRAS* **433**, 2240

Gelman, A., Carlin, J. B., Stern, H. S., and Rubin, D. B.: 2014, *Bayesian data analysis*, Vol. 2, Chapman & Hall/CRC Boca Raton, FL, USA

Gerdes, D., Sako, M., Hamilton, S., et al.: 2017, arXiv:1702.00731

Gibbs, M. G. and Berendsen, M.: 2006, *Astronomy Education Review* 5(2)

Gilbank, D. G., Baldry, I. K., Balogh, M. L., Glazebrook, K., and Bower, R. G.: 2010, *MNRAS* **405**, 2594

Goodman, J. and Weare, J.: 2010, *Communications in applied mathematics and computational science* **5(1)**, 65

Grieb, J. N., Sánchez, A. G., Salazar-Albornoz, S., et al.: 2017, *MNRAS* **467(2)**, 2085

Griffin, I.: 2003, *The Hubble Space Telescope Education and Outreach Program*, pp 139–156, Springer Netherlands, Dordrecht

Gull, S. F.: 1989, in *Maximum Entropy and Bayesian Methods*, pp 511–518, Springer

Gunn, J. E., Carr, M., Rockosi, C., et al.: 1998, *AJ* **116**, 3040

Gunn, J. E., Siegmund, W. A., Mannery, E. J., et al.: 2006, *AJ* **131**, 2332

Gupta, R. R., D'Andrea, C. B., Sako, M., et al.: 2011, *ApJ* **740**, 92

Guy, J., Astier, P., Baumont, S., et al.: 2007, *A&A* **466**, 11

Guy, J., Sullivan, M., Conley, A., et al.: 2010, *A&A* **523**, A7

Hamuy, M., Phillips, M. M., Suntzeff, N. B., et al.: 1996, *AJ* **112**, 2391

Hamuy, M., Trager, S. C., Pinto, P. A., et al.: 2000, *AJ* **120**, 1479

Hayden, B. T., Gupta, R. R., Garnavich, P. M., et al.: 2013, *ApJ* **764**, 191

Haywood, B. K. and Besley, J. C.: 2014, *Public Understanding of Science* **23(1)**, 92

Heck, A. and Madsen, C.: 2013, *Astronomy communication*, Vol. 290, Springer Science & Business Media

Hillebrandt, W. and Niemeyer, J. C.: 2000, *ARA&A* **38**, 191

Hinshaw, G., Larson, D., Komatsu, E., et al.: 2013, *ApJS* **208**, 19

Hlozek, R., Kunz, M., Bassett, B., et al.: 2012, *ApJ* **752**, 79

Holtzman, J. A., Marriner, J., Kessler, R., et al.: 2008, *AJ* **136**, 2306

Howell, D. A.: 2011, *Nature Communications* **2**, 350

Howell, D. A., Sullivan, M., Brown, E. F., et al.: 2009, *ApJ* **691**, 661

Hubble, E.: 1929, *Proceedings of the National Academy of Science* **15**, 168

Iben, Jr., I. and Tutukov, A. V.: 1984, *ApJS* **54**, 335

Ivezić, Ž., Smith, J. A., Miknaitis, G., et al.: 2007, *AJ* **134**, 973

Ivie, R. and Ray, K.: 2005, in *American Institute of Physics Report*, Women in Physics and Astronomy, 2005

Jennings, E., Wolf, R., and Sako, M.: 2016, arXiv:1611.03087

Jensen, E. and Holliman, R.: 2016, *International Journal of Science Education, Part B* **6(1)**, 68

Jensen, P., Rouquier, J.-B., Kreimer, P., and Croissant, Y.: 2008, arXiv:0810.4672

Jha, S., Riess, A. G., and Kirshner, R. P.: 2007, *ApJ* **659**, 122

Johansson, J., Thomas, D., Pforr, J., et al.: 2013, *MNRAS* **435**, 1680

Kaiser, N., Aussel, H., Burke, B. E., et al.: 2002, in J. A. Tyson and S. Wolff (eds.), *Survey and Other Telescope Technologies and Discoveries*, Vol. 4836 of *Proc. SPIE*, pp 154–164

Kasen, D.: 2010, *ApJ* **708**, 1025

Kasen, D., Röpke, F. K., and Woosley, S. E.: 2009, *Nature* **460**, 869

Kasen, D. and Woosley, S. E.: 2007, *ApJ* **656**, 661

Kauffmann, G., Heckman, T. M., Tremonti, C., et al.: 2003a, *MNRAS* **346**, 1055

Kauffmann, G., Heckman, T. M., White, S. D. M., et al.: 2003b, *MNRAS* **341**, 33

Kelly, B. C.: 2007, *ApJ* **665**, 1489

Kelly, P. L., Fox, O. D., Filippenko, A. V., et al.: 2014, *ApJ* **790**, 3

Kelly, P. L., Hicken, M., Burke, D. L., Mandel, K. S., and Kirshner, R. P.: 2010, *ApJ* **715**, 743

Kennicutt, Jr., R. C.: 1998, *ARA&A* **36**, 189

Kessler, R., Becker, A. C., Cinabro, D., et al.: 2009a, *ApJS* **185**, 32

Kessler, R., Bernstein, J. P., Cinabro, D., et al.: 2009b, *PASP* **121**, 1028

Kessler, R., Guy, J., Marriner, J., et al.: 2013, *ApJ* **764**, 48

Kessler, R., Marriner, J., Childress, M., et al.: 2015, *AJ* **150**, 172

Kessler, R. and Scolnic, D.: 2017, *ApJ* **836**, 56

Kewley, L. J. and Dopita, M. A.: 2002, *ApJS* **142**, 35

Kewley, L. J., Dopita, M. A., Sutherland, R. S., Heisler, C. A., and Trevena, J.: 2001, *ApJ* **556**, 121

Kewley, L. J. and Ellison, S. L.: 2008, *ApJ* **681**, 1183

Kewley, L. J., Jansen, R. A., and Geller, M. J.: 2005, *PASP* **117**, 227

Kobulnicky, H. A., Kennicutt, Jr., R. C., and Pizagno, J. L.: 1999, *ApJ* **514**, 544

Kobulnicky, H. A. and Kewley, L. J.: 2004, *ApJ* **617**, 240

Komatsu, E., Smith, K. M., Dunkley, J., et al.: 2011, *ApJS* **192**, 18

Konishi, K., Cinabro, D., Garnavich, P. M., et al.: 2011, arXiv:1101.4269

Kroupa, P.: 2001, *MNRAS* **322**, 231

Kunz, M., Hlozek, R., Bassett, B. A., et al.: 2013, in J. M. Hilbe (ed.), *Astrostatistical Challenges for the New Astronomy, Edited by Joseph M. Hilbe. Springer, 2013, p. 1013, p. 63-86*, p. 1013

Lampeitl, H., Smith, M., Nichol, R. C., et al.: 2010, *ApJ* **722**, 566

Lemaître, G.: 1927, *Annales de la Société Scientifique de Bruxelles* **47**, 49

Lévy-Leblond, J.-M.: 1992, *Public Understanding of Science* **1(1)**, 17

Li, T. S., Simon, J. D., Drlica-Wagner, A., et al.: 2016, arXiv:1611.05052

Li, W., Bloom, J. S., Podsiadlowski, P., et al.: 2011, *Nature* **480**, 348

Losh, S. C.: 2010, *Public Understanding of Science* **19(3)**, 372

LSST Science Collaboration, Abell, P. A., Allison, J., et al.: 2009, arXiv:0912.0201

Madsen, C. and West, R. M.: 2003, *Public Communication of Astronomy*, pp 3–18, Springer Netherlands, Dordrecht

Maeda, K. and Terada, Y.: 2016, *International Journal of Modern Physics D* **25**, 1630024

Mandel, K. S., Scolnic, D., Shariff, H., Foley, R. J., and Kirshner, R. P.: 2016, arXiv:1609.04470

Mandel, K. S., Wood-Vasey, W. M., Friedman, A. S., and Kirshner, R. P.: 2009, *ApJ* **704**, 629

Mannucci, F., Cresci, G., Maiolino, R., Marconi, A., and Gnerucci, A.: 2010, *MNRAS* **408**, 2115

Maraston, C. and Strömbäck, G.: 2011, *MNRAS* **418**, 2785

March, M. C., Trotta, R., Berkes, P., Starkman, G. D., and Vaudrevange, P. M.: 2011, *Monthly Notices of the Royal Astronomical Society* **418(4)**, 2308

Marietta, E., Burrows, A., and Fryxell, B.: 2000, *ApJS* **128**, 615

Marion, G. H., Brown, P. J., VinkÃş, J., et al.: 2016, *The Astrophysical Journal* **820(2)**, 92

Markwardt, C. B.: 2009, in D. A. Bohlender, D. Durand, and P. Dowler (eds.), *Astronomical Data Analysis Software and Systems XVIII*, Vol. 411 of *Astronomical Society of the Pacific Conference Series*, p. 251

Marriner, J., Bernstein, J. P., Kessler, R., et al.: 2011, *ApJ* **740**, 72

McGaugh, S. S.: 1991, *ApJ* **380**, 140

Metropolis, N., Rosenbluth, A. W., Rosenbluth, M. N., Teller, A. H., and Teller, E.: 1953, *J. Chem. Phys.* **21**, 1087

Miknaitis, G., Pignata, G., Rest, A., et al.: 2007, *The Astrophysical Journal* **666(2)**, 674

Miller, J. D.: 1998, *Public understanding of science* **7(3)**, 203

Miller, S.: 2001, *Public understanding of science* **10(1)**, 115

Morrison, C. B. and Schneider, M. D.: 2013, *Journal of Cosmology and Astroparticle Physics* **11**, 009

Mosher, J., Guy, J., Kessler, R., et al.: 2014, *ApJ* **793**, 16

National Research Council: 2001, *Astronomy and Astrophysics in the New Millennium*, The National Academies Press, Washington, DC

National Research Council: 2010a, *Gender Differences at Critical Transitions in the Careers of Science, Engineering, and Mathematics Faculty*, The National Academies Press, Washington, DC

National Research Council: 2010b, *New Worlds, New Horizons in Astronomy and Astrophysics*, The National Academies Press, Washington, DC

Neill, J. D., Sullivan, M., Howell, D. A., et al.: 2009, *ApJ* **707**, 1449

Nisbet, M. C. and Scheufele, D. A.: 2009, *American journal of botany* **96(10)**, 1767

Nomoto, K.: 1982, *ApJ* **253**, 798

Nordin, J., Östman, L., Goobar, A., et al.: 2011, *A&A* **526**, A119

Nugent, P. E., Sullivan, M., Cenko, S. B., et al.: 2011, *Nature* **480**, 344

Olmstead, M. D., Brown, P. J., Sako, M., et al.: 2014, *AJ* **147**, 75

Osterbrock, D. E.: 1989, *Astrophysics of gaseous nebulae and active galactic nuclei*, (Mill Valley, CA: Univ. Science Books)

Pan, Y.-C., Sullivan, M., Maguire, K., et al.: 2014, *MNRAS* **438**, 1391

Parrent, J., Friesen, B., and Parthasarathy, M.: 2014, *Astrophysics and Space Science* **351(1)**, 1

Perlmutter, S., Aldering, G., Goldhaber, G., et al.: 1999, *ApJ* **517**, 565

Perlmutter, S. and Schmidt, B. P.: 2003, in K. Weiler (ed.), *Supernovae and Gamma-Ray Bursters*, Vol. 598 of *Lecture Notes in Physics, Berlin Springer Verlag*, pp 195–217

Perrett, K., Sullivan, M., Conley, A., et al.: 2012, *AJ* **144**, 59

Phillips, M. M.: 1993, *ApJL* **413**, L105

Planck Collaboration, Adam, R., Ade, P. A. R., et al.: 2016, *A&A* **594**, A1

Poliakoff, E. and Webb, T. L.: 2007, *Science Communication* **29(2)**, 242

Price, L. F., Drovandi, C. C., Lee, A., and Nott, D. J.: 2017, *Journal of Computational and Graphical Statistics*

Ptolemy and Toomer, G. J.: 1984, *Ptolemy's Almagest / translated and annotated by G.J. Toomer*, Duckworth London

Raddick, M. J.: 2002, in *American Astronomical Society Meeting Abstracts*, Vol. 34 of *Bulletin of the American Astronomical Society*, p. 1150

Raddick, M. J.: 2008, in C. Garmany, M. Gibbs, and J. W. Moody (eds.), *EPO and a Changing World: Creating Linkages and Expanding Partnerships*, Vol. 389 of *Astronomical Society of the Pacific Conference Series*, p. 461

Riess, A. G., Filippenko, A. V., Challis, P., et al.: 1998, *AJ* **116**, 1009

Riess, A. G., Macri, L. M., Hoffmann, S. L., et al.: 2016, *ApJ* **826**, 56

Riess, A. G., Press, W. H., and Kirshner, R. P.: 1996, *ApJ* **473**, 88

Rigault, M., Copin, Y., Aldering, G., et al.: 2013, *A&A* **560**, A66

Röpke, F. K., Kromer, M., Seitenzahl, I. R., et al.: 2012, *ApJL* **750**, L19

Rosendhal, J., Sakimoto, P., Pertzborn, R., and Cooper, L.: 2004, *Advances in Space Research* **34(10)**, 2127

Rubin, D., Aldering, G., Barbary, K., et al.: 2015, *ApJ* **813**, 137

Rubin, D. B.: 1984, *Ann. Statist.* **12(4)**, 1151

Ryden, B.: 2003, *Introduction to cosmology*, Cambridge University Press

Sakimoto, P.: 2008, in *EPO and a Changing World: Creating Linkages and Expanding Partnerships*, Vol. 389, p. 453

Sako, M., Bassett, B., Becker, A., et al.: 2008, *AJ* **135**, 348

Sako, M., Bassett, B., Becker, A. C., et al.: 2014, arXiv:1401.3317

Sako, M., Bassett, B., Connolly, B., et al.: 2011, *ApJ* **738**, 162

Salpeter, E. E.: 1955, *ApJ* **121**, 161

Sarzi, M., Falcón-Barroso, J., Davies, R. L., et al.: 2006, *MNRAS* **366**, 1151

Schlafly, E. F. and Finkbeiner, D. P.: 2011, *ApJ* **737**, 103

Schlegel, D. J., Finkbeiner, D. P., and Davis, M.: 1998, *ApJ* **500**, 525

Scolnic, D. and Kessler, R.: 2016, *ApJL* **822**, L35

Scolnic, D., Rest, A., Riess, A., et al.: 2014a, *ApJ* **795**, 45

Scolnic, D. M., Riess, A. G., Foley, R. J., et al.: 2014b, *ApJ* **780**, 37

Scott, D. W.: 2015, *Multivariate density estimation: theory, practice, and visualization*, John Wiley & Sons

SDSS Collaboration, Albareti, F. D., Allende Prieto, C., et al.: 2016, arXiv:1608.02013

Shariff, H., Jiao, X., Trotta, R., and van Dyk, D. A.: 2016, *ApJ* **827**, 1

Silverman, B. W.: 1986, *Density estimation for statistics and data analysis*, Vol. 26, CRC press

Smartt, S. J.: 2009, *ARA&A* **47**, 63

Smee, S. A., Gunn, J. E., Uomoto, A., et al.: 2013, *AJ* **146**, 32

Stoughton, C., Adelman, J., Annis, J. T., et al.: 2002, in J. A. Tyson and S. Wolff (eds.), *Survey and Other Telescope Technologies and Discoveries*, Vol. 4836 of *Proc. SPIE*, pp 339–349

Strauss, M. A., Weinberg, D. H., Lupton, R. H., et al.: 2002, *AJ* **124**, 1810

Stritzinger, M., Mazzali, P. A., Sollerman, J., and Benetti, S.: 2006, *A&A* **460**, 793

Sturges, H. A.: 1926, *Journal of the american statistical association* **21(153)**, 65

Sullivan, M., Conley, A., Howell, D. A., et al.: 2010, *MNRAS* **406**, 782

Sullivan, M., Guy, J., Conley, A., et al.: 2011, *ApJ* **737**, 102

Sullivan, M., Le Borgne, D., Pritchet, C. J., et al.: 2006, *ApJ* **648**, 868

Suzuki, N., Rubin, D., Lidman, C., et al.: 2012, *ApJ* **746**, 85

Tan, A.-L., Jocz, J. A., and Zhai, J.: 2015, *Public Understanding of Science* p. 0963662515615086

The Dark Energy Survey Collaboration: 2005, arXiv:astro-ph/0510346

Thomas, D., Steele, O., Maraston, C., et al.: 2013, *MNRAS* **431**, 1383

Thorley, C.: 2016, *Ph.D. thesis*, UCL (University College London)

Timmes, F. X., Brown, E. F., and Truran, J. W.: 2003, *ApJL* **590**, L83

Tripp, R.: 1998, *A&A* **331**, 815

Trotta, R.: 2008, *Contemporary Physics* **49**, 71

Webbink, R. F.: 1984, *ApJ* **277**, 355

Weyant, A., Schafer, C., and Wood-Vasey, W. M.: 2013, *ApJ* **764**, 116

Whelan, J. and Iben, Jr., I.: 1973, *ApJ* **186**, 1007

Wolf, R. C., D'Andrea, C. B., Gupta, R. R., et al.: 2016, *ApJ* **821**, 115

Wood, S. N.: 2010, *Nature* **466(7310)**, 1102

Yocco, V., Jones, E. C., and Storksdieck, M.: 2012, *Astronomy Education Review* **11(1)**, 010109